162

ISSN 1343-2230
CNS-REP-32
April, 2001

CNS Report

Measurement of Single and Double Spin-Flip-Probabilities in Inelastic Deuteron Scattering on ^{28}Si at 270 MeV

Y. Satou

Center for Nuclear Study, Graduate School of Science, the University of Tokyo
Hongo 7-3-1, Bunkyo-ku, Tokyo 113-0033, Japan

Center for Nuclear Study (CNS)

Graduate School of Science, the University of Tokyo
Wako Branch at RIKEN, Hirosawa 2-1, Saitama 351-0198, Japan
Correspondence: cnsoffice@cns.s.u-tokyo.ac.jp

Measurement of Single and Double Spin-Flip-Probabilities in Inelastic Deuteron Scattering on ^{28}Si at 270 MeV

Doctoral Dissertation
by
Yoshiteru Satou

February, 2001; revised on April 24, 2001

Department of Physics
School of Science
University of Tokyo
Hongo 7-3-1, Bunkyo-ku, Tokyo 113-0033, Japan

Abstract

The purpose of this work is to study the isoscalar spin excitations in nuclei through the polarization transfer measurement in inelastic deuteron scattering at E_d=270 MeV. The selective excitation of isoscalar transitions together with the capability of transferring spins to the target nucleus should make the reaction as one of the essential probes of the isoscalar spin excitations. The measurement of deuteron spin-flip probability S_1 provides a means of disentangling between spin and non-spin excitations, while the measurement of deuteron double spin-flip probability S_2 provides a possibility of identifying a new class of spin excitations with two units of spin-transfer.

A focal plane deuteron polarimeter DPOL has been developed at RIKEN Accelerator Research Facility (RARF) by our group. The polarimeter can determine both the vector and tensor polarization components of the deuterons by making simultaneous use of the $\vec{d}$+^{12}C elastic scattering and the ^{1}H($\vec{d}, 2p$) charge exchange reaction as the analyzer reactions.

We have performed the deuteron polarization transfer measurement by using DPOL on ^{28}Si target at E_d=270 MeV for an excitation energy range between 4 and 21 MeV and an angular range between 2.5° and 7.5°. The deuteron single and double spin-flip probabilities have been extracted. A large S_1 value of about 0.2 is observed for the isoscalar spin-flip 1^+ state at 9.50 MeV, while small S_1 values of around 0.05 are obtained for other non-spin-flip states. The S_2 values are close to zero over the measured excitation energy region.

Besides we have measured the cross section and analyzing powers A_y and A_{yy} for discrete levels including the ground state (elastic scattering) in ^{12}C and ^{28}Si using the $(\vec{d}, d')$ reaction at E_d=270 MeV. The measurement is intended to explore the validity of the distorted wave impulse approximation as a reaction model. A deuteron-nucleon t-matrix in free space derived from the three-nucleon Faddeev calculations is utilized as the projectile-nucleon effective interaction. The agreement between the data and theory is found to be well compared to that in the (p, p') reaction at similar incident energies per nucleon.

Contents

List of Tables

List of Figures

Chapter 1

Introduction

1.1 Spin Excitations and Nucleon Induced Reactions

Spin excitations in nuclei have been extensively studied over the past several decades, especially since 1980's with the advent of intermediate energy accelerator facilities producing beams of hadrons and electrons suitable for high resolution nuclear spectroscopy. The spin excitations involve a spin transfer to the nucleus and are called magnetic transitions. The interest in understanding this basic mode of nuclear excitation is due to its close connection to the properties of nuclear matter in the spin-dependent channels. For instance, from the excitation energy systematics one can deduce the strength of spin-dependent interactions inside the nucleus. The magnetic strength distributions are sensitive to various correlation effects and are the testing ground of theoretical models. Furthermore, since the spin excitations are truly microscopic excitations of the nucleus involving the rearrangement of only a few nucleons, they provide a good opportunity to test various microscopic reaction models and spin-dependent projectile-nucleon effective interactions when they are probed through hadron induced reactions.

Most of the recent progress in our understanding of spin excitations comes from the nucleon charge-exchange and inelastic scattering experiments performed at intermediate energy region (100-1000 MeV). These experiments took advantages of the high selectivity of spin-flip excitation modes due to the strong spin-dependence of the nucleon-nucleon interaction at such energy region. Furthermore, interpretation of the data in terms of the distorted wave impulse approximation (DWIA) is expected to be reliable due to the simplicity in the reaction mechanism.

The charge-exchange (p,n) reactions at forward angles have revealed the systematic presence of the 1^+ ($L = 0$) giant Gamow-Teller (GT) resonance in a wide region of the nuclear mass table [1, 2, 3]. The GT transition is a spin-flip, ΔS=1, and isospin-flip, Δ T=1 transition. The GT cross section measured in the (p,n) experiments can be converted into the GT strength. Experimentally only 60 % of the expected total GT strength could be found in the GT peak region. Two different mechanisms have been proposed to explain the so-called quenching of this GT strength, one is the coupling of the delta-hole (Δ-h) states into the low-lying 1^+ states and the other is the configuration mixing due to the two-particle-two-hole ($2p$-$2h$) states. There has been considerable debate as to the relative importance of the two mechanisms.

The giant magnetic dipole (M1) resonance in heavy-mass nuclei was discovered in the forward angle (p, p') reactions [4, 5, 6, 7]. The M1 transition is in an analog relation to the GT state which has an isospin quantum number T equal to that of the M1 state. The measured (p, p') cross sections were compared with theoretical predictions, and again evidence was found of substantial quenching for these M1 transitions.

With the advent of focal plane polarimeters capable of working at intermediate energy region, several experiments aiming at measuring the spin-flip probability in the (p, p') reaction were carried out [8, 9, 10]. The excitation energy spectrum was separated into ΔS=0 and ΔS=1 contributions. An evidence was found of the spin-flip dipole and spin-flip quadrupole resonances by performing a multipole decomposition of the spin-flip cross section [11, 12, 13]. A previously unknown strong rise of the ΔS=1 strength relative to the ΔS=0 strength as the energy loss increases up to and above 40 MeV was observed in the momentum transfer region of around $q \approx 100$ MeV/c [14, 15, 16, 17, 18]. The enhancement of the relative spin response in the continuum has been extensively discusses, since it provides for the first time a picture of the relative strength of S=0 and S=1 correlations in nuclei at low momentum transfer.

1.2 Isoscalar Spin Excitations and Deuteron Inelastic Scattering

The spin transitions excited through nucleon induced reactions, however, are mostly isovector ΔT=1 transitions. The charge-exchange reactions exclusively excite isovector states. Although the (p, p') reaction can excite isoscalar ΔT=0 transitions, the spin-flip spectrum is dominated by the isovector transitions due to the relative dominance of the isovector part of the projectile-nucleon effective interaction in the spin dependent channel. Therefore, except for a few isolated states mostly in light nuclei, there is only limited information on the ΔT=0, ΔS=1 transitions so far by the (p, p') reaction. The primarily isoscalar spin transitions that have received most attention are listed in Table 1.1 [18].

It is expected that the information on the ΔT=0, ΔS=1 transitions is helpful in understanding the quenching mechanism of spin transitions, because the "quenching" produced by Δ-h excitations is only effective to the isovector transitions. It should be

Table 1.1: The isoscalar spin transitions that have received most attention in the past [18].

nucleus	J^π(Excitation Energy)
^{12}C	1^+ (12.71 MeV), 2^- (18.3 MeV),
	Broad resonances in the low energy continuum.
^{16}O	2^- (8.87 MeV), 0^- (10.95 MeV), 4^- (17.79 MeV), 4^- (19.80 MeV).
sd shell	Isolated low spin states.
nuclei	*e.g.* 1^+ (9.83 and 9.97 MeV) in ^{24}Mg and 1^+ (9.50 MeV) in ^{28}Si.
	Stretched states.
	e.g. 6^- (11.58 MeV) in ^{28}Si.
^{208}Pb	1^+ (5.85 MeV).

also useful in elucidating the problem of the enhancement of the relative spin response in the continuum found in the (p, p') reaction.

The polarization transfer measurement in inelastic deuteron scattering should be one of the essential probes of the isoscalar spin excitations. Since deuterons have an isospin quantum number of $T = 0$, the conservation of charge places a restriction on the isospin of the residual nucleus, which is forced to be equal to that of the target nucleus. Thus the reaction is selective of isoscalar ΔT=0 transitions. The spin $S = 1$ nature of the deuteron allows spin transfer to the target. The measurement of deuteron spin-flip probability will provide a means to disentangle between spin and non-spin excitations. Therefore a similar polarization technique used to extract information on the spin-dependent structure from nucleon scattering may be also exploited for deuteron scattering. This led us to use the (d, d') reaction for the study of hitherto rarely observed isoscalar spin excitations.

1.3 Two-phonon spin-isospin states and the (d, d') reaction

Another goal of this experiment is related to the search for possible existence of two-phonon spin-isospin states. Recently double giant resonances have attracted attention. The double giant dipole resonances have been identified in experiments using the pion double change exchange reaction [19] and the semi-relativistic heavy ion Coulomb excitation [20, 21]. The double giant quadrupole resonances have been observed in proton decay measurements through heavy ion inelastic scattering [22]. The two-phonon excitations of such an electric mode are now accepted to be a general feature of nuclei, which persist not only in low-lying surface vibrations but also in giant resonances [23]. On the other hand, two-phonon spin (magnetic) excitation has been identified neither in low-lying states nor in giant resonances up to now.

Of particular interest in the two-phonon spin excitation is the proposed double Gamow-Teller (DGT) states [24, 25]. The DGT states are closely related to the ground-state double-beta transitions. The double-beta transitions exhaust only a minor portion of the DGT sum rule, while the major part of the DGT strength is expected to be contained in high-lying resonances [24]. Revealing the major part of the DGT strength in experiments should give constraints on the theoretical calculations of double-beta decay matrix elements. It would also improve our understanding on the spin-isospin properties of nuclei as did the single GT investigations. The double charge exchange reactions involving unstable heavy ions and pions, and the (p, Δ^-) reaction have been suggested as the probe of the DGT states [24, 25]. Although an experimental search for the DGT states using the double charge exchange reactions of intermediate energy heavy ions has been performed [26], no identification of the DGT states could be obtained. The double charge exchange reactions make use of the $\Delta T = 2$ selectivity as the signature to identify the DGT states.

The (d, d') reaction should provide an individual and an alternative probe of the DGT states since this reaction, by taking full advantages of the variety of spin observables, has a possibility of measuring the new class of spin excitations with two units of spin-transfer (ΔS=2). As they carry spin by one unit, the inelastic scattering of deuterons is capable of exciting ΔS=2 transitions through two-step processes involving spin-flip of at least two nucleons in the target. We may expect that the deuteron double spin-flip probability has possible enhanced sensitivity to the presence of such transitions.

1.4 Deuteron Spin-Flip Probability

The observables of interest here are the deuteron single and double spin-flip probabilities, S_1 and S_2. They are defined as fractions of deuterons undergoing spin-flip by 1 and 2 units along an axis normal to the reaction plane. Following the notation of Ohlsen [27] the deuteron spin-flip probabilities are given in terms of polarization observables by the relations (see Appendix C for derivation):

$$S_1 = \frac{1}{9}(4 - P^{y'y'} - A_{yy} - 2K_{yy}^{y'y'}), \tag{1.1}$$

$$S_2 = \frac{1}{18}(4 + 2P^{y'y'} + 2A_{yy} - 9K_y^{y'} + K_{yy}^{y'y'}). \tag{1.2}$$

The quantities A, P and K refer to the analyzing power, polarizing power and polarization transfer coefficient, one (two) indices stand for the vector (tensor) polarization, and lower (upper) indices stand for the incident (outgoing) beam. The quantity S_1 includes the tensor polarizing power $P^{y'y'}$ and the tensor to tensor polarization transfer coefficient $K_{yy}^{y'y'}$, and thus we must measure the tensor polarization components of scattered deuterons to obtain S_1. This makes the systematic study of S_1 much more difficult than in the case for nucleon induced reactions, where the spin-flip probability S_{nn} can be extracted from the vector to vector polarization transfer coefficient $K_y^{y'}$ alone as,

$$S_{nn} = \frac{1}{2}(1 - K_y^{y'}). \tag{1.3}$$

To obtain S_2, both vector and tensor polarization transfer components of the scattered deuterons must be determined. The quantities S_1 and S_2 are expected to provide sensitive signatures of spin transfers with 1 and 2 units, respectively.

It should be stressed here that these spin-flip probabilities represent the projectile spin-flip and do not necessarily indicate the target spin-flip [28]. This means that one needs to rely on a suitable reaction model in order to understand the measured quantities in terms of the projectile-nucleon effective interaction and of the structure of the target nucleus.

1.5 Reaction Model for Deuteron Inelastic Scattering

Owing to the composite nature of the deuteron the reaction mechanism for deuteron-nucleus scattering is not as well understood as in the case of nucleon-nucleus scattering. Recently Wiele *et al.* [29] have developed a microscopic distorted wave impulse approximation (DWIA) model for the (d, d') reaction at intermediate energies. The model is based on the double folding method, where the deuteron-nucleus (dA) transition matrix is calculated, first by folding the on-shell NN t-matrix with the deuteron wave function to yield the deuteron-nucleon (dN) t-matrix (folding dN t-matrix), then with the target transition density. In a previous application of the model, however, it was pointed out that the $d + N$ elastic differential cross section is overestimated in the first folding by a factor of 1.2-2.0, which directly leads to too large dA differential cross sections [18]. The shortcoming of the folding model was attributed to the break-up effects associated with the weakly bound nature of the deuteron [30].

Today, three-nucleon Faddeev calculations make it possible to describe the deuteron-nucleon (dN) scattering processes even at intermediate energies with a reliable accuracy [31]. Figure 1.1 compares the $\vec{d} + p$ elastic scattering data at E_d=270 MeV taken at RIKEN [32, 33] with predictions of the folding calculations (dashed lines) and of the Faddeev calculations (solid lines). Clearly the data are better reproduced by the Faddeev calculations. It is quite conceivable that a more precise DWIA description of the (d, d') reaction could be obtained by using the dN t-matrix based on the Faddeev calculations (three-body dN t-matrix) as the projectile-nucleon effective interaction.

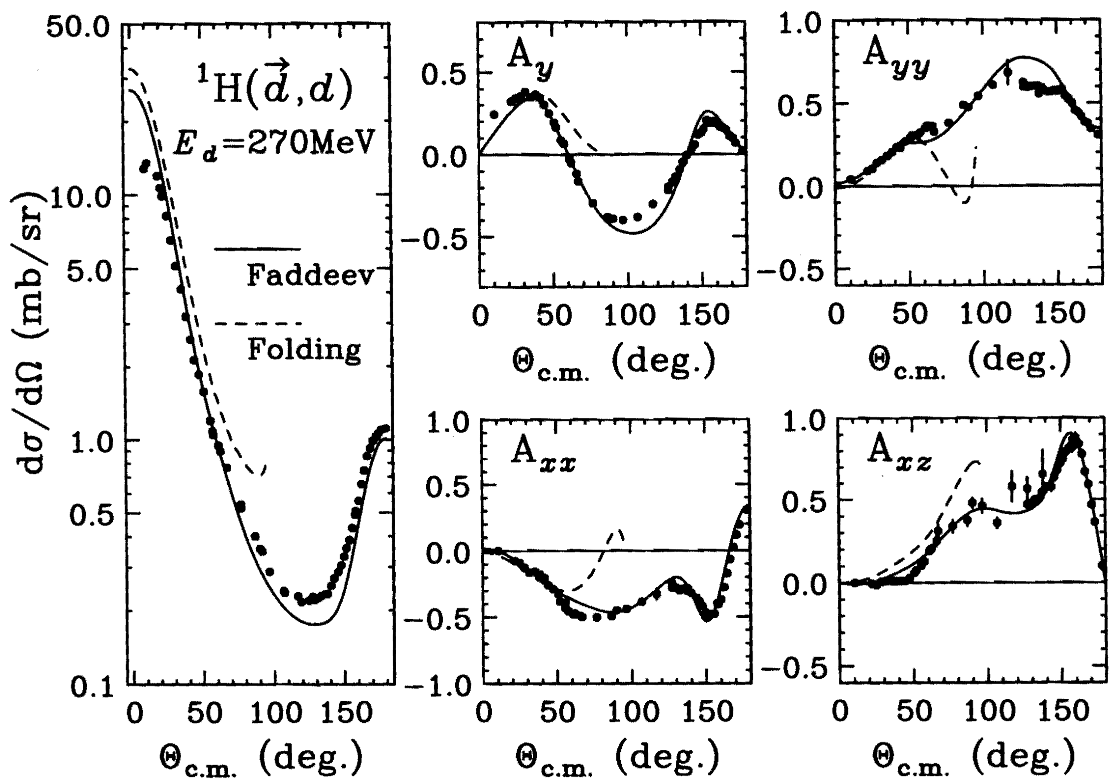

Figure 1.1: Measured $\vec{d}+p$ elastic scattering data at E_d=270 MeV[32, 33] are compared with calculated results using dN t-matrices obtained from the folding and Faddeev calculations.

In a recent work such rigorous three-nucleon amplitudes have been successfully employed in a PWIA framework [34] for interpreting analyzing power data in the ^{3}He($\vec{d}$,p) backward elastic scattering at E_d = 140, 200 and 270 MeV taken at RIKEN [35].

1.6 Existing Deuteron Spin-Flip Measurements

The earliest measurement of S_1 is the use of the $(d, d'\gamma)$ method for the 2^+ (4.44 MeV) and 1^+ (12.71 MeV) states in ^{12}C at E_d = 56 MeV [36]. It was shown that the correlation measurements of the scattered deuterons and the emitted γ-rays could yield S_1 values without measuring polarization observables. But this method is applicable only for transitions for which γ decay branch to the 0^+ ground state is known. The first direct measurement of S_1 was made using a tensor polarimeter POLDER [37] at E_d=400 MeV [38]. The limited coverage of the experimental setup, however, confined the measurement to be done only for the 1^+, T=0 (12.71 MeV) state in ^{12}C at 4°. The $(\vec{d}, \vec{d}')$

measurements were performed using a vector polarimeter POMME [39] for nuclei covering a wide mass number region [40, 41, 42, 43]. In these measurements a vector quantity S_d^y was defined and used as the signal for isoscalar spin states. The quantity S_d^y can be obtained by measuring only the vector polarization of the scattered deuterons,

$$S_d^y = \frac{4}{3} + \frac{2}{3}A_{yy} - 2K_y^{y'}. \tag{1.4}$$

This quantity, however, is an approximate one which coincides with S_1 only when $A_{yy} = P^{y'y'}$ and $S_2 = 0$. It has been pointed out that for a complete separation of the ΔS =0 and ΔS =1 transitions the combination of a tensor polarized beam and a tensor polarimeter would be needed [44]. Moreover these measurements provided essentially no information on the double spin-flip strengths.

In a recent work, the first polarization transfer $(\vec{d}, \vec{d}')$ measurement with a 270 MeV deuteron beam at RIKEN was performed in order to explore the possibility of using the deuteron single and double spin-flip probabilities as probes of isoscalar single and double spin-flip excitations [45, 46]. A focal plane deuteron polarimeter DPOL, capable of measuring both vector and tensor polarization components of deuterons, was developed for this experiment. The measurement was done on ^{12}C target, as it has well known isoscalar 1^+ (12.71 MeV) and 2^- (18.3 MeV) states. The primary result is shown in Fig. 1.2, where plotted are (a) the double differential cross section, (b) the cross section multiplied by S_1 and (c) the cross section multiplied by S_2 as a function of target excitation energy. The apparent enhancement of the spin-flip cross section (Fig. 1.2 (b)) at the energy bin where the isoscalar 1^+ and 2^- states are known clearly demonstrates the usefulness of S_1 as a tool identifying the presence of isoscalar spin strengths in the spectrum. The measured S_2 values were very close to zero and no appreciable double spin-flip strength was identified. The feasibility of measuring both S_1 and S_2 at the same time over a wide region of the target excitation energy was demonstrated.

1.7 Thesis Objective

The goals of the present thesis are two-folding. Firstly it is intended to extend the previous deuteron spin-flip measurement on ^{12}C to a heavier *sd*-shell nucleus ^{28}Si as a first step towards a systematic study of isoscalar single and double spin-flip excitations. The ^{28}Si nucleus was chosen as it provides at least one pure isoscalar 1^+ state known from (p, p') studies [47, 48]. A measurement was made on the cross section and eight polarization observables with respect to the y-axis, A_y, A_{yy}, $P^{y'}$, $P^{y'y'}$, $K_y^{y'}$, $K_{yy}^{y'}$, $K_y^{y'y'}$ and $K_{yy}^{y'y'}$, for the ^{28}Si$(\vec{d}, \vec{d}')$ reaction at E_d=270 MeV. The measured excitation energy range was between 4 and 21 MeV and the angular range between 2.5° and 7.5° in the laboratory

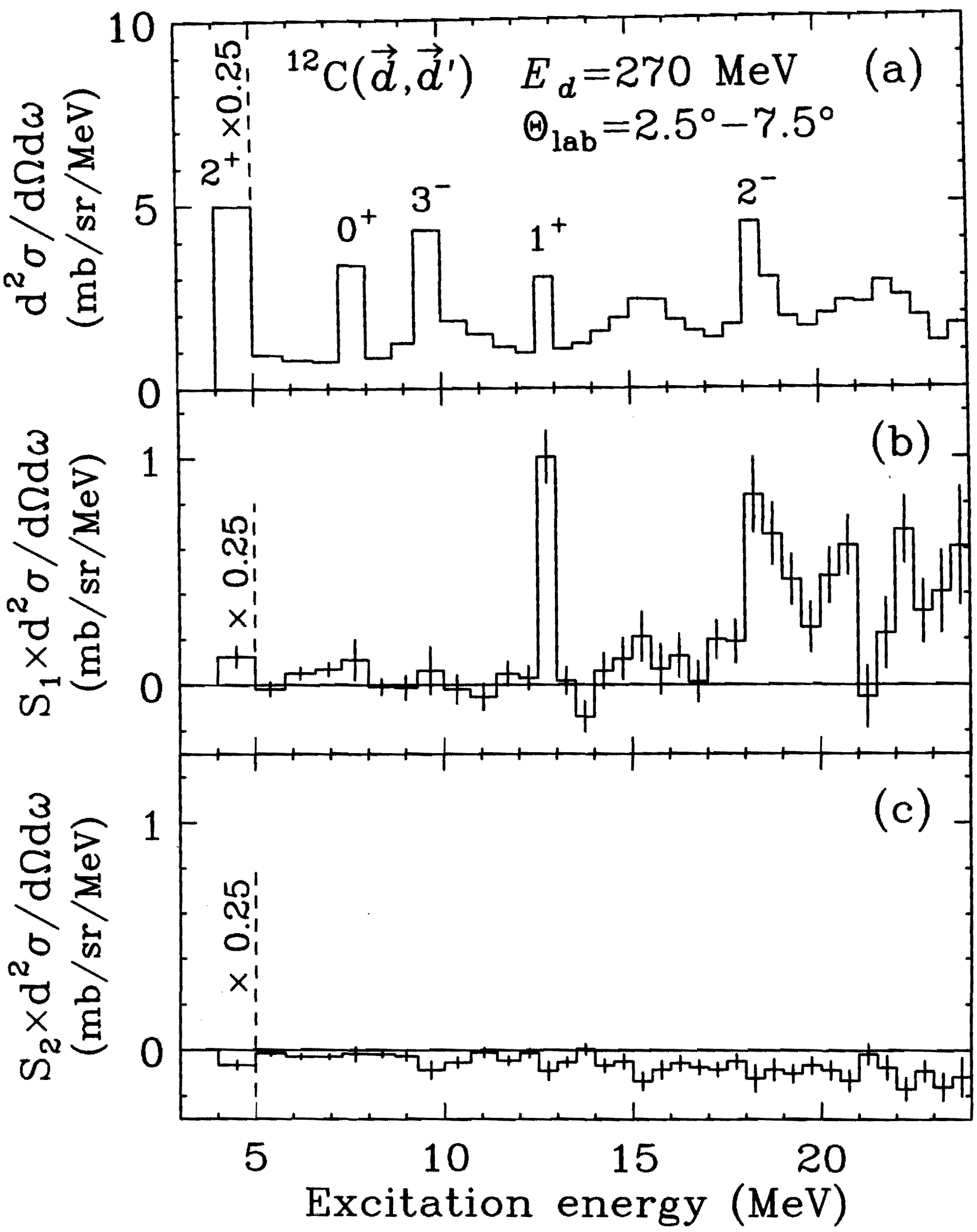

Figure 1.2: Excitation energy spectra for the $^{12}C(\vec{d},\vec{d}')$ reaction at E_d = 270 MeV integrated over Θ_{lab} = 2.5°-7.5 ° [45]. (a) The double differential cross section. (b) The cross section multiplied by S_1. (c) The cross section multiplied by S_2.

frame. The vector and tensor polarized deuteron beams were incident on a ^{28}Si target and the inelastically scattered deuterons were analyzed in momentum by using the magnetic spectrometer SMART. A focal plane deuteron polarimeter DPOL was used to extract the vector and tensor polarization components of the scattered deuterons. The deuteron single and double spin-flip probabilities, S_1 and S_2, were determined as a function of excitation energy.

A second motivation is to investigate the applicability of the DWIA formalism [29] for the interpretation of the (d, d') scattering data at E_d=270 MeV. For this purpose part of the experiment was dedicated to an additional angular distribution measurement of cross sections and analyzing powers for transitions to low-lying discrete states with known nuclear structure in ^{12}C and ^{28}Si. The elastic scattering was also measured to determine the optical potentials. At the same time, the DWIA model (T-matrix) given in Ref. [29] has been extended to accept the three-body dN t-matrix as the projectile target-nucleon effective interaction, in addition to the folding dN t-matrix. Up to now there have been very few conventional DWIA codes which can calculate microscopically the deuteron inelastic scattering at intermediate energy region using a realistic projectile target-nucleon effective interaction. By writing a code which is based on the extended DWIA T-matrix, a method to analyze the data on the deuteron inelastic scattering has been developed. Comparison of the model predictions with the data will give constraints on the model. The model is then applied to interpret the spin-flip probability data for selected transitions in ^{12}C and ^{28}Si.

The experimental consideration concerning the focal plane polarimetry is given in Chapter 2. The experimental apparatus is described in Chapter 3, and the data analysis procedure in Chapter 4. The experimental results are described in Chapter 5. Comparison of angular distribution data with DWIA calculations is presented in Chapter 6. A conclusion is given in Chapter 7.

Chapter 2

Experimental Consideration

2.1 Experimental Target ^{28}Si

In this thesis, we investigate the ^{28}Si nucleus. It is an even-even self-conjugate (N=Z) nucleus having the ground state spin and parity of $J^{\pi} = 0^{+}$ with the isospin of $T_0 = 0$. The ^{28}Si nucleus has a spin-unsaturated shell configuration which, in a simple jj shell-model picture, is characterized by the filled $d_{5/2}$ orbit and the empty $d_{3/2}$ orbit. Due to this shell configuration it is expected that this nucleus has large M1 type spin excitation strengths concentrated on relatively small number of states among the sd shell nuclei. Note that the M1 type spin excitation is formed, in a naive picture, by promoting a nucleon from a $j = l+\frac{1}{2}$ orbit to its spin orbit partner $j = l-\frac{1}{2}$. Both T=0 (isoscalar) and T=1 (isovector) 1^{+} states has been identified by means of the (p,p') reaction performed at intermediate energy region [47, 48]. The isospin structure of the 1^{+} states has been discussed by comparing high resolution spectra obtained with (p,p') and $(^{3}\mathrm{He},t)$ reactions [49]. In the (d,d') reaction only the isoscalar states are excited due to the isospin selection rule. The T=0, 1^{+} states at 9.50 MeV has been established from the existing (p,p') and other experiments. This state should be helpful in making a calibration of the detection system for the (d,d') polarization transfer experiment. In addition data on such a state together with those already acquired for the T=0, spin-flip states in ^{12}C [45] will provide an important bases for the systematic study of isoscalar spin-flip transitions probed with the (d,d') reaction.

The nucleus ^{28}Si has attracted attention in connection with the quenching phenomena of spin excitations [47, 48, 50]. As mentioned above it has both T=0 and T=1, 1^{+} states. The $2p$-$2h$ mechanism is common to the quenching of both the T=0 and T=1 strengths, while the Δ-h mechanism contributes only to the T=1 strengths. The measured cross sections for the T=0 and T=1, 1^{+} states have been compared with the theoretical ones calculated using the realistic nuclear wave functions. Note that there is no model independent sum rule for M1 transitions and the total M1 strength depends strongly on the properties of the nuclear ground state wave function. In the analysis of the (p, p') data the unified *sd* shell model wave functions based on the semi-empirical two-body effective interaction of Wildenthal [51, 52] was utilized. This interaction gives excellent fits to the binding energies for the ground states and the excited states of the *sd*-shell nuclei, From the comparison it was found that both isoscalar and isovector 1^+ transitions are quenched by a similar amount. Based on this observation it was suggested that the Δ-h explanation of the quenching is not the most important one [47, 48, 50].

It is one of the purpose of this work to see whether the reaction mechanism of the (d, d') reaction at intermediate energy is simple and tractable enough to allow one to use this reaction for the study of quenching problem in the same quantitative manner as that for the (p, p') reaction at similar incident energies per nucleon.

2.2 Analyzer Reactions for A Focal Plane Deuteron Polarimeter

The polarization transfer observables are determined in an experiment, in which polarizations of outgoing particles are measured using a polarimeter after the scattering of incident polarized particles by the primary target. In the energy region of interest here the polarimeter inevitably relies on certain nuclear reactions (analyzer reactions) capable of producing asymmetries related to the beam polarizations. The experiment thus involves double scattering. Since in such a double scattering experiment the number of incident particles into the polarimeter is less by several orders of magnitude than that into the primary target, it is indispensable to develop a high efficiency polarimeter. In order to improve the performance of the polarimeter, the polarimeter system must have large enough acceptance for suitable analyzer reactions, which should have large cross sections and effective analyzing powers for the energy region of interest. In addition, for the present particular application aiming at extracting both single and double spin-flip probabilities S_1 and S_2 in inelastic deuteron scattering, it is crucial for the polarimeter to have high sensitivity to both vector and tensor components of the deuteron polarization.

In order to meet the above requirements, a focal plane Deuteron POLarimeter DPOL has been developed at RIKEN. It was designed to measure both vector and tensor polarization components by combining two nuclear reactions,

- The $\vec{d} + {}^{12}\mathrm{C}$ elastic scattering,
- The ${}^{1}\mathrm{H}(\vec{d}, 2p)$ charge exchange reaction,

which show large angular asymmetries depending respectively on the vector and tensor components of the incident deuterons. Large effective analyzing powers ($\langle T_{11}\rangle = 0.17 \sim 0.27$, $\langle T_{20}\rangle = 0.18 \sim 0.19$ and $\langle T_{22}\rangle = 0.13 \sim 0.18$) and high efficiencies (ϵ=1.20$\sim$1.00% for vector and ϵ=0.082$\sim$0.090% for tensor) are confirmed in calibration experiments performed at incident deuteron energies between 230 and 270 MeV, whose results are summarized in appendix A. Characteristic features of the analyzer reactions and comparison in performance with other polarimeters are described below.

2.2.1 The $\vec{d}+{}^{12}$C Elastic Scattering

At intermediate energy region, the $\vec{p}+{}^{12}$C inclusive scattering has been in a conventional use as a vector polarization analyzer for proton polarimeters. It has been shown that any intermediate energy proton polarimeter can easily be transformed into a deuteron vector polarimeter by adding an absorber in front of the final particle trigger. The semi-inclusive $\vec{d}+{}^{12}$C scattering gives a sizeable vector analyzing power provided most of the break-up protons are eliminated by the absorber. Other polarimeter system based on this reaction, POMME [39] has been developed at SATURNE.

2.2.2 The ^{1}H$(\vec{d}, 2p)$ Charge Exchange Reaction

Bugg and Wilkin [53, 54] examined the ^{1}H$(d, 2p)$ reaction within a single scattering plane wave impulse approximation (PWIA) model. They predicted large tensor analyzing powers and sizeable cross sections for deuteron energy range between 200 and 400 MeV, in the case where outgoing two protons are detected in the peak of the singlet (${}^1S_0$) final state interaction. Their predictions were confirmed in experiments performed at E_d=200 and 350 MeV [55, 56, 57]. In these works, following advantages as a polarization analyzer were reported:

- Large figure of merits for tensor analyzing powers above 200 MeV.
- Clear event selection due to coincidence detection of two protons.
- Simple reaction mechanism well described by the impulse approximation.

These properties were also confirmed in experiments at RIKEN. Figure 2.1 compares experimental distributions of various quantities (shaded histograms) for the ^{1}H$(d, 2p)$ reaction measured at E_d=270 MeV, (a) the missing mass, (b) the kinetic energy of individual protons, (c) half the $2p$ relative momentum and (d) the momentum transfer, with PWIA model calculations (solid lines) refined by Carbonell *et al.* [58]. A good agreement of the data with theory is seen over a large phase space region. The applicability of PWIA was helpful for energy interpolation and efficiency correction in data analysis procedure. Details on the event selection and model calculations are given in section 4.4 and appendix B, respectively. The polarimeter POLDER [37] based on this reaction has been developed at SATURNE.

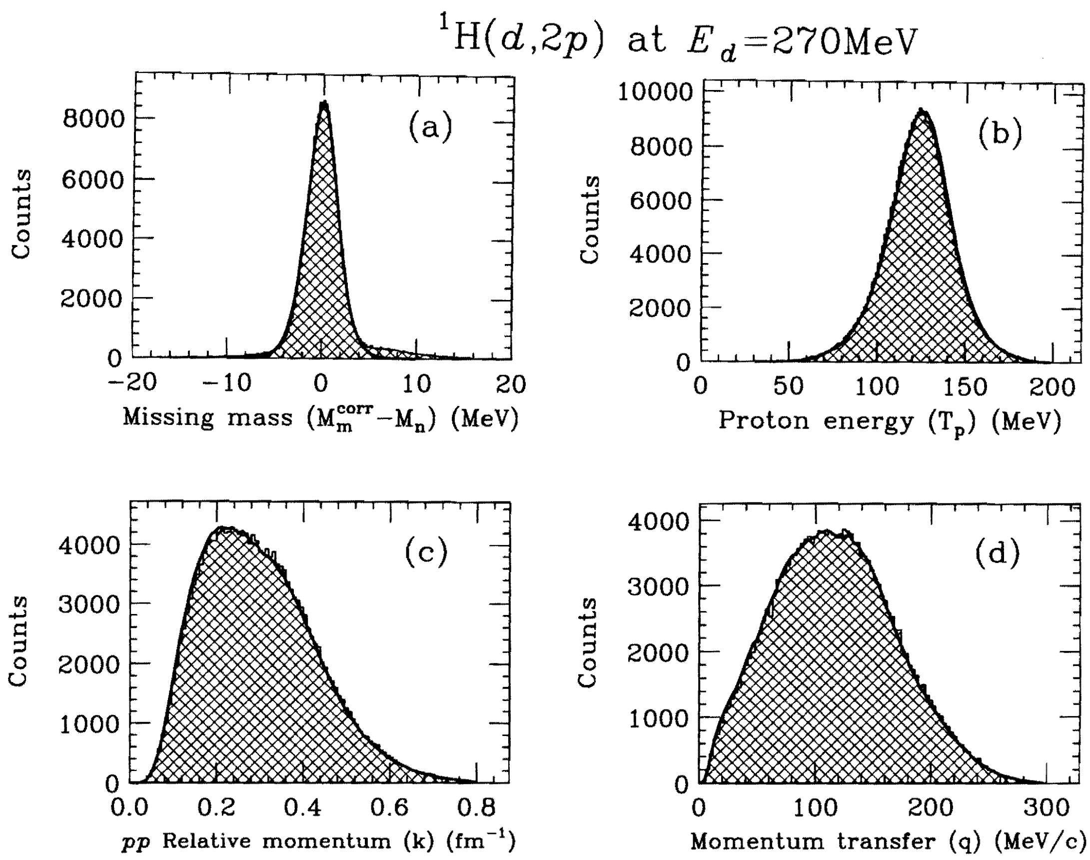

Figure 2.1: Comparison of the experimental data for the ^{1}H$(d, 2p)$ reaction at E_d=270 MeV with Monte Carlo predictions using a PWIA model of Carbonell *et al.* [58]. The data (shown as shaded histograms) are obtained after rejection of the background events. The predictions (shown as solid lines) are filtered by the experimental setup. The figures display spectra on (a) the missing mass M_m, (b) the kinetic energy of individual protons T_p, (c) half the $2p$ relative momentum k and (d) the momentum transfer q. The range in k is restricted below $k = 0.4$ fm^{-1} except for panel (c).

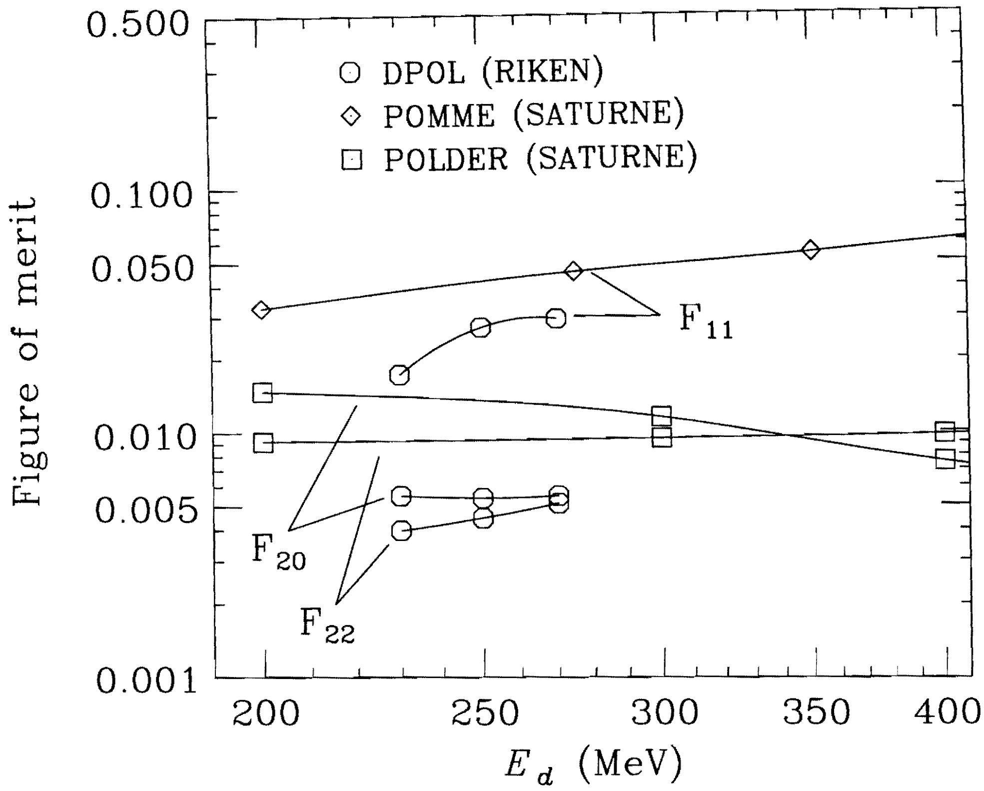

Figure 2.2: Comparison of figures of merit among intermediate energy deuteron polarimeters DPOL, POMME and POLDER.

2.2.3 Comparison with Other Polarimeters

The figure of merit (FOM) of a polarimeter is an important quantity which characterizes the performance of the polarimeter. The definition is given in appendix A. It allows one to compare different apparatus. Figure 2.2 compares FOM values of DPOL with those of other polarimeters POMME and POLDER. Although the FOM values of DPOL are slightly lower that those of the others (this is mostly due to the thickness of the analyzer target), DPOL has a characteristic feature with the FOM values which are high enough for both vector and tensor analyzing powers. Since the secondary reactions are measured simultaneously in a single counter configuration in the DPOL polarimeter system, one can reduce systematic uncertainties, compared to those attainable from sequential measurements using different polarimeters.

Chapter 3

Experimental Arrangement

The experiment was performed at the E4 experimental room of RIKEN accelerator research facility (RARF) (see Fig. 3.1). The 270 MeV deuteron beams from the Ring Cyclotron polarized normal to the scattering plane with an average current of 10 nA were led through a beam twister and a beam swinger onto an experimental target placed in a scattering chamber. The magnitude of the beam polarization was measured using the $\vec{d}+p$ elastic scattering at 270 MeV. Scattered deuterons were detected using the SMART spectrometer consisting of three quadrupoles (Q) and two horizontally bending dipoles (D) in the QQDQD configuration. It was instrumented with a multiwire drift chamber (MWDC) for track reconstruction and two plastic scintillation detectors (SC1 and SC2) for triggering. The scattering plane was perpendicular to the dispersive plane, and the beam polarization axis was rotated by using a Wien filter at the ion source. The vector and tensor polarizations of outgoing deuterons were measured in a deuteron polarimeter DPOL at the focal plane of SMART by using the $\vec{d}+{}^{12}\mathrm{C}$ and ${}^{1}\mathrm{H}(\vec{d},2p)$ reactions.

The calibration of the polarimeter was performed in a separate measurement by letting direct beams with known polarizations onto the analyzer target of the polarimeter.

The relevant experimental setup is described in this chapter.

3.1 Polarized Deuteron Beam

3.1.1 Polarized Ion Source

The vector and tensor polarized deuteron beams were produced with an atomic-beam-type RIKEN polarized ion source [59] in the following sequence. Firstly, the deuterium molecules were dissociated into atoms with 13.56 MHz radio frequency (RF) discharge in the dissociator. Secondly, the nuclear polarization was produced by using two sextupoles, where atoms which had electrons with spin up were selected, and three RF transition units, where in the presence of magnetic field adiabatic transitions between hyper-fine

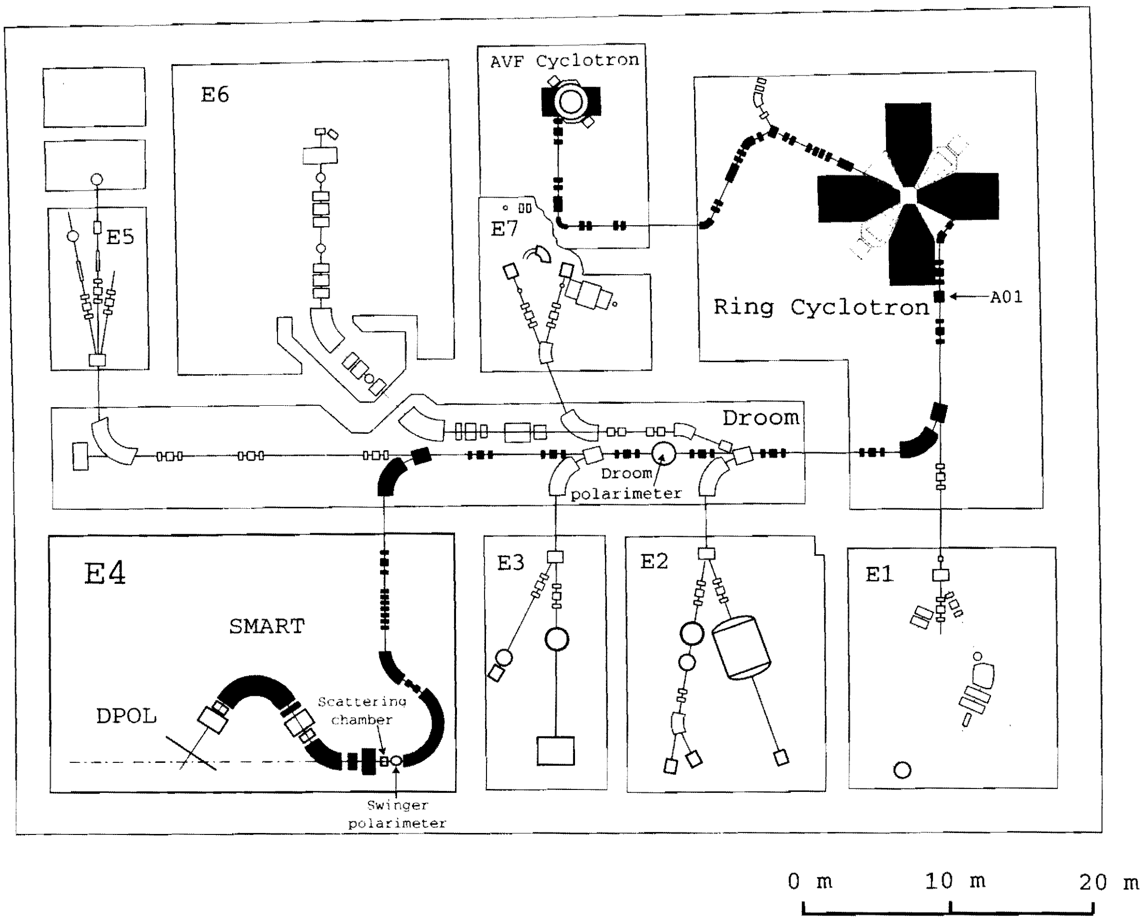

Figure 3.1: RIKEN Accelerator Research Facility. The experiment was performed at E4 experimental room.

levels took place. Finally, the polarized atoms were ionized by an electron cyclotron resonance (ECR) ionizer. The spin states were exchanged at 0.2 Hz.

3.1.2 Wien Filter

In order to control the polarization axis of symmetry of the beam into a desired direction, a Wien filter was located at the exit of the ion source. It generated a magnetic field and an electric field on the beam path perpendicularly to each other. With a suitable adjustment of the field strengths, it allowed us to rotate the polarization axis by a certain amount of angle while keeping the beam trajectory straight (unchanged). In addition the whole Wien filter system was mechanically turnable around the beam path so that we could choose the direction in which the polarization axis was tilted. Figure 3.2 shows the transverse vector polarization P_x measured with the D-room polarimeter (see subsection 3.1.4) plotted as a function of Wien filter rotation angle ρ. The data points are well fitted by a sine curve.

3.1.3 Beam Acceleration and Transport

After pre-acceleration up to 14 MeV with the K70 AVF cyclotron, operated at an RF frequency of 16.3 MHz with a harmonic number of 2, the polarized deuteron beam was injected into the main K540 Ring cyclotron, operated at an RF frequency of 32.6 MHz with a harmonic number of 5, in which the beam was accelerated up to 270 MeV. The beam bunch interval was 61.3 ns and the bunch width was less than 1 ns. The single turn extraction in both AVF and Ring cyclotrons was maintained during the experiment. It was indispensable in attaining arbitrary control of the polarization axis on the experimental target using the Wien filter located at the ion source.

Figure 3.3 shows the beam envelops through the 73 m transport line calculated with the TRANSPORT [60]. Following requirements were imposed on the transport parameters: (1) the small beam spots at the experimental and polarimeter targets, (2) the beam size as small as possible in the SMART beam swinger to prevent producing background beam halos and (3) the achromatic focus onto the experimental target. The beam spot size at the experimental target was typically 1.5 (H) $\times$ 0.6 (V) mm^2.

3.1.4 Beam Line Polarimeter

Two beam line polarimeters based on the $\vec{d}+p$ elastic scattering at E_d=270 MeV [32] were use to measure the beam polarizations. The D-room polarimeter was composed of four pairs (left/right/up/down) of counter telescope, each consisted of a plastic scintillator (NE102) directly mounted on a photomultiplier tube (Hamamatsu, H1161). The counter specification is given in Table 3.1. Each pair of telescope detected a scattered deuteron and a recoil proton from the CH_2 target in coincidence at a center-of-mass (c.m.) scattering angle of 86.5°. The anode signals from the "d" and "p" counters were transmitted to constant-fraction discriminators (CFDs), which generated 20 ns wide logic pulses. The number of coincidence of each pair was counted by CAMAC scalers. By appropriately setting the CFD threshold, the coincidence signal became almost corresponding to the $\vec{d}+p$ elastic scattering. The accidental coincidence was taken into account by counting the number of coincidence in which one of the logic pulses was delayed by an amount of the beam bunch interval. The swinger polarimeter had a similar detector arrangement to the D-room polarimeter. The counter specification is given in Table 3.1. It was located 80 cm upstream from the experimental target so that it could measure the beam polarization on target directly. The swinger polarimeter was used in a frequent check of the beam polarization during experiment. The effective analyzing powers of these polarimeters are

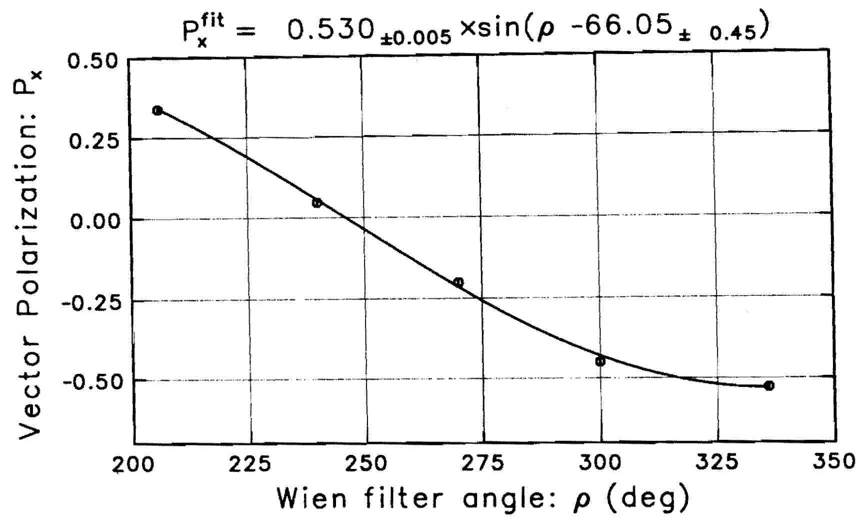

Figure 3.2: The transverse vector polarization P_x of the deuteron beam measured with the D-room polarimeter as a function of the Wien filter rotation angle ρ.

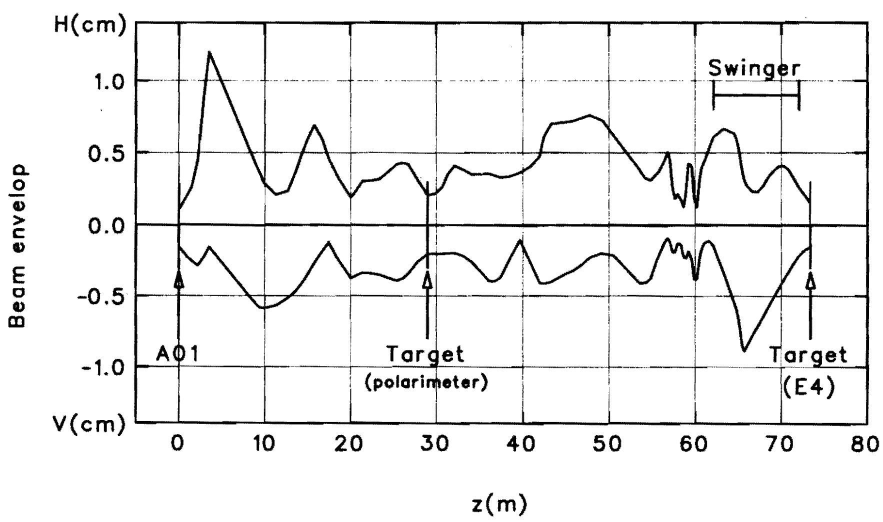

Figure 3.3: The horizontal (H) and vertical (V) beam envelopes through the transport line calculated by TRANSPORT.

summarized in Table 3.2.

Due to the Larmor precession of the polarization axis inside the beam swinger, the direction of the polarization axis on target at the D-room polarimeter does not coincide with that on the experimental target at SMART, except when the beam swinger is set at zero degree (see section 3.3 for the SMART beam swinger). Figure 3.4 defines the coordinate systems to describe the beam polarizations at the D-room polarimeter and at the SMART scattering chamber. Referring to these coordinate systems the polarization vectors $\hat{p}_D$ and $\hat{p}_T$, which respectively specify the polarization axis at the D-room polarimeter and at the SMART scattering chamber, are related by the orthogonal transformation:

$$\hat{p}_D = M^t \hat{p}_T, \tag{3.1}$$

with

$$M^t = \begin{pmatrix} -\sin\alpha\sin\Theta_{\mathrm{SW}} & -\cos^2\alpha - \sin^2\alpha\cos\Theta_{\mathrm{SW}} & \cos\alpha\sin\alpha(1-\cos\Theta_{\mathrm{SW}}) \\ \cos\Theta_{\mathrm{SW}} & -\sin\alpha\sin\Theta_{\mathrm{SW}} & -\cos\alpha\sin\Theta_{\mathrm{SW}} \\ \cos\alpha\sin\Theta_{\mathrm{SW}} & -\cos\alpha\sin\alpha(1-\cos\Theta_{\mathrm{SW}}) & \cos^2\alpha\cos\Theta_{\mathrm{SW}} + \sin^2\alpha \end{pmatrix}, \tag{3.2}$$

where Θ_{SW} is the swinger rotation angle. The angle α is the precession angle of the polarization axis when the beam is deflected by $\theta_{\mathrm{orb}} = 90°$. It is given by

$$\alpha = (1 + g\frac{M_d}{2M_p}\gamma - \gamma)\Delta\theta_{\mathrm{orb}}, \tag{3.3}$$

where g is the gyromagnetic ratio of the deuteron, M_d and M_p are the deuteron and proton masses and γ is the Lorentz factor. For 270 MeV deuterons α is calculated to be 75.28°. For each setting of the SMART beam swinger the Wien filter parameters (the rotation angle and the electric and magnetic field strengths) were adjusted using the relation in Eq.(3.1) in such a way that the beam polarization axis on the experimental target was directed toward a certain desired direction.

Table 3.1: Counter specification of the beam line polarimeters.

Polarimeter	Arm	Lab. angle (deg.)	Size (mm^3)	Distance (mm)	Degrader (mm)
D-room	d	25.5	$10^T \times 20^\theta \times 36^\phi$	515.0	33.5 (Al)
pol.	p	45.0	$10^T \times 25^\theta \times 36^\phi$	365.0	32.0 (Al)
Swinger	d	26.2	$10^T \times 8^\theta \times 12^\phi$	155.0	6.0 (Fe)
pol.	p	43.3	$10^T \times 8^\theta \times 12^\phi$	115.0	11.0 (Fe)

Table 3.2: Effective analyzing powers [61] for the $\vec{d}+p$ elastic scattering at E_d=270 MeV.

Polarimeter	$\theta_{c.m.}$	A_y	A_{yy}	A_{xx}
D-room pol.	86.5 °	-0.381 ± 0.006	0.491 ± 0.016	-0.492 ± 0.014
Swinger pol.	90.0 °	-0.391 ± 0.007	0.478 ± 0.016	-0.450 ± 0.014

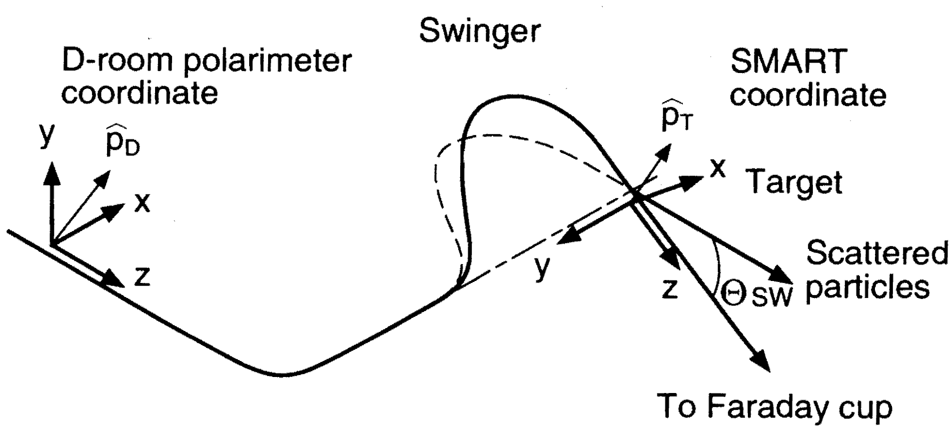

Figure 3.4: The coordinate systems which specify the beam polarization at the D-room polarimeter and at the SMART scattering chamber. The swinger rotation angle is denoted by Θ_{SW}.

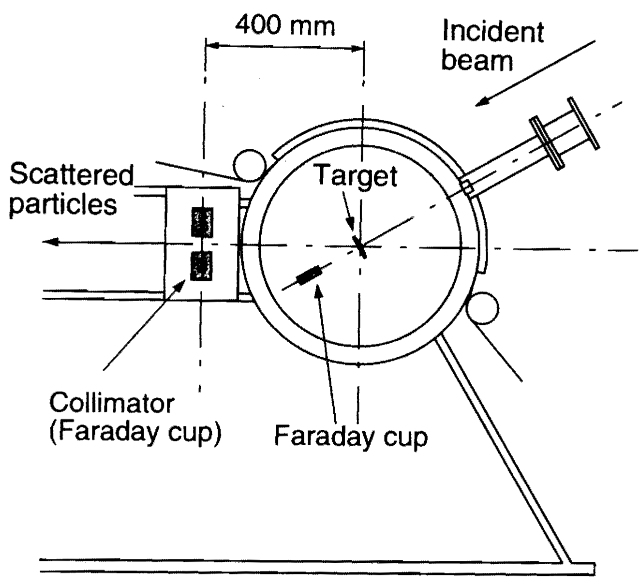

Figure 3.5: A vertical section view of the SMART scattering chamber.

3.2 Target and Scattering Chamber

Figure 3.5 shows a vertical section view of the scattering chamber. The silicon target was a self supporting foil of natural abundance (92.2 % ^{28}Si) with a thickness of 58.14 $\pm$ 0.36 mg/cm^2. The carbon target was a self supporting foil of natural abundance (98.9 % ^{12}C) with a thickness of 31.30 $\pm$ 0.06 mg/cm^2. The thicknesses of the targets were chosen so that enough scattering yields could be obtained while at the same time a good energy resolution is maintained. The estimated energy loss, root mean square Coulomb multiple scattering angle and energy struggling (in standard deviation) for 270 MeV deuterons is summarized in Table 3.3. Both targets had a large areal dimension of 44 mm (width) $\times$ 26 mm (hight) in order to reduce background due to edge scattering from the holder.

Table 3.3: The estimated energy loss, Coulomb multiple scattering angle and energy struggling for 270 MeV deuterons on the experimental target used in this experiment.

Target	Energy loss (MeV)	Multiple scattering (rms) (deg.)	Energy straggling (σ) (MeV)
^{12}C	0.17	0.03	0.05
^{28}Si	0.28	0.06	0.07

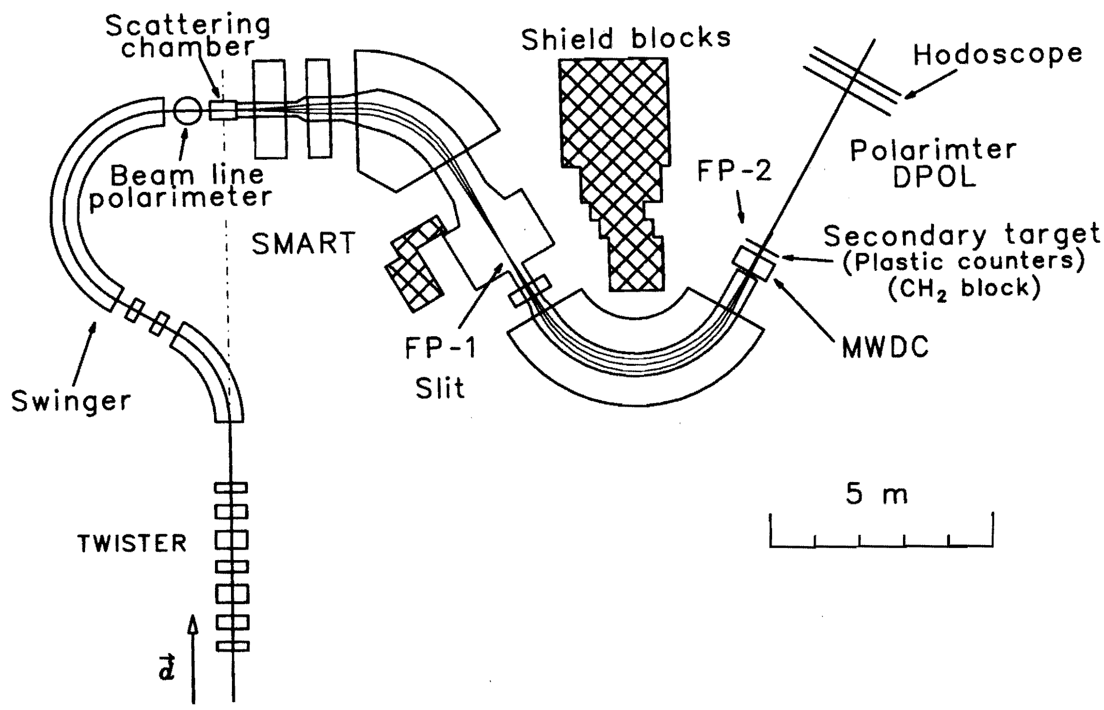

Figure 3.6: Layout of the experimental setup. The SMART spectrometer consists of three quadrupoles (Q) and two horizontally bending dipoles (D) in the QQDQD configuration. The polarimeter DPOL is placed at the focal plane of SMART.

The scattering chamber had a cylindrical shape with an inside diameter of ϕ = 510 mm. It had a target holder capable of mounting up to 4 targets. To keep the target thickness constant the holder was rotated in such a way that the normal direction to the target plane always coincides with the incident beam axis. The solid angle of the scattered deuterons was defined with a 5 cm-thick lead collimator located 40 cm downstream from the target. For measurements at the swinger angle of 5° a collimator bored with a wedge shaped hole, defining the azimuthal scattering angles within ±12° and the polar angles to 2.5° − 7.5°, was used in order to reduce out-of-plane scattering. The beam was stopped by the insulated collimator for measurements with swinger angles less than 13°, otherwise it was stopped by a Faraday cup mounted on a turn table.

3.3 Magnetic Spectrometer SMART

The primary scattering was measured with a magnetic spectrometer SMART, a Swinger and a Magnetic Analyzer with Rotators and Twisters [62]. The layout of the spectrometer system is shown in Fig. 3.6.

Table 3.4: Characteristics of the SMART focal planes.

focal plane	FP-1	FP-2
Type	Q-Q-D	Q-Q-D-Q-D
p/δp	3000	12000
Momentum range	20 %	4 %
Dispersion	3.4 m	7.5 m
Maximum aperture	200 mr^V × 100 mr^H	200 mr^V × 50 mr^H
Maximum solid angle	20 msr	10 msr
Mean orbit radius	2.4 m	2.4 m
Maximum magnetic field	1.5 T	1.5 T
Bending angle	60°	60°-120°
Size of the focal plane	120 cm^H×40 cm^V	50 cm^H×10 cm^V
reaction plane	perpendicular	

3.3.1 SMART Magnetic Analyzer

The incident deuteron beam was lead onto the experimental target from various incident angles by rotating the beam swinger. The angular distribution measurement was carried out without rotating the analyzer magnets. The reaction plane was vertical in this system. The beam twister [63] consisted of a septet of quadrapoles mounted on a rigid frame turnable around the beam axis. It worked as a beam inverter which could match the ion optical symmetry plane of the upper-stream transport system to that of the beam swinger. Using the beam twister the beam spot on target was kept unchanged against the swinger rotation.

The inelastically scattered deuterons were analyzed in momentum with the magnetic analyzer consisting of a QQD-QD magnet sequence. The system had two focal planes. The first three elements QQD dispersed the outgoing particles from the primary target on the first focal plane (FP-1). The last two elements QD further magnified a part of image produced at the FP-1 to give the second focal plane (FP-2), where focal plane detectors were placed. Typical characteristics of the SMART two focal planes are summarized in Table 3.4.

It was not practical to have elastic and inelastic peaks simultaneously in the focal plane detectors at FP-2 due to the overwhelmingly large counting rate of the elastic peak. A movable slit system located at FP-1 was used to cut unwanted peaks. Figure 3.7 shows typical excitation energy spectra taken for the ^{28}Si(d,d) reaction at E_d=270 MeV and at $\Theta_{\rm lab}$ = 7° obtained with (hatched region) and without (unhatched region) a cut by the slit. By carefully setting the position of the slit the elastic peak could be well suppressed

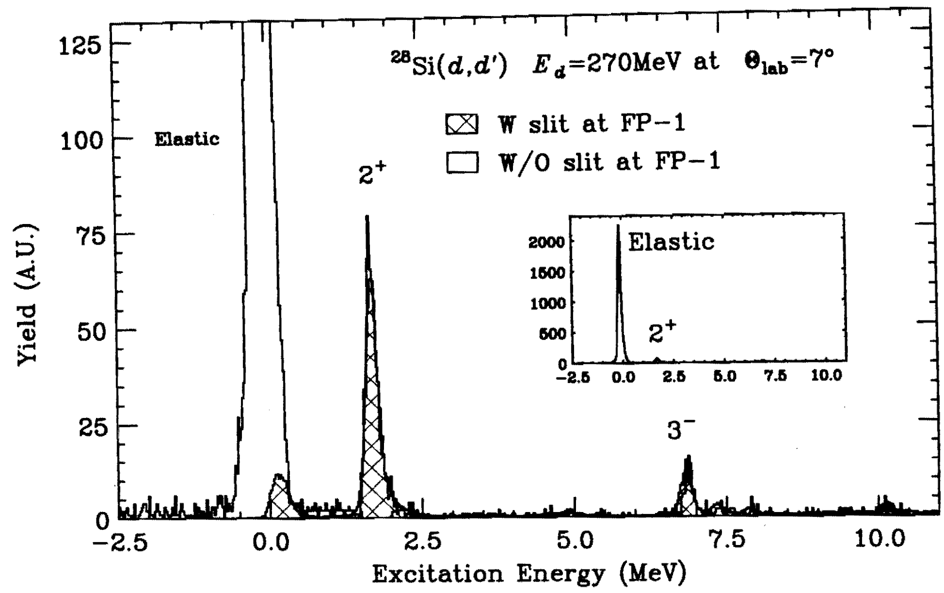

Figure 3.7: The slit system at FP-1 is used to suppress the elastic peak without affecting other inelastic peaks. The spectra are obtained for the ^{28}Si(d, d) reaction at E_d=270 MeV and at $\Theta_{\text{lab}} = 7°$ with and without a cut by the slit.

without affecting other inelastic peaks. This allowed us to take reliable data at angles as small as 2.5° and at excitation energies as small as 1 MeV.

Typical first order transfer matrix for FP-2 calculated with the code OPTRACE [64] is listed in Table 3.5. The horizontal and vertical beam envelopes through the spectrometer are shown in Figs. 3.8 and 3.9, respectively. Point-to-point focusing was obtained in the dispersive plane, while the point-to-parallel optics property was achieved in the vertical plane.

Table 3.5: A typical first-order transfer matrix of SMART FP-2 calculated with the code OPTRACE [64], x, y and z are expressed in cm, θ and ϕ in mrad and δ in %.

$$\begin{bmatrix} x' \\ \theta' \\ y' \\ \phi' \\ z' \\ \delta' \end{bmatrix} = \begin{bmatrix} 0.5212 & -0.0007 & 0.0000 & 0.0000 & 0.0000 & -7.5131 \\ 18.8574 & 1.9009 & 0.0000 & 0.0000 & 0.0000 & -38.0819 \\ 0.0000 & 0.0000 & -0.8337 & -0.0573 & 0.0000 & 0.0000 \\ 0.0000 & 0.0000 & 16.0780 & -0.0946 & 0.0000 & 0.0000 \\ 0.0000 & 0.0000 & 0.0000 & 0.0000 & 1.0000 & 0.0000 \\ 0.0000 & 0.0000 & 0.0000 & 0.0000 & 0.0000 & 1.0000 \end{bmatrix} \begin{bmatrix} x \\ \theta \\ y \\ \phi \\ z \\ \delta \end{bmatrix}$$

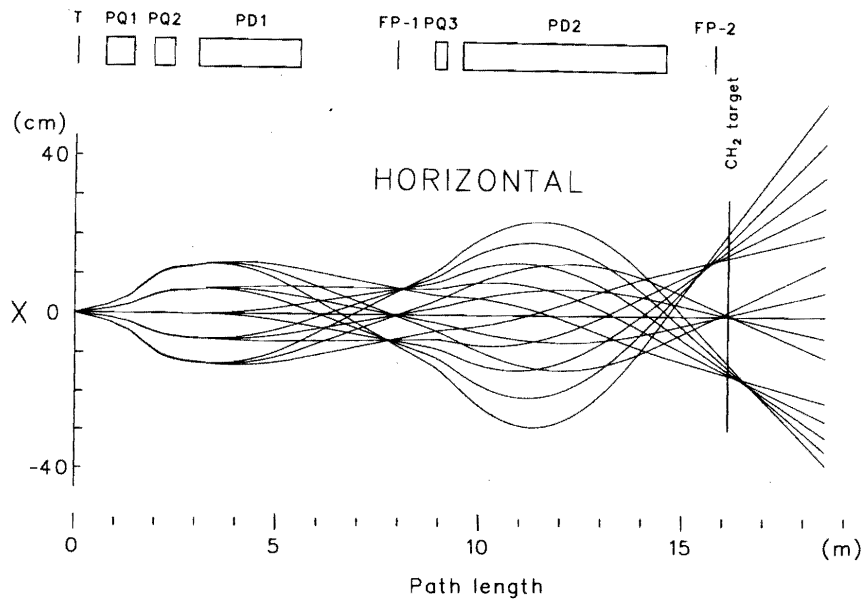

Figure 3.8: Horizontal beam envelopes through the spectrometer. The lines show horizontal displacements of the rays with horizontal scattering angles of $\alpha = \pm 25, \pm 12.5$ and 0 mr, and with momentum deviations of $\delta = \pm$ 2 and 0 %.

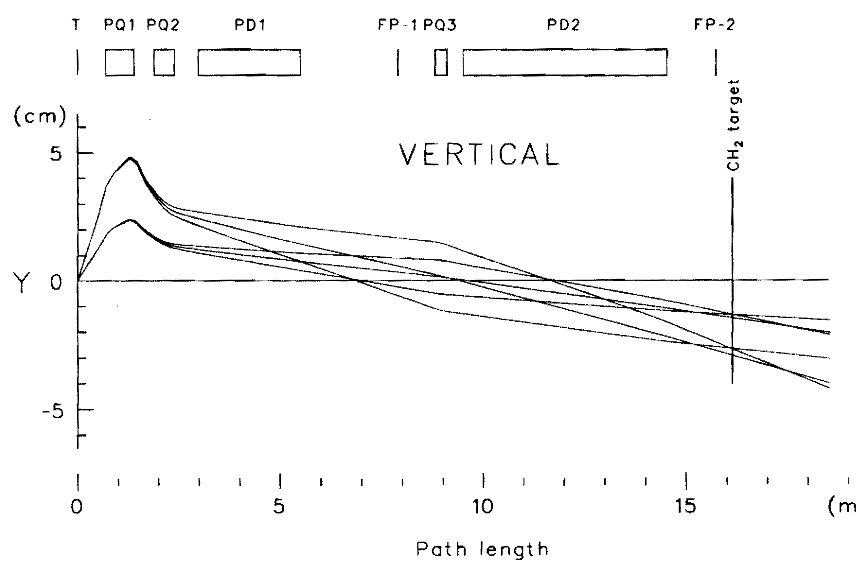

Figure 3.9: Vertical beam envelopes through the spectrometer. The lines show vertical displacements of the rays with vertical scattering angles of $\beta = 50$, 25 and 0 mr, and with momentum deviations of $\delta = \pm$ 2 and 0 %.

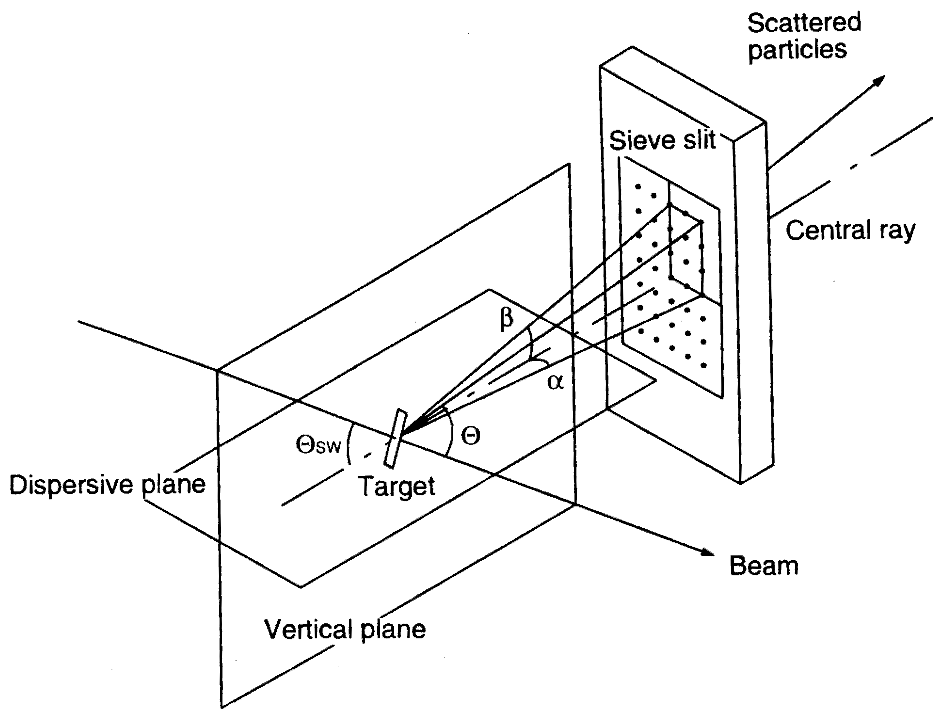

Figure 3.10: A sieve slit located at a distance of 405 mm from the target was used to investigate the ion optical property of SMART FP-2.

3.3.2 Optics Study

The ion optical property of SMART FP-2 was studied prior to measurements. Elastically scattered deuterons from an Au strip target (2 mm wide and 60 μ m thick) were measured at several spectrometer excitations with a 'sieve-slit' having a grid of holes (1mm ϕ) (see Fig. 3.10) to calibrate the trajectory reconstruction coefficients for the scattering angles and the momentum reconstruction coefficients. The slit was positioned 405 mm behind the target. Figure 3.11 shows a two-dimensional plot of the reconstructed image of the slit. Also shown in the figure are the projections of the image on both horizontal and vertical axes. The angular resolution is found to be better than 3 and 4 mrad in FWHM for dispersive (α) and vertical (β) scattering angles, respectively. The values include contributions of 2.4 mrad from the finite size of a hole in the slit. Due to the good angular resolution achieved it was possible to subdivide acceptance solid angles of the spectrometer by software cuts.

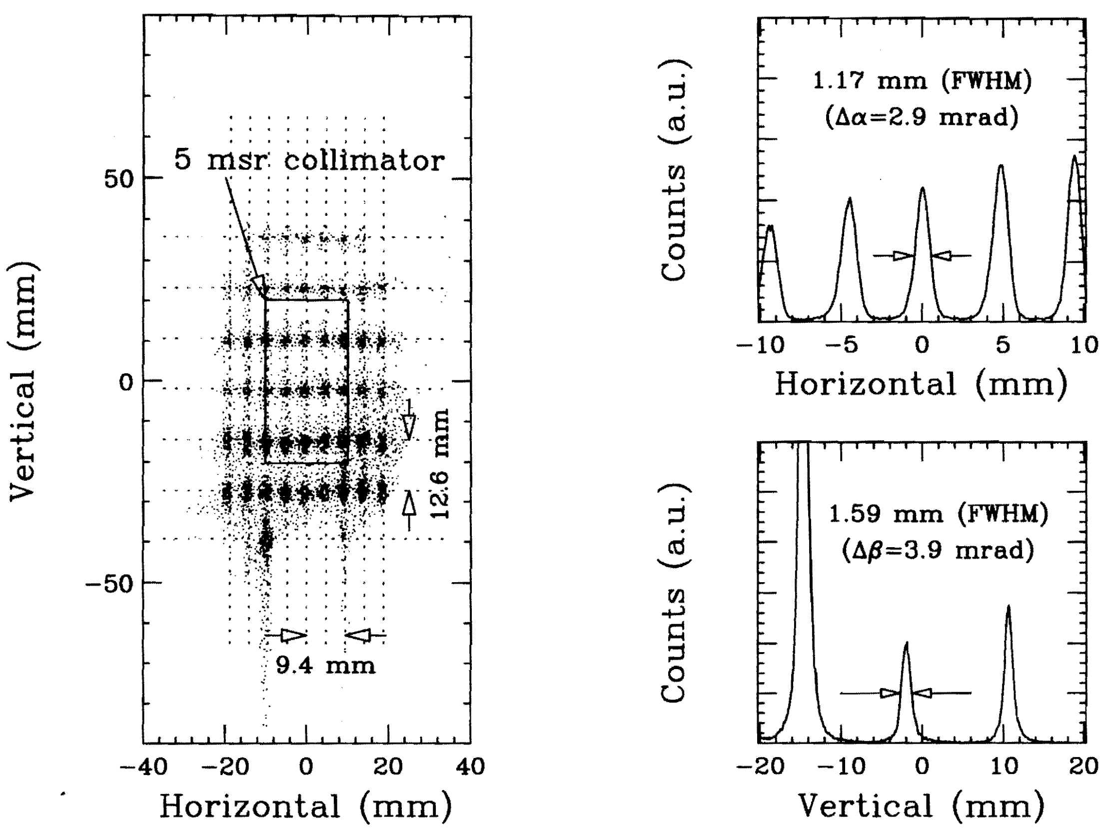

Figure 3.11: Reconstructed images of the sieve-slit obtained from the optics study of SMART FP-2. The angular resolution of the spectrometer system is estimated to be less than 3 and 4 mrad in FWHM for dispersive (α) and vertical (β) scattering angles, respectively.

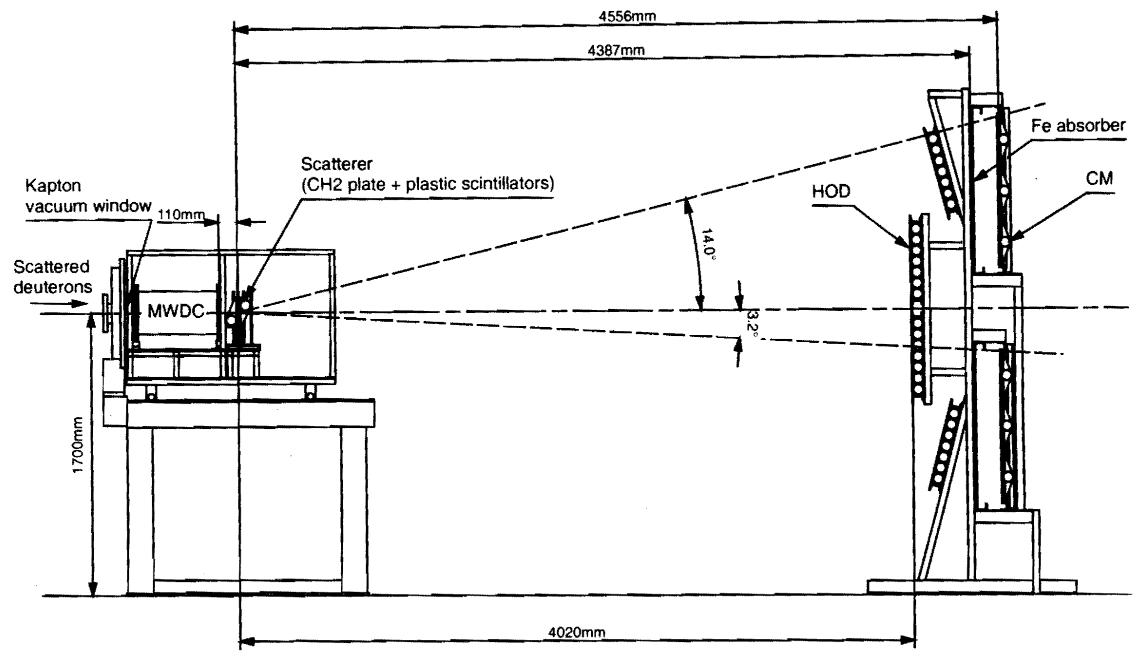

Figure 3.12: A scale drawing of the polarimeter DPOL (side view).

3.4 Focal Plane Deuteron Polarimeter DPOL

The focal plane deuteron polarimeter DPOL was located at SMART FP-2. It consisted of three parts, a multiwire drift chamber (MWDC), an analyzer target and a counter hodoscope system. Schematic layouts of the counter configuration are shown in Figs. 3.12 and 3.13. The deuterons from the primary scattering were incident on the analyzer target behind the MWDC. The analyzer target is comprised of two plastic trigger counters, SC1 and SC2, equipped with a polyethylene block. The hodoscope system, located 4 m behind the analyzer target, was used to detect proton pairs in a $^1S_0$ state produced by the $^1\mathrm{H}(\vec{d}, 2p)$ charge exchange reaction, and deuterons from the $\vec{d}+{}^{12}\mathrm{C}$ elastic scattering. In order to discriminate between the two analyzer reactions in a trigger decision level the hodoscope system is composed of two planes of segmented plastic scintillator array, the front plane is named HOD and the rear one CM.

3.4.1 Multiwire Drift Chamber

The multiwire drift chamber (MWDC) was used to determine the particle trajectory incident on the analyzer target at SMART FP-2. A schematic drawing of the MWDC is shown in Fig. 3.14. The characteristics are summarized in Table 3.6.

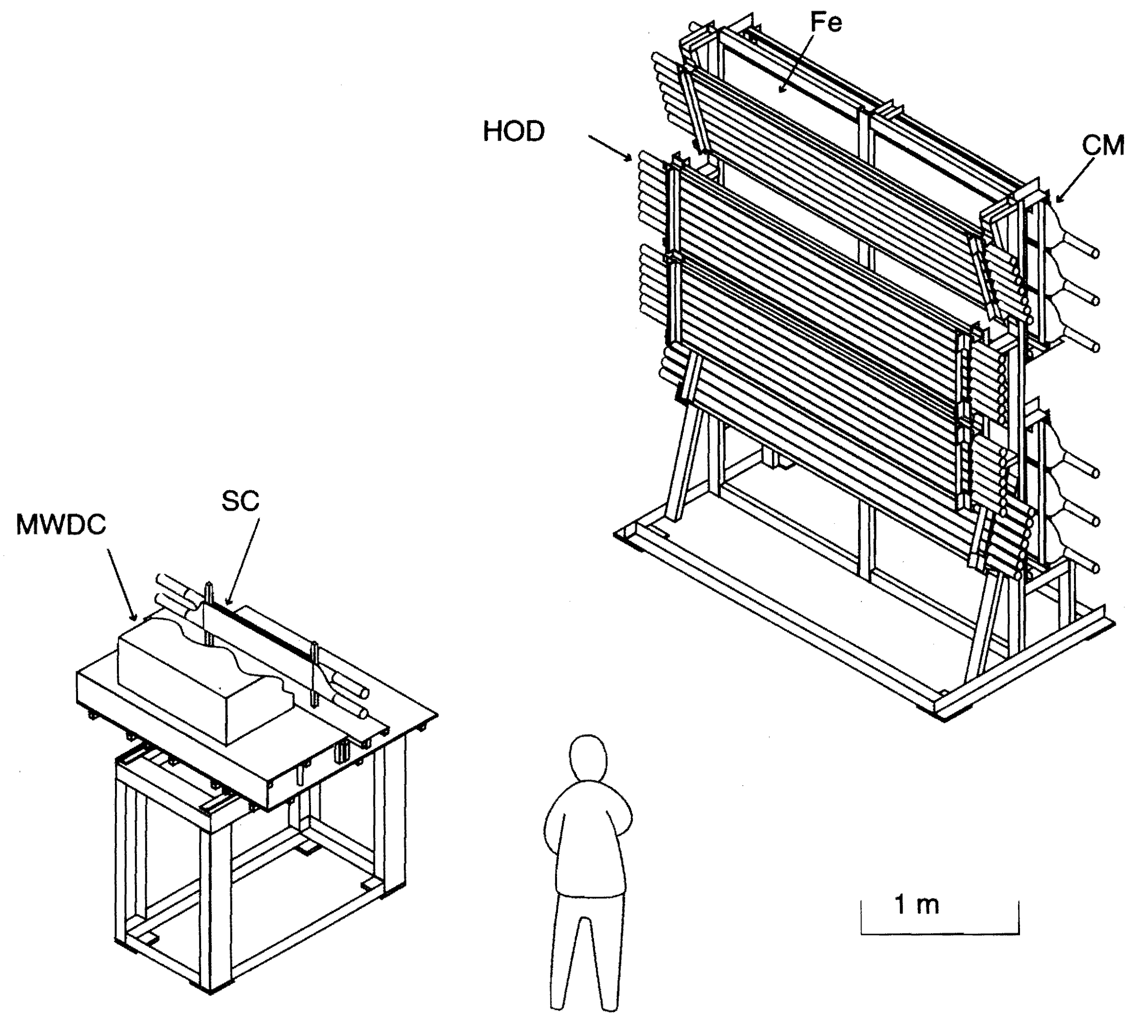

Figure 3.13: A schematic representation of the polarimeter DPOL.

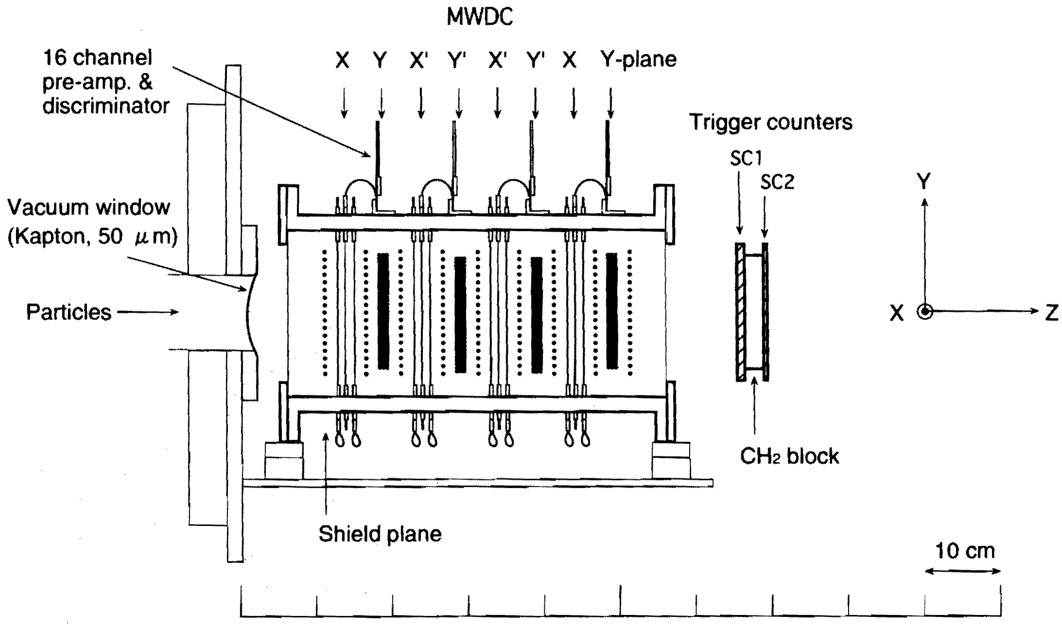

Figure 3.14: A cross sectional side view of the focal plane MWDC.

The MWDC was operated at atmospheric pressure. It was located with its front myler window 4 cm behind the rear end of a vacuum flange having a 50 μm-thick Kapton window. It had a sensitive area of 64 cm(W) $\times$ 16 cm(H) encompassing the full length of FP-2. The chamber had eight layers of sense-wire planes with X-Y-X'-Y'-X'-Y'-X-Y configuration, where the coordinates were chosen along the optic axis (Z), parallel to the dipole field (Y) and in the dispersive (X) direction. All the sense planes were normal to the Z axis and were separated by a distance of 5 cm from each other. In order to solve the left-right ambiguity the primed planes were half cell displaced relative to the unprimed ones. The sense planes were consisted of alternating anode and potential wires. The cathode planes were consisted of equally spaced cathode wires. The anode wires were grounded through amplifier/discriminator cards. The cathode and potential wires were at negative high voltages.

A gas mixture was Ar (50 %) + C_2H_6 (50 %). It was bubbled through iso-propyl alcohol which was cooled down to 0° in order to reduce an ageing effect caused by hydrocarbon accumulation on wires [65]. The gas flow rate was kept at 50 cc/min.

Typical plateau curves measured for 270 MeV deuterons and operation high voltages are shown in Fig. 3.15. The overall detection efficiency was more than 99 %. A typical intrinsic position resolution was 90 μm in σ for one plane, as shown in Fig. 3.16. The figure shows the drift-length sum for pairs of planes half cell displaced to each other, where the width of a peak represents $\sqrt{2}$ times the intrinsic resolution.

Table 3.6: MWDC parameters.

Parameter	X(X') plane	Y(Y') plane
Inside volume x, y, z	80 cm × 22 cm × 50 cm	
Number of planes	8 planes (X,Y,X',Y',X',Y',X,Y)	
Active area	64 cm(x) × 16 cm(y)	
Separation of XY planes	5 cm	
Cell size	20 mm × 20 mm	10 mm × 10 mm
Number of cells	32 cells/plane	16 cells/plane
Anode wire (tension)	ϕ 30 μm Tungsten (80 g)	
Cathode wire	ϕ 100 μm Cu-Be (120 g)	
Potential wire	ϕ 100 μm Cu-Be (120 g)	
Gas mixture	Argon (50%) : Ethane (50%)	
Cathode voltage	-3.2 kV	-2.4 kV
Potential voltage	-3.2 kV	-2.4 kV
Window material	Myler (25 μ m)	

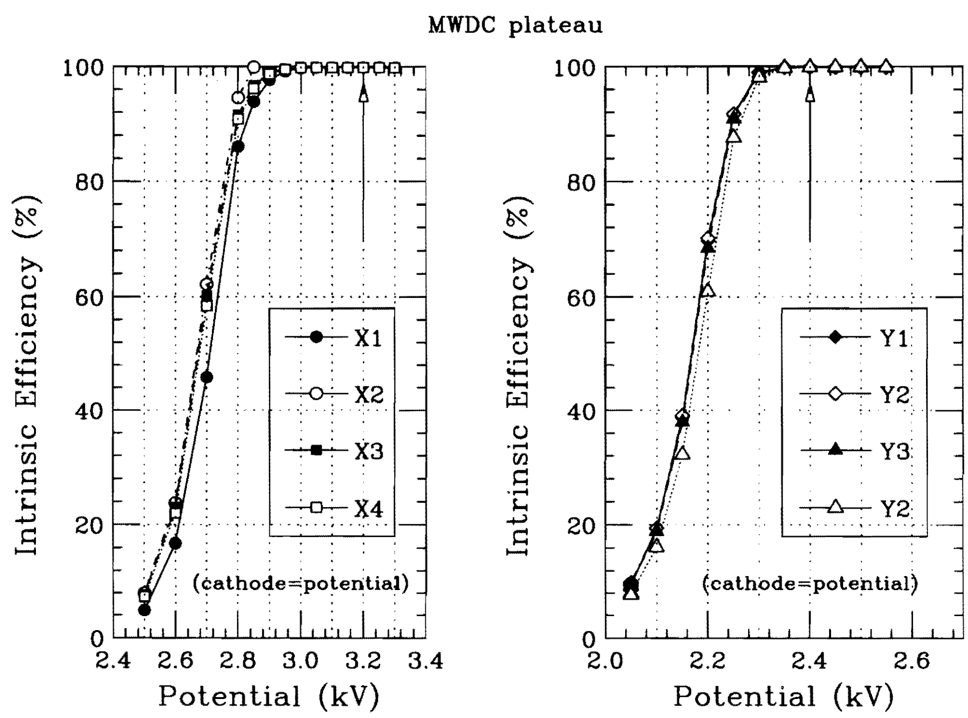

Figure 3.15: Typical plateau curves and operation high voltages of the MWDC.

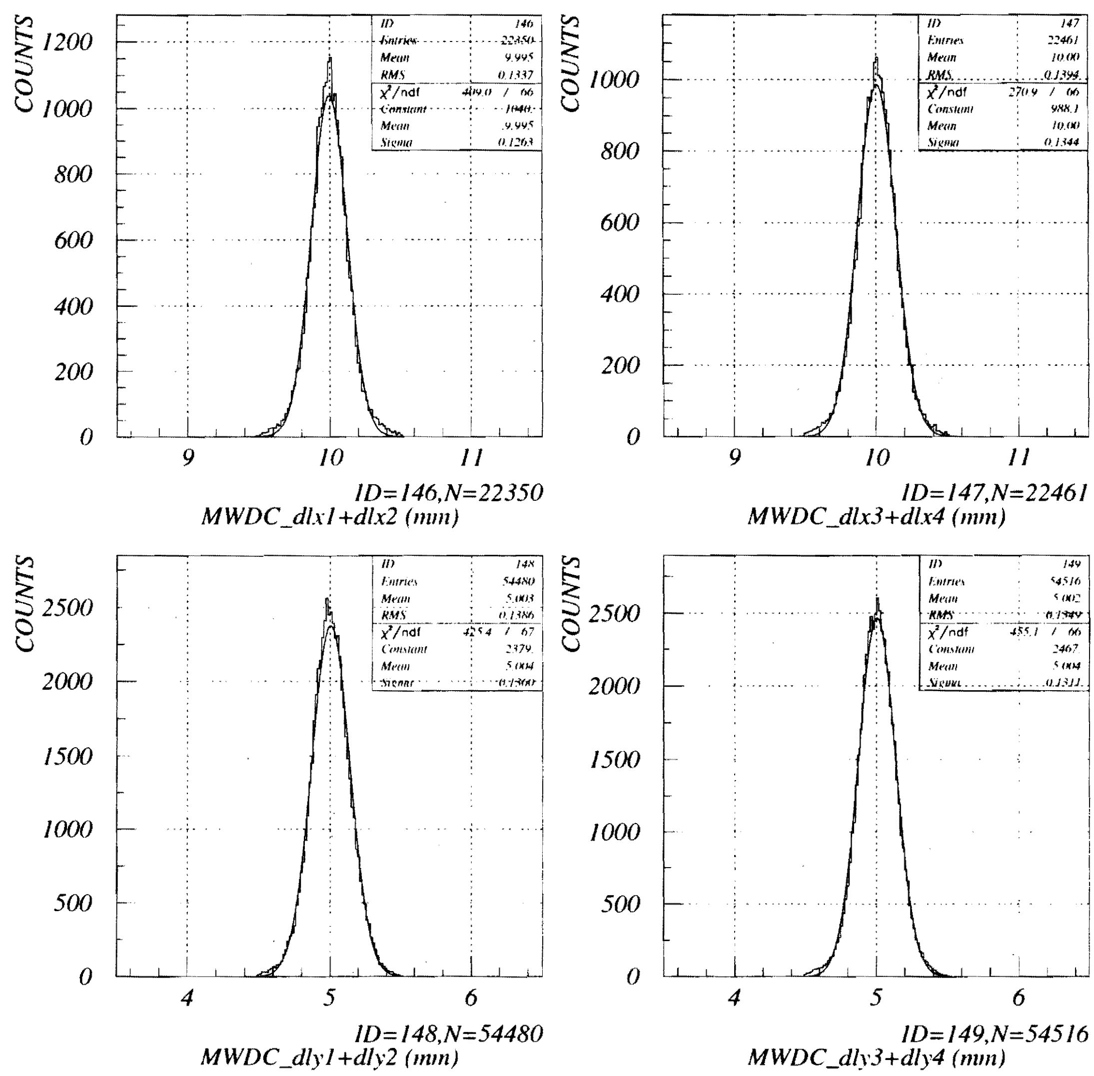

Figure 3.16: Typical distributions of the drift-length sum for pairs of planes which are displaced by a half cell to each other. The width of a peak represents $\sqrt{2}$ times the intrinsic position resolution, while the position of a peak represents the maximum drift length.

Table 3.7: The thicknesses of carbon and hydrogen material contained in the scatterer.

Target	Thickness (cm)	Density (g/cm^3)	H/C ratio	H (g/cm^2)	C (g/cm^2)
SC1	1.0	1.032	1.104	0.087	0.945
CH_2	2.5	0.944	2.0	0.337	2.023
SC2	0.5	1.032	1.104	(0.044)	0.473
total	4.0	—	—	0.424	3.440

3.4.2 Analyzer Target

Two plastic scintillation counters (Bicron BC-408), SC1 and SC2, and a polyethylene (CH_2) block in between was used as an analyzer target (scatterer) (see Fig. 3.14). The SC1 and SC2 counters had a same areal dimension of 18.0 cm (height) × 80 cm (width), and thicknesses of 1.0 cm and 0.5 cm, respectively. The CH_2 block had a dimension of 15 cm (hight) × 75 cm (width) × 2.5 cm (thick). The thicknesses of carbon and hydrogen material contained in the scatterer are listed in Table 3.7.

The total thickness of the scatterer was determined so as to have enough reaction rates while keeping the multiple Coulomb scattering to an acceptable level. The resulting reaction rates were as much as 10^{-3} and 10^{-4} per one incident deuteron for the elastic scattering and the charge exchange reaction, respectively (see Appendix A). The estimated values on the energy loss, multiple Coulomb scattering and energy straggling for 270 MeV deuterons are summarized in Table 3.8. Furthermore, the scatterer must be thin enough to ensure 100 % detection efficiency for proton pairs produced by the charge exchange reaction within the acceptance of the detector system. This is because large systematic errors can be brought about through an unpredictable threshold effect in the t_{20} polarization component, which manifest itself in the change of the overall efficiency of the scattering yield. Figure 3.17 compares the velocity distributions of each proton for the charge exchange reaction at 270, 250 and 230 MeV with those obtained from the Monte

Table 3.8: The estimated energy loss, Coulomb multiple scattering angle and energy struggling for 270 MeV deuterons on the secondary target.

Energy loss (MeV)	Multiple scattering (rms) (deg.)	Energy straggling (σ) (MeV)
18.67	0.42	0.57

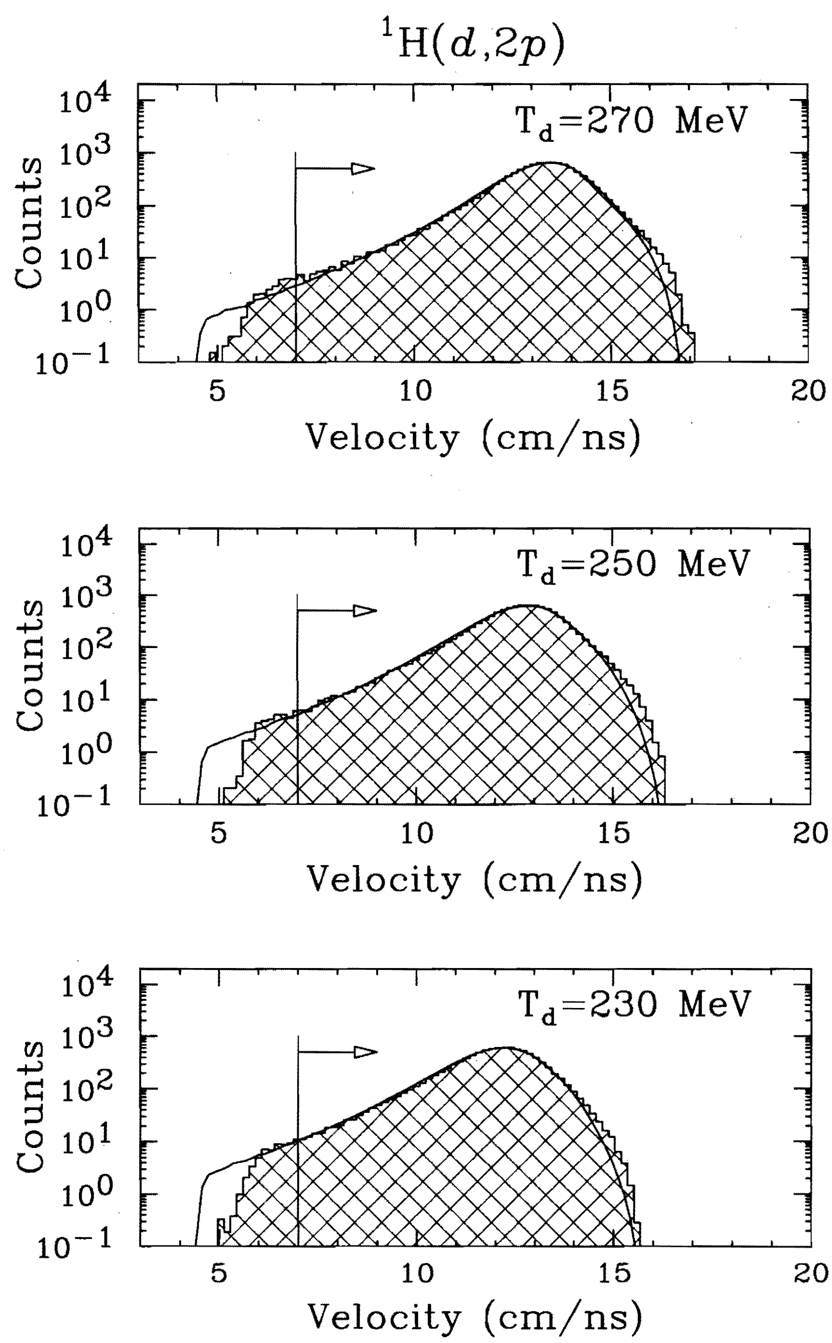

Figure 3.17: Velocity distributions of individual protons produced through the charge exchange $^1\mathrm{H}(d, 2p)$ reaction at 270, 250 and 230 MeV. The shaded histograms are experimental results, while the solid lines are results of a Monte Carlo simulation given in Appendix B. The thickness of the scatterer in this experiment ensures 100 % detection efficiency for individual protons having velocity above 7 (cm/ns) within the experimental acceptance.

Carlo simulation (see Appendix B). We see that the proton events having velocity below 7 (cm/ns) suffer from detection losses presumably due to insufficient amount of energies deposited in the HOD counter, while those having velocity exceeding 7 (cm/ns) are free from such an unwanted threshold effect.

The SC1 and SC2 counters were equipped with photomultipliers (Hamamatsu H1161) on both ends through fish-tail shaped light guides. They were also used as trigger counters. A coincidence signal from SC1 and SC2 provided the main trigger. The averaged timing of signals from all the four PMTs given by

$$T(\mathrm{SC}) = \frac{T_L(\mathrm{SC1}) + T_R(\mathrm{SC1}) + T_L(\mathrm{SC2}) + T_R(\mathrm{SC2})}{4}, \tag{3.4}$$

gave time zero for drift time measurement in MWDC and time-of-flight measurement of the secondary scattering.

3.4.3 Counter Hodoscope

The DPOL counter hodoscope was located about 4 m downstream of the scatterer. It measured the arrival timing and hit position of charged particles produced through the secondary reactions. The hodoscope had an areal dimension of about 2×2 m^2 covering an angular region where large figure of merits are ensured for both of the analyzer reactions. The front plastic counter wall, HOD, detected both protons and deuterons, while the rear wall, CM, having an iron absorber in front of it, was only sensitive to high energy particles (mostly deuterons). In the off-line analysis, the time-of-flight measurement between SC and HOD offered the finer event selection. The ADC data of HOD and CM were also used for particle identification. All counters were arranged symmetrically with respect to the dispersive plane. There was no counter placed near the dispersive plane in order to reduce hits caused by deuterons without any scattering in the analyzer target.

Figure 3.18 (a) shows a schematic view of the HOD counter, a plastic scintillation counter (BC-408) wall comprising twenty-eight independent horizontal segments. Each of HOD counter had a size of 6.5 cm (height) $\times$ 6.5 cm (thickness) $\times$ 220 cm (width), and was viewed by Hamamatsu H1161 photomultiplier tubes (PMTs) at both ends. The PMTs were coupled directory to the scintillator by the optical cement NE581. Seven counters were put together into an aluminium box, the innermost two boxes were oriented normal to the beam axis, while the outermost ones were tilted by $\pm 15°$ so as to reduce subsequent hits of adjacent counters caused by a single charged particle. The arrival timing of a charged particle at HOD was determined by the averaged timing of two signals from PMTs at both ends. The time-of-flight between SC and HOD was give by

$$TOF = \frac{T_L(\mathrm{HOD}) + T_R(\mathrm{HOD})}{2} - T(\mathrm{SC}). \tag{3.5}$$

Figure 3.19 shows the time-of-flight spectrum measured for the $\vec{d}$ + C elastic events. Typical timing resolution after the slewing correction (see section 4.3) was 220 ps in FWHM. With a flight path of 4 m, it corresponds to kinetic energy resolution of $\delta T/T$=1.7 % (in FWHM) for 250 MeV deuterons. The $\vec{d}$ + C elastic data were used to determine timing offset parameters, the fluctuation of which during measurement was corrected for run by run in the off-line analysis. The horizontal hit position, Y, was determined by the timing difference between two signals from PMTs at both ends given by

$$Y = c_{\text{eff}} \times \frac{T_L(\text{HOD}) - T_R(\text{HOD})}{2}, \tag{3.6}$$

where c_{eff} is the propagation velocity of light within the HOD scintillator. Position calibration was made off line using radioactive source. The averaged value of c_{eff} was measured to be 15.6 cm/ns. Typical position resolution in the horizontal direction was 4.0 cm in FWHM as shown in Fig. 3.20. The figure shows the hit position difference for a pair of adjacent HODs hit by a single charged particle, the width of the spectrum represents $\sqrt{2}$ times the intrinsic position resolution. The hit position in the vertical direction was determined by identifying the counter that had hit.

Figure 3.18 (b) shows a schematic view of the CM counter, a plastic scintillation counter (BC-408) wall comprising six independent horizontal segments. Each of CM counter had a size of 29.0 cm (height) × 1.0 cm (thickness) × 220 cm (width), viewed by Hamamatsu H1161 photomultiplier tubes (PMTs) at both ends through fish-tail shaped light guides. It was used to select high energy deuterons coming from the $\vec{d}$ + C elastic scattering. An iron absorber (energy degrader) with a thickness of 13.5 mm in front of CM was used to stop break-up protons through range selection.

3.5 Trigger and Data Acquisition

The trigger diagram is shown in Fig. 3.21. The logic was constructed with standard NIM modules. Three kinds of trigger were generated. The signals from counters SC1 and SC2 were transmitted to constant fraction discriminators (CFDs). The coincidence among SC1 and SC2 defined the singles (SI) event trigger. This trigger was used to calculate double differential cross sections for the primary scattering, as well as to record the number and profile of the deuterons incident on the polarimeter before the second scattering. Events with this trigger was prescaled with a typical scaling factor of 1/1000 using a rate divider (R.D.) before recording in order to reduce the load of data acquisition. The signals from counters HOD and CM were transmitted to leading-edge discriminators (Discri.). The $\vec{d}$+C elastic (EL) event trigger was defined by [HOD(1-12) × CM(1-3) × SC] or [HOD(17-28) × CM(4-6) × SC]. This event trigger was also prescaled by a factor of 1/5. The trigger

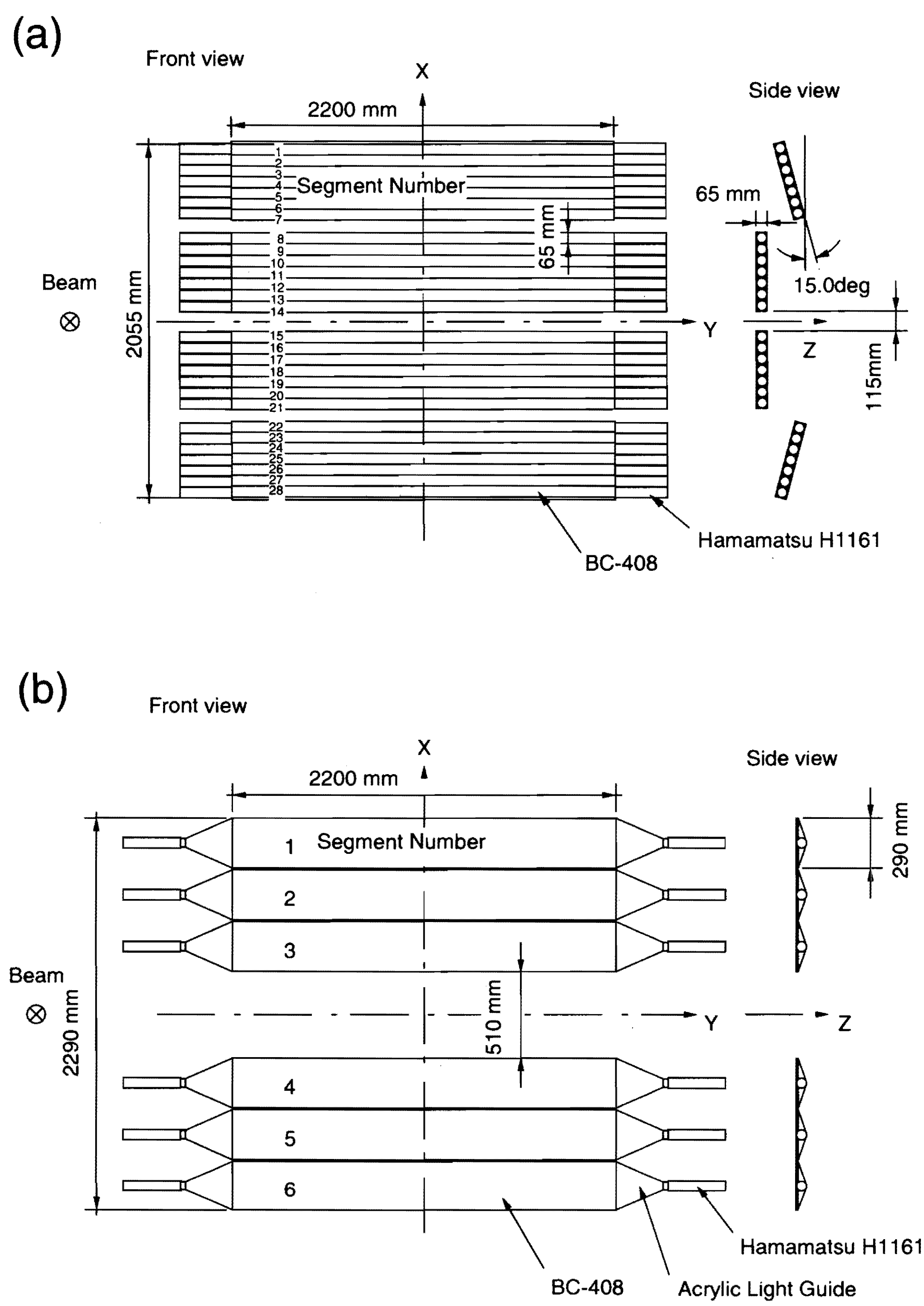

Figure 3.18: Schematic views of the DPOL counter hodoscope, (a) HOD and (b) CM.

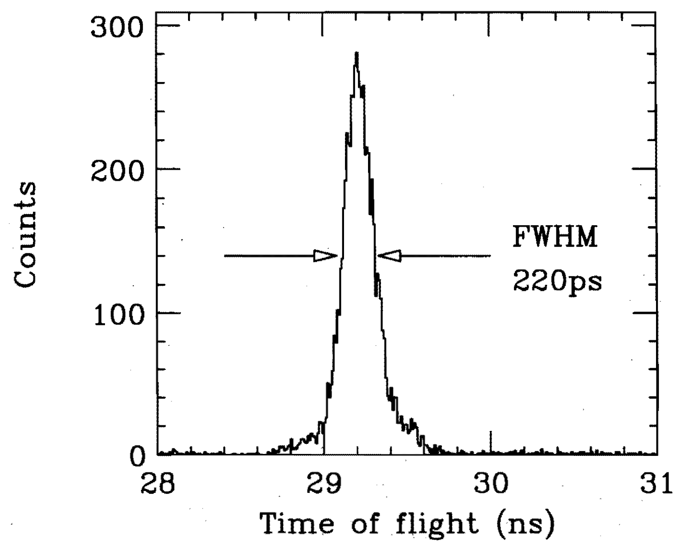

Figure 3.19: A typical time-of-flight spectrum between SC and HOD for a 270 MeV deuteron beam elastically scattered by ^{12}C in the scatterer.

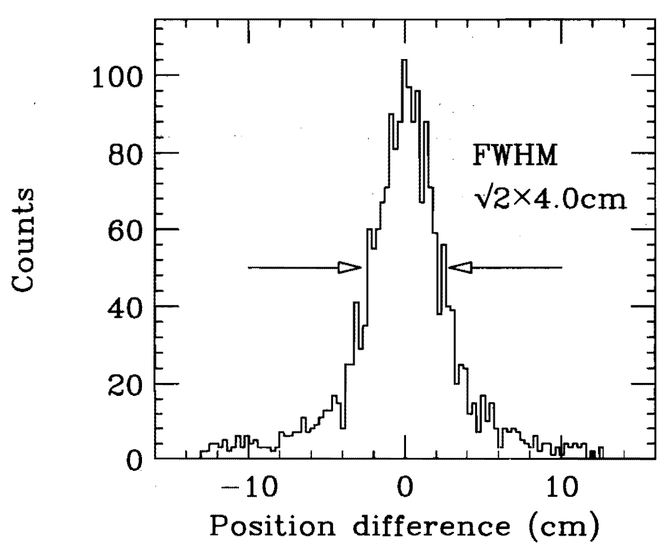

Figure 3.20: A typical hit position difference for a pair of adjacent HODs hit by a single charged particle, the width of the spectrum represents $\sqrt{2}$ times the intrinsic position resolution.

for the ^{1}H($\vec{d}$, $2p$) charge exchange (CE) events was made by a coincidence detection of two charged particles within the HOD counters. The CE event trigger was defined by [HOD(1-14) $\times$ HOD(1-14) $\times$ SC] or [HOD(15-28)$\times$ HOD(15-28)$\times$ SC] or [HOD(1-14) $\times$ HOD(15-28)$\times$ SC]. In order to avoid misidentifying double hits caused by a single charged particle as a charge exchange event, those events in which only an adjacent pair of HODs had hits were excluded from the trigger. To specify such a coincidence condition Kaizu matrix logic units (M.L.U), which had 12 $\times$ 12 inputs and 144 dip switches, were used.

A schematic diagram of the data acquisition system is shown in Fig. 3.22. The timing and pulse height signals from the plastic scintillators and the timing signals from MWDC were encoded and taken by a CAMAC system. Scalar information was also recorded via the CAMAC system, separately for each spin state. The CAMAC ADC, TDC and scalar data were read by an auxiliary crate controller (CES 2180 STARBURST J-11), and then DMA transfered to a DEC VAX workstation (VAX 4000/106A) and recorded on digital data storage (DDS2) tapes by using the RIKEN standard data-acquisition software [66]. In a typical experimental condition 250 events per second were acquired with 20 % loss.

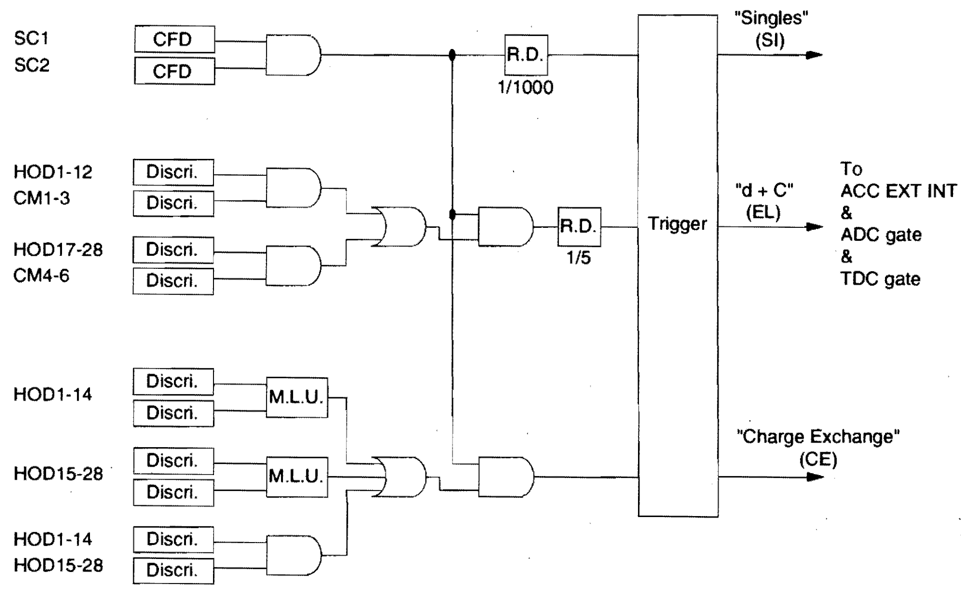

Figure 3.21: A trigger logic diagram.

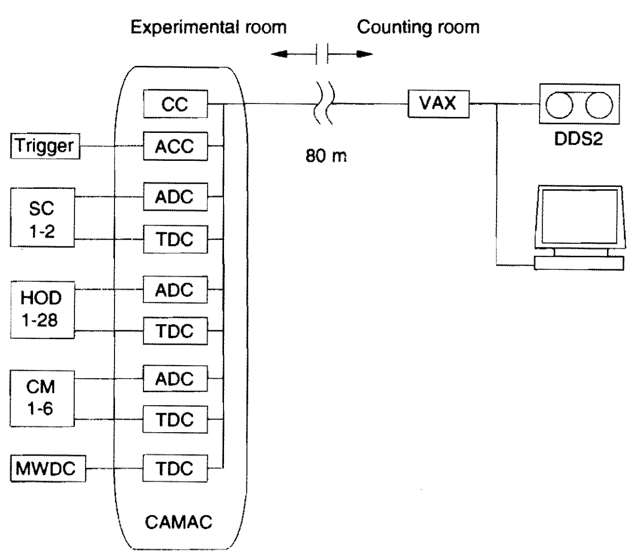

Figure 3.22: A schematic diagram of the data acquisition system.

Chapter 4

Data Reduction

The data reduction process required many steps, including an extensive Monte Carlo simulation. The subsequent procedures were followed.

1. Particle identification and kinematics reconstruction for the primary scattering.
2. Timing and position calibration of the DPOL counter hodoscope.
3. Event selection for the secondary scattering.
4. Extraction of cross section and polarization observables.

Details of these procedures are presented in this section. The data reduction of the polarimeter for the double scattering was proceeded in the same way as that for the calibration data.

Different coordinate systems used to describe the deuteron polarization at various spectrometer positions are shown in Fig. 4.1.

4.1 Beam Polarization

The vector and tensor polarization components (p_y, p_{yy}) of the primary beam were determined from the coincidence yields for four pairs of (left/right/up/down) scintillator telescope in the beam line polarimeter, $N'(L), N'(R), N'(U)$ and $N'(D)$, which are normalized by the beam current after subtraction of accidental coincidence, by the relations:

$$p_y = \frac{N'(L) - N'(R)}{3A_y}, \tag{4.1}$$

$$p_{yy} = \frac{N'(L) + N'(R) - N'(U) - N'(D)}{A_{yy} - A_{xx}}, \tag{4.2}$$

where A_y, A_{yy} and A_{xx} are the analyzing powers for the $\vec{d} + p$ elastic scattering (see Table 3.2). Figure 4.2 shows a series of polarization values for each beam spin state

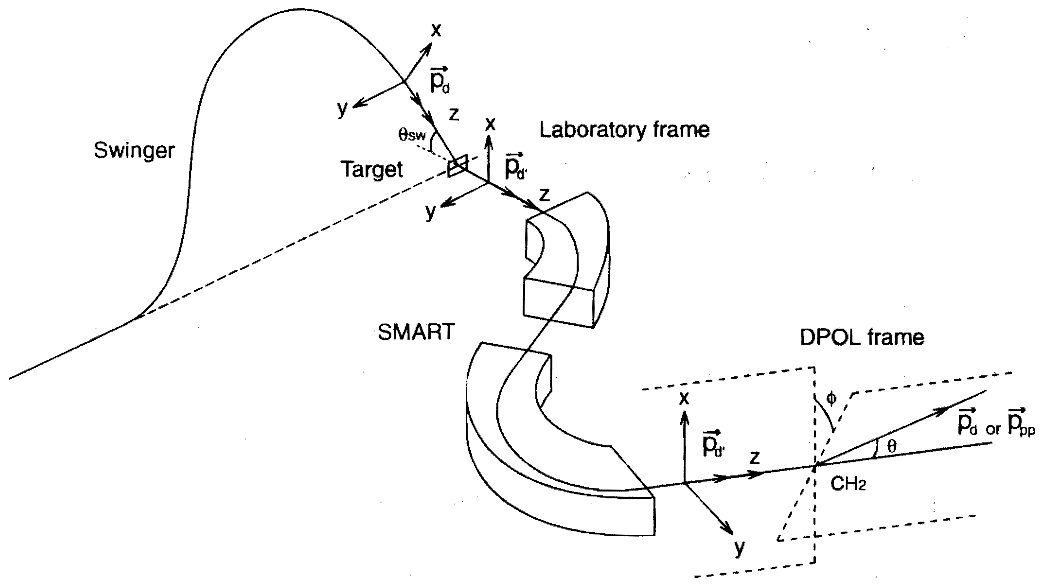

Figure 4.1: Definition of different helicity frames to describe deuteron polarization at various experimental site. The z-axis is taken to be in the beam direction, the y-axis perpendicular to the reaction plane ($y = k_{\text{in}} \times k_{\text{out}}$) and the x-axis to form the right-handed system. The helicity frame is rotated when passing through the spectrometer.

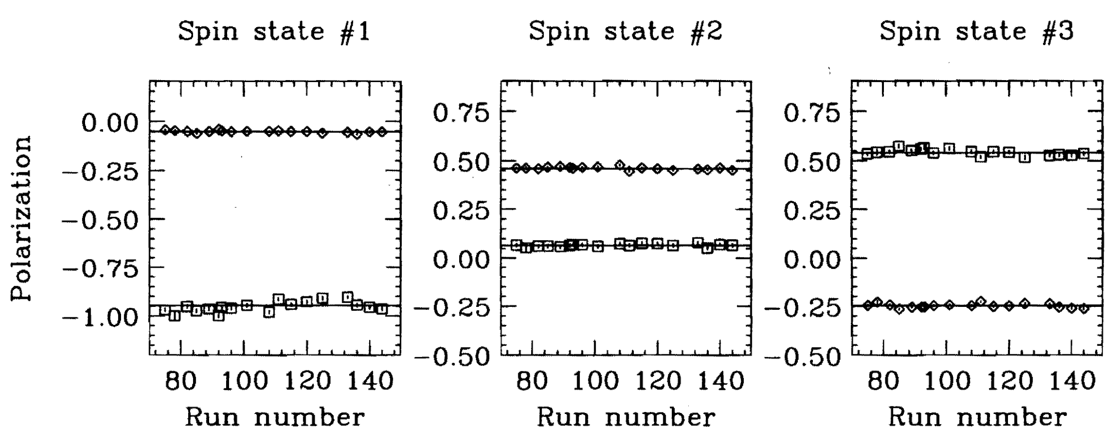

Figure 4.2: Beam polarization values during experiment, as a function of run number for each spin state. Open diamond (◇) represents vector polarization p_y; open square (□) tensor polarization p_{yy}.

measured during experiment lasted for four days. The beam polarization was stable to within 1.7 % and 2.8 % for vector and tensor components, respectively. The average

Table 4.1: The average values of measured beam polarization for each spin state. The ideal values for vector and tensor polarization components are shown in parentheses.

	#0 (0,0)	#1 (0,-2)	#2 (2/3,0)	#3 (-1/3,1)
p_y	—	-0.052	0.459	-0.247
p_{yy}	—	-0.948	0.067	0.540

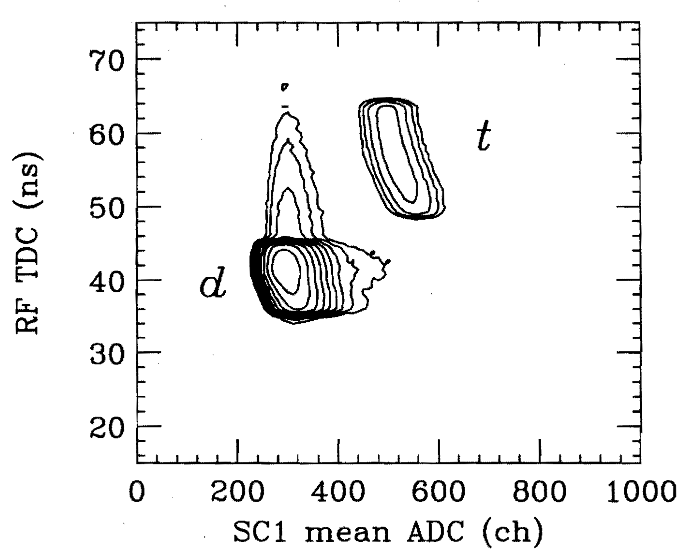

Figure 4.3: A two-dimensional histogram of SC1 mean ADC versus cyclotron RF timing.

values, as indicated by solid lines in Fig. 4.2 and listed in Table 4.1, were used in data analysis.

4.2 Analysis in the Primary Scattering

4.2.1 Particle Identification

The possible background particles in the primary scattering were tritons. Figure 4.3 shows a two-dimensional histogram of SC1 mean ADC versus cyclotron RF timing measured for the ^{12}C(d,d') reaction at a swinger angle of 25° and at E_d=270 MeV. Deuterons and tritons were easily differentiated. In measurements at forward angles below 10° the triton events were generally negligible.

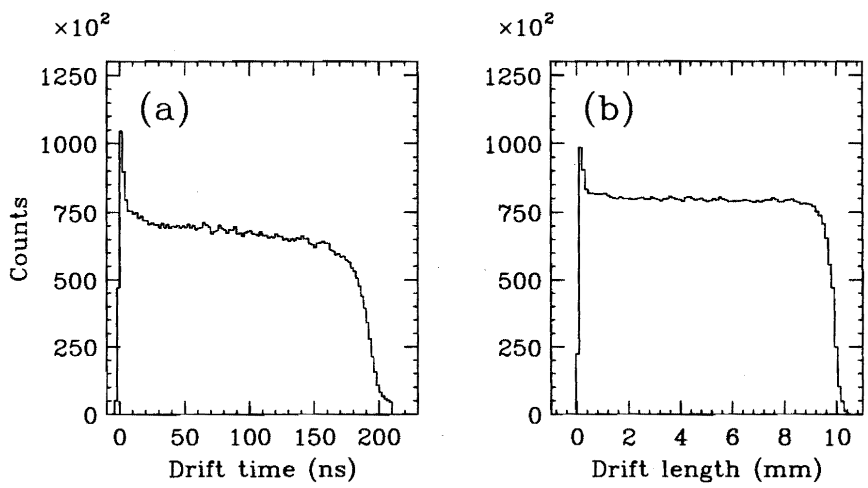

Figure 4.4: Typical distributions of (a) drift time and (b) drift length within a cell.

4.2.2 Kinematics Reconstruction

The polar (Θ) and azimuthal (Φ) scattering angles and the target excitation energy (E) in the primary reaction were obtained from MWDC data and SMART optics information as follows. Firstly, the MWDC drift time information was converted to the drift distance using empirically determined third order polynomial functions. Typical (a) drift time and (b) drift length distributions are shown in Fig. 4.4. Secondly, a straight line track was determined by finding a good combination of hit wires which gave minimum χ^2 value in the straight line fit. At least three hits out of four were required in both x and y planes. Thirdly, the focal plane positions and angles thus determined were used to calculate dispersive and vertical scattering angles α and β of the primary scattering (see Fig. 3.10) using the trajectory reconstruction coefficients, and the momentum p_f using the momentum reconstruction coefficients. Finally, the kinematics quantities Θ, Φ and E were calculated by the relations:

$$\Theta = \arccos \frac{\cos(\Theta_{SW} + \beta)}{\sqrt{1 + \tan^2\alpha\cos^2\beta}}, \tag{4.3}$$

$$\Phi = \arctan \frac{\tan\alpha\cos\beta}{\sin(\Theta_{SW} + \beta)}, \tag{4.4}$$

$$E = \sqrt{(E_d + M_t - E_d')^2 - |\boldsymbol{p}_i - \boldsymbol{p}_f|^2} - M_t, \tag{4.5}$$

where Θ_{SW} refers to the swinger rotation angle, $(E_d, \boldsymbol{p}_i)$ and $(E'_d, \boldsymbol{p}_f)$ four-momenta of the incident and scattered deuterons and M_t and M_d the target and deuteron masses.

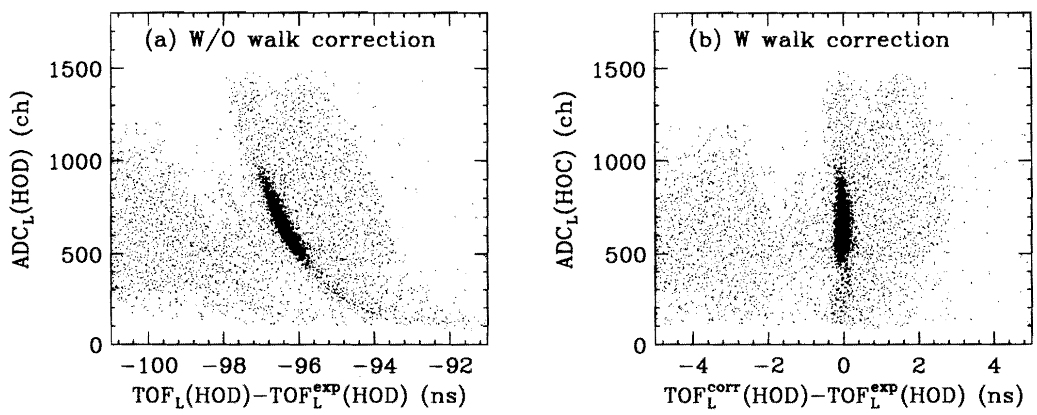

Figure 4.5: Two-dimensional histograms of time-of-flight $\mathrm{TOF_L(HOD)}$ measured with a left PMT of a HOD counter versus corresponding ADC, (a) before the slew correction and (b) after the slew correction. Expected TOF values $\mathrm{TOF_L}^{\mathrm{exp}}\mathrm{(HOD)}$ are subtracted in abscissa.

The number of events acquired with the singles (SI) event trigger was not only used to calculate double differential cross sections and analyzing powers of the primary reaction but also gave information on the initial conditions of the incident deuterons on the polarimeter (the number of deuterons and their spatial and energy distributions). For each beam spin state (i) the number of valid events was stored in a two-dimensional histogram $N_{SI}^{(i)}(\Theta, E)$.

4.3 Timing and Position Calibration of the Counter Hodoscope

The DPOL counter hodoscope HOD was used as timing as well as position counter for the second scattering. Timing and position calibration was made by using the $\vec{d} + {}^{12}\mathrm{C}$ elastic scattering with a direct deuteron beam on the scatterer.

Since the anode signal from the PMT of the counter hodoscope was transmitted to a leading-edge discriminator, the timing data $T_{L(R)}(\mathrm{HOD})$ had to be corrected for a shift due to pulse hight $A_{L(R)}(\mathrm{HOD})$ variations (slew effect). The slew correction was made by the relation:

$$T_{L(R)}^{\mathrm{corr}}(\mathrm{HOD}) = T_{L(R)}(\mathrm{HOD}) - a_{L(R)}/\sqrt{A_{L(R)}(\mathrm{HOD})} + b_{L(R)} - T(\mathrm{SC}), \tag{4.6}$$

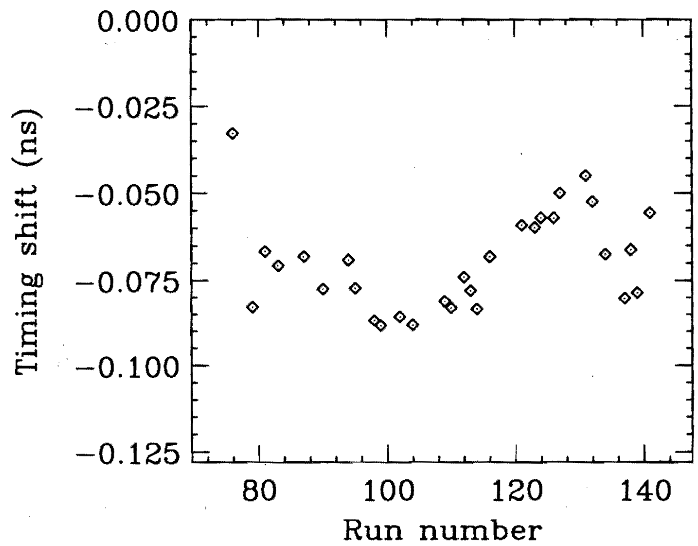

Figure 4.6: Timing shift during experiment as a function of run number.

where $T^{\rm corr}_{L(R)}$(HOD) is the corrected TDC value for a left (right) PMT signal and $a_{L(R)}$ and $b_{L(R)}$ are adjustable parameters which were determined by fitting the function to the data for the $\vec{d}+{}^{12}$C elastic scattering. Figure 4.5 (a) shows a two-dimensional histogram of the timing versus ADC for a particular PMT signal before the slew correction, while Figure 4.5 (b) shows the same histogram after the correction. The slew correction was made for each PMT of all the HOD counters. The hit position along the HOD scintillator Y(HOD) was determined, from the timing difference between signals from left and right PMTs (see Eq.(3.6)). The propagation velocity of light within a HOD scintillator $c_{\rm eff}$ was obtained from the position calibration data using a well collimated β-radiation from a source. Since the adjustable parameters, $a_{L(R)}, b_{L(R)}$ and $c_{\rm eff}$, were closely related to each other, the timing and position calibration procedures were repeated until sufficiently saturated values were obtained for these parameters.

Once the timing calibration was done, it was possible to know the global timing shift run by run during experiment by monitoring the missing mass peak position of the $\vec{d}+{}^{12}$C elastic scattering. Figure 4.6 shows the timing shift determined by requiring that the missing mass peak be located at the correct position. The shift may be caused by changes in the signal propagation velocity in cables and electronics circuit due to temperature variation.

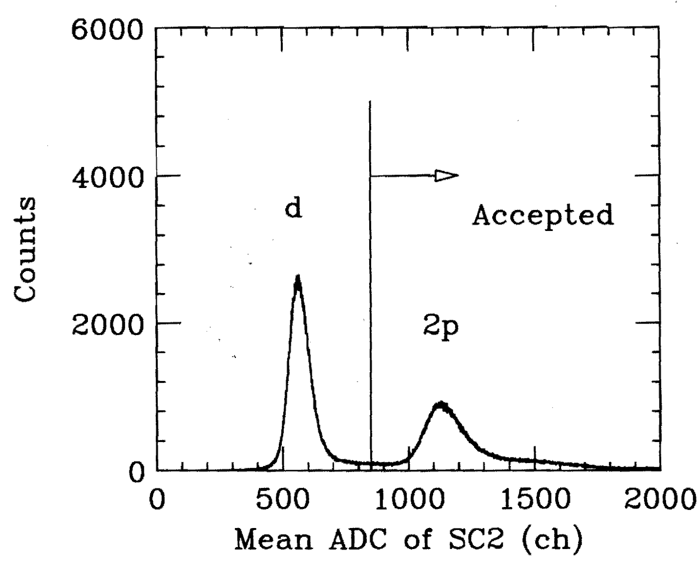

Figure 4.7: The ADC spectrum of SC2 measured with CE event trigger.

4.4 Event Selection in the Secondary Scattering

The polarimeter DPOL made use of the $\vec{d}+{}^{12}$C elastic scattering (EL) and the ^{1}H($\vec{d}$, $2p$) charge exchange (CE) reaction to measure both vector and tensor polarization components of the incident deuterons. Timing and pulse height information as well as constraints on kinematics were used to eliminate background contributions.

4.4.1 The ^{1}H($\vec{d}$, $2p$) Charge Exchange Reaction

The ^{1}H($\vec{d}$, $2p$) CE event trigger was generated by a coincidence detection of two charged particles in HOD. Most of the background events recorded by the CE event trigger was associated with accidental coincidence in which one of the particles detected was a beam deuteron.

Each of the protons produced by the $(d, 2p)$ reaction had approximately the same velocity as that of the incident deuteron. Since the energy loss per unit length is proportional to the charge number, the energy deposit of the two protons was about twice as large as that of the deuteron. If the reaction occurred in SC1 or CH_2 block in the scatterer, the pulse height measured with SC2 should be twice as high as that of the deuteron. Figure 4.7 shows the mean ADC spectrum of SC2 scintillator for events registered by the CE event trigger. In the figure the $2p$ peak is clearly seen at 1120 ch well separated from the d peak at 560 ch. Gates were applied on the mean ADC spectrum to select useful CE events contained in the $2p$ peak as shown in Fig. 4.7. The incident energy dependence of the mean ADC value was taken into account in setting the gate position.

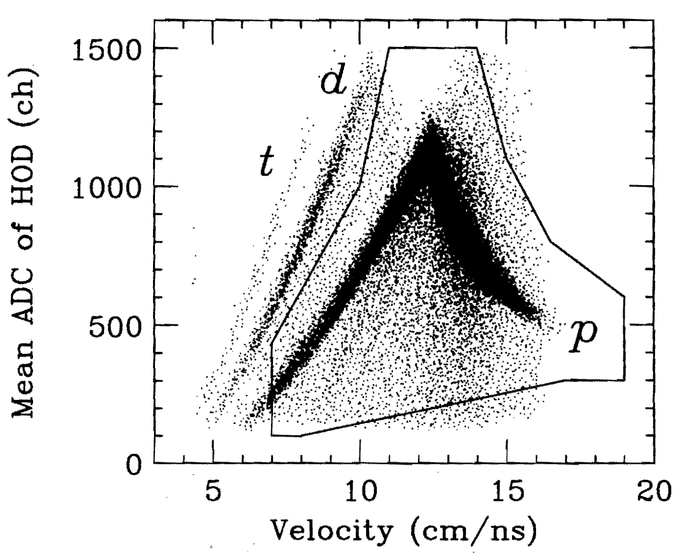

Figure 4.8: A two-dimensional plot of the velocity (v) versus the mean ADC value of HOD for events registered by the CE event trigger. Proton events enclosed by the solid line were selected.

The flight-path length (FPL) of an outgoing charged particle from the scatterer is defined as a distance from the intercept of the incident deuteron trajectory with the scatterer plane to the hit position in HOD. Using the FPL and TOF values the velocity (v) was calculated by taking account of energy losses in the scatterer and in the air. Figure 4.8 shows a two-dimensional histogram of the velocity (v) and the mean ADC value of HOD for events registered by the CE event trigger. Three pieces of particle, proton, deuteron and triton, can be identified in the histogram. Proton events enclosed by the solid line were selected. In order to avoid unwanted threshold effects a lower limit for the velocity of individual protons was set at 7 (cm/ns) (see subsection 3.4.2 for more details). If the total number of proton hit was one or less, the event was rejected.

The ${}^1\mathrm{H}(\vec{d}, 2p)$ CE reaction has three body final states, the kinematics of which is completely specified by five independent variables. We chose $(q, k, \theta_k, \phi_k, \phi)$ as such variables, where $q(=\sqrt{-t})$ is the momentum transfer to the neutron with t being the four momentum transfer, $2k$ the relative momentum of the two protons in their rest frame, θ_k and ϕ_k the polar and azimuthal angles of the relative momentum vector $2k$ with respect to the momentum transfer vector, and ϕ the overall azimuthal scattering angle between the zx-plane and the reaction plane of the second scattering (see Fig. 4.1). Provided the momentum vector of an incident deuteron is given by $P_d = (E_d, \boldsymbol{P}_d)$, and the momentum vectors of outgoing two protons by $P_{p1} = (E_{p1}, \boldsymbol{P}_{p1})$ and $P_{p2} = (E_{p2}, \boldsymbol{P}_{p2})$, the relevant kinematical quantities, the missing mass M_m, q, $\hbar ck$ and ϕ, are calculated by

$$
\begin{aligned}
M_m &= \sqrt{(E_d + M_p - E_{p1} - E_{p2})^2 - |\boldsymbol{P}_d - \boldsymbol{P}_{p1} - \boldsymbol{P}_{p2}|^2}, && (4.7)\\
q &= \sqrt{|\boldsymbol{P}_d - \boldsymbol{P}_{p1} - \boldsymbol{P}_{p2}|^2 - (E_d - E_{p1} - E_{p2})^2}, && (4.8)\\
\hbar ck &= \sqrt{\frac{M_{in}^2}{4} - M_p^2}, && (4.9)\\
\cos\phi &= \frac{(\boldsymbol{n}_y \times \boldsymbol{P}_d)\cdot\{|\boldsymbol{P}_d|^2(\boldsymbol{P}_{1p} + \boldsymbol{P}_{2p}) - [\boldsymbol{P}_d\cdot(\boldsymbol{P}_{1p} + \boldsymbol{P}_{2p})]\boldsymbol{P}_d\}}{||\boldsymbol{P}_d|^3(\boldsymbol{P}_{1p} + \boldsymbol{P}_{2p}) - [|\boldsymbol{P}_d|\boldsymbol{P}_d\cdot(\boldsymbol{P}_{1p} + \boldsymbol{P}_{2p})]\boldsymbol{P}_d|}, && (4.10)
\end{aligned}
$$

where M_p is the proton mass, $\hbar c$ is the conversion constant, $\boldsymbol{n}_y$ the unit vector in the y-direction at the focal plane (perpendicular to the incident ray and lying in the horizontal plane (see Fig. 4.1)) and M_{in} the invariant mass of the two protons given by

$$M_{in} = \sqrt{(E_{p1} + E_{p2})^2 - |\boldsymbol{p}_{p1} + \boldsymbol{p}_{p2}|^2}. \qquad (4.11)$$

The positive sense of ϕ is in the sense of a right-handed screw with x going into y in the polarimeter helicity frame. [1]

Figure 4.9 (a) shows a typical missing mass spectrum. A large neutron peak due to the ^{1}H$(d, 2p)$ reaction is clearly observed at a correct position. One can see another cluster of events on the higher mass side of the neutron peak. Most of the parasitic component in this region has its origin in detecting two protons from the ^{12}C$(d, 2p)$ reaction. This can be understood by looking at Fig. 4.9 (b), where a two-dimensional plot of $M_m - M_n$ and q are shown. The solid lines in the figure represent how the quantity, $M_m - M_n$, is related to q for the ^{12}C$(d, 2p)$ reaction if the target is intentionally assumed to be a proton. Results are shown for several values of the excitation energy (E_x) of the residual nucleus ^{12}B, and of the $2p$ center-of-mass scattering angle ($\theta_{\text{c.m.}}$). The boundary at the lower q side of the parasitic component is well described by the calculated curve with $\theta_{\text{c.m.}} = 0°$. The analysis including this parasitic component resulted in lower effective analyzing powers. Thus the parasitic events were rejected by a gate set on the missing mass spectrum indicated in Fig. 4.9 (a). The position of the gate on the missing mass spectrum is chosen by requiring that large enough figure-of-merit (FOM) values are obtained for relevant analyzing powers and that the dependence of the FOM values on the gate position is moderate. Although some portion of the background component still remains within the accepted region, such background is less significant at lower q region due to the large Q-value (=-14.3 MeV) of the ^{12}C$(d, 2p)$ reaction.

[1] The sign convention of ϕ in the present analysis is different from that of G. Ohlsen [27] but coincides with that of W. Haeberli [67].

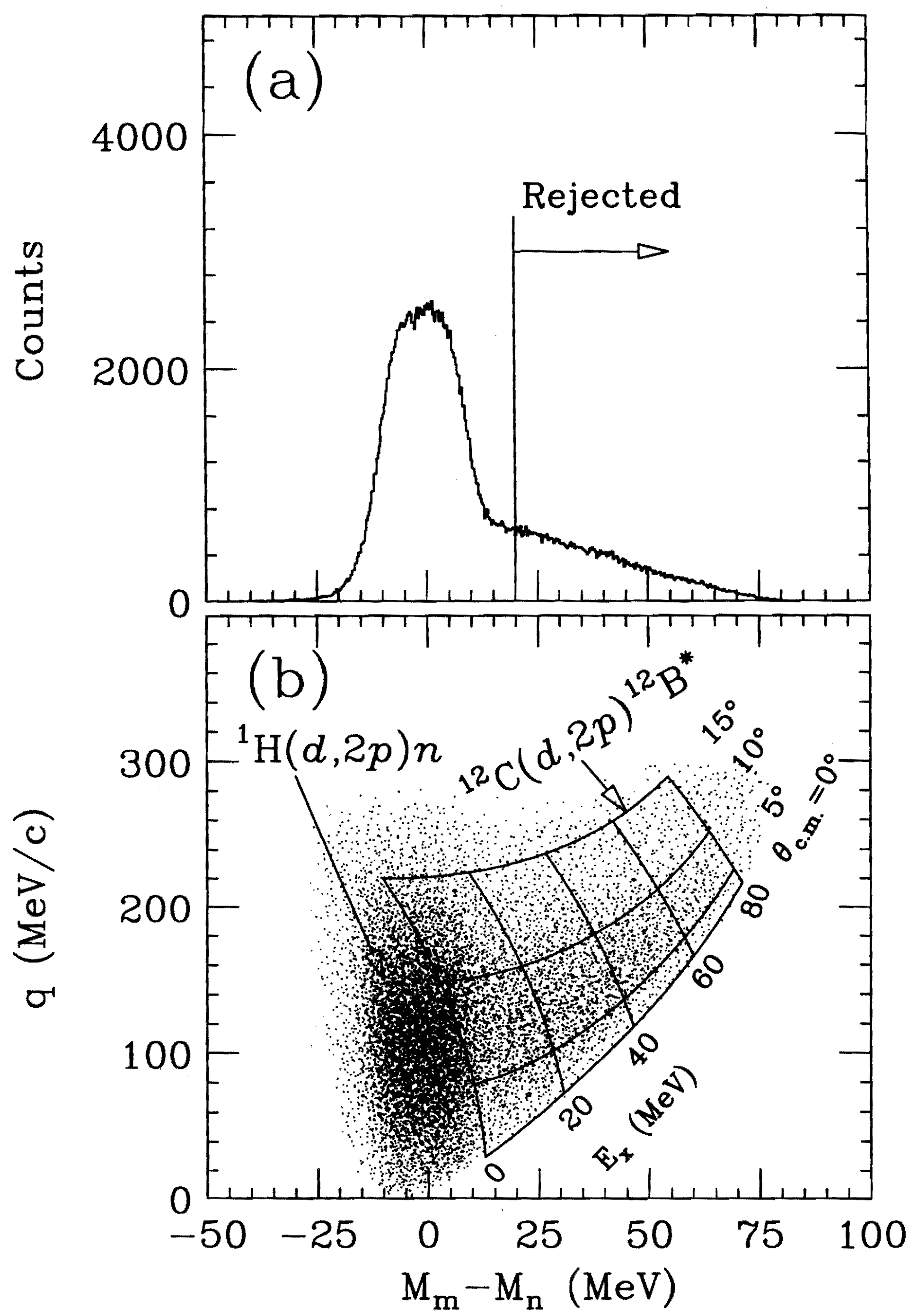

Figure 4.9: (a) A typical missing mass M_m spectrum and (b) a two-dimensional plot of $M_m - M_n$ and q for events taken with the CE event trigger. The neutron mass M_n is subtracted in abscissa.

The width of the missing mass (M_m) peak in Fig. 4.9 (a) was about 20 MeV in FWHM. The ambiguity in the reaction vertex within the scatterer is responsible for this large width in M_m. It also resulted in an uncertainty in q of about Δq = 35 MeV/c in FWHM. Such an ambiguity, however, could be partially removed by looking for a reaction point (vertex) in the scatterer along the beam direction in such a way that the correct missing mass value was obtained after a suitable energy loss correction. The vertex search was possible because (1) six kinematics variables are experimentally determined while five variables are sufficient to specify the three body final states (one degrees of freedom was overdetermined), (2) the energy loss calculation can be performed with enough accuracy and (3) the residual neutron does not have excited states in the energy scale considered here. Figure 2.1 (a) shows a missing mass (M_m^{corr}) spectrum obtained after the vertex search. The search was performed so that the resulting M_m^{corr} spectrum follows a normal distribution having a width of 3.9 MeV in FWHM estimated by a Monte Carlo simulation. Assuming the new vertex all the kinematics parameters were recalculated. With this vertex search procedure, the ambiguity in q was reduced to about Δq = 10 MeV/c.

The number of CE events was stored in a multidimensional histogram $N_{CE}^{(i)}(\Theta, E, q, \phi)$, by which the events were subdivided, for each (Θ, E) bin of the primary scattering and for each beam spin state (i), into 10 bins in q with an equal width of 30 MeV/c and into 12 bins in ϕ with a 30° bin width. Since the large tensor analyzing powers are expected only for kinematical region with small relative momentum $2k$ of two protons, where the singlet ($^1S_0$) final state interaction is dominant, events with $k \leq 0.4$ fm^{-1} were selected.

Figure 2.1 compares the experiment data (shown as shaded histograms) with predictions of a Monte Carlo simulation (shown as solid lines) on distributions of (a) missing mass M_m, (b) kinetic energy of individual protons E_p, (c) half the $2p$ relative momentum k and (d) the momentum transfer q for the ^{1}H$(d, 2p)$ reaction at E_d=270 MeV. In the simulation charge exchange events appropriately weighted by their reaction cross section calculated with a PWIA model of Carbonell *et al.* [58] were generated over the full experimental acceptance. Details on the simulation are given in Appendix B. The data are well described by the predictions, giving us confidence in the present background rejection and data handling. The simulation was used to help deal with differences in the efficiency of detecting two protons between the calibration and double scattering experiments. Such differences could arise from differences in the beam geometry between the two experiments. The simulation was also used to make energy interpolation between the calibration points.

4.4.2 The $\vec{d}+{}^{12}$C Elastic Scattering

The $\vec{d}+{}^{12}$C EL event trigger was generated by a consecutive hit of HOD and CM counters. Background events due to break-up protons as well as to deuterons originating from the ^{1}H(d,d) reaction were removed with the procedure described below.

Figure 4.10 shows (a) a scatter plot between the velocity (v) and the mean ADC value of HOD and (b) its projection onto the horizontal (v) axis, for data taken with the EL event trigger. It is clearly seen that the proton events are well suppressed in the region of the elastic deuteron events due to the iron absorber in from of the CM counter. Deuteron events were selected by a two-dimensional cut shown in Fig. 4.10 (a).

The missing mass M_m and polar and azimuthal scattering angles (θ, ϕ) (see Fig. 4.1) were calculated from the momentum vectors of incoming and outgoing deuterons. The energy loss correction in the scatterer was made by taking account of the effective target length $l_{\text{eff}} = l_{\text{sc}}/\cos\theta_t$, where l_{sc} is the thickness of the scatterer material θ_t the angle between the axis normal to the scatterer and the particle trajectory. The reaction vertex was assumed to the middle of the scatterer. Figure 4.11 (a) shows a typical missing mass $(M_m - M_{^{12}\text{C}})$ spectrum, where $M_{^{12}\text{C}}$ denotes the mass of ^{12}C. The width of the peak was about 4.2 MeV, which reflects the TOF resolution between SC and HOD (see subsection 3.4.3). Figure 4.11 (b) shows a two-dimensional plot of $M_m - M_{^{12}\text{C}}$ and θ. The solid line in the figure shows the kinematics for the ^{1}H(d,d) reaction. The deuteron events due to the elastic scattering on ^{1}H can be seen in the spectrum. Those events which had missing mass values of $M_m - M_{^{12}\text{C}} > 10$ MeV were rejected by a cut shown in Fig. 4.11 (a).

The number of EL events was stored in a multidimensional histogram $N_{EL}^{(i)}(\Theta, E, \theta, \phi)$, by which the events were subdivided into 20 bins in θ with an equal width of 1° and into 12 bins in ϕ with a 30° bin width, for each (Θ, E) bin of the primary scattering and for each beam spin state (i).

4.5 Cross Section and Analyzing Power

The differential cross section $\frac{d^2\sigma}{d\Omega dE}(\Theta, E)$ and the vector and tensor analyzing powers $A_y(\Theta, E)$, $A_{yy}(\Theta, E)$ for the primary scattering are related to the number of singles events $N_{SI}^{(i)}(\Theta, E)$ by

$$\begin{aligned} N_{BI}^{(i)}(\Theta, E) &= BI^{(i)} \cdot LT^{(i)} \cdot T \cdot RD \cdot \frac{d^2\sigma}{d\Omega dE}(\Theta, E) \cdot \Delta\Omega \cdot \Delta E \\ &\times \ \{1 + \frac{3}{2} p_y^{(i)} A_y(\Theta, E) + \frac{1}{2} p_{yy}^{(i)} A_{yy}(\Theta, E)\}. \end{aligned} \tag{4.12}$$

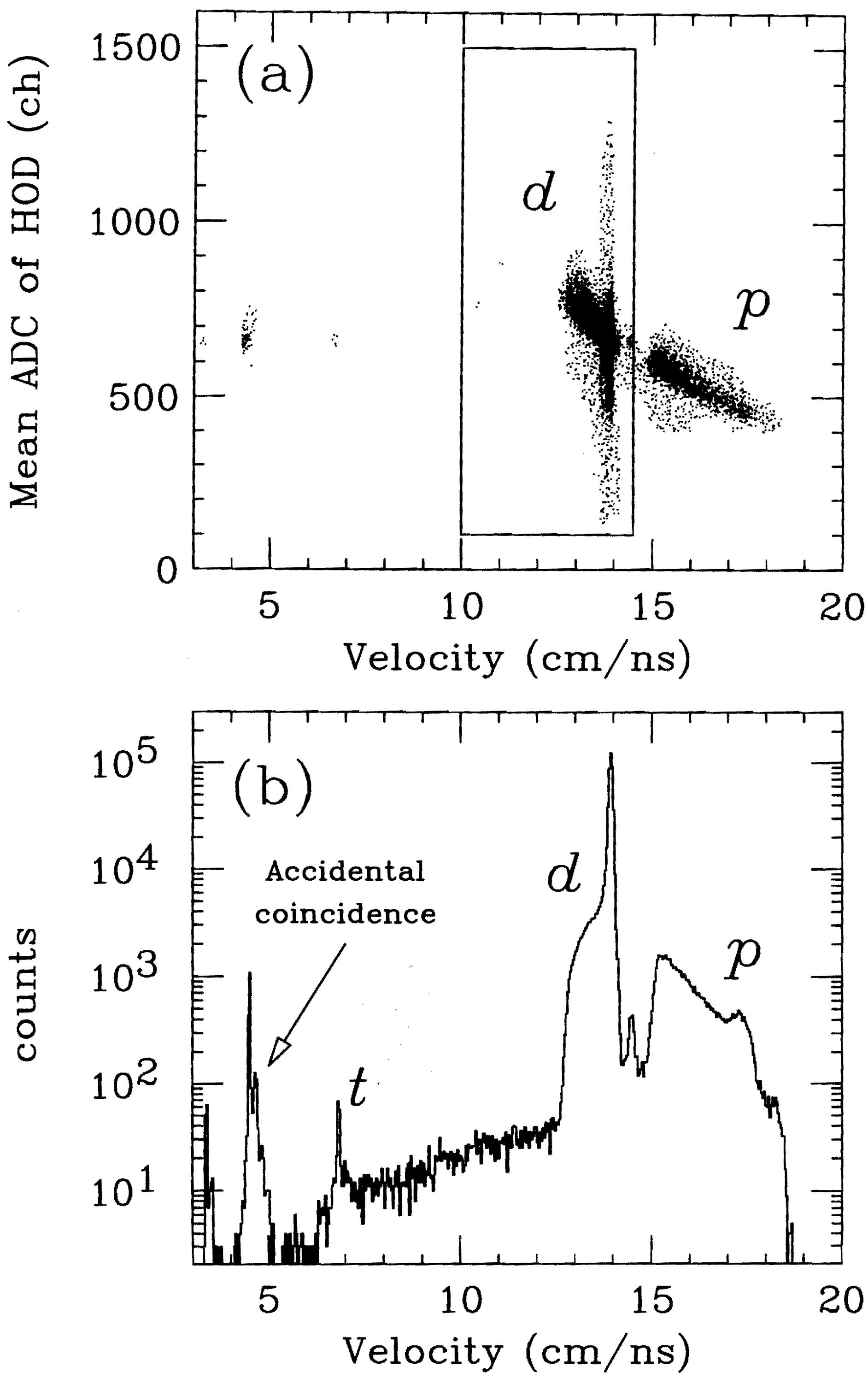

Figure 4.10: (a) A two-dimensional plot of the velocity (v) versus the mean ADC value of HOD for events registered by the EL event trigger. Deuteron events enclosed by the solid line were selected. (b) Projection onto the abscissa (the velocity axis).

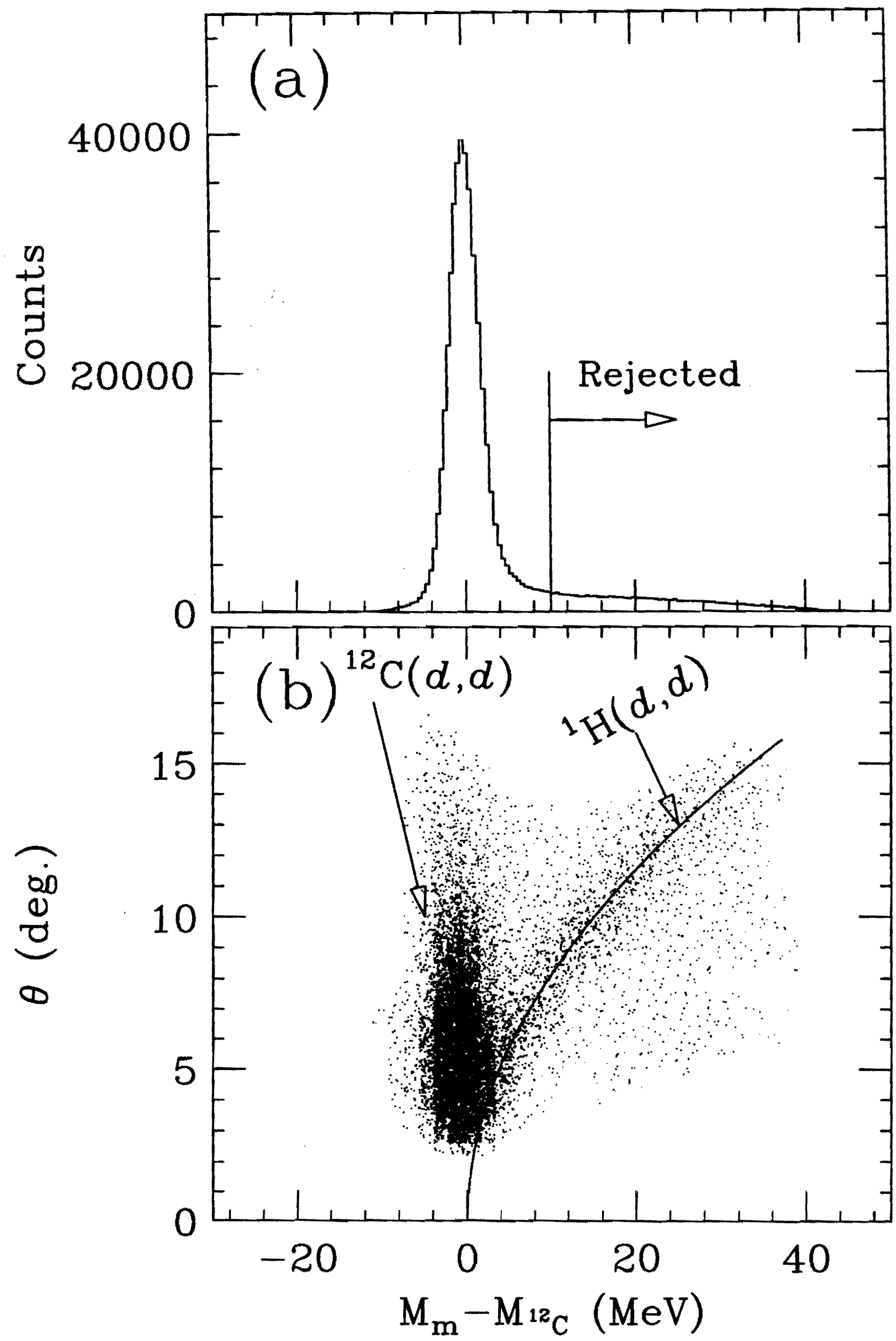

Figure 4.11: (a) A typical missing mass M_m spectrum and (b) a two-dimensional plot of $M_m - M_{^{12}C}$ and θ for events taken with the EL event trigger. The ^{12}C mass $M_{^{12}C}$ is subtracted in abscissa.

Here $BI^{(i)}$, $(p_y^{(i)}, p_{yy}^{(i)})$ and $LT^{(i)}$ refer to the number of beam deuterons, the beam polarizations and the live time of data taking for each beam spin state (i=0~3). The quantity T is the number of target nucleus per unit area, RD is the downscaling factor of the singles event (SI) trigger, $\Delta\Omega$ is the solid angle of SMART and ΔE is the bin width of the target excitation energy. The differential cross section was calculated by

$$\frac{d^2\sigma}{d\Omega dE}(\Theta, E) = \frac{N_{SI}^{(0)}(\Theta, E)}{BI^{(0)} \cdot LT^{(0)} \cdot T \cdot RD \cdot \Delta\Omega \cdot \Delta E}. \tag{4.13}$$

By defining ratio $R_I^{(i)}(\Theta, E)$ of the polarized cross section relative to the unpolarized cross section by

$$R_I^{(i)}(\Theta, E) = \frac{N_{SI}^{(i)}(\Theta, E) BI^{(0)} LT^{(0)}}{N_{SI}^{(0)}(\Theta, E) BI^{(i)} LT^{(i)}}, \tag{4.14}$$

$A_y(\Theta, E)$ and $A_{yy}(\Theta, E)$ were calculated by,

$$A_y(\Theta, E) = \frac{2}{3p_y^{(\text{eff})}}\left(R_I^{(2)}(\Theta, E) - R_I^{(3)}(\Theta, E) - T_{(1)}^{(23)}\{R_I^{(1)}(\Theta, E) - 1\}\right), \tag{4.15}$$

$$A_{yy}(\Theta, E) = \frac{2}{p_{yy}^{(\text{eff})}}\left(R_I^{(1)}(\Theta, E) - R_I^{(3)}(\Theta, E) - V_{(2)}^{(13)}\{R_I^{(2)}(\Theta, E) - 1\}\right), \tag{4.16}$$

where the quantities $p_y^{(\text{eff})}$ and $p_{yy}^{(\text{eff})}$ were given by

$$p_y^{(\text{eff})} = p_y^{(2)} - p_y^{(3)} - T_{(1)}^{(23)} p_y^{(1)}, \tag{4.17}$$

$$p_{yy}^{(\text{eff})} = p_{yy}^{(1)} - p_{yy}^{(3)} - V_{(2)}^{(13)} p_{yy}^{(2)}, \tag{4.18}$$

with

$$V_{(2)}^{(13)} = (p_y^{(1)} - p_y^{(3)})/p_y^{(2)}, \tag{4.19}$$

$$T_{(1)}^{(23)} = (p_{yy}^{(2)} - p_{yy}^{(3)})/p_{yy}^{(1)}. \tag{4.20}$$

4.6 Polarizing Power and Polarization Transfer Coefficient

Polarizing powers, $P^{y'}(\Theta, E)$ and $P^{y'y'}(\Theta, E)$, and polarization transfer coefficients, $K_y^{y'}(\Theta, E)$, $K_{yy}^{y'}(\Theta, E)$, $K_y^{y'y'}(\Theta, E)$ and $K_{yy}^{y'y'}(\Theta, E)$, relate vector and tensor polarizations in the initial $(p_y^{(i)}, p_{yy}^{(i)})$ and final $(p_{y'}^{(i)}(\Theta, E), p_{y'y'}^{(i)}(\Theta, E))$ deuterons as follows,

$$p_{y'}^{(i)} R_I^{(i)} = P^{y'} + \frac{3}{2} p_y^{(i)} K_y^{y'} + \frac{1}{2} p_{yy}^{(i)} K_{yy}^{y'}, \tag{4.21}$$

$$p_{y'y'}^{(i)} R_I^{(i)} = P^{y'y'} + \frac{3}{2} p_y^{(i)} K_y^{y'y'} + \frac{1}{2} p_{yy}^{(i)} K_{yy}^{y'y'}. \tag{4.22}$$

where the quantities $R_I^{(i)}$ are defined by Eq.(4.14). In Eqs.(4.21) and (4.22) the dependence of all the quantities except for the incident beam polarizations on (Θ, E) is implicit. By solving Eqs.(4.21) and (4.22) following expressions can be obtained for each polarization observable:

$$
\begin{aligned}
P^{y'} &= p_{y'}^{(0)}, & (4.23)\\
P^{y'y'} &= p_{y'y'}^{(0)}, & (4.24)\\
K_y^{y'} &= \frac{2}{3\hat{p}_y^{(eff)}}\left(p_{y'}^{(2)} - p_{y'}^{(3)} - \hat{T}_{(1)}^{(23)}p_{y'}^{(1)} + \tilde{T}_{(1)}^{(23)}p_{y'}^{(0)}\right), & (4.25)\\
K_{yy}^{y'} &= \frac{2}{\hat{p}_{yy}^{(eff)}}\left(p_{y'}^{(1)} - p_{y'}^{(3)} - \hat{V}_{(2)}^{(13)}p_{y'}^{(2)} + \tilde{V}_{(2)}^{(13)}p_{y'}^{(0)}\right), & (4.26)\\
K_y^{y'y'} &= \frac{2}{3\hat{p}_y^{(eff)}}\left(p_{y'y'}^{(2)} - p_{y'y'}^{(3)} - \hat{T}_{(1)}^{(23)}p_{y'y'}^{(1)} + \tilde{T}_{(1)}^{(23)}p_{y'y'}^{(0)}\right), & (4.27)\\
K_{yy}^{y'y'} &= \frac{2}{\hat{p}_{yy}^{(eff)}}\left(p_{y'y'}^{(1)} - p_{y'y'}^{(3)} - \hat{V}_{(2)}^{(13)}p_{y'y'}^{(2)} + \tilde{V}_{(2)}^{(13)}p_{y'y'}^{(0)}\right), & (4.28)\\
& & (4.29)
\end{aligned}
$$

with

$$
\begin{aligned}
\hat{p}_y^{(eff)} &= \frac{p_y^{(2)}}{R_I^{(2)}} - \frac{p_y^{(3)}}{R_I^{(3)}} - \hat{T}_{(1)}^{(23)}\frac{p_y^{(1)}}{R_I^{(1)}}, & (4.30)\\
\hat{p}_{yy}^{(eff)} &= \frac{p_{yy}^{(1)}}{R_I^{(1)}} - \frac{p_{yy}^{(3)}}{R_I^{(3)}} - \hat{V}_{(2)}^{(13)}\frac{p_{yy}^{(2)}}{R_I^{(2)}}, & (4.31)\\
\hat{V}_{(2)}^{(13)} &= \left(\frac{p_y^{(1)}}{R_I^{(1)}} - \frac{p_y^{(3)}}{R_I^{(3)}}\right)/\left(\frac{p_y^{(2)}}{R_I^{(2)}}\right), & (4.32)\\
\hat{T}_{(1)}^{(23)} &= \left(\frac{p_{yy}^{(2)}}{R_I^{(2)}} - \frac{p_{yy}^{(3)}}{R_I^{(3)}}\right)/\left(\frac{p_{yy}^{(1)}}{R_I^{(1)}}\right), & (4.33)\\
\tilde{V}_{(2)}^{(13)} &= \hat{V}_{(2)}^{(13)}\frac{1}{R_I^{(2)}} - \frac{1}{R_I^{(1)}} + \frac{1}{R_I^{(3)}} & (4.34)\\
\tilde{T}_{(1)}^{(23)} &= \hat{T}_{(1)}^{(23)}\frac{1}{R_I^{(1)}} - \frac{1}{R_I^{(2)}} + \frac{1}{R_I^{(3)}},. & (4.35)
\end{aligned}
$$

Since the beam polarization axis was set in the y-direction, the normal to the scattering plane (see Fig. 4.1), Larmor precession of the y-axis around the spectrometer dipole field took place. Consequently, the y-axis in the outgoing helicity frame at the primary scattering did not coincide with that in the helicity frame of the polarimeter. The precession angle of the axis relative to the direction of motion is given by [68]

$$\eta = \gamma(g\frac{M_d}{2M_p} - 1)\Psi, \tag{4.36}$$

where Ψ is the orbital deflection angle, $g = 0.8574$ is deuteron gyromagnetic ratio, M_p and M_d are the proton and deuteron masses and $\gamma = E_d/M_d$ is the Lorentz factor where E_d is the total deuteron energy. For the case of 270 MeV deuterons with $\Psi = 60°$ this angle is calculated to be $\eta = -9.82°$. The deuteron spherical polarization components in the polarimeter helicity frame $\{t"_{kq}\}$ are related to those in the outgoing helicity frame $\{t'_{kq}\}$ using the usual D-function [69] by

$$t"_{kq} = \sum_m t'_{km} \mathcal{D}^k_{mq}(-\frac{\pi}{2}, -\eta, \frac{\pi}{2}). \tag{4.37}$$

Due to the parity conservation only real parts in $\{t'_{kq}\}$ were allowed [27] for primary beams with only y-components, while Eq.(4.37) implies that there are imaginary components in $\{t"_{kq}\}$.

The yield of each analyzer reaction $N^{(i)}_{CE(\mathrm{or}EL)}(\Theta, E, \theta, \phi)$ for each spin state (i) is related to $\{t"^{(i)}_{kq}(\Theta, E)\}$ by

$$\begin{aligned} N^{(i)}_{CE(\mathrm{or}EL)}(\theta,\phi) &= \frac{N^{(i)}_{SI}}{RD} \cdot N_{H(\mathrm{or}C)} \cdot \overline{\sigma}(\theta) \cdot D(\theta,\phi) \\ &\times \{1 + 2iT_{11}(\theta)\mathrm{Re}(it"^{(i)}_{11})\cos\phi + T_{20}(\theta)\, t"^{(i)}_{20} \\ &+ 2T_{21}(\theta)[\mathrm{Re}(t"^{(i)}_{21})\cos\phi + \mathrm{Im}(t"^{(i)}_{21})\sin\phi] \\ &+ 2T_{22}(\theta)[\mathrm{Re}(t"^{(i)}_{22})\cos 2\phi + \mathrm{Im}(t"^{(i)}_{22})\sin 2\phi]\}, \end{aligned} \tag{4.38}$$

where $N_{H(\mathrm{or}C)}$ is the number of target nuclei per unit area in the scatterer, $\overline{\sigma}(\theta)$ is the cross section in a bin specified by the angle θ, given by

$$\overline{\sigma}(\theta) = \begin{cases} \frac{\mathrm{d}^2\sigma}{\mathrm{d}\phi \mathrm{d}t} 2q\Delta q\Delta\phi & \text{for } CE, \\ \frac{\mathrm{d}\sigma}{\mathrm{d}\Omega}\Delta\Omega & \text{for } EL, \end{cases} \tag{4.39}$$

where $\frac{\mathrm{d}^2\sigma}{\mathrm{d}\phi\mathrm{d}t}$ and $\frac{\mathrm{d}\sigma}{\mathrm{d}\Omega}$ are the unpolarized cross sections for the CE and EL reactions, respectively. D is the local detection efficiency of the polarimeter and T_{kq} are the effective analyzing powers. The dependence on (Θ, E) of such quantities as $N^{(i)}_{CE(\mathrm{or}EL)}$, $N^{(i)}_{SI}$, $\{t"^{(i)}_{kq}\}$ and D, and the incident energy dependence of $\frac{\mathrm{d}\sigma}{\mathrm{d}\Omega}$ and T_{kq} through (Θ, E) are implicit in Eq.(4.38). Since the same acquisition live time factor $LT^{(i)}$ is applied to both $N^{(i)}_{CE(\mathrm{or}EL)}$ in the l.h.s. and $N^{(i)}_{SI}$ in the r.h.s., this factor does not appear in Eq.(4.38). The same is true for the MWDC efficiency. The quantity $\frac{\mathrm{d}\sigma}{\mathrm{d}\Omega}$ and T_{kq} were obtained from the polarimeter calibration experiment (see Appendix A). The difference in D between the calibration experiment and the double scattering experiment was estimated by using the Monte Carlo simulation (see Appendix B). The simulation was also used to make energy interpolation of $\frac{\mathrm{d}\sigma}{\mathrm{d}\Omega}$.

The procedure to extract scattered deuteron polarization is as follows. Firstly, ratios $R_{II}^{(i)}$ of the measured yield relative to the yield expected for unpolarized incident beam were calculated by

$$R_{II}^{(i)}(\theta,\phi) = \frac{N_{CE(\mathrm{or}EL)}^{(i)}(\theta,\phi)\cdot RD}{N_{SI}^{(i)}\cdot N_{H(\mathrm{or}C)}\cdot\overline{\sigma}(\theta)\cdot D(\theta,\phi)} - 1. \tag{4.40}$$

Secondly, vector R_{II}^{V} and tensor R_{II}^{T} ratios were calculated by the relations

$$R_{II}^{V} = R_{II}^{(2)} - R_{II}^{(3)} - \hat{T}_{(1)}^{(23)}R_{II}^{(1)} + \tilde{T}_{(1)}^{(23)}R_{II}^{(0)}, \tag{4.41}$$

$$R_{II}^{T} = R_{II}^{(1)} - R_{II}^{(3)} - \hat{V}_{(2)}^{(13)}R_{II}^{(2)} + \tilde{V}_{(2)}^{(13)}R_{II}^{(0)}. \tag{4.42}$$

It is to be noted that possible false asymmetries, which may commonly enter into the ratios $R_{II}^{(i)}$, irrespective of the beam spin state, such as those arising from misalignment of the detector position and misestimation of the unpolarized cross sections by the simulation, could cancel out in the ratios R_{II}^{V} and R_{II}^{T}, because these are defined as differences of the ratios $R_{II}^{(i)}$. R_{II}^{V} and R_{II}^{T} have the form

$$\begin{aligned} R_{II}^{V(\mathrm{or}T)} &= T_{20}\,t"_{20}^{V(\mathrm{or}T)} + 2\{iT_{11}it"_{11}^{V(\mathrm{or}T)} + T_{21}\mathrm{Re}(t"_{21}^{V(\mathrm{or}T)})\}\cos\phi \\ &+ 2T_{21}\mathrm{Im}(t"_{21}^{V(\mathrm{or}T)})\sin\phi \\ &+ 2T_{22}\mathrm{Re}(t"_{22}^{V(\mathrm{or}T)})\cos 2\phi + 2T_{22}\mathrm{Im}(t"_{22}^{V(\mathrm{or}T)})\sin 2\phi, \end{aligned} \tag{4.43}$$

where the polarization components $t"_{kq}^{V}$ and $t"_{kq}^{T}$ are related to $\{t"_{kq}\}$ for each beam spin state by

$$t"_{kq}^{V} = t"_{kq}^{(2)} - t"_{kq}^{(3)} - \hat{T}_{(1)}^{(23)}t"_{kq}^{(1)} + \tilde{T}_{(1)}^{(23)}t"_{kq}^{(0)}, \tag{4.44}$$

$$t"_{kq}^{T} = t"_{kq}^{(1)} - t"_{kq}^{(3)} - \hat{V}_{(2)}^{(13)}t"_{kq}^{(2)} + \tilde{V}_{(2)}^{(13)}t"_{kq}^{(0)}. \tag{4.45}$$

Finally, using a χ^2 minimization procedure, the unknown polarization components $t"_{kq}^{V}$ and $t"_{kq}^{T}$ were extracted.

Figure 4.12 shows an example of the vector and tensor ratios in the second scattering as a function of azimuthal scattering angle ϕ. The solid lines in the figure are the fitted results performed over ϕ bins after averaging over θ bins. Clearly large vector asymmetry is observed in the R_{II}^{V} ratio for the $\vec{d}+{}^{12}\mathrm{C}$ elastic scattering, while large tensor asymmetry is seen in the R_{II}^{T} ratio for the ${}^{1}\mathrm{H}(\vec{d},2p)$ reaction.

The deuteron polarization components at the primary target $\{t'_{kq}\}$ were calculated from those in the helicity frame of the polarimeter $\{t"_{kq}\}$ through the relations, which can be derived from Eq.(4.37):

$$it'_{11} = \frac{it"_{11}}{\cos\eta}, \tag{4.46}$$

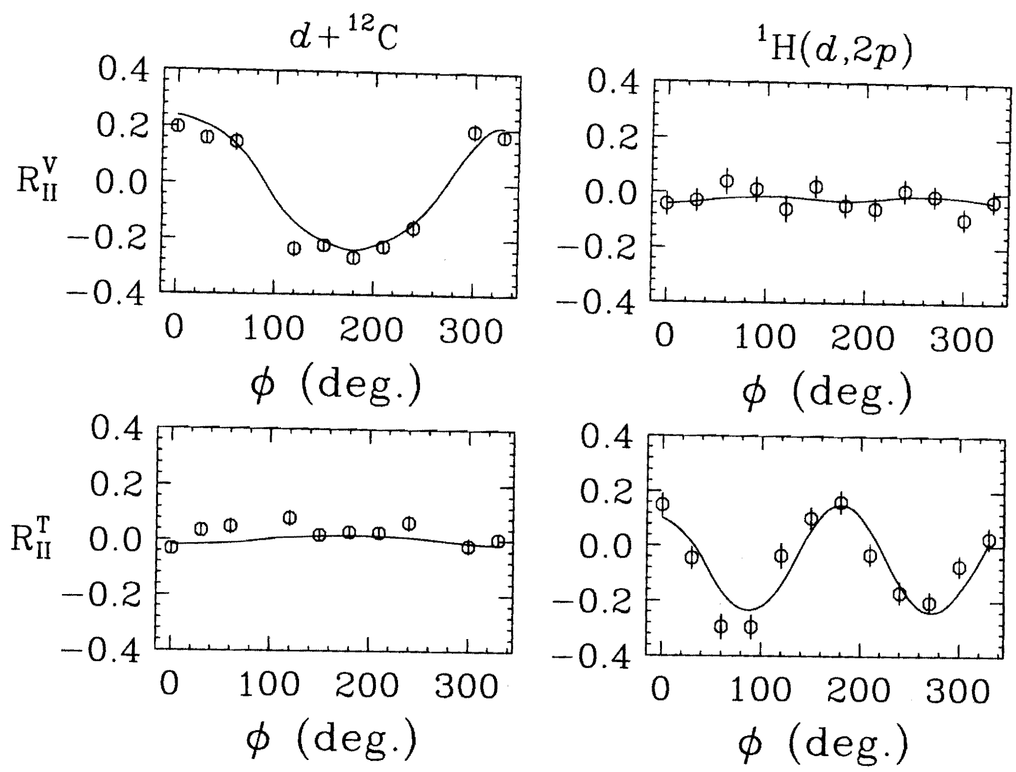

Figure 4.12: A sample of azimuthal distributions of ratios, R^V_{II} and R^T_{II}, for the $d+{}^{12}$C EL scattering and for the ^{1}H($d,2p$) CE reaction. Open circles represent the data; solid curves are results of the fitting. The figure is for the target excitation energy bin of $E = 6.6 - 7.2$ MeV and for the scattering angular bin of $\Theta = 4.0 - 6.0°$.

$$t'_{20} = \frac{(2-\sin^2\eta)t"_{20} + \sqrt{6}\sin^2\eta \mathrm{Re}(t"_{22})}{2(1-2\sin^2\eta)}, \tag{4.47}$$

$$t'_{22} = \frac{\sqrt{\frac{3}{2}}\sin^2\eta t"_{20} + (3\cos^2\eta - 1)\mathrm{Re}(t"_{22})}{2(1-2\sin^2\eta)}. \tag{4.48}$$

$$\tag{4.49}$$

The Cartesian polarization components $(p_{y'}, p_{y'y'})$ are related to the spherical ones by

$$p_{y'} = \frac{2}{\sqrt{3}} i t'_{11}, \tag{4.50}$$

$$p_{y'y'} = -\sqrt{3}t'_{22} - \frac{1}{\sqrt{2}}t'_{20}. \tag{4.51}$$

These are used in Eqs.(4.25)-(4.28) to calculate polarization transfer coefficients. (Indices V and T are omitted in t_{kq} and $p_{y(y)}$ in Eqs.(4.46)-(4.51).)

In deriving polarizations, $P^{y'}$ and $P^{y'y'}$, the ratio for the unpolarized beam $R^{(0)}_{II}$ was used in the fitting procedure. No cancellation of instrumental asymmetry could be made in this case.

4.7 Error Estimation

The uncertainty in the absolute cross section measurement with DPOL for the ${}^1\mathrm{H}(d,2p)$ reaction is responsible for the errors of the measured t_{20} component Δt_{20}, because t_{20} is obtained by measuring the variation of the absolute scattering yield. We have the following approximate relation on Δt_{20},

$$\Delta t_{20} \approx \frac{1}{T_{20}} \frac{\Delta\sigma}{\sigma}, \tag{4.52}$$

where σ represents the absolute scattering yield for the ${}^1\mathrm{H}(d,2p)$ reaction, and $\Delta\sigma$ the associated error. Figure 4.13 shows the overall efficiency for the ${}^1\mathrm{H}(d,2p)$ reaction measured in different calibration runs of DPOL at E_d=270, 250 and 230 MeV. We see that the cross section is reproduced to within $\frac{\Delta\sigma}{\sigma} \approx 2\%$. Since the averaged T_{20} is about 0.2 (see Appendix A), the systematic error in t_{20} is estimated to be about ± 0.10 using the Eq.(4.52).

Once the calibration is completed, the polarimeter is now able to measure incident beam polarizations. The systematic uncertainties on the other polarization components, it_{11} and t_{22}, are estimated by comparing polarization values deduced by using the beam line polarimeter (BLP) with those obtained by DPOL. In determining the beam polarizations with DPOL the efficiency correction is made by using a Monte Carlo simulation (see Appendix B). Table 4.2 compares the beam polarization components it_{11}, t_{20}, t_{22} extracted with the two polarimeters for each spin state. The errors represent statistical ones. We estimate the systematic uncertainties in it_{11} and t_{22} components measured with DPOL to be ± 0.03 and ± 0.05, respectively.

The polarization transfer coefficients were extracted using differences of double scattering cross sections obtained with different polarization modes in the incident beam. They were almost unaffected by the systematic uncertainties due to the efficiency misestimation in the simulation. On the other hand, the polarizing powers were extracted from double scattering cross sections obtained with an unpolarized beam. From the systematic uncertainties in t_{kq} the uncertainties in $P^{y'}$ and $P^{y'y'}$ are calculated to be ± 0.04 and ± 0.16, respectively. Since the systematic uncertainty in the analyzing powers are only related to the uncertainty in the beam polarization measurement which is expected to be small (see below), the analyzing powers can be relatively accurately determined. Therefore the leading term in the uncertainty in S_1 and S_2 is the uncertainty in $P^{y'y'}$. The systematic uncertainty in $P^{y'y'}$, however, contributed less than $\pm$ 0.02 to the uncertainties in S_1 and

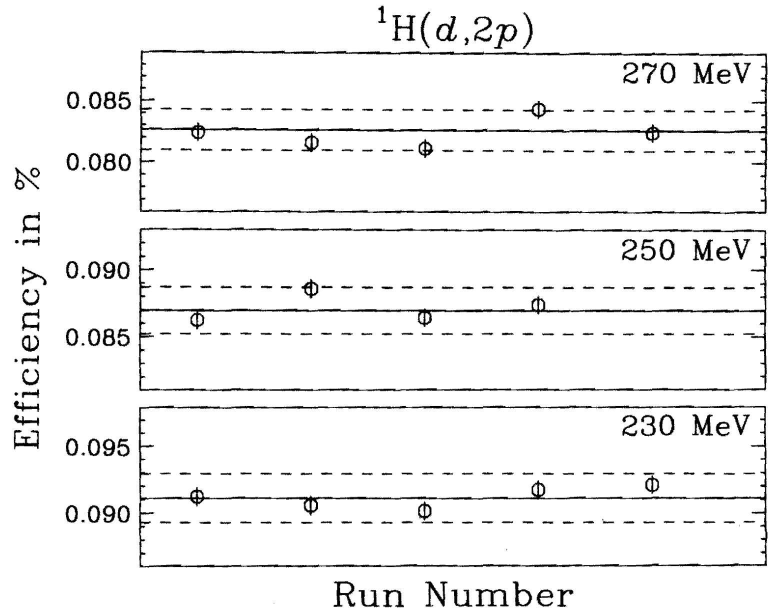

Figure 4.13: Total efficiency of DPOL for the ^{1}H$(d,2p)$ reaction measured in different calibration runs of DPOL at E_d=270, 250 and 230 MeV. The relative energy range of the final two protons is limited to be less than k=0.4 fm^{-1}. The mean value is drawn as solid lines with the $\pm2\%$ dashed lines.

S_2 due to the coefficients which appear in the definition of these spin-flip probabilities (see Eqs.(1.1) and (1.2)).

The uncertainty in the differential cross section for the primary scattering is estimated to be less than 15 % including the uncertainty in the target thickness, charge correction and solid angle estimation.

The uncertainties in the analyzing powers A_y and A_{yy} are estimated to be less than 4 % and 6 %, respectively.

Table 4.2: Beam polarizations measured with the beam line polarimeter (BLP) and DPOL at E_d=270 MeV. The errors are statistical ones.

Polarization component	Spin state	BLP	Incident deuterons	DPOL
it_{11}	0	0.0	2.0×10^7	-0.018±0.006
	1	-0.005±0.006	1.8×10^7	-0.018±0.006
	2	0.472±0.008	2.0×10^7	0.470±0.006
	3	0.025±0.009	1.8×10^7	-0.004±0.006
t_{20}	0	0.0	1.0×10^8	0.043±0.019
	1	0.475±0.006	0.9×10^8	0.430±0.019
	2	-0.029±0.006	1.0×10^8	-0.012±0.019
	3	-0.272±0.006	0.9×10^8	-0.255±0.021
t_{22}	0	0.0	1.0×10^8	0.014±0.015
	1	0.582±0.007	0.9×10^8	0.551±0.015
	2	-0.036±0.007	1.0×10^8	-0.025±0.016
	3	-0.332±0.007	0.9×10^8	-0.328±0.017

Chapter 5

Experimental Results

The data acquired in this thesis work are classified into two categories: (1) The polarization transfer observables on ^{28}Si as a function of excitation energy. (2) The cross section and analyzing power angular distributions for selected transitions in ^{12}C and ^{28}Si. The polarization transfer data and the angular distribution data are presented in section 5.1 and 5.2, respectively. The angular distribution data for selected transitions with known nuclear structure information are compared with microscopic distorted wave impulse approximation calculations in the next chapter in order to gain an insight into the reaction mechanism for the deuteron inelastic scattering at 270 MeV.

5.1 Polarization Transfer Data on ^{28}Si

The polarization transfer data were obtained on ^{28}Si at a spectrometer angle of 5°, spanning an angular range between 2.5° and 7.5° and an excitation energy range between 4 and 21 MeV. From the polarization observables, the deuteron single and double spin-flip probabilities, S_1 and S_2, are calculated according to Eqs.(1.1) and (1.2). The spectroscopic information on the isoscalar spin strengths in ^{28}Si that can be gained from the data is presented.

5.1.1 Excitation Energy Spectrum

Figure 5.1 shows an excitation energy spectrum of ^{28}Si at $\Theta_{\text{lab}} = 6.75°$. The energy resolution was about 200 keV. At forward scattering angles the spectrum is dominated by the ground state due to the elastic scattering and the first excited 2_1^+(1.78 MeV) state. Other natural parity states are clearly excited. These include the 4_1^+(4.62 MeV), 0_2^+(4.98 MeV), 3_1^-(6.88 MeV), 2_2^+(7.38 MeV), 2_3^+(7.42 MeV), 2_4^+(7.93 MeV), 2_6^+(9.48 MeV) and 3_2^-(10.18 MeV) states. Among them a known isoscalar unnatural parity 1_2^+(9.50 MeV) state is clearly observed. Pairs of states, the 2_2^+ and 2_3^+ states and the 2_6^+ and 1_2^+ states,

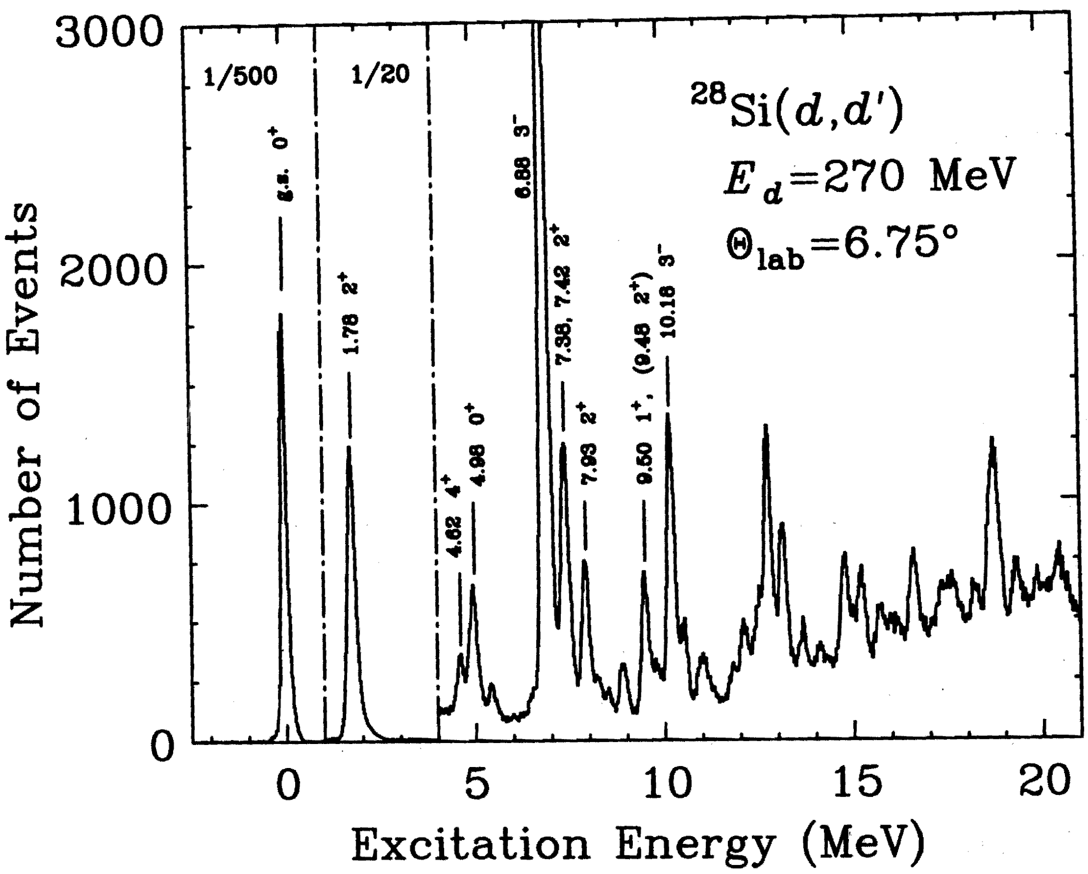

Figure 5.1: A typical excitation energy spectrum for the ^{28}Si(d,d') reaction at E_d=270 MeV and at $\Theta_{\rm lab}$ = 6.75°. The ground and first excited 2_1^+(1.78 MeV) states are scaled by factors of 1/500 and 1/20, respectively.

could not be resolved with the present energy resolution and these were analyzed as doublets. The 5_1^-(9.72 MeV) state becomes prominent at larger scattering angles. The first 1_1^+ state at 8.33 MeV, known from γ-decay systematics [70], is almost unseen due to the weak transition probability from the ground state to this state (see Table 6.12). The isovector 1^+ states, such as those known at 10.59, 11.45, 12.33, 13.35 and 14.03 MeV, which are prominent in the forward angle (p,p') spectra [47, 48], are masked due to the isoscalar selectivity of the (d,d') reaction.

In order to obtain reasonable counting statistics for polarization observables, the excitation energy bins and the scattering angular bins with larger widths were adopted. The bin widths were chosen so as to preserve the structure of the spectrum as much as possible. The energy and angular bins are given in Tables 5.1 and 5.2, respectively. The excitation energy spectrum summed in larger size bins of the excitation energy, and averaged over

Table 5.1: Energy bins (in MeV) used in binned spectra.

No.	E	ΔE	States
1	4.30 - 4.70	0.40	4_1^+
2	4.70 - 5.10	0.40	0_2^+
3	5.10 - 6.60	1.50	
4	6.60 - 7.20	0.60	3_1^-
5	7.20 - 7.60	0.40	$2_2^+, 2_3^+$
6	7.60 - 8.20	0.60	2_4^+
7	8.20 - 8.70	0.50	
8	8.70 - 9.30	0.60	1_1^-
9	9.30 - 9.60	0.30	$1_2^+, 2_6^+$
10	9.60 - 9.80	0.20	
11	9.80 - 10.05	0.25	
12	10.05 - 10.40	0.35	3_2^-
13	10.40 - 10.80	0.40	
14	10.80 - 11.50	0.70	
15	11.50 - 12.00	0.50	
16	12.00 - 12.60	0.60	
17	12.60 - 13.00	0.40	
18-21	0.5 MeV bins for 13.0-15.0 MeV		
22-27	1 MeV bins for 15.0-21.0 MeV		

Table 5.2: Scattering angular bins and corresponding solid angles in the laboratory frame used in the analysis.

No.	Θ (deg)	$\Delta\Omega$ (msr)
1	2.5 - 4.0	0.671
2	4.0 - 6.0	1.340
3	6.0 - 7.5	1.321

the scattering angles between $\Theta_{\text{lab}} = 2.5$ and $7.5°$, is shown in Fig. 5.2 (a). The cross section is calculated in terms of the laboratory solid angle.

5.1.2 Spectra of Polarization Observables

The vector and tensor analyzing powers, A_y and A_{yy}, for each excitation energy bin are shown in Figs. 5.2 (b) and (c), respectively. The values are those averaged over the scattering angular range between Θ_{lab}=2.5 and 7.5°, by weighting with the yield in each angular bin. The error bars are statistical ones (the same is true for other polarization observables). Calculated curves corresponding to the free deuteron-nucleon scattering at the same momentum transfer are presented as dotted lines for reference purpose. Such a comparison with the free values has been often done in a discussion on the continuum spin response [41, 42]. Below 15 MeV in excitation energy, the A_y spectrum fluctuates at around the free values of about 0.2, reflecting the presence of low-lying discrete levels. For example, the values of A_y are distinctively lower in the bins where the 3_1^- states at 6.88 MeV and 10.18 MeV are known. Above 15 MeV in excitation energy, the values of A_y decrease smoothly with increasing excitation energy, showing some intriguing departure from the free values. The A_{yy} values are positive and almost constant at the free value of 0.08 across the spectrum, with some fluctuations seen in the low excitation energy region. We see a relatively small value of A_{yy} at the 9.5 MeV bin where a 1_2^+ state is known.

The measured $P^{y'}$, $K_y^{y'}$ and $K_{yy}^{y'}$ spectra, and the $P^{y'y'}$, $K_y^{y'y'}$ and $K_{yy}^{y'y'}$ spectra are respectively shown in Figs. 5.3 and 5.4 for completeness. The data are compared to values for free deuteron-nucleon scattering shown as dotted lines.

5.1.3 Single and Double Spin-Flip Probability Spectra

The S_1 and S_2 spectra for angles between Θ_{lab}=2.5 and 7.5° are respectively shown in Figs. 5.5 (b) and (c), together with the excitation energy spectrum in Fig. 5.5 (a) shown for reference. The largest positive S_1 value is obtained at the 9.45 MeV bin which has a value of 0.22. This large value of S_1 corresponds to the 1_2^+ state at 9.50 MeV. Present results provides a direct confirmation of the isoscalar spin-flip nature for this state. Large S_1 values of the order of 0.1, which are relatively enhanced from values for free deuteron-nucleon scattering shown as a dotted line in Fig. 5.5 (b), are observed in the energy interval between 9.6 and 20 MeV, indicating the presence of isoscalar spin strengths in this energy range. For the natural parity 0_2^+ state at 4.98 MeV, the S_1 value is compatible with zero, as required from the symmetry relations which hold generally for the $\vec{1}+0 \rightarrow \vec{1}+0'$ reactions, where 1(1') and 0(0') indicate spin-1 and spin-0 particles, respectively [71]. Non zero S_1 values of around 0.05 for predominantly non-spin-flip natural parity transitions,

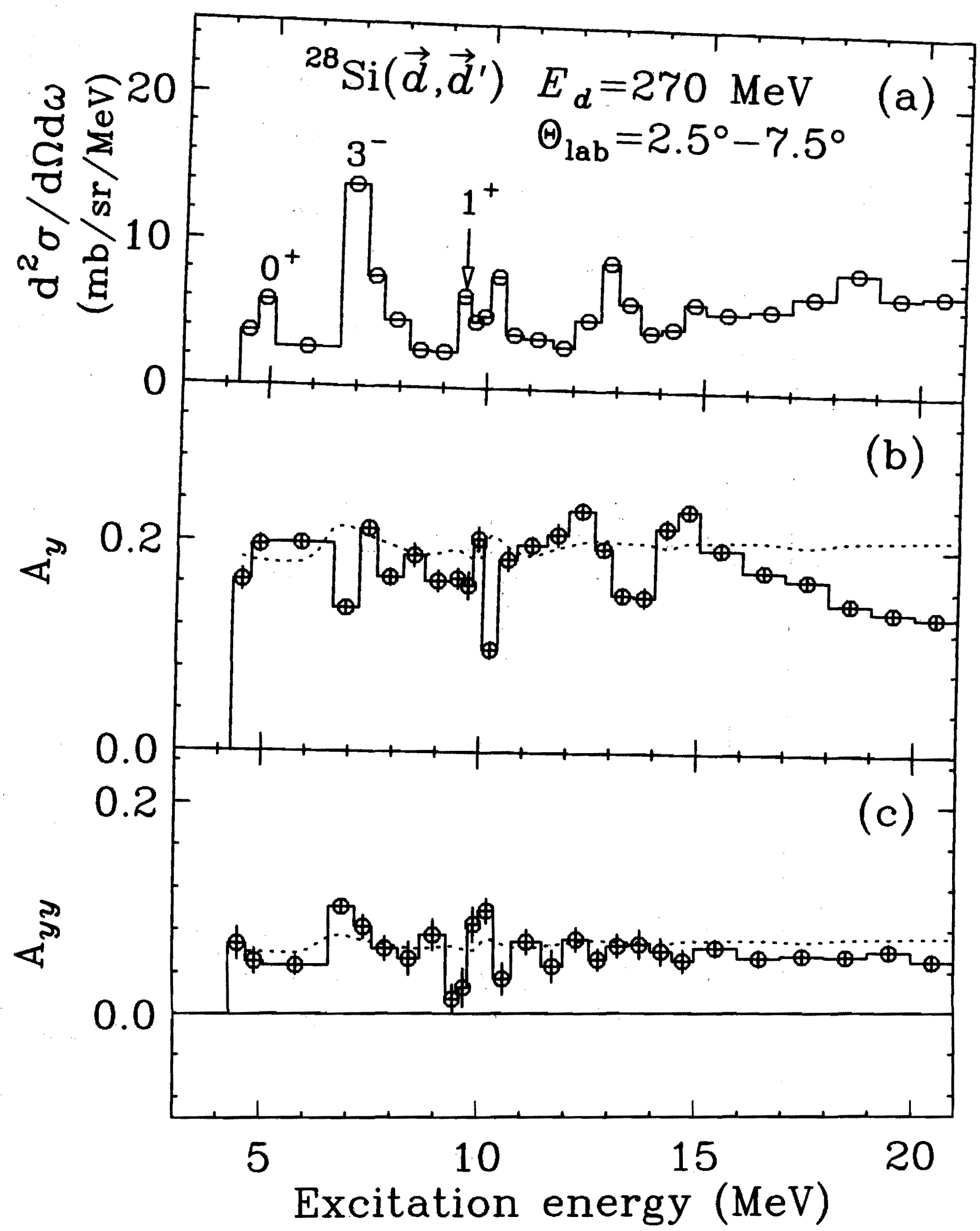

Figure 5.2: Results for the ^{28}Si($\vec{d},\vec{d'}$) reaction at E_d=270 MeV for angular range between $\Theta_{\rm lab}$=2.5 and 7.5°. (a) The excitation energy spectrum, (b) the vector analyzing power, A_y and (c) the tensor analyzing power, A_{yy}. A_y and A_{yy} are compared to values for free deuteron-nucleon scattering.

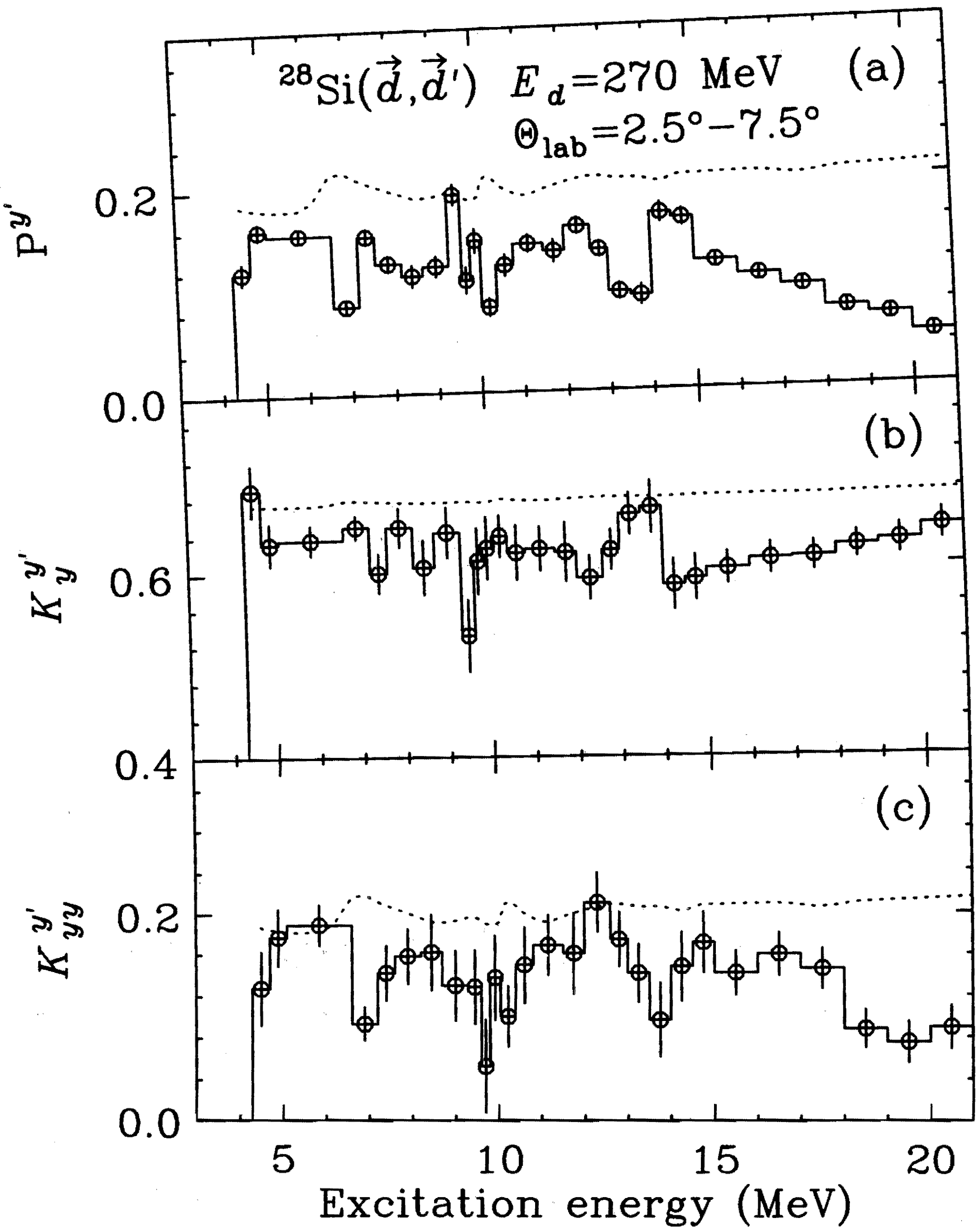

Figure 5.3: Results for the ^{28}Si$(\vec{d},\vec{d}')$ reaction at E_d=270 MeV for angular range between Θ_{lab}=2.5 and 7.5°. (a) the vector polarizing power, $P^{y'}$, the polarization transfer coefficients (b) $K_y^{y'}$ and (c) $K_{yy}^{y'}$. Polarization observables are compared to values for free deuteron-nucleon scattering.

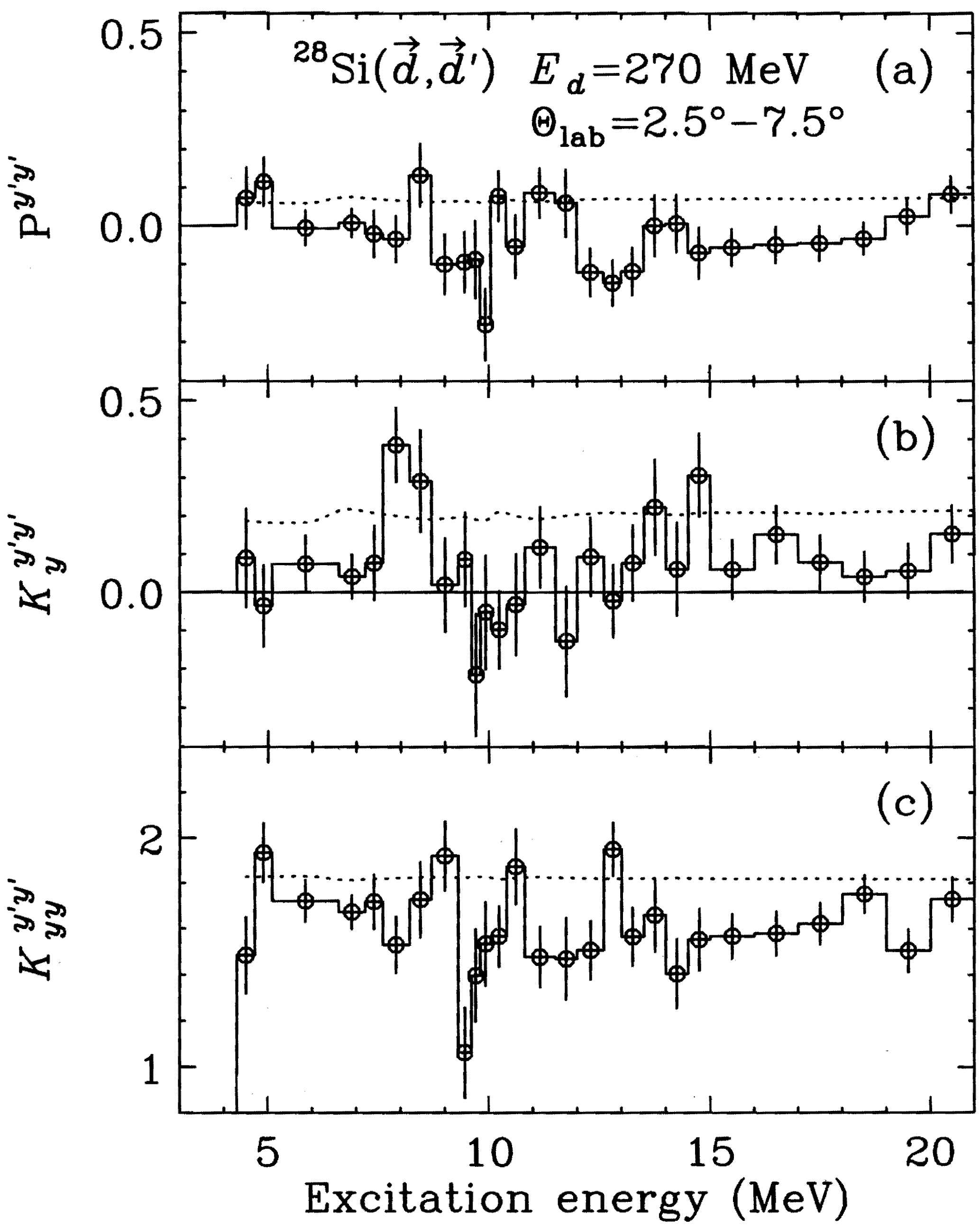

Figure 5.4: Results for the ^{28}Si($\vec{d}$, $\vec{d}'$) reaction at E_d=270 MeV for angular range between Θ_{lab}=2.5 and 7.5°. (a) the tensor polarizing power, $P^{y'y'}$, the polarization transfer coefficients (b) $K_y^{y'y'}$ and (c) $K_{yy}^{y'y'}$. Polarization observables are compared to values for free deuteron-nucleon scattering.

such as the 4_1^+, 2_2^+, 2_3^+ and 3_1^- states, implies that the effects of distortion can not be entirely neglected. Note that S_1 value is zero within PWIA for non-spin-flip transitions.

The S_2 values are found to be close to zero, and the presence of double spin-flip states such as the double Gamow-Teller states has not been indicated over the measured excitation energy and scattering angle region.

5.1.4 Single and Double Spin-flip Cross Section Spectra

One way of looking at possible spin-flip strength is to plot the spin-flip cross section which is just the product of the measured cross section and the spin-flip probability. The spin-flip cross section spectrum is shown in Fig. 5.6 (b). A concentration of spin-flip strength can be seen between 9.3 and 10.5 MeV. The spin-flip cross section above 11 MeV fluctuates at around a value of 0.5 mb/sr/MeV. This indicates that there are isoscalar spin-flip strengths fragmentary existing in this excitation energy region. The information on the isoscalar spin strengths is roughly consistent to that obtained by Fujita *et al.* [49], who identified several isoscalar 1^+ states in the excitation energy range between 9.7 and 16.0 MeV by making level by level comparison of the available spectra from the (p, p') and $(^3\mathrm{He}, t)$ reactions. The present measurement was performed at finite scattering angles where higher multipoles other than the $L = 0$ could contribute. More quantitative understandings of the isoscalar spin strengths including contributions from individual multipolarities might be obtained by comparing the present spin-flip spectrum with theoretical ones based on realistic nuclear structure and reaction calculations.

A small spin-flip cross section obtained for the 12.8 MeV bin implies that the 12.8 MeV peak, which is prominent in the cross section spectrum (see Figs. 5.6 (b) and 5.1), is predominantly of non-spin-flip nature. One sees a relatively large spin-flip cross section at the 6.9 MeV bin where the 3_1^- state is known. However, this state is known from an electron scattering experiment [72] to be almost a pure non-spin-flip transition. Furthermore there is no strong spin state known in this energy bin. Thus it is likely that the large spin-flip cross section at the 6.9 MeV bin is reflecting possible sensitivity of S_1 for natural parity transitions (with $L > 0$) to distortion effects.

The double spin-flip cross section is shown in Fig. 5.6 (c). The cross section values are consistent with zero over the excitation energy region, and no clear structure is seen in the spectrum.

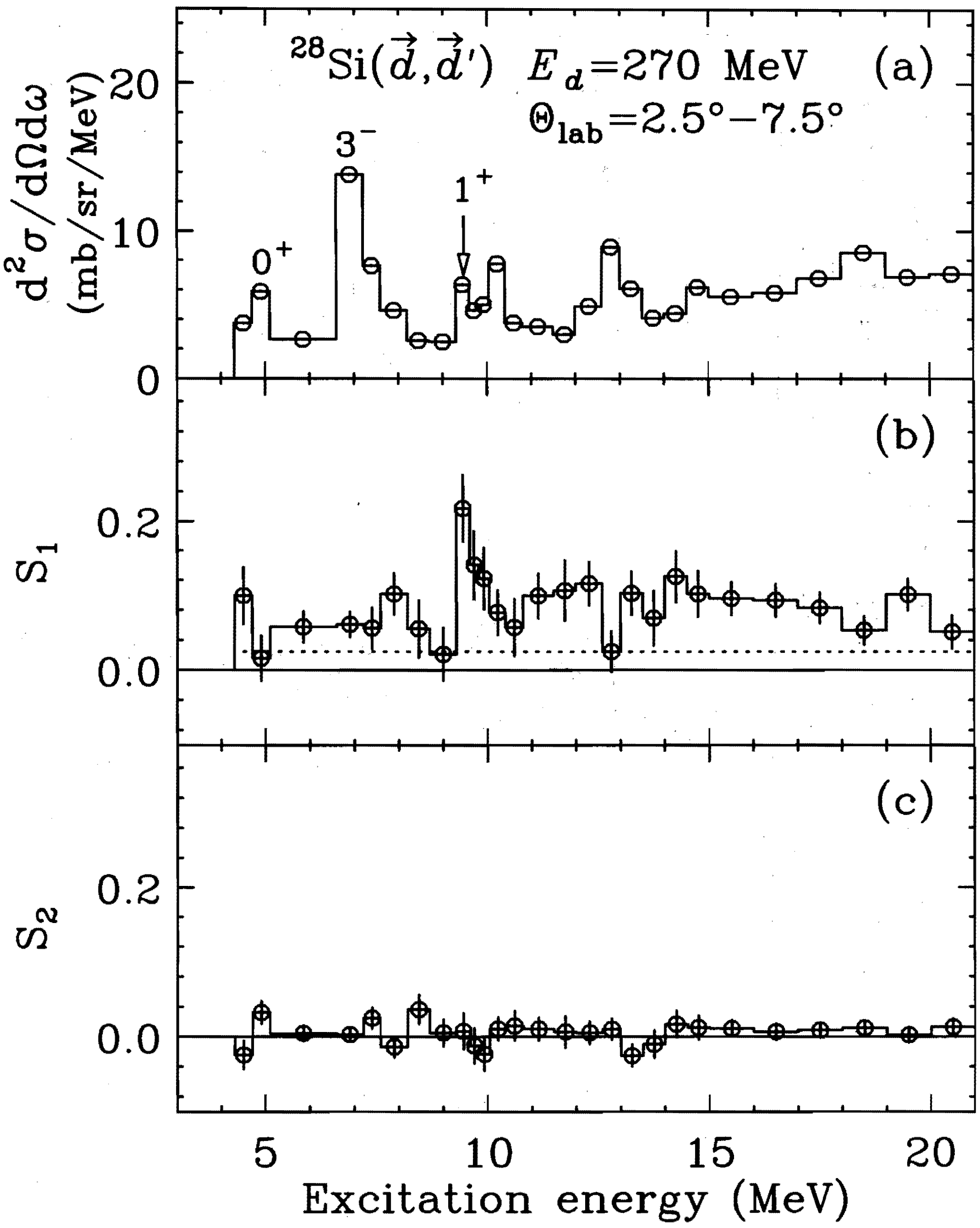

Figure 5.5: Excitation energy spectra for the ^{28}Si($\vec{d},\vec{d}'$) reaction at E_d = 270 MeV for angles between Θ_{lab} = 2.5°–7.5°. (a) The double differential cross section. (b) The spin-flip probability S_1. (c) The spin-flip probability S_2. The S_1 values are compared to those for free deuteron-nucleon scattering.

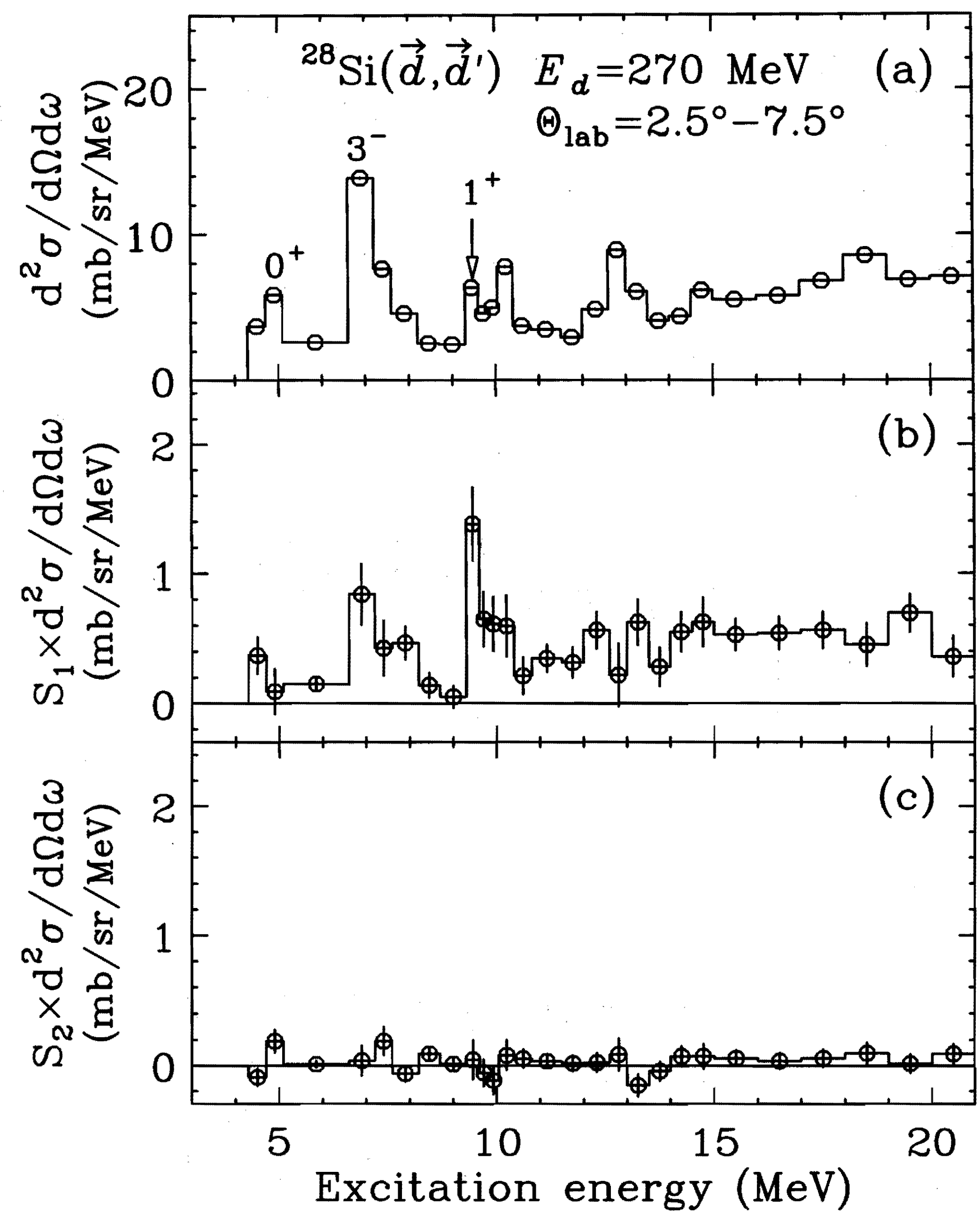

Figure 5.6: Excitation energy spectra for the ^{28}Si($\vec{d}$,$\vec{d}'$) reaction at E_d = 270 MeV for angles between Θ_{lab} = 2.5°–7.5°. (a) The double differential cross section. (b) The cross section multiplied by S_1. (c) The cross section multiplied by S_2.

5.2 Angular Distribution Data for Selected Transition

The angular distribution data on the cross section and analyzing powers A_y and A_{yy} for the 0_1^+ (ground), 2_1^+(4.44 MeV), 3_1^-(9.64 MeV), 1_1^+(12.71 MeV) and 2_2^-(18.3 MeV) states in ^{12}C and for the 0_1^+ (ground), 2_1^+(1.78 MeV), 3_1^-(6.88 MeV), 1_2^+(9.50 MeV) and 5_1^-(9.72 MeV) states in ^{28}Si are presented in this section. These states are conveniently divided into two classes, the natural parity transitions with parity change $\Delta\pi$=(-1)^J and the unnatural parity transitions with $\Delta\pi$=(-1)$^{J+1}$, which are excited through different parts of the projectile-nucleon effective interaction. The angular distribution data on the spin-flip probabilities S_1 and S_2 for transitions to the 2_1^+(4.44 MeV) and 1_1^+(12.71 MeV) states in ^{12}C and to the 3_1^-(6.88 MeV) and 1_2^+(9.5 MeV) states in ^{28}Si are also presented. The spin-flip probability data on ^{12}C are from the previous measurement [45].

Figure 5.7 shows an excitation energy spectrum of ^{12}C obtained via the (d, d') reaction at E_d = 270 MeV for an angular range between $\Theta_{\rm lab} = 4° - 6°$. We see that the spin-flip 1_1^+(12.71 MeV) and 2_2^-(18.3 MeV) states are clearly excited among other non-spin-flip 2_1^+(4.44 MeV), 0^+(7.65 MeV) and 3_1^-(9.64 MeV) states. A well-known isovector 1_1^+ state at 15.11 MeV is absent due to the isoscalar nature of the (d, d') reaction. The spectra were analyzed by using the program SPECFIT [73] to extract the yield contained in each peak. The continuum background and other overlapping states are subtracted in the cross section as well as the analyzing power data.

5.2.1 Elastic Scattering

The angular distributions of the differential cross section and analyzing powers A_y and A_{yy} for the elastic scattering on ^{12}C and ^{28}Si are shown in Figs. 5.8 and 5.9, respectively. The solid lines represent the results of the optical model (OM) calculations described in chapter 6.

5.2.2 Natural Parity Transition

The angular distributions of the differential cross sections for natural parity transitions to the 2_1^+ and 3_1^- states in ^{12}C and to the 2_1^+, 3_1^- and 5_1^- states in ^{28}Si are shown in Figs. 5.10 and 5.11, respectively. We see that the angular distribution shape of the cross section is characteristic of the transferred angular momentum ΔL, the larger the ΔL value the peak position occurs at a larger angle. The angular distributions of the analyzing powers A_y and A_{yy} for the same natural parity transitions are shown in Figs. 5.12 and 5.13 for the ^{12}C and ^{28}Si results, respectively. The curves in the figures are results of the microscopic DWIA and PWIA calculations described in chapter 6.

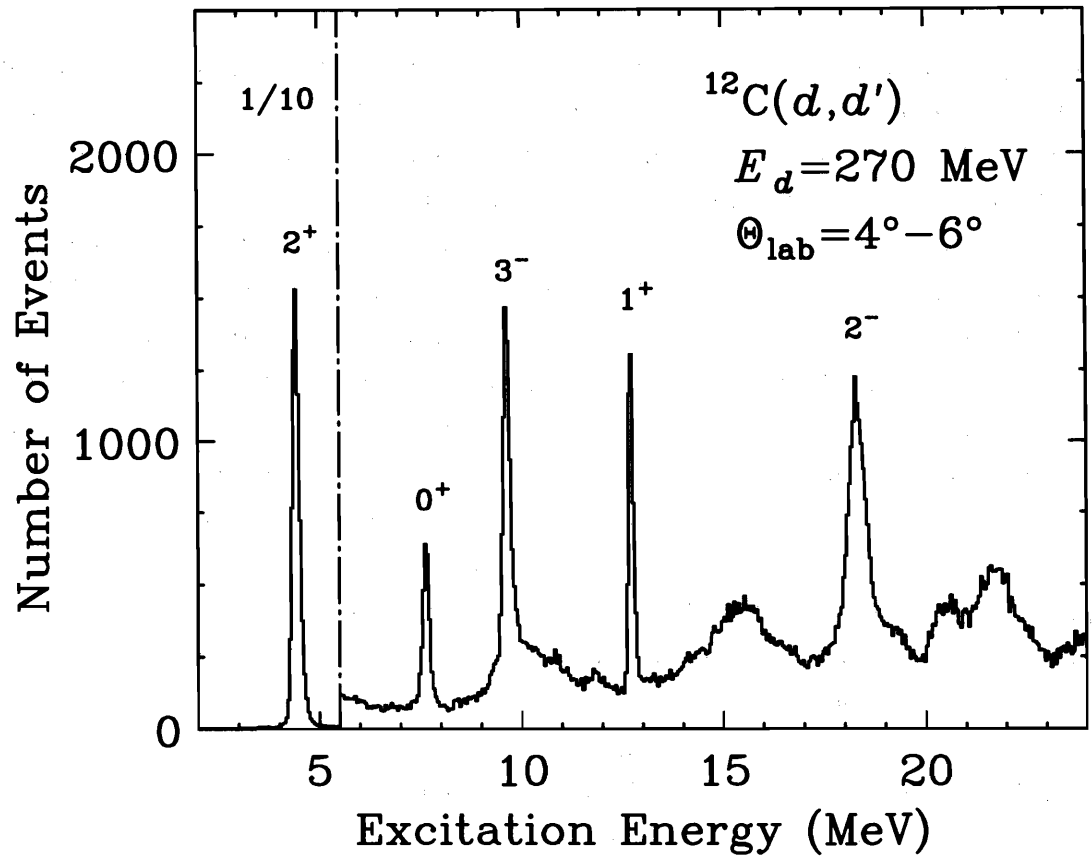

Figure 5.7: A typical excitation energy spectrum for the ^{12}C(d, d') reaction at E_d=270 MeV and at $\Theta_{\text{lab}} = 4° - 6°$. The first excited 2^+(4.44 MeV) state is scaled by a factor of 1/10.

5.2.3 Unnatural Parity Transition

The angular distributions of the differential cross sections for unnatural parity transitions to the 1_1^+ and 2_2^- states in ^{12}C and to the 1_2^+ state in ^{28}Si are shown in Fig. 5.14. Again we see angular distribution shapes which are characteristic of the transferred angular momentum ΔL. The angular distributions of the analyzing powers A_y and A_{yy} for the same unnatural parity transitions are shown in Fig. 5.15. It is interesting to note that A_y for these unnatural parity transitions decreases towards negative values with increasing scattering angle in the angular range between 3° and 15° (this is not so obvious for A_y of the 1_2^+ state in ^{28}Si due to the increasing contribution from the 2_6^+ state at larger angles). This behavior of A_y for the unnatural parity transitions is quite in contrast to that for the natural parity transitions for which a monotonous increase in A_y in the same angular interval is observed. We can also see similar transferred spin ΔS dependence in the angular distributions of A_{yy}.

5.2.4 Spin-Flip Probability

The angular distributions of the spin-flip probabilities S_1 and S_2 for natural parity transitions to the 2_1^+ state in ^{12}C and to the 3_1^- state ^{28}Si are shown in Fig. 5.16, and those for unnatural parity transitions to the 1_1^+ state in ^{12}C and to the 1_2^+ state ^{28}Si are shown in Fig. 5.17.

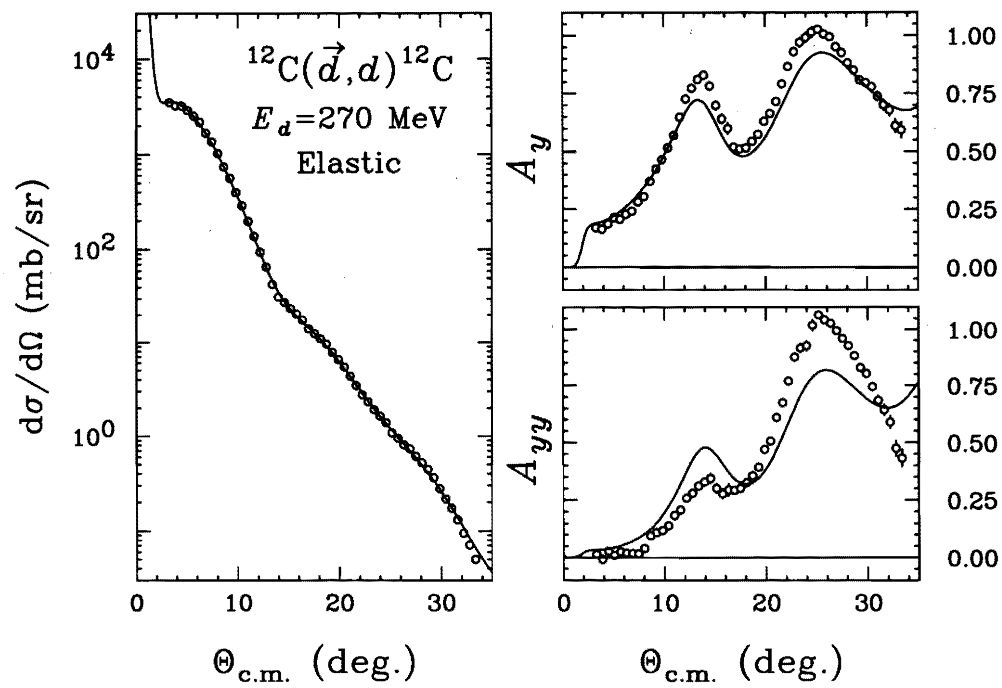

Figure 5.8: The measured elastic scattering cross section and analyzing powers A_y and A_{yy} for ^{12}C at E_d = 270 MeV compared to the optical model calculations (solid lines) using the parameters given in Table 6.1.

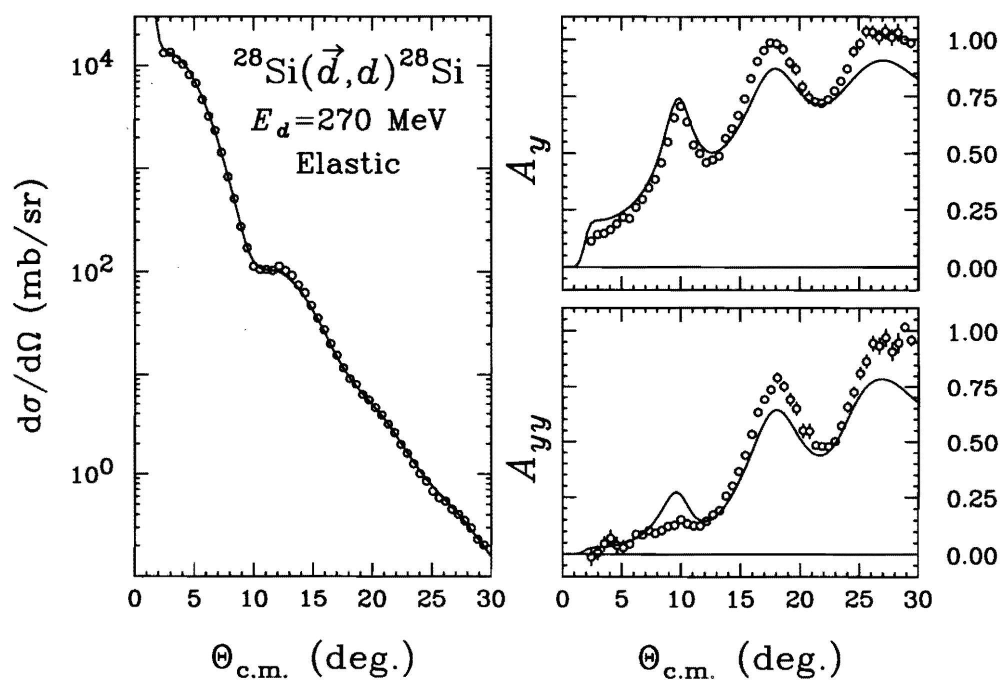

Figure 5.9: The measured elastic scattering cross section and analyzing powers A_y and A_{yy} for ^{28}Si at E_d = 270 MeV compared to the optical model calculations (solid lines) using the parameters given in Table 6.2.

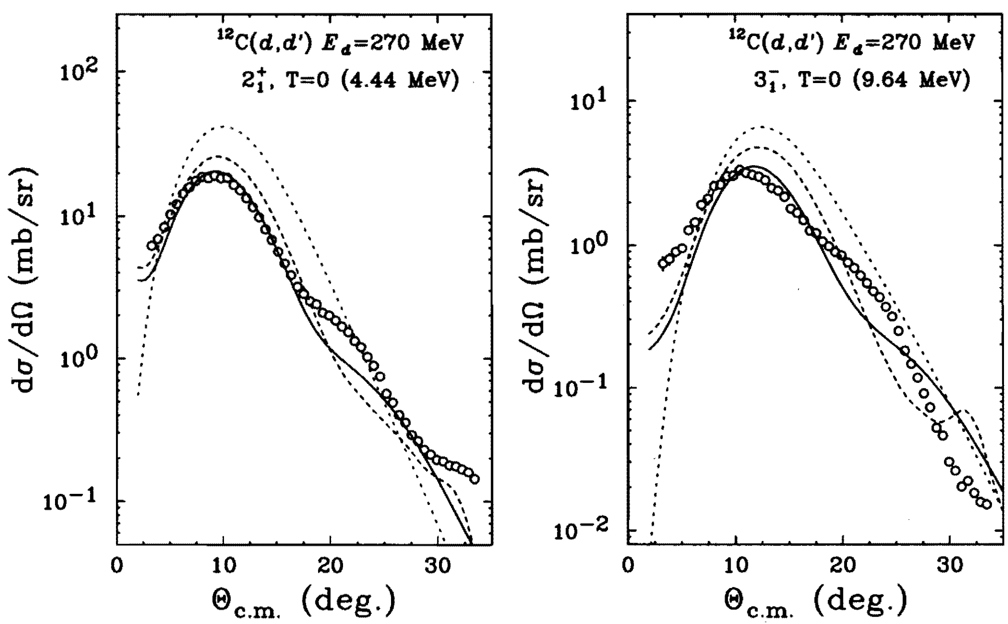

Figure 5.10: Angular distributions of the cross section for the 2^+_1(4.44 MeV) and 3^-_1(9.64 MeV) states in ^{12}C excited via the (d, d') reaction at E_d=270 MeV. The solid and dotted lines are results of the DWIA and PWIA calculations using the three-body dN t-matrix interaction. The dashed line is a result of the DWIA calculation using the folding dN t-matrix interaction.

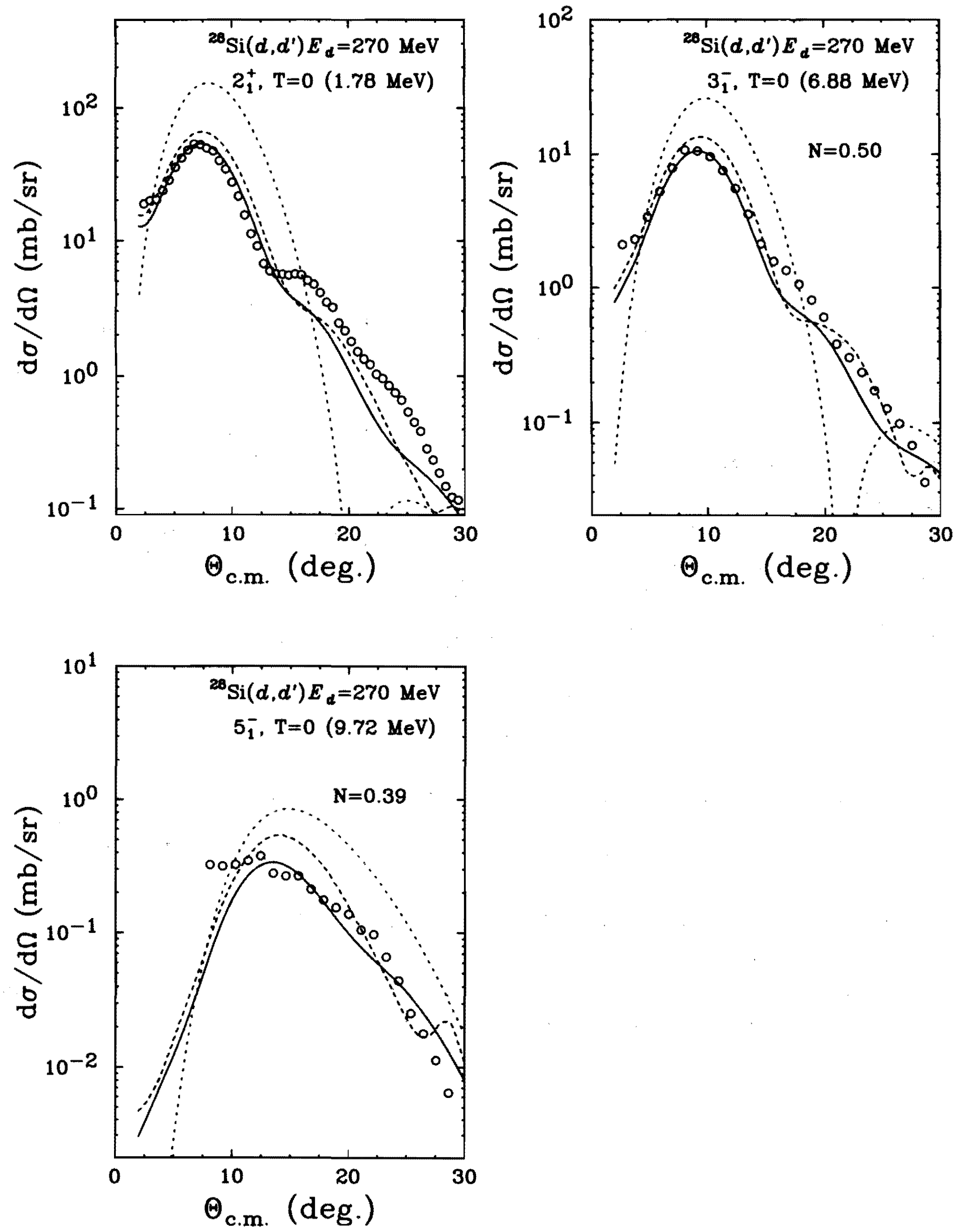

Figure 5.11: The same as Fig. 5.10 but for the 2_1^+(1.78 MeV), 3_1^-(6.88 MeV) and 5_1^-(9.72 MeV) states in ^{28}Si. The calculated curves for the 3_1^- and 5_1^- states are normalized by factors 0.50 and 0.39, respectively.

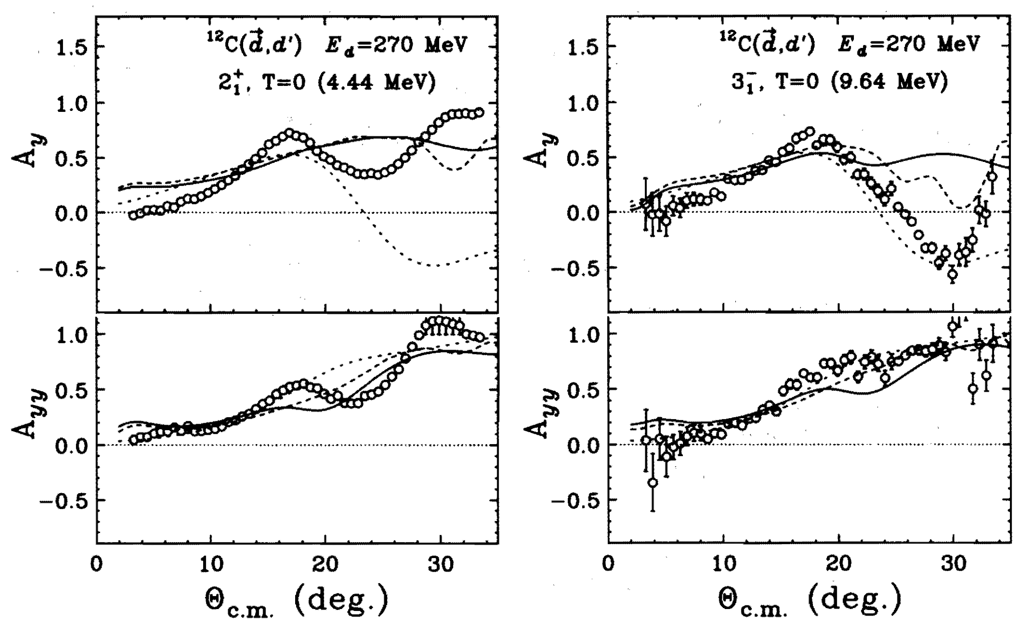

Figure 5.12: Angular distributions of the analyzing powers A_y and A_{yy} for the 2_1^+(4.44 MeV) and 3_1^-(9.64 MeV) states in ^{12}C excited via the (d, d') reaction at E_d=270 MeV. The solid and dotted lines are results of the DWIA and PWIA calculations using the three-body dN t-matrix interaction. The dashed line is a result of the DWIA calculation using the folding dN t-matrix interaction.

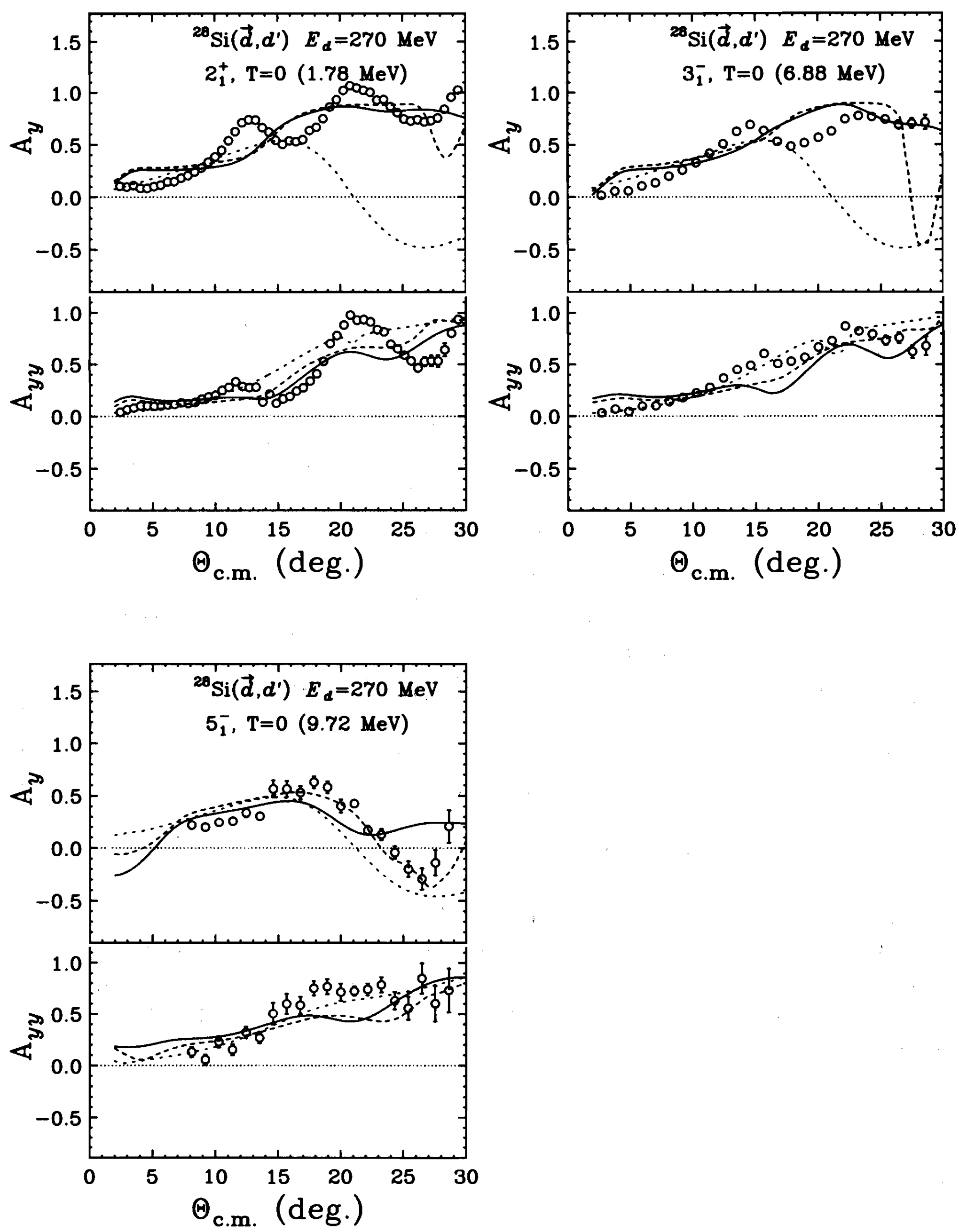

Figure 5.13: The same as Fig. 5.12 but for the 2_1^+(1.78 MeV), 3_1^-(6.88 MeV) and 5_1^-(9.72 MeV) states in ^{28}Si.

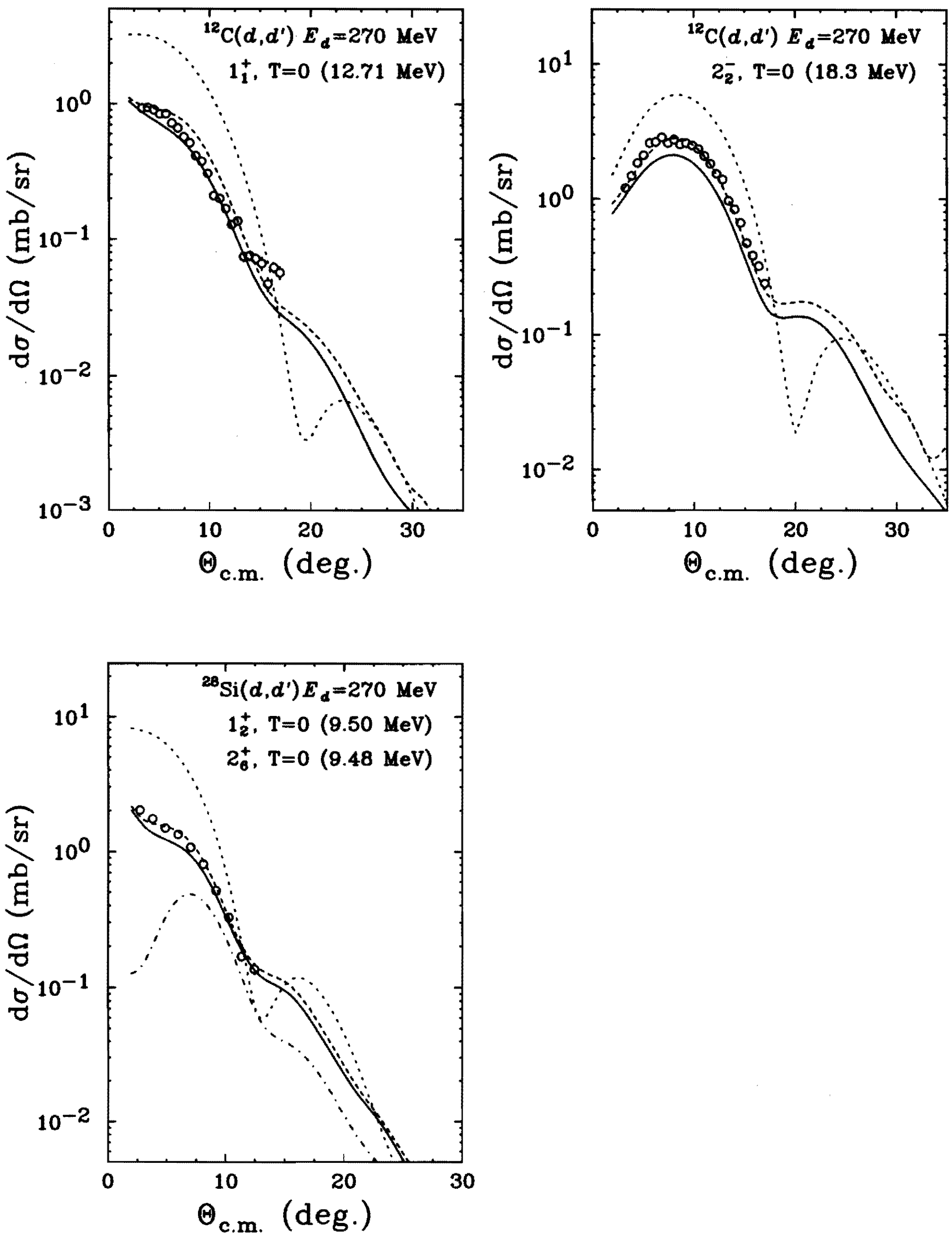

Figure 5.14: Angular distributions of the cross section for the 1_1^+(12.71 MeV) and 2_2^-(18.3 MeV) states in ^{12}C and for the 1_2^+(9.50 MeV) state in ^{28}Si excited via the (d, d') reaction at E_d=270 MeV. The solid and dotted lines are results of the DWIA and PWIA calculations using the three-body dN t-matrix interaction. The dashed line is a result of the DWIA calculation using the folding dN t-matrix interaction. The dot-dashed line for the 1_2^+ state in ^{28}Si represents an estimated contribution from the 2_6^+ state.

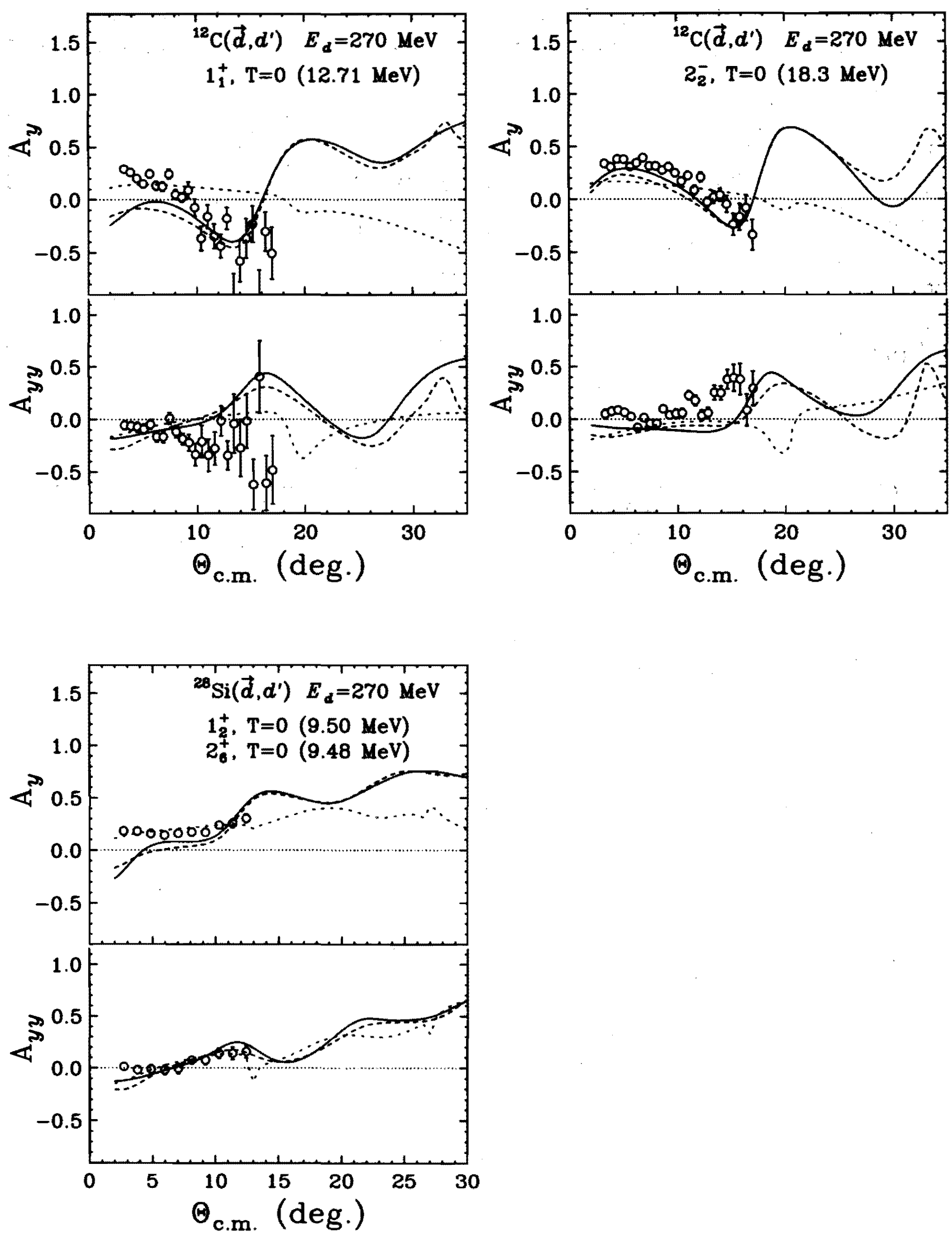

Figure 5.15: Angular distributions of the analyzing powers A_y and A_{yy} for the 1_1^+(12.71 MeV) and 2_2^-(18.3 MeV) states in ^{12}C and for the 1_2^+(9.50 MeV) state in ^{28}Si excited via the (d, d') reaction at E_d=270 MeV. The solid and dotted lines are results of the DWIA and PWIA calculations using the three-body dN t-matrix interaction. The dashed line is a result of the DWIA calculation using the folding dN t-matrix interaction.

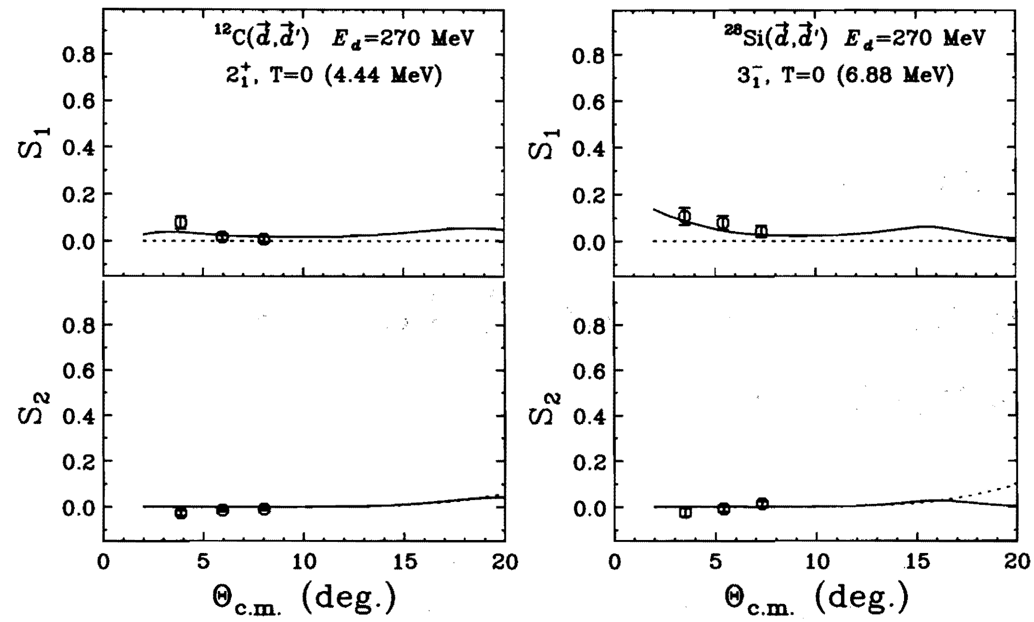

Figure 5.16: Angular distributions of the spin-flip probabilities S_1 and S_2 for natural parity transitions to the 2_1^+(4.44 MeV) state in ^{12}C [45] and to the 3_1^-(6.88 MeV) state in ^{28}Si excited via the (d, d') reaction at E_d=270 MeV. The solid (dotted) lines are the DWIA (PWIA) calculations.

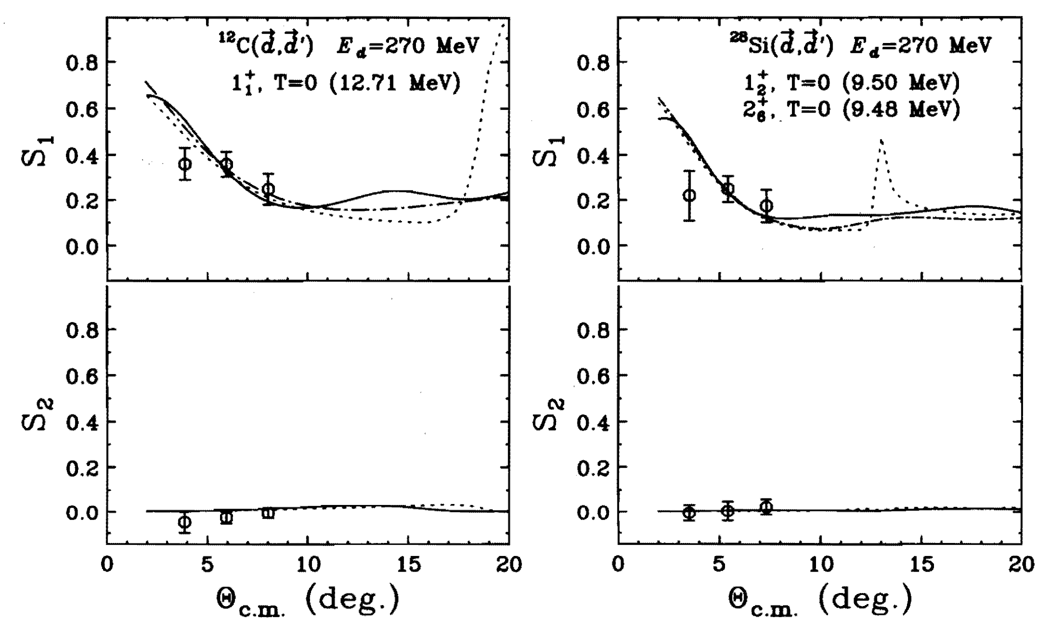

Figure 5.17: The same as Fig. 5.16 but for unnatural parity transitions to the 1_1^+(12.71 MeV) state in ^{12}C [45] and to the 1_2^+(9.50 MeV) state in ^{28}Si excited via the (d, d') reaction at E_d=270 MeV. The solid (dotted) lines are the DWIA (PWIA) calculations. The dot-dash lines are the impulse approximation estimates for LSJ=(011).

Chapter 6

Theoretical Calculation and Discussion

There are in general three aspects to be considered in the microscopic treatment of a nucleus-nucleus inelastic scattering: (1) the structure of the projectile and target, (2) the effective interaction and (3) the reaction mechanism. Before one can use the deuteron inelastic scattering as a quantitative tool for spectroscopy, it is important to have an insight into the reaction mechanism and the effective interaction. In this chapter we examine a distorted wave impulse approximation (DWIA) model formulated by Wiele *et al.* [29], and modified to accept the deuteron-nucleon t-matrix deduced from the three-nucleon Faddeev calculations [31] (the three-body dN interaction) as the projectile-nucleon effective interaction (see Appendix C). The eight transitions chosen are the 2_1^+(4.44 MeV), 3_1^-(9.64 MeV), 1_1^+(12.71 MeV) and 2_2^-(18.3 MeV) states in ^{12}C and the 2_1^+(1.78 MeV), 3_1^-(6.88 MeV), 1_2^+(9.50 MeV) and 5_1^-(9.70 MeV) states in ^{28}Si, which include transitions differing in multi-polarity and spin transfer. For these transitions reliable nuclear structure information is available from shell model and other structure calculations. The eventual goal is to see whether the DWIA using a consistent set of wave functions for the states involved and using a realistic effective projectile-nucleon interaction can provide a simultaneous description of the scattering observables obtained in this experiment. It is also intended to clarify the role of correlation among the three nucleons in the projectile-nucleon system by comparing calculated results using the three-body dN interaction with those obtained by the folding dN interaction which is based on the deuteron-nucleon impulse approximation calculations [29].

The calculations scheme is presented in section 6.1. The calculated cross section and analyzing powers are compared with the data for natural and unnatural parity transitions in section 6.2 and 6.3, respectively. The DWIA calculations are then applied to make interpretation of the spin-flip probability data for transitions to the 2_1^+ and 1_1^+ states in

^{12}C and to the 3_1^- and 1_2^+ states in ^{28}Si in section 6.4.

6.1 Microscopic DWIA Calculation

6.1.1 Transition Matrix

The transition matrix for the (d, d') reaction within the DWIA [29, 74, 75, 76, 77] is given by

$$T_{dA}^{\rm DWIA} = \langle X^{(-)}(\vec{R})\chi_{d'}\Phi_{A^*}(\vec{\rho})|t_{dN}(q)e^{i\vec{q}\cdot(\vec{\rho}-\vec{R})}|X^{(+)}(\vec{R})\chi_d\Phi_A(\vec{\rho})\rangle, \tag{6.1}$$

where the distorted waves in the initial and final channels are denoted by $X^{(+)}(\vec{R})$ and $X^{(-)}(\vec{R})$, the target wave functions by $\Phi_A(\vec{\rho})$ and $\Phi_{A^*}(\vec{\rho})$, and the deuteron spinors by χ_d and $\chi_{d'}$, respectively. $t_{dN}(q)$ is the projectile-nucleon effective interaction with q being the momentum transfer. The integral over q in $T_{dA}^{\rm DWIA}$ was carried out over the range of q where t_{dN} is known, i.e. $q_{\rm max}$=3.41 and 2.52 fm^{-1} for the three-body and folding dN interactions, respectively. (See subsection 6.1.3 and appendix C for these interactions.) Since the form factor decreases rapidly with q, the results with the three-body dN interaction did not depend on the choice of the above $q_{\rm max}$ values. Details on $T_{dA}^{\rm DWIA}$ is given in Appendix C.

6.1.2 Optical Potential

The distorted waves in the entrance and exit channels were generated by using the optical model (OM) potential parameters in Tables 6.1 and 6.2 for ^{12}C and ^{28}Si, respectively. The OM potential, $U(r)$, was determined by fitting the elastic scattering data using the code ECIS79 [78]. In the fitting procedure the elastic scattering data up to about 30° (center of mass) were analyzed. The OM potential was parameterized by the volume Wood-Saxon real and imaginary terms, V_R and W_I, the real and imaginary spin-orbit terms, V_{RSO} and W_{ISO}, and the Coulomb term, $V_{\rm Coul}$, as

$$\begin{aligned} U(r) &= V_R f(x_R) + iW_I f(x_I) + V_{\rm Coul}(r) \\ &+ \left[-V_{RSO}\frac{1}{r}\frac{d}{dr}f(x_{RSO}) - iW_{ISO}\frac{1}{r}\frac{d}{dr}f(x_{ISO})\right] \boldsymbol{L}\cdot\boldsymbol{s}, \end{aligned} \tag{6.2}$$

where $\boldsymbol{s}$ and $\boldsymbol{L}$ are the deuteron spin and orbital angular momentum operators, $f(x_i)$ has a Woods-Saxon form, $f(x_i) = f(r; r_i, a_i) = [1 + \exp\{(r - r_i A^{\frac{1}{3}})/a_i\}]^{-1}$. The Coulomb term $V_{\rm Coul}(r)$ is due to a uniformly charged sphere of radius $R_C = r_c A^{\frac{1}{3}}$. The tensor terms in the optical potential are ignored in the present analysis. The OM predictions are compared with the data in Figs. 5.8 and 5.9 for ^{12}C and ^{28}Si, respectively. The data are well reproduced by the OM calculations.

Table 6.1: Phenomenological Woods-Saxon optical model parameters for the deuteron elastic scattering on ^{12}C at E_d=270 MeV. The Coulomb radius parameter was fixed at r_C=1.3 fm.

V_R (MeV)	r_R (fm)	a_R (fm)	W_I (MeV)	r_I (fm)	a_I (fm)
-19.271	1.408	0.752	-19.644	1.081	0.889
V_{RSO} (MeV)	r_{RSO} (fm)	a_{RSO} (fm)	W_{ISO} (MeV)	r_{ISO} (fm)	a_{ISO} (fm)
-7.196	0.907	0.714	1.637	0.888	0.708

Table 6.2: The same as in Table 6.1 but for ^{28}Si target.

V_R (MeV)	r_R (fm)	a_R (fm)	W_I (MeV)	r_I (fm)	a_I (fm)
-21.572	1.384	0.806	-20.093	1.044	1.041
V_{RSO} (MeV)	r_{RSO} (fm)	a_{RSO} (fm)	W_{ISO} (MeV)	r_{ISO} (fm)	a_{ISO} (fm)
-5.466	1.032	0.797	1.582	1.008	0.738

6.1.3 Effective Interaction

The projectile-nucleon effective interaction, t_{dN}, is assumed to be the on-shell deuteron-nucleon (dN) t-matrix. The most general form of the scattering matrix allowed for an dN (spin-1 on spin-$\frac{1}{2}$) interaction that is invariant under parity and time reversal in the dN center of mass frame is given by [79]

$$\begin{aligned} t_{dN}(q) &= \alpha + \beta S_n + \gamma\sigma_n + \delta S_n\sigma_n + \epsilon S_q\sigma_q + \zeta S_p\sigma_p + \eta Q_{qq} + \xi Q_{pp} \\ &\quad + \kappa Q_{qq}\sigma_n + \lambda Q_{pp}\sigma_n + \mu Q_{nq}\sigma_q + \nu Q_{np}\sigma_p, \end{aligned} \tag{6.3}$$

where σ is Pauli spin matrix, S and Q deuteron spin operators, and $\alpha, \ldots, \nu$ are complex parameters which depend on the incident energy and $\vec{q}$. Unit vectors are given by $\hat{q}//\vec{k}_{\rm in} - \vec{k}_{\rm out}$, $\hat{n}//\vec{k}_{\rm in} \times \vec{k}_{\rm out}$ and $\hat{p} = \hat{n} \times \hat{q}$.

Two different sets of parameters for t_{dN} are examined. The first set is calculated by folding the on-shell NN t-matrix at half the incident deuteron energy with a full deuteron wave function as given in the original study by Wiele *et al.* [29] (the folding dN interaction). In the folding dN interaction one of the nucleon in the deuteron is treated merely as a spectator. The second set is obtained by solving the $3N$ Faddeev equations as

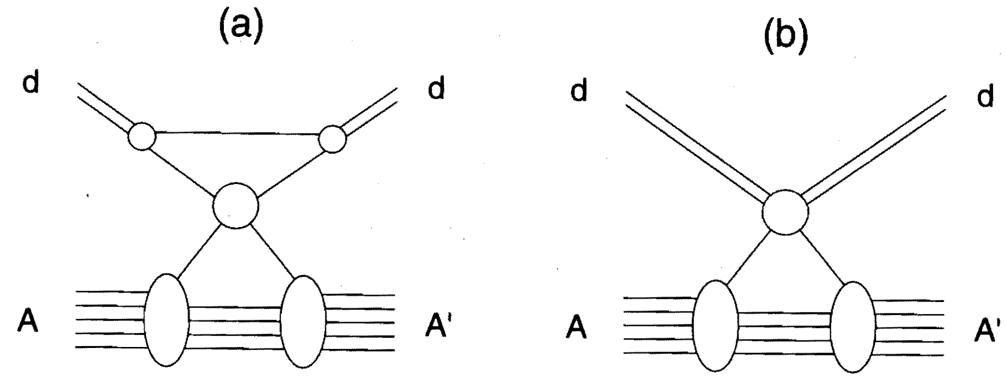

Figure 6.1: Diagramatic representations of the deuteron-nucleus (dA) scattering matrix in terms of (a) the folding dN interaction and (b) the three-body dN interaction.

given in Ref. [31] at $E_d = 270$ MeV (the three-body dN interaction). [1] In the three-body dN interaction the multiple scattering, rearrangement and deuteron break-up effects are fully included. In both calculations the CD-Bonn potential [80] was used for the NN interaction. Diagramatic representations of the deuteron-nucleus (dA) scattering matrix in Eq.(6.1) in terms of the folding dN interaction and of the three-body dN interaction are given in Figs. 6.1 (a) and (b), respectively.

Experimental data for the $\vec{d} + p$ elastic scattering at 270 MeV are compared with theoretical predictions based on the two t_{dN} matrices in Fig. 1.1. It is clearly seen that a better description of the data is obtained with the three-body dN interaction. More details on the t_{dN}-matrices are given in Appendix C.

6.1.4 Transition Density

Other inputs required for the DWIA calculations are the spectroscopic amplitudes and transition densities. These are calculated from wave functions derived from models appropriate for the nuclear levels of interest. The transition densities are presented in terms of the coefficients of an expansion in products of single-particle radial wave functions. The definitions of the transition densities and spectroscopic amplitudes in this study are given respectively in Eqs.(C.12) and (C.14) in Appendix C.

The spectroscopic amplitudes for positive and negative parity states in ^{12}C were calculated by using the shell model wave functions of Cohen and Kurath (CK) [81] and of Millener and Kurath (MK) [82], respectively. The calculations were carried out by using the shell model code OXBASH [83]. The amplitudes are listed in Tables 6.3 and 6.4 for

[1] The three-body dN amplitudes are provided by Dr. Kamada.

Table 6.3: Spectroscopic amplitudes $S^{j_c}_{00}(j_f j_i)$ for the positive parity 2^+(4.44 MeV) and 1^+(12.71 MeV) states in ^{12}C.

State	E_x (MeV)	$0p_{1/2}$ $0p^{-1}_{1/2}$	$0p_{1/2}$ $0p^{-1}_{3/2}$	$0p_{3/2}$ $0p^{-1}_{1/2}$	$0p_{3/2}$ $0p^{-1}_{3/2}$
2^+	4.44		0.7594	-0.5014	-0.3101
1^+	12.71	-0.0434	0.7187	0.3544	0.0137

Table 6.4: Spectroscopic amplitudes $S^{j_c}_{00}(j_f j_i)$ for the negative parity states 3^-(9.64 MeV) and 2^-(18.3 MeV) states in ^{12}C.

State	E_x (MeV)	$0d_{3/2}$ $0p^{-1}_{1/2}$	$0d_{3/2}$ $0p^{-1}_{3/2}$	$0d_{5/2}$ $0p^{-1}_{1/2}$	$0d_{5/2}$ $0p^{-1}_{3/2}$	$1s_{1/2}$ $0p^{-1}_{3/2}$
3^-	9.64		-0.3209	0.2728	0.5020	
2^-	18.3	-0.0309	0.0899	0.1070	-0.7065	-0.2669

positive and negative parity states, respectively. The single particle wave functions were those of a harmonic oscillator well with a length parameter of b=1.756 fm [84] which is consistent with elastic electron scattering data.

The spectroscopic amplitudes for positive parity states in ^{28}Si were calculated by using the shell model wave functions of Wildenthal (W) [51]. The amplitudes are listed in Tables 6.5 for the 2^+_1 state, and in Table 6.6 for the 1^+_1 and 1^+_2 states. The harmonic oscillator length parameter was chosen to be b=1.80 fm on the basis of the electron scattering data in Ref. [72]. For negative parity levels in ^{28}Si the spectroscopic amplitudes obtained from the open-shell random phase approximation (OSRPA) of Rowe and Wong [85] were used. The OSRPA predictions given in Ref. [72] are listed in Tables 6.7 and 6.8 for the 3^-_1 and 5^-_1 states, respectively. The coefficients in Ref. [72] were multiplied by appropriate phase factors to agree with the present convention for the spectroscopic amplitude. Based on the projected Hartree-Fock prolate ground state and on the Kuo shell model ground state, the amplitudes give satisfactory account of the electron form factors in both shape and magnitude with harmonic oscillator length parameters of b=1.80 and 1.91 fm for the 3^-_1 and 5^-_1 states, respectively [72].

Table 6.5: Spectroscopic amplitudes $S_{00}^{j_c}(j_f j_i)$ for the positive parity 2_1^+(1.78 MeV) state in ^{28}Si.

State	E_x (MeV)	$0d_{3/2}$ $0d_{3/2}^{-1}$	$0d_{3/2}$ $0d_{5/2}^{-1}$	$0d_{3/2}$ $1s_{1/2}^{-1}$	$0d_{5/2}$ $0d_{3/2}^{-1}$	$0d_{5/2}$ $0d_{5/2}^{-1}$	$0d_{5/2}$ $1s_{1/2}^{-1}$	$1s_{1/2}$ $0d_{3/2}^{-1}$	$1s_{1/2}$ $0d_{5/2}^{-1}$
2_1^+	1.78	-0.1714	0.3835	0.1532	-0.3038	-0.2986	-0.4066	-0.0862	-0.5949

Table 6.6: Spectroscopic amplitudes $S_{00}^{j_c}(j_f j_i)$ for the positive parity 1_1^+(8.33 MeV) and 1_2^+(9.50 MeV) states in ^{28}Si.

State	E_x (MeV)	$0d_{3/2}$ $0d_{3/2}^{-1}$	$0d_{3/2}$ $0d_{5/2}^{-1}$	$0d_{3/2}$ $1s_{1/2}^{-1}$	$0d_{5/2}$ $0d_{3/2}^{-1}$	$0d_{5/2}$ $0d_{5/2}^{-1}$	$1s_{1/2}$ $0d_{3/2}^{-1}$	$1s_{1/2}$ $1s_{1/2}^{-1}$
1_1^+	8.33	-0.0314	-0.2963	0.1808	-0.1292	0.0390	0.0928	-0.1311
1_2^+	9.50	-0.0880	0.5563	-0.0548	0.2083	0.0483	-0.0372	-0.0071

Table 6.7: Spectroscopic amplitudes $S_{00}^{j_c}(j_f j_i)$ for the negative parity 3_1^-(6.88 MeV) state in ^{28}Si.

State	E_x (MeV)								
		$0d_{5/2}$ $0p_{3/2}^{-1}$	$0d_{5/2}$ $0p_{1/2}^{-1}$	$0d_{3/2}$ $0p_{3/2}^{-1}$	$0f_{7/2}$ $0d_{5/2}^{-1}$	$0f_{7/2}$ $0d_{3/2}^{-1}$	$0f_{7/2}$ $1s_{1/2}^{-1}$	$0f_{5/2}$ $0d_{5/2}^{-1}$	$0f_{5/2}$ $1s_{1/2}^{-1}$
3_1^-	6.88	0.068	0.099	-0.191	-0.449	-0.173	-0.240	0.165	-0.141
		$0f_{5/2}$ $0d_{5/2}^{-1}$	$1p_{3/2}$ $0d_{3/2}^{-1}$	$1p_{3/2}$ $0d_{5/2}^{-1}$	$1p_{1/2}$ $0d_{5/2}^{-1}$	$0p_{3/2}$ $0d_{5/2}^{-1}$	$0p_{1/2}$ $0d_{3/2}^{-1}$	$0p_{3/2}$ $0d_{3/2}^{-1}$	$0d_{5/2}$ $0f_{7/2}^{-1}$
		0.159	-0.285	-0.181	0.263	0.053	-0.065	0.133	-0.186
		$0d_{3/2}$ $0f_{7/2}^{-1}$	$1s_{1/2}$ $0f_{7/2}^{-1}$	$0d_{5/2}$ $0f_{5/2}^{-1}$	$0d_{3/2}$ $0f_{5/2}^{-1}$	$1s_{1/2}$ $0f_{5/2}^{-1}$	$0d_{5/2}$ $1p_{3/2}^{-1}$	$0d_{3/2}$ $1p_{3/2}^{-1}$	$0d_{5/2}$ $1p_{1/2}^{-1}$
		0.084	-0.154	-0.091	-0.088	-0.106	-0.130	0.090	-0.127

Table 6.8: Spectroscopic amplitudes $S_{00}^{j_c}(j_f j_i)$ for the negative parity 5_1^-(9.70 MeV) state in ^{28}Si.

State	E_x (MeV)	$0f_{7/2}$ $0d_{5/2}^{-1}$	$0f_{7/2}$ $0d_{3/2}^{-1}$	$0f_{5/2}$ $0d_{5/2}^{-1}$	$0d_{5/2}$ $0f_{7/2}^{-1}$	$0d_{3/2}$ $0f_{7/2}^{-1}$	$0d_{5/2}$ $0f_{5/2}^{-1}$
5_1^-	9.70	0.175	0.558	-0.121	0.041	-0.050	0.046

Table 6.9: Polarization observables and corresponding spin operators for spin-1 deuteron.

Observables	O^a	O^b
A_y	S_y	1
$P^{y'}$	1	S_y
$K_y^{y'}$	S_y	S_y
A_{yy}	S_{yy}	1
$P^{y'y'}$	1	S_{yy}
$K_{yy}^{y'y'}$	S_{yy}	S_{yy}
$K_{yy}^{y'}$	S_{yy}	S_y
$K_y^{y'y'}$	S_y	S_{yy}

6.1.5 Observable

The cross section for the unpolarized beam is calculated by

$$\frac{d\sigma}{d\Omega} = \frac{\mu_a \mu_b}{(2\pi\hbar^2)^2} \frac{k_b}{k_a} \frac{1}{(2S_d+1)(2I_A+1)} \sum_{\substack{M_A M_B \\ m_a m_b}} |T^{\mathrm{DWIA}}_{M_B m_b M_A m_a}|^2. \tag{6.4}$$

Here μ_a and k_a (μ_b and k_b) are the reduced mass and the momentum before (after) the collision calculated relativistically. S_d and I_A are the spin magnitudes of the deuteron and the ground state of the target. In Eq.(6.4) an average over the initial spin orientations and a sum over the final spin orientations are taken. The polarization observables are given by

$$X(a,b) = \frac{\mathrm{Tr}\{TO^a T^\dagger O^b\}}{\mathrm{Tr}\{TT^\dagger\}}, \tag{6.5}$$

where O^a and O^b are the spin operators for the initial and final deuterons, respectively. In Table 6.9 the correspondence between the polarization observables $X(a,b)$ and the associated operators is shown. The Cartesian operators S_y and $S_{yy}(= \mathcal{P}_{yy})$ are given in appendix C. The calculations were made by using the code DWUCK4 [86] after a suitable modification.

6.2 Comparison with Data for Natural Parity Transition

We first consider cross section and analyzing powers for transitions to the natural parity 2_1^+ and 3_1^- states in ^{12}C and to the 2_1^+, 3_1^- and 5_1^- states in ^{28}Si. The excitations of these states are almost ΔS=0 transitions which proceed predominantly through the

Table 6.10: Comparison of theoretical and experimental transition probability for the natural parity states in ^{12}C and ^{28}Si. The $B(\mathrm{EL}\uparrow)$ values are in units of $e^2\mathrm{fm}^{2L}$.

Nucleus	State	E_x (MeV)	$B(\mathrm{EL}\uparrow)_{\mathrm{th.}}$	$B(\mathrm{EL}\uparrow)_{\mathrm{exp.}}$
^{12}C	2_1^+	4.44	23.3	38.7±2.1[a]
	3_1^-	9.64	246.7	746.3±5.0[a]
^{28}Si	2_1^+	1.78	111.8	332.5±6.3[b]
	3_1^-	6.88	3194.6	4529.1±51.4[b]

[a]) Ref. [87].
[b]) Ref. [88].

spin-independent parts of the projectile-nucleon interaction. For each transition two calculations, PWIA and DWIA calculations, were made with the three-body dN interaction in order to see the effects of distortion. The results of these calculations are shown as dotted and full lines. The DWIA calculations using the folding dN interaction were also performed, and the results are shown as dashed lines. The DWIA calculations with the two interactions utilized the identical NN potential as input. Therefore the differences between the solid and dashed lines can be attributed to correlation among the three nucleons in the projectile-nucleon system (the three-nucleon correlation).

Table 6.10 summarizes the current information on the electromagnetic transition rates for the natural parity states in ^{12}C and ^{28}Si.

6.2.1 Cross Section

The calculated cross sections for the natural parity transitions in ^{12}C and ^{28}Si are compared with the data .in Figs. 5.10 and 5.11, respectively. The curves for the 3_1^- and 5_1^- states in ^{28}Si are scaled in such a way that the DWIA curves using the three-body dN interaction agree with the data near the cross section maxima. The resultant scale factors are 0.50 and 0.39 for the 3_1^- and 5_1^- states, respectively. Comparison of the dotted and solid lines shows that the effects of distortion substantially improve the fit to the angular distribution shapes of the cross section, although some discrepancy between the data and theory still remains at backward scattering angles. Comparison of the solid and dashed lines shows that the three-nucleon correlation has an effect to reduce the calculated cross sections near the peak. The DWIA cross sections with the two dN interactions at the cross section maxima are shown in the columns 4 and 5 of Table 6.11. We see that the reduction in the calculated cross sections due to the three-nucleon correlation amounts to $19 \sim 34\%$.

Table 6.11: Calculated and experimental differential cross sections at the peak position for natural parity transitions. Also shown are the normalization factors (N) which would be required for the DWIA cross sections (with the three-body dN interactions) to fit the experimental values when the transition densities are normalized to the electric measurements.

Nucleus	State	$\Theta_{c.m.}$ (deg.)	$\frac{d\sigma}{d\Omega})^{Fold}_{th.}$ (mb/sr)	$\frac{d\sigma}{d\Omega})^{3N}_{th.}$ (mb/sr)	$\frac{d\sigma}{d\Omega})_{exp.}$ (mb/sr)	N
^{12}C	2_1^+	9.0	25.6	20.5	18.9	0.54[a]
	3_1^-	11.0	4.6	3.5	3.2	0.31[a]
^{28}Si	2_1^+	7.5	66.3	53.7	51.7	0.32[a]
	3_1^-	9.0	26.7	21.1	10.6	0.50[b]
	5_1^-	13.0	1.28	0.84	0.33	0.39[b]

[a]) N= $[\frac{d\sigma}{d\Omega})_{exp.}\ B(\mathrm{EL}\uparrow)_{th.}] / [\frac{d\sigma}{d\Omega})^{3N}_{th.}\ B(\mathrm{EL}\uparrow)_{exp.}]$

[b]) N= $\frac{d\sigma}{d\Omega})_{exp.} / \frac{d\sigma}{d\Omega})^{3N}_{th.}$

The shell model calculations do not describe the absolute magnitudes of the experimental electric transition probabilities due to the core polarization effect [89]. The theoretical and experimental electric transition probabilities, $B(\mathrm{EL}\uparrow)_{th.}$ and $B(\mathrm{EL}\uparrow)_{exp.}$, for the 2_1^+ and 3_1^- states in ^{12}C and for the 2_1^+ state in ^{28}Si are listed in Table 6.10. If the theoretical (d, d') cross sections (calculated with the three-body dN interaction) are adjusted with the factors $B(\mathrm{EL}\uparrow)_{exp.}/\ B(\mathrm{EL}\uparrow)_{th.}$,[2] they would require normalization factors to fit the data as listed in the column 7 of Table 6.11, where the aforementioned scale factors for the 3_1^- and 5_1^- states are also listed. We see that DWIA cross sections must be multiplied by factors 0.31 $\sim$ 0.54 to obtain correct magnitudes when the nuclear transition densities are normalized to reproduce the electric transition probabilities.

The problem in normalization of the calculated cross sections for the natural parity transitions as seen in the present DWIA analysis has been noted in analyses of the (p, p') reaction at comparable incident energies per nucleon using an effective interaction based on free nucleon-nucleon scattering [90, 91]. Comfort *et al.* made DWIA calculations for transitions to the 2_1^+ state excited via the ^{12}C(p, p') reaction at E_p=120 MeV [90], and to the 2_1^+ and 3_1^- states in ^{12}C at E_p=200 MeV [91]. Their calculations made use of the Love and Franey effective interaction [92], and the same shell model wave functions used here with the same normalization procedure. To obtain correct peak cross sections the calculated values needed to be multiplied by 0.59 for the 2_1^+ state at 120 MeV and 0.53 and 0.45 respectively for the 2_1^+ and 3_1^- states at 200 MeV. The required normalization

[2]The renormalizations have not been included in the curves for the 2_1^+ and 3_1^- states in Fig. 5.10 and the 2_1^+ state in Fig. 5.11.

factors are very close to those found in the present (d, d') analysis. This indicates that the failure in the present DWIA analysis to reproduce the cross section magnitude for ΔT=0, ΔS=0 transitions arises from failures in some features of the effective interaction or the reaction mechanism, which are common to the usual DWIA analysis of the (p, p') reactions, rather than from reaction mechanism uncertainties related to the composite nature of the deuteron projectile. It has been suggested that Pauli blocking correction to the isoscalar spin independent central component of the effective interaction is important in obtaining qualitative description of scattering observables for natural parity transitions in the (p, p') reactions in the incident energy range between 100 and 200 MeV [93, 94, 95, 96].

6.2.2 Analyzing Power

The measured vector and tensor analyzing powers for the natural parity transitions in ^{12}C and ^{28}Si are compared with the calculations in Figs. 5.12 and 5.13, respectively. DWIA calculations with the folding dN interaction generally give results which differ only in details from those with the three-body dN interaction. Comparison of PWIA and DWIA curves indicates that the effect of distortion is minor below 15° while it becomes large at larger angles. The A_y data for the 2_1^+ state in ^{12}C and for the 2_1^+ and 3_1^- states in ^{28}Si exhibit weakly oscillating structure, and approach unity at larger angles. By completely missing the oscillation pattern, the DWIA calculations give only qualitative description of A_y data for these states. The A_y angular distributions for the 3_1^- state in ^{12}C and for the 5_1^- state in ^{28}Si exhibit a general trend of positive values at small scattering angles, followed by a decrease towards negative values with increasing scattering angle. In the region beyond 15° somewhat better results could be obtained by the PWIA calculations. For these states the DWIA calculations with the folding dN interaction give better account of the A_y data beyond 15° than those with the three-body dN interaction, indicating the sensitivity to the choice of the effective interaction.

The effect of distortion is not significant for A_{yy} for the natural parity transitions. The DWIA calculations provide reasonable description of the A_{yy} data over the angular range up to 30°.

6.3 Comparison with Data for Unnatural Parity Transition

We then consider unnatural parity transitions to the 1_1^+ and 2_2^- states in ^{12}C and to the 1_2^+ state in ^{28}Si. The excitations of these states are ΔS=1 transitions, which proceed only through the spin-dependent parts of the projectile-nucleon effective interaction. For each transition, calculations were made within PWIA and DWIA frameworks as in the same

Table 6.12: Comparison of theoretical and experimental transition probability for the unnatural parity states in ^{12}C and ^{28}Si. The B(ML$\uparrow$) values are in units of $\mu_N^2\text{fm}^{2L-2}$. The discrepancy in the theoretical and experimental values of B(ML$\uparrow$) for the T=0, 1^+ transition in ^{12}C is most likely due to small isospin mixing between T=0 and T=1 levels [97, 98].

Nucleus	State	E$_x$ (MeV)	B(EL$\uparrow$)$_{\text{th.}}$	B(EL$\uparrow$)$_{\text{exp.}}$
^{12}C	1_1^+	12.7	0.014	0.044±0.006[a]
	2_1^-	18.3	45.5	—
^{28}Si	1_1^+	8.33	0.0079	0.0004±0.0003[b]
	1_2^+	9.50	0.031	0.024±0.010[b]

[a]) Ref. [87].
[b]) Ref. [88].

manner for the natural parity transitions.

The 9.5 MeV peak in ^{28}Si is a doublet state consisting of the 1_2^+(9.50 MeV) and 2_6^+(9.48 MeV) states. In a multipole analysis of the data, following three points were assumed: (1) The angular distribution shape of the 2_6^+ state follows the prediction of a macroscopic DWBA calculation. (2) The strength of the DWBA cross section is determined by using the proportionality relation expected to hold among transition rates for low-lying 2^+ states obtained from the present (d, d') measurement and those obtained from other measurements (see Appendix D for details). (3) The spin observables for the 2_6^+ state are replaced with those for the 2_1^+ state calculated using the wave functions listed in Table 6.5. For the 9.5 MeV double state the calculated cross sections are given by the sum of the individual cross sections, and the polarization observables by the mean weighted by the calculated cross sections.

Table 6.12 summarizes the current information on the electromagnetic transition rates for the unnatural parity states in ^{12}C and ^{28}Si.

6.3.1 Cross Section

The calculated cross sections for the unnatural parity transitions are compared with the data in Fig. 5.14. The calculations are shown without any normalizations. In the cross section figure for the 1_2^+ state in ^{28}Si the estimated contribution from the 2_6^+ state is shown as a dot-dashed line. Comparison of the DWIA (solid) and PWIA (dotted) curves shows that the distortion effects again substantially improve the fit to the cross section angular distributions. Comparison of the solid and dashed lines shows that the three-nucleon correlation has an effect to reduce cross sections near the peak as in the case for

Table 6.13: Calculated and experimental differential cross sections at representative angles for unnatural parity transitions. The normalization factors (N) required for DWIA results with the three-body dN interaction to fit the experimental values are also shown.

Nucleus	State	$\Theta_{c.m.}$ (deg.)	$\frac{d\sigma}{d\Omega})^{Fold}_{th.}$ (mb/sr)	$\frac{d\sigma}{d\Omega})^{3N}_{th.}$ (mb/sr)	$\frac{d\sigma}{d\Omega})_{exp.}$ (mb/sr)	N[a]
^{12}C	1^+_1	5.0	0.91	0.72	0.84	1.17
		10.0	0.41	0.28	0.28	1.01
	2^-_2	8.0	2.81	2.12	2.75	1.30
^{28}Si	1^+_2	5.0	1.52	1.21	1.46	1.21

[a]) N= $\frac{d\sigma}{d\Omega})_{exp.}$ / $\frac{d\sigma}{d\Omega})^{3N}_{th.}$

the natural parity transitions. The DWIA cross sections with the folding and three-body dN interactions at representative angles are shown in the columns 4 and 5 of Table 6.13. We see that the three-nucleon correlation has an effect to reduce DWIA cross sections by $20 \sim 33\%$. It is to be noted that the problem of the cross section overestimation with the folding dN interaction could previously be identified only in the ΔS=0 channel [18], while the present analysis suggests that it persists in the ΔS=1 channel as well.

Due to the strong sensitivity to admixture of the isovector components in the wave functions, the electron scattering is generally of little help to normalize the shell model wave functions for isoscalar spin-flip states. At the representative angles the ratios of the experimental cross sections relative to the DWIA values calculated using the three-body dN interaction are deduced (see column 7 of Table 6.13). It is found that DWIA calculations using the free dN interaction reproduce the cross section data for the spin transitions with normalization factors close to unity.

In the incident energy range between 100 and 200 MeV, the theoretical (p,p') cross sections for the isoscalar spin-flip transition are known to depend sensitively on the choice of the effective interaction. Comfort *et al.* made DWIA analysis for transitions to the 1^+_1 state in ^{12}C excited via the (p,p') reaction at E_p=120 MeV [90] and to the 1^+_1 and 2^-_2 states in ^{12}C at E_p=200 MeV [91]. Their calculations made use of the Love and Franey effective interaction [92], and the same shell model wave functions as employed here. The calculations over-predicted the data by a factor of about 2 at forward angles. Willis *et al.* [99] made DWIA calculations for the 1^+_2 state in ^{28}Si and for the 1^+_1 state in ^{12}C excited via the (p,p') reaction at E_p=200 MeV using the nucleon-nucleon (NN) t-matrix generated directly from the NN phase shifts as the effective interaction, and the same shell model wave functions as employed here. The calculations reproduced the cross section data at forward angles without any normalizations, in agreement with the present

(d, d') analysis.

In the ^{12}C(d, d') study at E_d=400 MeV [29, 42], it has been pointed out that the DWIA cross section using the folding dN interaction for the 1^+ states at 12.71 MeV was larger than the data by about a factor of 1.5 at forward angles. It is interesting to see whether or not the three-body dN interaction at 400 MeV would reduce the DWIA cross section, as in the present 270 MeV case, so that it might in fact come close to the experiment.

The spectroscopic information that is gained from the present comparison of the cross section data with the calculated results using the realistic projectile-nucleon effective interaction is that there is essentially no quenching observed for the isoscalar spin transitions in ^{12}C and ^{28}Si. The result indicates that the Δ-h explanation, which is responsible only for isovector transitions but not for isoscalar transitions, could not be entirely excluded as the quenching mechanism for spin transitions, contrary to the conclusion given in Ref. [48].

In order to further pin down the origin of the quenching mechanism for the $M1$-type transitions, however, it would be important to see whether the strength for the T=1 spin transitions is more quenched than that for the T=0 spin transitions. It is preferable to use the same deuteron induced reaction to reduced systematic uncertainty due to possible reaction mechanism ambiguities. The deuteron charge exchange $(d,^2\mathrm{He})$ reaction has been established as a probe for the T=1 spin transitions [100]. Since the realistic deuteron-nucleon charge exchange amplitudes are available from the three-nucleon Faddeev calculations [31], [3] and the impulse approximation is expected to be applicable, the charge exchange reaction will provide a good way to examine the degree of quenching in the T=1 channel. The advantage of using deuteron induced reactions for the study of quenching for spin transitions is that the reactions often show stringent selectivity in isospin transfer so that they can separate isoscalar and isovector transitions experimentally even for $N \neq Z$ target nuclei, for which the (p, p') reaction can not distinguish between the two types of the transition.

6.3.2 Analyzing Power

The experimental analyzing powers A_y and A_{yy} for the unnatural parity transitions are compared with calculated results in Fig. 5.15. The DWIA calculations with the three-body and folding dN interactions give results which are close to each other. The DWIA calculations well describe the analyzing power data, with a possible exception for A_y below 5° for the 1^+ states where the predictions strongly underestimate the data.

[3] Strictly speaking the current framework of the Faddeev calculations do not take into account the Coulomb interaction in an exact manner above the deuteron break-up threshold. The Coulomb repulsion in the final state di-proton system (^{2}He) in the deuteron-nucleon charge exchange amplitudes must be incorporated in an approximate manner.

The agreement between the data and theory is more satisfactory for the unnatural parity transitions than for the natural parity transitions.

6.4 Single Spin-Flip Probability

6.4.1 Natural Parity Transition

The angular distributions of the single spin-flip probability S_1 for the 2_1^+ state in ^{12}C and for the 3_1^- state in ^{28}Si are compared with calculations in Fig. 5.16. These natural parity states are dominated by the ΔS=0 transition. The S_1 value for the ΔS=0 transition is constrained to be zero within PWIA [79]. Thus the PWIA predictions (dotted lines) of S_1 for these transitions are almost consistent with zero. The DWIA curve (solid line) of S_1 for the 2_1^+ state slightly deviates from zero. For the 3_1^- state, the DWIA curve becomes large at forward angles. These finite DWIA values of S_1 are due to the spin-orbit distortion in the optical potential. We see that the effect of distortion can be somewhat substantial and cannot be entirely ignored. The data are well described by the DWIA calculations.

6.4.2 Unnatural Parity Transition

The experimental angular distributions of S_1 for the 1^+ states in ^{12}C and ^{28}Si are compared with PWIA and DWIA calculations (dotted and solid lines) using the three-body dN interaction in Fig. 5.17. The calculated S_1 values are large at small scattering angles and decreases with increasing scattering angle up to about 10°. The data points at 5.4° and 7.3° are in good agreement with the calculation, while the 3.5° data points are slightly overestimated. It is to be noted that a similar discrepancy has been reported for S_{nn} at forward angles for a transition to the isoscalar 1^+ state in ^{12}C excited via the (p, p') reaction at E_p=397 MeV [8]. The differences between PWIA and DWIA calculations below 10° are relatively small, showing the minor importance of the effects of distortion on S_1 in this angular range. The dot-dashed lines for S_1 in Fig. 5.17 represent theoretical curves corresponding to the transferred orbital, spin and total angular momenta of LSJ = (011), calculated using the impulse approximation amplitudes as give by the relation [79]:

$$S_1 = \frac{2|\epsilon|^2 + 2|\zeta|^2 + 2|\mu|^2 + 2|\nu|^2}{3|\gamma|^2 + 2|\delta|^2 + 2|\epsilon|^2 + 2|\zeta|^2 + |\kappa|^2 + |\lambda|^2 - 3|\psi|^2 + |\mu|^2 + |\nu|^2}, \tag{6.6}$$

where the coefficients $\alpha, ..., \nu$ are defined in Eq.(6.3) and $\psi = (\kappa + \lambda)/3$. This simple IA estimate is seen to produce essentially the same S_1 values below 10° as does the DWIA calculation with the full CK and W wave functions. Thus it seems that the S_1 values for the $\Delta S = 1$ transitions are also insensitive to details of the transition density in this angular region, instead it is mainly determined by the relative strengths of different parts of the dN impulse approximation amplitudes.

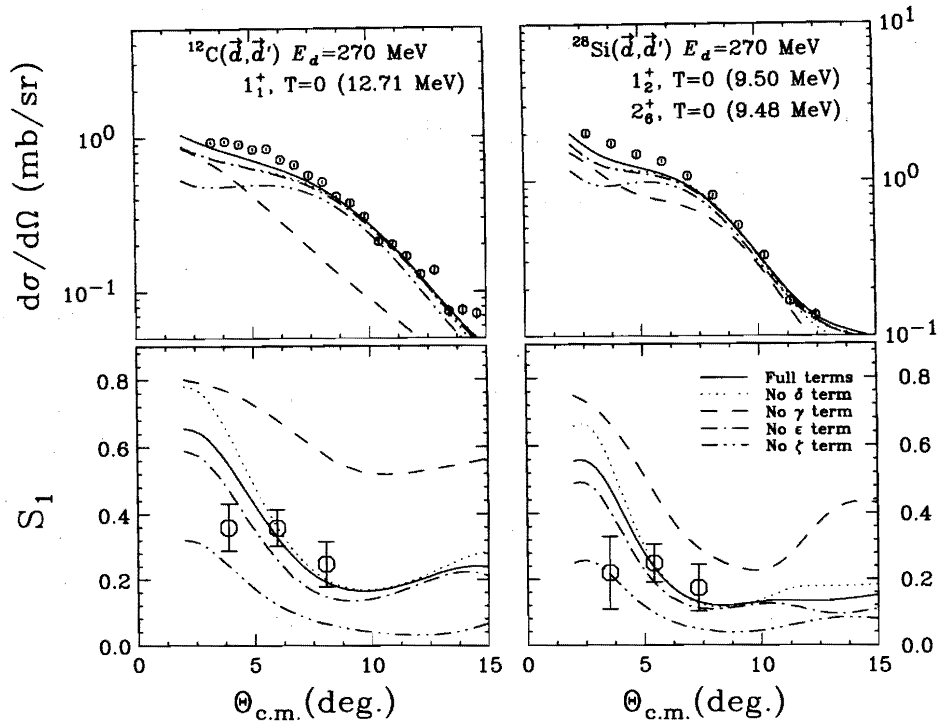

Figure 6.2: The sensitivities of the cross section and spin-flip probability for the 1^+ transitions in ^{12}C and ^{28}Si to various parts of the dN t-matrix interaction.

The contribution of each term in the dN t-matrix interaction to the cross section and S_1 for the 1^+ states in ^{12}C and ^{28}Si is shown in Fig. 6.2. The curves were calculated within DWIA by using the three-body dN interaction. In the cross section, spin-orbit like γ term contributes significantly. Since the γ term produces very small S_1 values, the S_1 curves with no γ term (dashed lines) are enhanced relative to the full interaction (solid lines) by more than a factor of two over most of the angular range. The spin-transverse δ term produces a similar effect to the γ term but to a lesser extent. On the other hand, when the spin-longitudinal ϵ and spin-transverse ζ terms are ignored, the values of S_1 are reduced. When the higher order terms with respect to the spin transfer to the deuteron are neglected (not shown in the figure), the effect is negligible. The contribution from the δ and ϵ terms to S_1 at forward angles are similar in magnitude and are oppositely signed. Therefore S_1 is primarily sensitive to the relative strengths of the γ and ζ terms of the dN interaction. The discrepancy between the data and the prediction at the 3.5° points in both ^{12}C and ^{28}Si nuclei therefore indicates that there might be problems with the momentum transfer dependence of the strengths of the γ term relative to the ζ term, the γ term is too small relative to the ζ term at 3.5°.

In-medium enhancement of the spin-orbit part of the NN interaction has been suggested by Hoffmann *et al.* [101], who by arbitrarily increasing the imaginary spin-orbit term for momentum transfer region below 0.75 fm^{-1} have obtained an improved impulse approximation description of the forward angle analyzing power data for proton elastic scattering at 500 and 800 MeV. Fayache *et al.* [102] have studied the effects of varying various components of a realistic NN interaction on $M1$ transition rates for nuclei in the $0p$ and $1s$-$0d$ shells in large model space structure calculations. For most of the nuclei a much better agreement with the experimental $B(M1)$ rates could be achieved by increasing the strength of the spin-orbit interaction relative to the free value.

6.5 Double Spin-Flip Probability

Figure 5.16 compares the measured angular distributions of the double spin-flip probability S_2 for the 2_1^+ state in ^{12}C and for the 3_1^- state in ^{28}Si with calculated results. The S_2 value for ΔS=0 transition is not constrained to be zero even within PWIA. However, due to the relative unimportance of the double spin-flip components of the projectile-nucleon interaction at low momentum transfer region (See Fig. C.3 for momentum transfer dependence of individual components of the three-body dN t-matrix), PWIA values of S_2 are consistent with zero below 15°. Comparison of PWIA and DWIA curves shows that the effects of distortion are very small in this angular range, leading to the DWIA values of S_2 which are compatible with zero. The data are well described by the calculations.

Figure 5.17 compares the experimental angular distributions of S_2 for the 1^+ states in ^{12}C and ^{28}Si with PWIA and DWIA calculations using the three-body dN interaction. The calculated S_2 values below 15° are consistent with zero in both PWIA and DWIA in agreement with the data.

It is found that for both ΔS=0 and ΔS=1 transitions the predicted S_2 values are consistent with zero below 15° within the present reaction model framework. This indicates that any non-zero S_2 values which would be present in this angular range would have to be explained by a certain reaction mechanism beyond the present one based on the one-step impulse approximation.

Experimentally we observed S_2 values which are close to zero across the excitation energy region below 21 MeV. Since one expects that the double spin-flip strengths are high up in the excitation energy, the present result on S_2 for low excitation energy region may be regarded as an indicator for the reliability of the present measurement and the data reduction procedure. Using the methodology developed and calibrated in this work, experiments in search for the double spin-flip strengths in the high excitation energy region are expected to be performed in the future work.

Chapter 7

Conclusion

The differential cross section and the eight polarization observables concerning the y-axis (i.e. A_y, A_{yy}, $P^{y'}$, $P^{y'y'}$, $K_y^{y'}$, $K_{yy}^{y'}$, $K_y^{y'y'}$, $K_{yy}^{y'y'}$) for the deuteron inelastic scattering on ^{28}Si at E_d=270 MeV have been measured over the target excitation energy range between 4 and 21 MeV and the scattering angular range between $\Theta_{\rm lab}$ =2.5 and 7.5° in the search for isoscalar spin excitation strengths in ^{28}Si. The experiment has been performed by means of the double scattering technique using a deuteron polarimeter DPOL developed at the focal plane of the RIKEN magnetic spectrometer SMART.

The polarimeter system DPOL involves a CH_2 scatterer and a large areal and highly segmented plastic counter hodoscope. The simultaneous measurement of both vector and tensor polarization components is realized by utilizing two nuclear reactions, the $\vec{d}+{}^{12}$C elastic scattering and the ^{1}H$(\vec{d},2p)$ charge exchange reaction. This feature, together with the large acceptance encompassing the focal plane, permits the extraction of all the eight polarization observables as a function of the target excitation energy. In order to extract the unpolarized cross sections and the effective analyzing powers the polarimeter system has been calibrated at three incident deuteron energies, 270, 250 and 230 MeV, prior to the double scattering measurement.

The deuteron single and double spin-flip probabilities S_1 and S_2 in the ^{28}Si$(\vec{d},\vec{d}')$ reaction have been determined from the eight polarization observables. Exhibiting a large S_1 value of about 0.2 for an isoscalar spin-flip 1^+ state know at 9.50 MeV, and small S_1 values of around 0.05 for non-spin-flip states such as the 3^- state at 6.88 MeV, the quantity S_1 is shown to be closely related to the spin-transfer in inelastic deuteron scattering. This confirms the usefulness of S_1 as a signature for isoscalar spin-flip transitions. Relatively large S_1 values of the order of 0.1 have been observed in the excitation energy range between 9.6 and 20 MeV suggesting the presence of isoscalar spin-flip strengths in this region. The S_2 values are close to zero over the measured excitation energies, and no indication has been obtained for the excitation of the double spin-flip transitions such as the double Gamow-Teller state.

In order to look insight into the reaction mechanism for the deuteron inelastic scattering at 270 MeV, the angular distributions of the cross section and analyzing powers A_y and A_{yy} leading to the 0_1^+(ground), 2_1^+(4.44 MeV), 3_1^-(9.64 MeV), 1_1^+(12.71 MeV) and 2_2^-(18.3 MeV) states in ^{12}C and to the 0_1^+(ground), 2_1^+(1.78 MeV), 3_1^-(6.88 MeV), 1_2^+(9.50 MeV) and 5_1^-(9.70 MeV) states in ^{28}Si have been measured. The elastic scattering data are used to extract optical model potential parameters. The data are compared with microscopic DWIA calculations. The calculations utilize the free deuteron-nucleon (dN) t-matrix derived from the three-nucleon Faddeev calculations as the projectile-nucleon effective interaction, and the realistic transition densities. It is found that the DWIA calculations give reasonably good account of the data. Especially for the unnatural parity transitions the cross sections are reproduced by the calculations with normalization factors close to unity, and no notable quenching of the isoscalar spin strengths is found in both ^{12}C and ^{28}Si. In order to identify the effect of correlation among the three nucleons in the projectile-nucleon system, the calculated results are compared to those obtained by using the simple folding dN interaction. It is found that for both natural and unnatural parity transitions the three-nucleon correlation effect reduces the calculated cross sections near the peak by about 20-35%.

The DWIA method is used to interpret the observed spin-flip probabilities S_1 and S_2 for transitions to the 2_1^+ and 1_1^+ states in ^{12}C and to the 3_1^- and 1_2^+ states in ^{28}Si. For the ΔS=0 transitions the small but non-zero values of S_1 can be explained by the effects of distortion due to the optical potential. The sensitivity of S_1 for the 1^+ states to the relative strengths of different parts of the dN effective interaction at low momentum transfer is noted. The S_1 angular distribution data are well reproduced by the DWIA calculations, except for the most forward angle data points where they are overestimated by the calculations. Considering the insensitivity of S_1 at low momentum transfer to the distortion effects and to the transition density, the discrepancy is likely to indicate the inaccuracy in relative strengths of the spin-orbit like γ term and other tensor terms. The S_2 values within the present DWIA calculations are extremely insensitive to distortion effects below $\Theta_{\mathrm{c.m.}} = 15°$, where the calculated values are consistent with zero in agreement with the data.

With the demonstrated availability of the polarization technique, including the polarized beam and the focal plane polarimetry, and the applicability of a DWIA method which can yield quantitative description of scattering observables in a level well compared to that for the (p,p') reactions at similar incident energies per nucleon, the polarization transfer measurement in inelastic deuteron scattering at intermediate energy region provides an important probe of nuclear structure in the isoscalar spin dependent channel.

Acknowledgment

I am much indebted to many people who have given me help and encouragement.

I would like to thank my supervisor, Professor Hideyuki Sakai, who gave me an opportunity to study this interesting field of intermediate energy nuclear spin physics. I could not imagine how much he has been troubled by me, and how much efforts he has made to assist me in studying physics, carrying out experiments, and completing the thesis work. Without his continuous patience, support, encouragement I could not have completed the thesis work.

I am deeply grateful to Professor Hiroyuki Okamura, who has been sincerely concerned about me and gave me countless pieces of advice and comment in the course of the experiment, data analysis and thesis writing.

I must express appreciation to the collaborators of this experiment. First of all, I am especially grateful to Dr. Satoru Ishida, who, as a close senior of mine and a chief designer of the polarimeter which played an important role in the polarization transfer experiment, gave me valuable advice and answered to my numerous questions on the experimental as well as data analysis issues. I thank the members of Sakai group. I am particularly indebted to Prof. H. Okamura, Dr. N. Sakamoto and Dr. T. Uesaka for their excellent operation of the polarized ion source. I must express appreciation to Dr. H. Otsu, Dr. T. Wakasa, Dr. T. Ohnishi, Mr. Nonaka, Mr. G. Yokoyama, Ms. K. Sekiguchi, Mr. K. Yako and Mr. S. Fukusaka for their elaborate assistances in the experiments. I wish also to acknowledge Dr. T. Niizeki, Mr. K. Katoh, Dr. T. Ichihara, Professor K. Hatanaka, Dr. N. Nishimori and Dr. K. S. Itoh for their helpful collaboration of the experiment. I would like to thank Dr. A. Tamii, Mr. S. Sakoda, Mr. K. Suda, Mr. M. Hatano, Mr. H. Kato, Ms. Y. Maeda, and Mr. J. Nishikawa for their help in later part of the experiment.

I am indebted to Dr. H. Kamada for invaluable discussions on the usage of the deuteron-nucleon amplitudes calculated by his group.

I would like to express my appreciation to all the staff members of the RIKEN Accelerator Research Facility, particularly Dr. Y. Yano, Dr. A. Goto and Dr. M. Kase, for their invaluable assistance in making the experiment.

Finally, I would like to thank my family for their continuous encouragement during the course of the study.

Appendix A

Calibration Results of DPOL Polarimeter

The calibration of the focal plane polarimeter DPOL was performed in order to determine the unpolarized cross section and effective analyzing powers of the analyzer reactions before being used in the double scattering experiment. In the calibration experiment direct polarized beams with known polarizations at E_d=270, 250 and 230 MeV, whose polarization axis was set in the y or xz direction in the helicity frame of the polarimeter, was lead onto the the scatterer. The $^1\mathrm{H}(\vec{d}, 2p)$ charge exchange reaction (CE) and the $\vec{d}+^{12}\mathrm{C}$ elastic scattering (EL) were measured. Events of these reactions were classified according to the polar and azimuthal scattering angles. For measurements at 250 and 230 MeV, the beams were energy degraded by letting pass through aluminium plates located at the target position of the spectrometer. The depolarization due to the energy degradation is expected to be negligible small [103]. The derivation of the unpolarized cross section and effective analyzing powers from the stored number of events in the polarimeter is presented along with the obtained results.

A.1 Unpolarized Cross Section and Analyzing Powers

Figure A.1 shows the coordinate system relevant for the calibration of the polarimeter. In the figure θ and ϕ refer to the polar and azimuthal scattering angles, and α and β specify the direction of beam polarization axis of symmetry. Denoting the magnitudes of the vector and tensor polarization of the beam by $(p_y^{(i)}, p_{yy}^{(i)})$, the yield $N_{CE(\mathrm{or}EL)}^{(i)}(\theta, \phi)$ measured in the (θ, ϕ) bin can be expressed as:

$$\begin{aligned} N_{CE(\mathrm{or}EL)}^{(i)}(\theta, \phi) &= \frac{N_{SI}^{(i)}}{RD} \cdot N_{H(\mathrm{or}C)} \cdot \overline{\sigma}(\theta) \cdot D(\theta, \phi) \\ &\times \ \{1 + \sqrt{3}p_y \sin\beta i T_{11}(\theta) \cos(\phi - \alpha) \end{aligned}$$

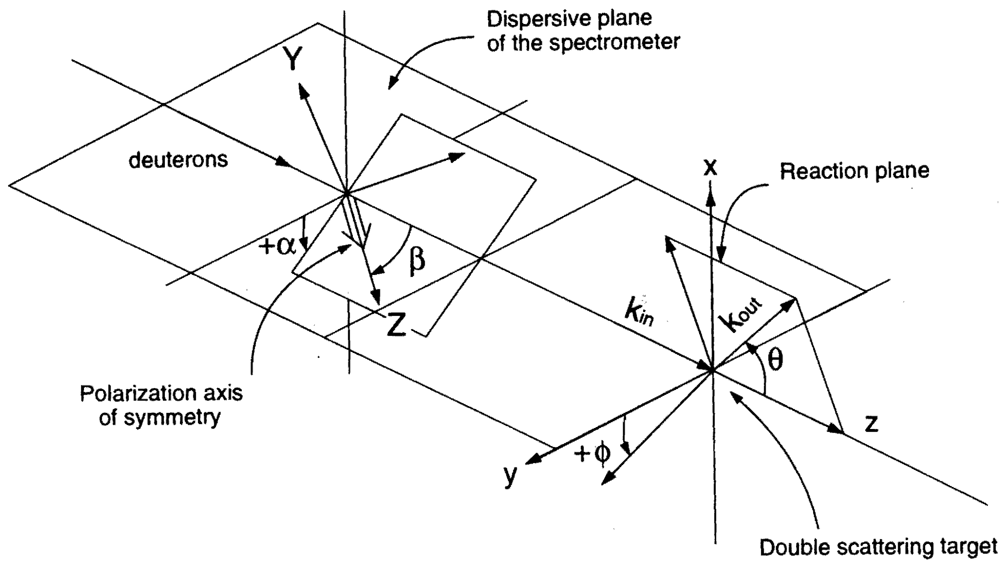

Figure A.1: The direction of the polarization axis of symmetry for deuteron beams incident on the polarimeter are specified by angles α and β. The angles θ and ϕ are the polar and azimuthal scattering angles.

$$\begin{aligned}
&+ \frac{1}{2\sqrt{2}} p_{yy}(3\cos^2\beta - 1)T_{20}(\theta) \\
&- \sqrt{3} p_{yy} \sin\beta\cos\beta T_{21}(\theta)\sin(\phi-\alpha) \\
&- \frac{\sqrt{3}}{2} p_{yy} \sin^2\beta T_{22}(\theta)\cos(2\phi - 2\alpha)\},
\end{aligned} \tag{A.1}$$

where $N_{H(\mathrm{or}C)}$ is the number of target nuclei per unit area in the scatterer, $\overline{\sigma}(\theta)$ is the cross section in a bin specified by the angle θ. D is the local detection efficiency of the polarimeter. The effective analyzing powers are denoted by T_{kq}. The data taking live time factor does not appear in Eq.(A.1). In the measurement of iT_{11}, T_{20} and T_{22} the polarization axis was directed in the y-direction specified by (α,β)=$(0,\frac{\pi}{2})$, while in the measurement of T_{21} it was set in the xz-direction specified by (α,β)=$(\frac{\pi}{2},\frac{3\pi}{4})$. In the latter measurement two spin-states of the beam, #0 and #1, were used.

Given the yield $N^{(i)}_{CE(\mathrm{or}EL)}(\theta,\phi)$ in the polarimeter, the unpolarized cross section is calculated by

$$\frac{\mathrm{d}^2\sigma}{\mathrm{d}t\mathrm{d}\phi}(q)_{\mathrm{eff}} = \frac{N^{(i)}_{CE}(\theta,\phi)\cdot RD}{N^{(i)}_{SI}\cdot N_H \cdot 2q\Delta q \cdot \Delta\phi}. \tag{A.2}$$

for the charge exchange reaction, and

$$\frac{\mathrm{d}\sigma}{\mathrm{d}\Omega}(\theta)_{\text{eff}} = \frac{N_{EL}^{(i)}(\theta,\phi)\cdot RD}{N_{SI}^{(i)}\cdot N_C\cdot\Delta\cos\theta\cdot\Delta\phi}. \tag{A.3}$$

for the elastic scattering.

The effective analyzing powers were determined as follows. Firstly, the ratio of the polarized cross section to the unpolarized cross section was calculated by

$$R^{(i)}(\theta,\phi) = \frac{N_{CE(\text{or}EL)}^{(i)}\cdot N_{SI}^{(0)}}{N_{CE(\text{or}EL)}^{(0)}\cdot N_{SI}^{(i)}}. \tag{A.4}$$

It depends only on the number of counts. Secondly, with this ratio and the known beam polarizations, $p_y^{(i)}$ and $p_{yy}^{(i)}$, the vector R_V and two tensor R_T and R_{T21} asymmetries were constructed using Eq.(A.1)

$$R_V(\theta,\phi) = R^{(2)} - 1 - \frac{p_{yy}^{(2)}}{p_{yy}^{(1)} - p_{yy}^{(3)}}(R^{(1)} - R^{(3)}), \tag{A.5}$$

$$R_T(\theta,\phi) = R^{(1)} - R^{(3)} - \frac{p_y^{(1)} - p_y^{(3)}}{p_y^{(2)}}(R^{(2)} - 1), \tag{A.6}$$

$$\begin{aligned} R_{T21}(\theta,\phi) &= R^{(4)} - 1 + \sqrt{\frac{3}{2}}iT_{11}(\theta)\sin\phi p_y^{(4)} \\ &\quad -\frac{1}{4\sqrt{2}}T_{20}(\theta)p_{yy}^{(4)} - \frac{\sqrt{3}}{4}T_{22}(\theta)p_{yy}^{(4)}\cos 2\phi. \end{aligned} \tag{A.7}$$

Here the fourth spin state #4 is introduced to describe the scattering with beams whose polarization axis in the xz direction. These asymmetries are related to the analyzing powers through:

$$R_V(\theta,\phi) = \sqrt{3}iT_{11}(\theta)p_y^{\text{eff}}\cos\phi, \tag{A.8}$$

$$R_T(\theta,\phi) = -\frac{1}{2\sqrt{2}}T_{20}(\theta)p_{yy}^{\text{eff}} - \frac{\sqrt{3}}{2}T_{22}(\theta)p_{yy}^{\text{eff}}\cos 2\phi, \tag{A.9}$$

$$R_{T21}(\theta,\phi) = -\frac{\sqrt{3}}{2}T_{21}(\theta)p_{yy}^{(4)}\cos\phi, \tag{A.10}$$

with

$$p_y^{\text{eff}} = p_y^{(2)} - \frac{p_{yy}^{(2)}(p_y^{(1)} - p_y^{(3)})}{p_{yy}^{(1)} - p_{yy}^{(3)}}, \tag{A.11}$$

$$p_{yy}^{\text{eff}} = p_{yy}^{(1)} - p_{yy}^{(3)} - \frac{p_{yy}^{(2)}(p_y^{(1)} - p_y^{(3)})}{p_y^{(2)}}. \tag{A.12}$$

Finally, a χ^2 minimization procedure was used to calculate the analyzing powers from Eqs.(A.8)-(A.10) for each θ bin. Typical fitting results are shown in Figs. A.2 and A.3 for the CE reaction and the EL scattering, respectively.

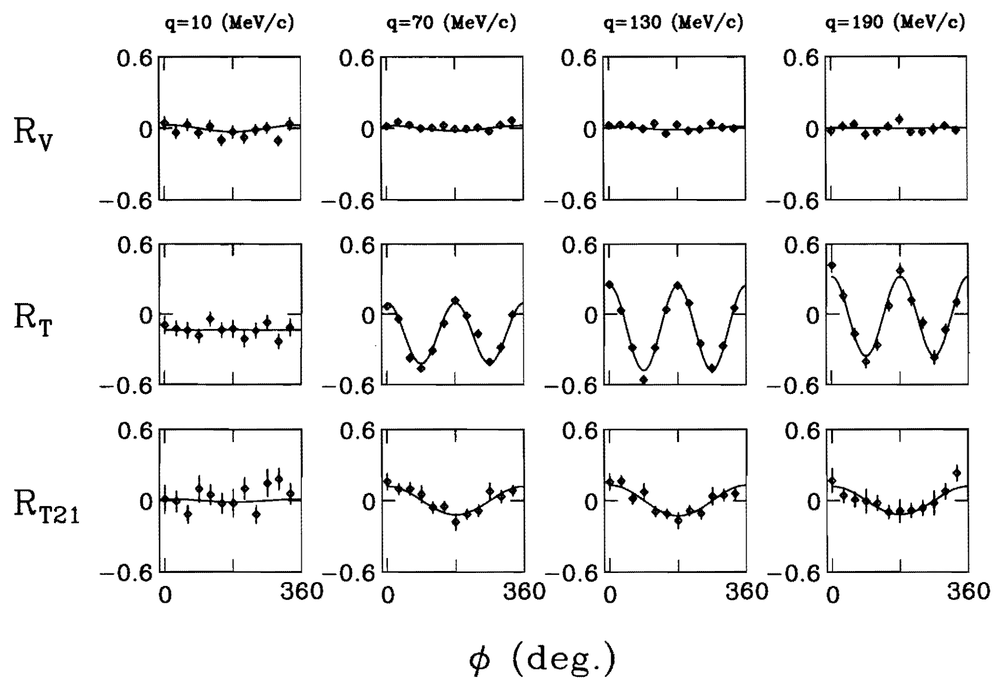

Figure A.2: Typical fitting results of the asymmetries, R_V, R_T and R_{T21}, observed with DPOL for the ^{1}H($\vec{d}$, 2p) reaction at E_d = 270 MeV.

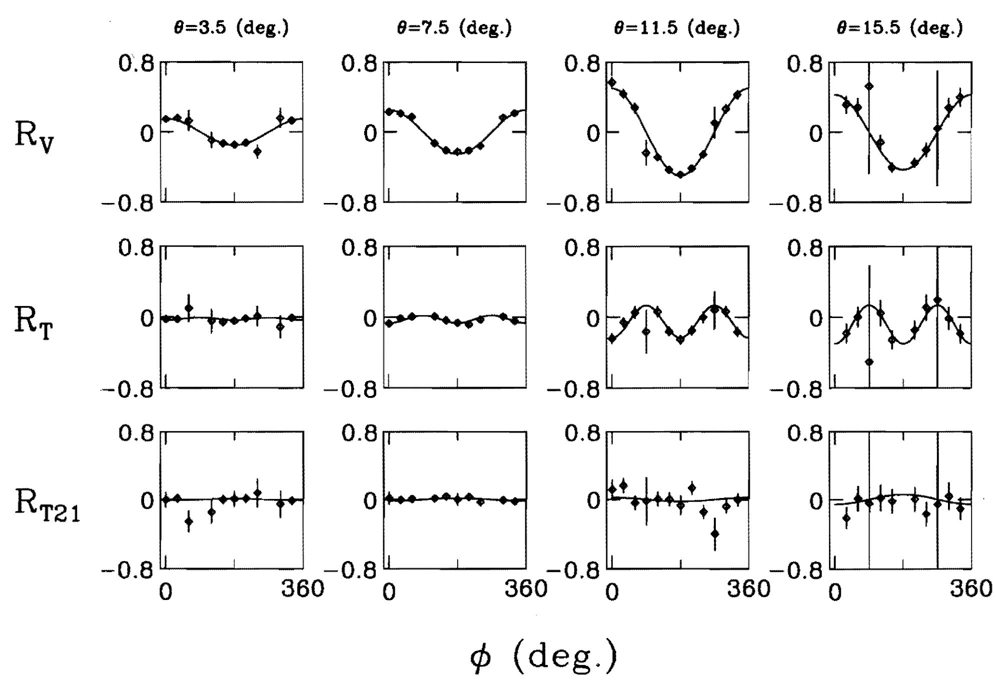

Figure A.3: Typical fitting results of the asymmetries, R_V, R_T and R_{T21}, observed with DPOL for the $\vec{d}$+^{12}C elastic scattering at E_d = 270 MeV.

A.2 Calibration Results

A.2.1 The $^1\mathrm{H}(\vec{d},2p)$ Charge Exchange Reaction

Figures A.4-A.6 shows the experimental results for the CE reaction at the three incident beam energies, 270, 250 and 230 MeV. The results shown are those obtained with a cut on final two proton relative momentum of $k < 0.4\ \mathrm{fm}^{-1}$. Error bars are statistical ones only. The effective cross sections are not corrected for the geometrical detection efficiency. The integrated CE cross section over k up to 0.4 fm^{-1} and q up to 210 MeV/c amounted to 0.31 fm^2 at 270 MeV. The cross section decreases rapidly for q greater that 200 MeV/c. The iT_{11} analyzing power is almost consistent with zero. Large values are obtained for all the tensor analyzing powers T_{20}, T_{21} and T_{22}. The T_{20} analyzing power shows rather flat angular distribution up to 150 MeV/c and crosses zero around 200 MeV/c. The T_{22} and T_{21} analyzing powers are positive below 200 MeV/c. Present data reproduce the general trends of reported analyzing powers for the calibration of POLDER polarimeter [37] based on the same $^1\mathrm{H}(\vec{d},2p)$ reaction.[1]

Solid lines in Figs. A.4-A.6 are predictions of a Monte Carlo simulation using the impulse approximation model of Carbonell *et.al.* [58] and described in Appendix B. The calculation reproduces the experimental cross sections to within a relative error of about ±10% over the q range between 0 and 215 MeV/c and over all the measured incident deuteron energies. The dashed lines in Figs. A.4-A.6 are calculated cross sections without taking account of detection losses caused by finite detector geometry. The ratio of the cross section shown by the solid line (for which geometrical effects are taken into account) to the cross section shown by the dashed line represents the geometrical detection efficiency. The ratio is found to remain at about 0.5 up to q=165 MeV/c at 270 MeV. The analyzing powers are qualitatively well reproduced by the calculations.

Table A.1 summarizes the calibration results for the CE reaction on the efficiency ε, the figure of merit F_{kq} and the average effective analyzing power $\langle T_{kq}\rangle$ defined by the relations,

$$\varepsilon = \frac{\text{number of useful event}}{\text{total number of incident deuterons}} \tag{A.13}$$

$$F_{kq}^2 = \int \varepsilon(\theta,\phi)\cdot T_{kq}^2 \cdot \mathrm{d}\Omega \tag{A.14}$$

$$\langle T_{kq}\rangle = \frac{F_{kq}}{\sqrt{\varepsilon}}. \tag{A.15}$$

[1] The sign of T_{21} analyzing power in Ref. [37] seems to be erroneously reported (See also Ref. [104]).

A.2.2 The $\vec{d}$+^{12}C Elastic Scattering

Figures A.7-A.9 shows the experimental results for the EL scattering at three incident beam energies, 270, 250 and 230 MeV. The main features obtained from the calibration data are the following: the vector analyzing power iT_{11} exhibits positive large values for all the measured incident energies. It becomes almost as large as 0.6 at backward scattering angles around 15°, but it has values exceeding 0.1 even at the smallest angle of 3.5°. The tensor analyzing powers are very small except for T_{22} at 270 MeV at large angles, where negative moderately large values are observed.

Table A.2 summarizes the calibration results on the efficiency ε, the figure of merit F_{kq} and the average effective analyzing power $\langle T_{kq}\rangle$ for the EL scattering. Slight deterioration of the efficiency and corresponding F_{11} values were found for the 230 MeV result. This was partly due to the present somewhat inadequate setting of the iron absorber thickness (13.5 mm), which was too thick to allow all the elastically scattered deuterons to pass through the absorber at 230 MeV. Therefore data on the 230 MeV beam energy are shown only for reference purpose.

A.3 Summary of the Calibration

In summary, a calibration experiment was performed in the deuteron energy range between 230 and 270 MeV. It confirmed large vector analyzing power iT_{11} for the $\vec{d}$+^{12}C elastic scattering, and large tensor analyzing powers T_{20}, T_{21} and T_{22} for the ^{1}H($\vec{d}$, 2p) reaction. By using these reactions for polarimetry the polarimeter DPOL can be used as a vector and tensor polarimeter. Angular distributions of these analyzing powers and the unpolarized cross sections (or efficiency) were determined from the calibration experiment.

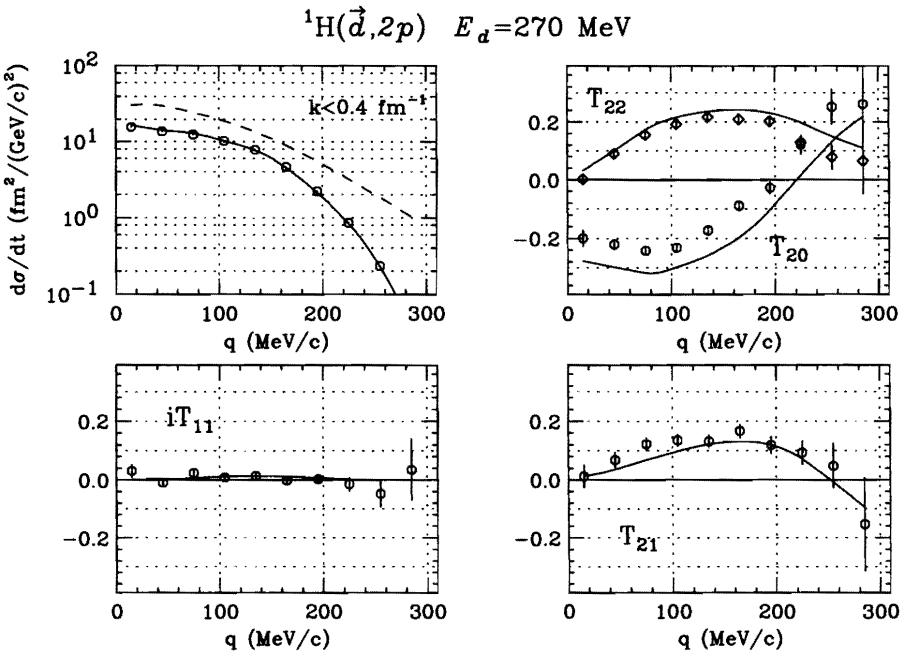

Figure A.4: Effective unpolarized cross section and spherical analyzing powers for the ^{1}H($\vec{d}$, 2p) reaction measured with DPOL at 270 MeV. The range in relative momentum of the final two protons is $k = 0 - 0.4$ fm^{-1}. The solid lines represent the Monte Carlo predictions, which is based on the impulse approximation (IA) model [58], and takes into account full geometry of the detector system. The dashed line is the same prediction but without taking into account the effect of detection loss due to the finite detector geometry.

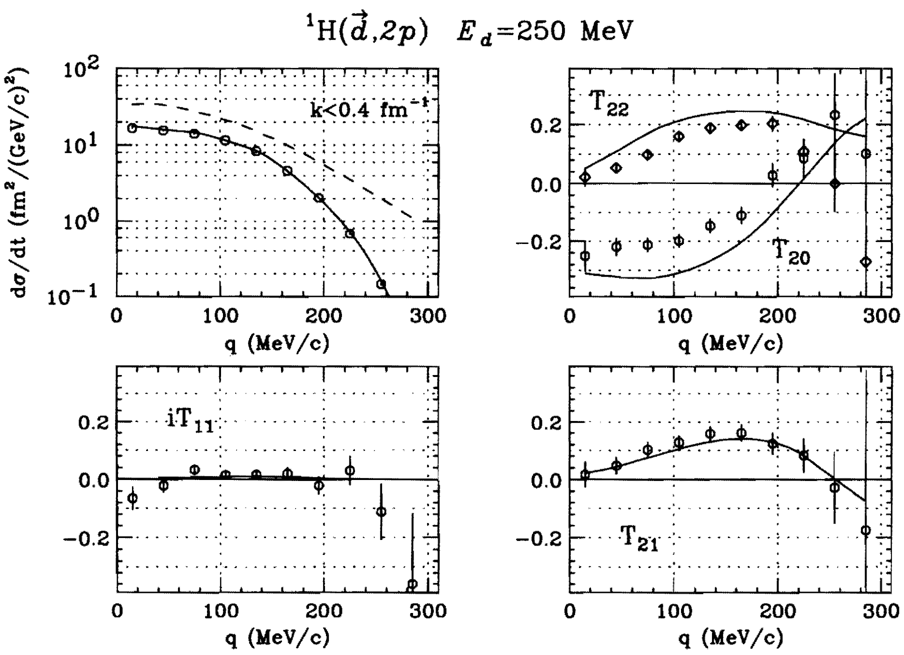

Figure A.5: Same as Fig. A.4 but at 250 MeV.

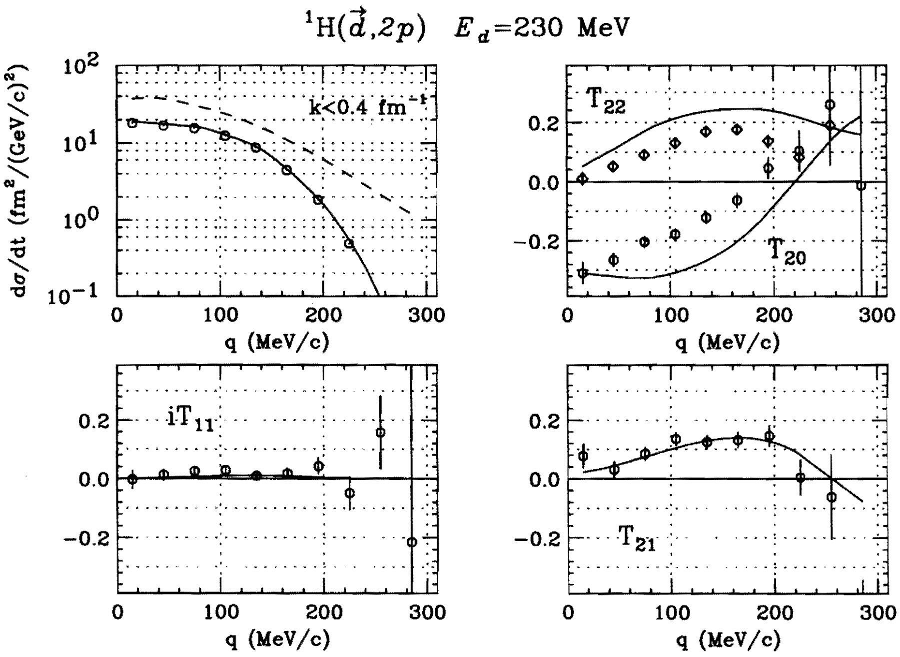

Figure A.6: Same as Fig. A.4 but at 230 MeV.

Table A.1: Summary of the DPOL calibration experiment for the ${}^1\mathrm{H}(\vec{d}, 2p)$ reaction. The range in relative momentum of the final two protons is $k = 0 - 0.4$ fm^{-1}.

E_d (MeV)	ε (%)	F_{11} $\times 10^{-3}$	F_{20} $\times 10^{-3}$	F_{21} $\times 10^{-3}$	F_{22} $\times 10^{-3}$	$\langle T_{11}\rangle$	$\langle T_{20}\rangle$	$\langle T_{21}\rangle$	$\langle T_{22}\rangle$
270	0.082	0.44	5.47	3.58	5.11	0.02	0.19	0.13	0.18
250	0.087	0.60	5.38	3.64	4.46	0.02	0.18	0.12	0.15
230	0.090	0.57	5.50	3.67	3.98	0.02	0.18	0.12	0.13

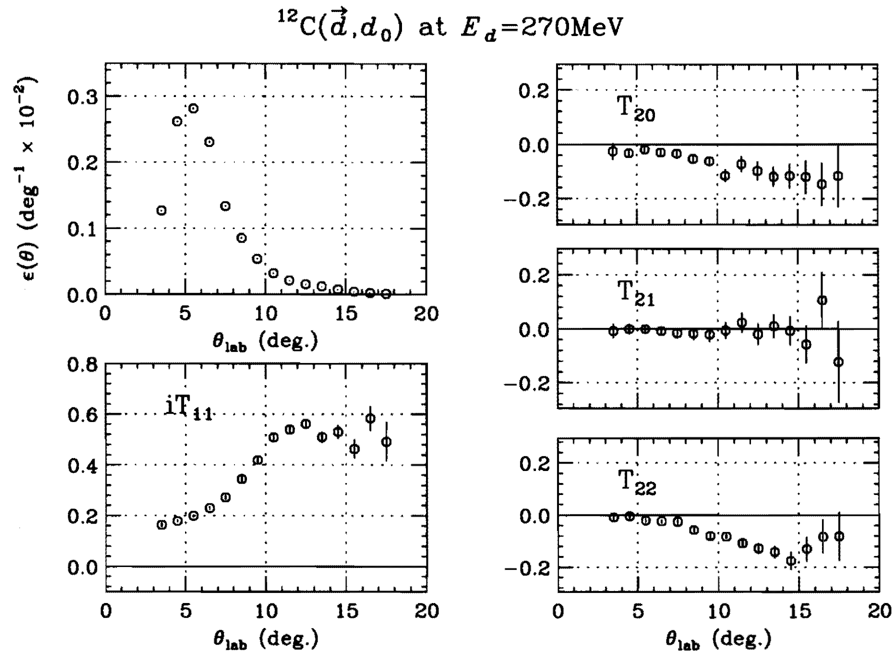

Figure A.7: Unpolarized efficiency ε and spherical analyzing powers for the $\vec{d}$+^{12}C elastic scattering measured with DPOL polarimeter at 270 MeV.

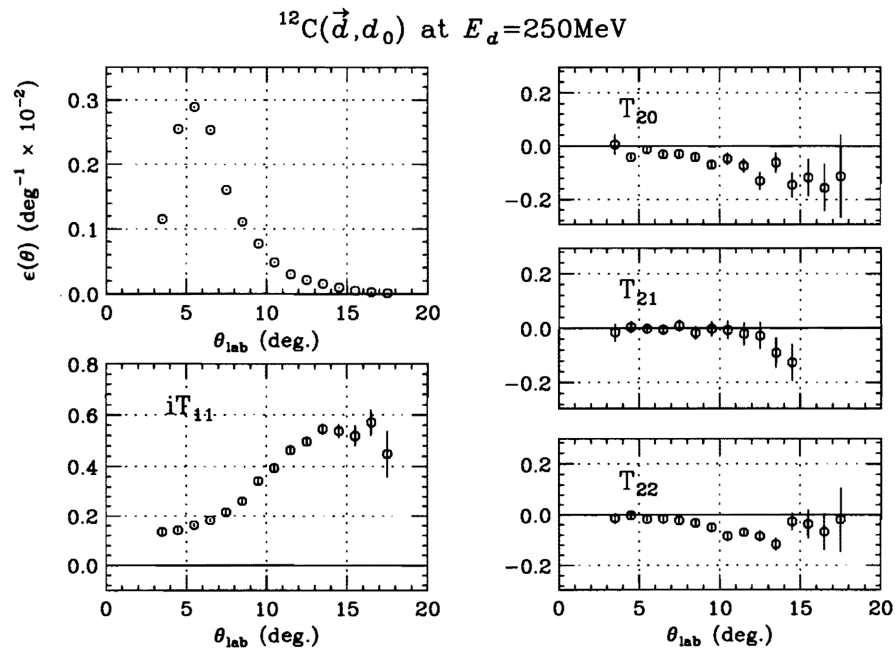

Figure A.8: Same as Fig. A.7 but at 250 MeV.

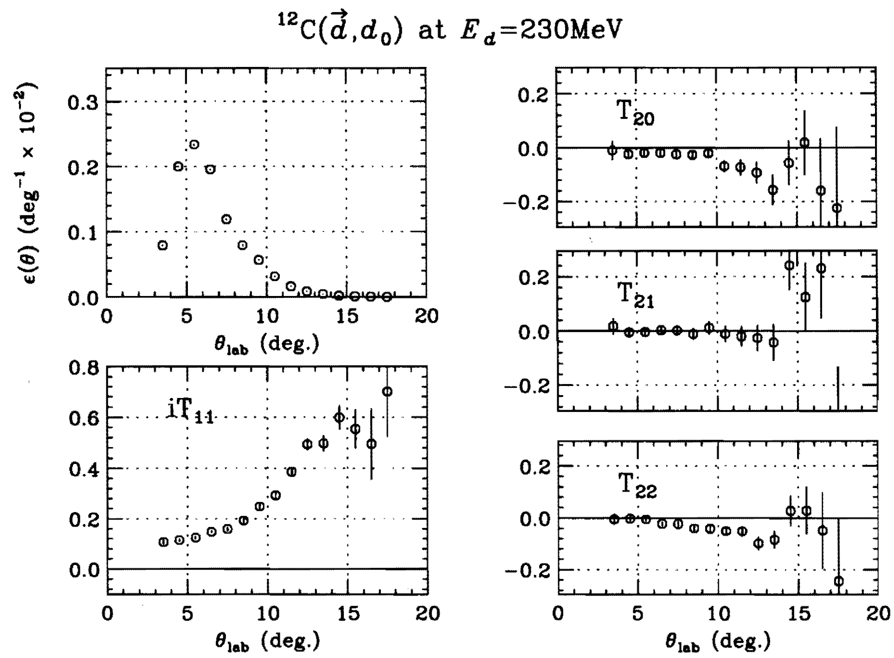

Figure A.9: Same as Fig. A.7 but at 230 MeV.

Table A.2: Summary of the DPOL calibration experiment for the $\vec{d}$+^{12}C Elastic Scattering.

E_d (MeV)	ε (%)	F_{11} $\times 10^{-2}$	F_{20} $\times 10^{-3}$	F_{21} $\times 10^{-3}$	F_{22} $\times 10^{-3}$	$\langle T_{11}\rangle$	$\langle T_{20}\rangle$	$\langle T_{21}\rangle$	$\langle T_{22}\rangle$
270	1.20	2.94	4.86	1.62	4.41	0.27	0.04	0.02	0.04
250	1.33	2.71	4.63	1.99	3.82	0.24	0.04	0.02	0.03
230	1.00	1.73	2.89	1.62	2.65	0.17	0.03	0.02	0.03

Appendix B

Monte Carlo Simulation of the ^{1}H$(d, 2p)$ Reaction

A Monte Carlo simulation program was written to simulate unpolarized cross section for the ^{1}H$(d, 2p)$ reaction. The program was used in the data analysis to correct for various effects which arise from possible differences in beam geometry between the calibration and double scattering experiments. The ability for the Monte Carlo simulation to reproduce experimental differential cross sections provides a test of the computer code and our knowledge on the polarimeter response. After a brief description of the physics model used to calculate the cross section for the ^{1}H$(d, 2p)$ reaction, and of the simulation formalism, the experimental distributions with respect to the momentum transfer q and the di-proton relative momentum k are compared with theoretical ones.

B.1 The PWIA Model and Calculation Scheme

The plane wave impulse approximation (PWIA) model of Carbonell [58] was used to calculate five dimensional differential cross sections, $\frac{\mathrm{d}^5\sigma}{\mathrm{d}t\mathrm{d}^3k\mathrm{d}\phi}$, for the ^{1}H$(d, 2p)$ reaction. In this model the impulse approximation amplitude is evaluated in the Breit frame (see Fig. B.1), where the average of the initial and final nucleon momenta is perpendicular to the momentum transfer. The scattering amplitude is given by

$$F^{\mathrm{PWIA}}_{dp\to(pp)n} = \langle \Psi^{(-)S}_{pp,k}\chi_n | f^{\mathrm{ce}} \mathrm{e}^{\mathrm{i}\frac{1}{2}\vec{q}\cdot\vec{r}} | \Phi_d \chi_p \rangle. \tag{B.1}$$

Here $\Psi^{(-)S}_{pp,k}(\vec{r})$ describes the outgoing pp wave function with relative momentum $2\boldsymbol{k}$ and total spin S (=0 or 1). $\Phi_d(\vec{r})$ is the initial deuteron wave function. The nucleon-nucleon (NN) charge exchange amplitude f^{ce} is given in the NN Breit frame by

$$f^{\mathrm{ce}} = \alpha - i\gamma_1\sigma_{1n} - i\gamma_3\sigma_{3n} + \beta\sigma_{1n}\sigma_{3n} + \delta\sigma_{1q}\sigma_{3q} + \varepsilon\sigma_{1p}\sigma_{3p}, \tag{B.2}$$

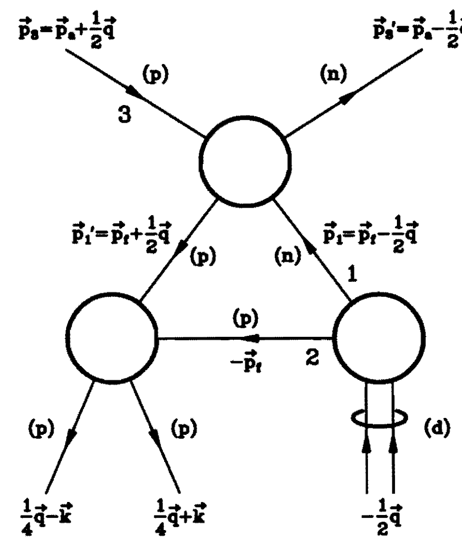

Figure B.1: Impulse approximation diagram of the ^{1}H(d, 2p) reaction, indicating the particle identification and kinematics in the deuteron Breit frame. The nucleon-nucleon change exchange amplitude is evaluated at p_f=0.

where σ is the Pauli matrix and unit vectors are given by $\hat{q}//\vec{p}_3 - \vec{p}'_3$, $\hat{n}//\vec{p}_3 \times \vec{p}'_3$ and $\hat{p} = \hat{n} \times \hat{q}$. The amplitude is normalized as

$$\frac{\mathrm{d}\sigma}{\mathrm{d}t} = \frac{1}{4}\mathrm{Tr}\{f^{\mathrm{ce}} f^{\mathrm{ce}\dagger}\} = |\alpha|^2 + |\beta|^2 + |\gamma_1|^2 + |\gamma_3|^2 + |\delta|^2 + |\varepsilon|^2. \tag{B.3}$$

In the present calculation, the pp wave function was generated using the Reid soft core NN potential [105] with Coulomb force. The total angular momenta of the pp system up to J =2 were taken into account. Both S and D-state components of the deuteron wave function were incorporated using the Paris parameterization [106]. The Fermi motion of a nucleon in the deuteron was neglected. The NN charge exchange amplitude in the Breit frame was obtained from that in the NN center of mass (c.m.) frame at the same invariant energy $\sqrt{s}$, by making a Lorentz boost along the average momentum of the initial and final nucleon. The Wigner rotation in the spinor space [107, 108] was also taken into account, although it produced only minor effects at E_d=270 MeV. The NN c.m. amplitude was the SM97 solution of Arndt [109] extracted from the phase shift analysis program SAID [110]. The cross section and analyzing powers are given by

$$\begin{aligned} \frac{\mathrm{d}^5\sigma}{\mathrm{d}t\mathrm{d}^3k\mathrm{d}\phi} &= \frac{1}{6}\frac{1}{2\pi}\mathrm{Tr}\{FF^\dagger\}, && \text{(B.4)} \\ T_{kq} &= \mathrm{Tr}\{F\Omega_{kq}F^\dagger\}/\mathrm{Tr}\{FF^\dagger\}, && \text{(B.5)} \end{aligned}$$

where Ω_{kq} are deuteron spin operators (see Appendix C). In the present case where there is no information on polarizations concerning final protons, the $S = 0$ (spin singlet) and $S = 1$ (spin triplet) amplitudes in Eq.(B.1) contribute incoherently to the cross section and polarization observables.

Given a theoretical differential cross section, $\frac{\mathrm{d}^5\sigma}{\mathrm{d}t\mathrm{d}^3k\mathrm{d}\phi}$, Metropolis Monte Carlo integration [111] is used to evaluate the integral:

$$\int \frac{\mathrm{d}^5\sigma}{\mathrm{d}t\mathrm{d}^3k\mathrm{d}\phi} \times I_{\mathrm{Beam}} \times I_{\mathrm{Hodo}} \mathrm{d}f_i \mathrm{d}f_f, \tag{B.6}$$

where I_{Beam} represents the constraint imposed on the integral over the initial phase space by the beam spread in direction, position and energy at the secondary target. The correlation between position and angle within the dispersive plane was taken into account. I_{Hodo} represents the restriction imposed on the integral over the final phase space by the polarimeter counter hodoscope. The position and timing resolution of the hodoscope was taken into account. In addition, effects such as energy loss, multiple scattering and energy straggling in the analyzer target, air, window and counter material were also taken into account, as well as the reaction loss in the analyzer target, which was incorporated assuming the following values for the total and elastic cross sections, $\sigma^{\mathrm{tot}}_{d+\mathrm{C}}$=760 mb, $\sigma^{\mathrm{tot}}_{d+p}$=85 mb and $\sigma^{\mathrm{el}}_{d+\mathrm{C}}$=140 mb. The simulation was performed separately for each excitation energy and scattering angle bin (E_x, Θ) of the primary scattering.

B.2 Comparison with Experiment

Figure B.2 compares data on k-distribution, $(\frac{\mathrm{d}\sigma}{\mathrm{d}k})$, obtained at incident deuteron energies E_d of 270, 250 and 230 MeV (shown by open circle) with the calculations. The solid histograms represent simulation results obtained with full $2p$ wave functions, while the dot dashed histograms results obtained with only the triplet final states in the di-proton system. In both calculations full detector geometry was incorporated. It is seen that the full calculations give a good account of the experimental incident energy and relative momentum k dependence without introducing any artificial normalizations. It is also clearly seen that the singlet final states dominate the spectra at small k, while the triplet final states become important as k increases. Since deuteron tensor polarizations for the triplet final states are oppositely signed to those for singlet final states [54], it was preferable to reduce contributions from the triplet final states so as not to deteriorate tensor signals. This was done by selecting events having k values less than 0.4 fm^{-1} as indicated in Fig. B.2. The uncertainty in k at k=0.4 fm^{-1} is estimated to be about 0.05 fm^{-1} in FWHM from the simulation.

Figure B.3 compares data on q-distribution, $(\frac{d\sigma}{dq})$, at E_d= 270, 250 and 230 MeV (shown by open circle) with the calculations. The solid and dashed histograms represent simulated results with and without the constraint on the final phase space due to the detector geometry, respectively. The dot dashed histograms show contributions from triplet final states in the di-proton system (with full detector geometry). The $2p$ relative momentum was restricted below 0.4 fm^{-1} with a cut on the k distribution (see Fig. B.2). The experimental differential cross sections are well reproduced by the solid histograms in both shape and magnitude over all the incident deuteron energies. The experimental cross section at the smallest q bin, where contributions of other parasitic reactions are expected to be small, increased as decreasing the incident deuteron energy, the value at E_d=230 MeV was 16.9 % larger than that at E_d=270 MeV. The increase in the theoretical cross section at the corresponding q bin between E_d=270 MeV and 230 MeV was 13.1 %, in reasonable agreement with the experiment. This shows that the energy dependence of the theoretical cross section is adequately evaluated in the present calculation. The dot dashed histograms show that contributions from triplet final states in the $2p$ system can not be neglected at all. It is of particular importance to reproduce the experimental q-distribution by the simulation, because the polarization response due to the t_{20} component manifests itself in changes in the measured q-distribution. The ratio of the experimental cross section to the calculated one was found to have a tendency to increase with q by at most 15 % in the q range of 0-210 MeV/c. Considering the situation that the ^{12}C$(d,2p)$ reaction could not be entirely eliminated with the cut applied on the neutron missing mass spectrum, and that it kinematically overlaps with the ^{1}H$(d,2p)$ reaction at large q, this rise in the ratio at large q may be attributed primarily to the detection of two protons from ^{12}C in the analyzer target. In order to account for such contributions, the simulated unpolarized cross section was multiplied by the ratio interpolated with respect to q and E_d.

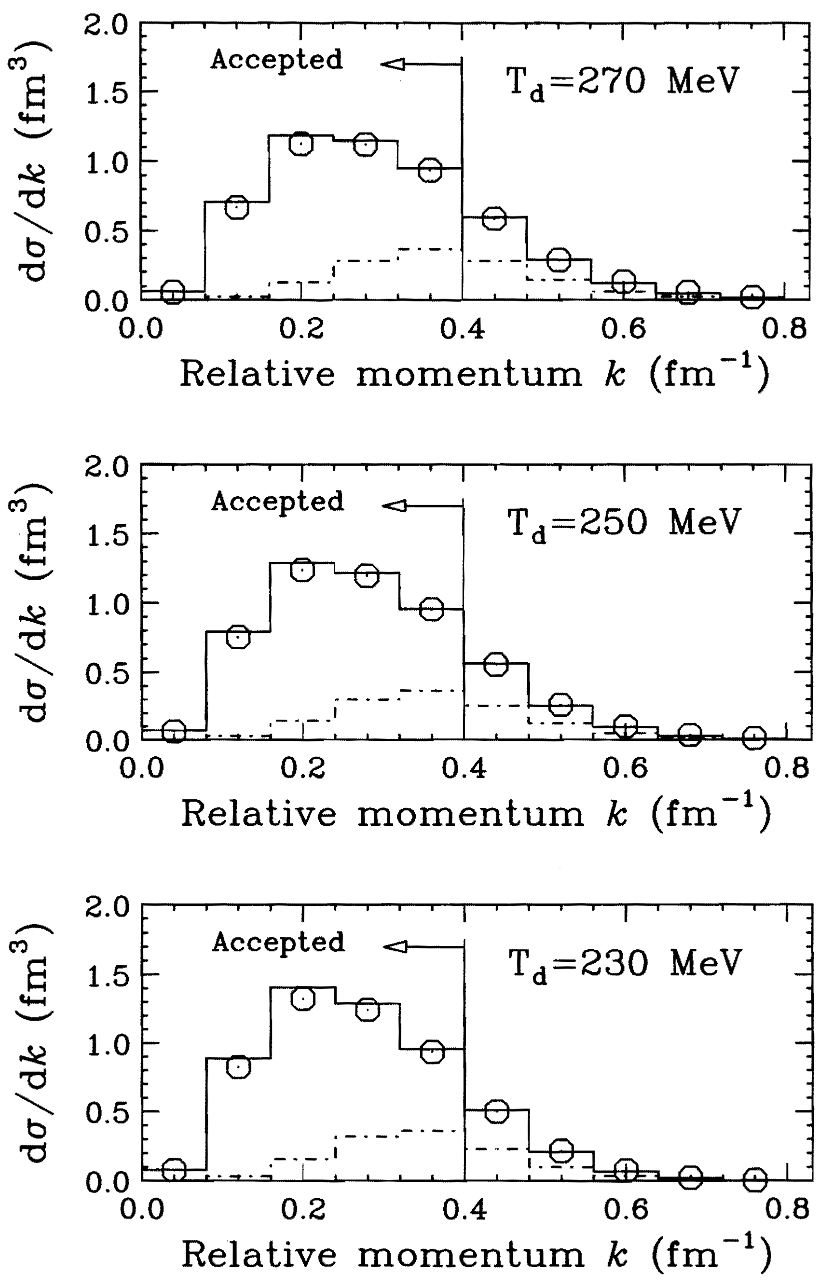

Figure B.2: The measured differential cross section $\frac{d\sigma}{dk}$ in the $^1\mathrm{H}(d,2p)$ reaction at E_d= 270, 250 and 230 MeV is plotted versus k and is shown by the open circles. The solid histograms represent simulation results obtained with full $2p$ wave functions, while the dot dashed histograms results with triplet final states in the di-proton system. Full detector geometry is incorporated in both calculations.

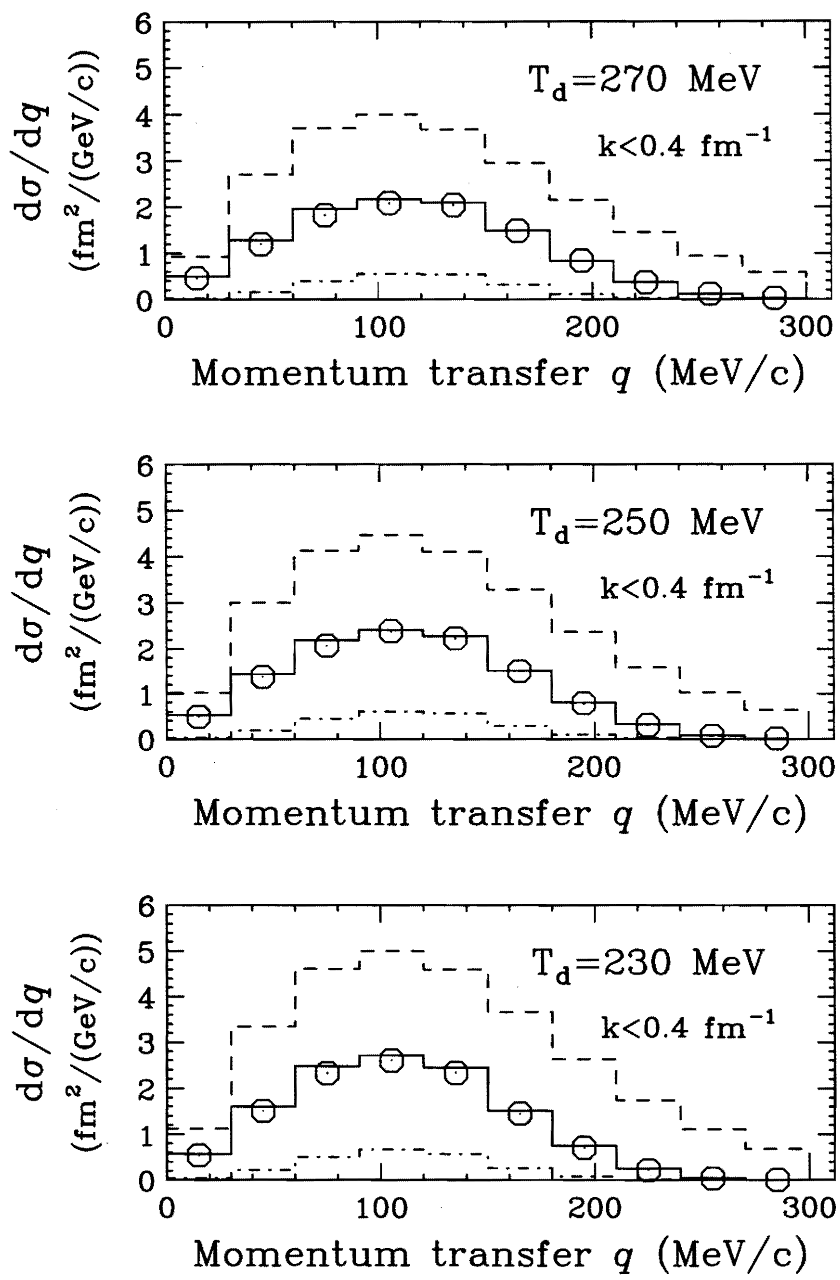

Figure B.3: The measured differential cross section $\frac{d\sigma}{dq}$ for the ^{1}H(d, 2p) reaction at E_d= 270, 250 and 230 MeV is plotted versus q and is shown by the open circles. The solid and dashed histograms are the Monte Carlo predictions taking into account and neglecting the polarimeter detector geometry, respectively. The dot dashed histograms show contributions from triplet final states in the di-proton system, obtained with the Monte Carlo simulation taking account of full detector geometry. The 2p relative momentum k is restricted below 0.4 fm^{-1}.

Appendix C

Distorted Wave Impulse Approximation Model

A microscopic distorted wave impulse approximation (DWIA) model for the deuteron-nucleus scattering is presented. It is based on a model recently proposed by Wiele *et al.* [29], in which the deuteron-nucleus (dA) scattering matrix is constructed by making a double folding of the free nucleon-nucleon (NN) t-matrix with the target transition density and with the deuteron ground state density (folding model dN t-matrix). However, considering the recent availability of rigorous three-nucleon Faddeev calculations at intermediate energy region [31], which yield more precise deuteron-nucleon (dN) t-matrix than the folding one (three-body dN t-matrix), it was felt advantageous to construct the dA scattering matrix by starting from the general form of the deuteron-nucleon scattering matrix. The model of Wiele *et al.* [29] was modified accordingly and presented in section C.1. The model is primarily based on the following assumptions:

1. The kinetic energy of the incident deuteron is much higher than the binding energy of the struck nucleon in the nucleus so that the collision between these particles is approximately the same as the collision between two free particles.

2. The deuteron makes a single collision with the target, and two step processes involving more than one nucleon in the target are not considered. This does not necessarily exclude the situation in which two nucleons in the deuteron interact with a single nucleon in the target.

A description of making the folding and three-body dN t-matrices are given in section C.2, where contributions of individual components of the dN t-matrices to the $d+p$ elastic cross section at E_d=270 MeV are presented. The relationship between the Cartesian and spherical representations of the dN t-matrix is also presented.

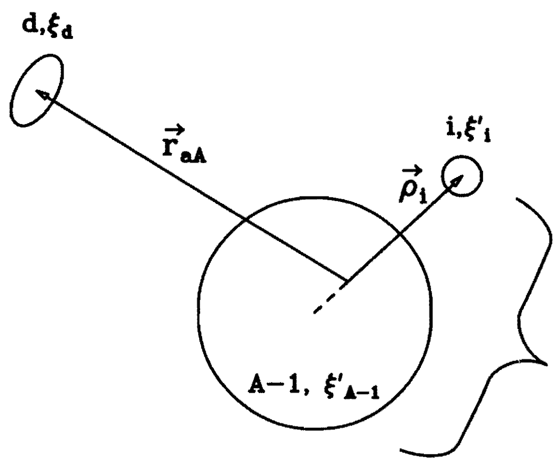

Figure C.1: Various coordinates used to describe the deuteron-nucleus scattering within DWIA. The relative distance between the center of mass of the target nucleus and the projectile deuteron is denotes by $\vec{r}_{aA}$, the position of the i-th single nucleon from the nucleus center of mass by $\vec{\rho}_i$. The spin variables of the deuteron, the i-th single particle and the core nucleus (A-1) are denoted as ξ_d, ξ'_i and ξ'_{A-1}, respectively.

C.1 The DWIA T-matrix

The dA T-matrix is given within DWIA [29, 74, 75, 76, 77] by

$$\begin{aligned}
T_{M_B m_b M_A m_a} &= \langle X^{(-)}(\vec{R})\chi_{d'}\Phi_{A^*}(\vec{\rho})|t_{dN}(q)e^{i\vec{q}\cdot(\vec{\rho}-\vec{R})}|X^{(+)}(\vec{R})\chi_d\Phi_A(\vec{\rho})\rangle \\
&= \mathcal{N}\mathcal{K}\sum_{i=1}^{A}\sum_{m'_a m'_b}\int d^3\vec{\rho}_i d^3\vec{r}_{aA} d\xi'_{A-1} d^3\vec{q} d\xi'_i d\xi_d \\
&\times\ X^{(-)*}_{m_b m'_b}(\vec{k}_b,\vec{r}_{aA})\mathcal{X}^{m'_b *}_{S_d}(\xi_d)\Psi^{M_B M_{T_B}*}_{J_B T_B}(\xi'_{A-1},\vec{\rho}_i,\xi'_i) \\
&\times\ M_{dN}(q)\exp(-i\vec{q}\cdot(\vec{r}_{aA}-\vec{\rho}_i)) \\
&\times\ \mathcal{X}^{m'_a}_{S_d}(\xi_d)\Psi^{M_A M_{T_A}}_{J_A T_A}(\xi'_{A-1},\vec{\rho}_i,\xi'_i)X^{(+)}_{m_a m'_a}(\vec{k}_a,\vec{r}_{aA}),
\end{aligned} \tag{C.1}$$

where the distorted waves in the initial and final channels are denoted by $X_a^{(+)}$ and $X_b^{(-)}$, the target wave functions by Ψ_A and Ψ_B, and the deuteron spinors by $\mathcal{X}_a$ and $\mathcal{X}_b$, respectively. $\vec{q} = \vec{k}_a - \vec{k}_b$ is the momentum transfer, where $\vec{k}_a$ and $\vec{k}_b$ represent the incident and outgoing deuteron momenta. The spin and spatial coordinates of relevant particles are shown in Fig. C.1. The projectile-nucleon effective interaction is taken to be the on-shell dN t-matrix t_{dN} (see Eqn. 6.3). The dN t-matrix is related to the dN scattering amplitude M_{dN} by

$$t_{dN}(q) = \mathcal{N} M_{dN}(q), \tag{C.2}$$

with

$$\mathcal{N} = -\frac{(\hbar c)^2}{(2\pi)^2}\frac{E_d^c + E_N^c}{E_d^c E_N^c}, \tag{C.3}$$

where E_d^c and E_N^c are the total energies of colliding deuteron and nucleon in their center of mass frame, respectively. The dN t-matrix can be expressed in terms of the deuteron and nucleon spin operators in spherical basis Ω_λ and $\sigma_{\lambda'}$ as

$$t_{dN}(q) = \sum_{\substack{\lambda\lambda' \\ \nu\nu'}} e_{\nu\nu'}^{\lambda\lambda'}(q)\Omega_\lambda^\nu \sigma_{\lambda'}^{\nu'}, \tag{C.4}$$

where λ (λ') represents the magnitude of spin transferred to the projectile (target nucleon), and ν (ν') its projection onto a certain quantization axis (z-axis). Coefficients $e_{\nu\nu'}^{\lambda\lambda'}$ are related with $\alpha, \ldots$ in Eq.(6.3) as described in subsection C.2.4. The factor $\mathcal{K}$ in Eq.(C.1) accounts for the mass-number-dependent kinematic effect [92, 112]. This is given by

$$\mathcal{K} = \frac{(M_d^2 + M_A^2 + 2E_d M_A)(M_d^2 + E_d M_N)(M_N + E_d)}{(M_d^2 + M_N^2 + 2E_d M_N)(M_d^2 + E_d M_A)(M_A + E_d)}, \tag{C.5}$$

where E_d refers to the laboratory deuteron total energy, M_d, M_N and M_A the deuteron, nucleon and target masses, respectively.

By choosing the z-axis along the incident beam direction, the initial and final distorted waves are written as [113]

$$\begin{aligned} \chi_{m_a m_a'}^{(+)}(\vec{k}_a, \vec{r}_{aA}) &= \frac{4\pi}{k_a r_{aA}} \frac{1}{\sqrt{4\pi}} \sum_{j_a L_a M_{La}} i^{L_a} \hat{L}_a \chi_{j_a L_a S_d}(k_a, r_{aA}) Y_{L_a}^{M'_{La}}(\hat{r}_{aA}) \\ &\quad \times \langle L_a 0 S_d m_a | j_a m_{j_a}\rangle \langle L_a M'_{L_a} S_d m'_a | j_a m_{j_a}\rangle \delta_{M_{La}0}, \qquad \text{(C.6)} \\ \chi_{m_b m_b'}^{(-)*}(\vec{k}_b, \vec{r}_{aA}) &= \frac{4\pi}{k_b r_{aA}} \sum_{j_b L_b M_{Lb}} i^{-L_b} \chi_{j_b L_b S_d}(k_b, r_{aA}) Y_{L_b}^{M_{Lb}}(\hat{k}_b) Y_{L_b}^{M'_{Lb}*}(\hat{r}_{aA}) \\ &\quad \times \langle L_b M_{L_b} S_d m_b | j_b m_{j_b}\rangle \langle L_b M'_{L_b} S_d m'_b | j_b m_{j_b}\rangle, \qquad \text{(C.7)} \end{aligned}$$

where $\hat{L} = \sqrt{2L+1}$. The time reversal invariance relates initial and final distorted waves as

$$\chi_{mm'}^{(-)*}(\vec{k}, \vec{r}) = (-1)^{m'-m} \chi_{-m,-m'}^{(+)}(-\vec{k}, \vec{r}). \tag{C.8}$$

Without distortion effects, the distorted waves become plane waves as follows

$$\chi_{mm'}^{(\pm)}(\vec{k}, \vec{r}) = \exp(i\vec{k}\cdot\vec{r})\delta_{mm'}. \tag{C.9}$$

The integration over the nuclear coordinates in Eq.(C.1) can be performed with the aid of Reyleigh's formula [114]

$$\exp(i\vec{q}\cdot\vec{\rho}_i) = 4\pi \sum_{l'm'} i^{l'} j_{l'}(q\rho_i) Y_{l'm'}^*(\hat{q}) Y_{l'm'}(\hat{\rho}_i), \tag{C.10}$$

to obtain

$$\begin{aligned}
&\sum_{i=1}^{A}\int \mathrm{d}^3\vec{\rho}_i \mathrm{d}\xi'_{A-1}\mathrm{d}\xi'_i \Psi_{J_BT_B}^{M_BM_{T_B}*}\sigma_{\lambda'}^{\nu'}\exp(i\vec{q}\cdot\vec{\rho}_i)\Psi_{J_AT_A}^{M_AM_{T_A}} \\
&= 4\pi\sum_{l'm'}\sum_{j_cm_c} Y^*_{l'm'}(\vec{q})\langle l'm'\lambda'\nu'|j_cm_c\rangle\langle J_AM_Aj_cm_c|J_BM_B\rangle \\
&\times \langle T_AM_{T_A}00|T_BM_{T_B}\rangle \mathcal{J}_{l'\lambda'j_c}(q). \qquad (C.11)
\end{aligned}$$

Here $\mathcal{J}_{l'\lambda'j_c}(q)$ is the Fourier transform of the nuclear transition density defined by

$$\mathcal{J}_{l'\lambda'j_c}(q) = i^{l'}\frac{1}{\hat{J}_B\hat{T}_B}\sum_i\langle\Psi_{J_BT_B}|||j_{l'}(q\rho_i)\left[Y_{l'}\otimes\sigma^{\lambda'}\right]_{j_c}\tau_0|||\Psi_{J_AT_A}\rangle, \qquad (C.12)$$

where l' and j_c are the orbital and total angular momenta transferred to the target. The reduced matrix element convention is that of Edmonds [115]. In the general case where the nuclear wave functions are written in the particle-hole (ph) formalism [116] the transition density $\mathcal{J}_{l'\lambda'j_c}(q)$ can be expanded as

$$\begin{aligned}
\mathcal{J}_{l'\lambda'j_c}(q) &= \sum_{j_{\rm part}j_{\rm hole}} i^{l_{\rm hole}-l'-l_{\rm part}}\frac{1}{\sqrt{\pi}}\frac{\hat{j}_{\rm part}\hat{j}_{\rm hole}\hat{j}_c\hat{l}'\hat{l}_{\rm hole}\hat{\lambda}'}{\hat{J}_B\hat{T}_B}\langle l_{\rm hole}0l'0|l_{\rm part}0\rangle \\
&\times S^{j_c}_{t,m_t}(j_{\rm part},j_{\rm hole}) \\
&\times \begin{Bmatrix} l_{\rm part} & l_{\rm hole} & l' \\ \frac{1}{2} & \frac{1}{2} & \lambda' \\ j_{\rm part} & j_{\rm hole} & j_c \end{Bmatrix} \\
&\times \int_0^\infty \rho^2 j_{l'}(q\rho_i)\mathcal{R}_{n_{\rm part}l_{\rm part}j_{\rm part}}(\rho)\mathcal{R}_{n_{\rm hole}l_{\rm hole}j_{\rm hole}}(\rho)\mathrm{d}\rho \\
&\times G_{\rm cm}(q). \qquad (C.13)
\end{aligned}$$

Here the spectroscopic amplitude $S^{j_c}_{t,m_t}(j_{\rm part},j_{\rm hole})$ is given by

$$S^{j_c}_{t,m_t}(j_{\rm part},j_{\rm hole}) = \frac{1}{\hat{j}_c\hat{t}}\langle\Psi_{J_BT_B}|||\left[a^\dagger_{j_{\rm part}1/2}\otimes\tilde{a}_{j_{\rm hole}1/2}\right]_{j_c,t=0}|||\Psi_{J_AT_A}\rangle, \qquad (C.14)$$

where $a^\dagger_{jm,1/2v}$ is the particle creation operator and $\tilde{a}_{jm,1/2v}$ $(= (-1)^{j+m+1/2+v}a_{j-m,1/2-v})$ is the adjoint of the annihilation operator $a_{jm,1/2v}$. The spherical harmonics function Y_l associated with the nuclear wave function is assumed to be carrying a phase factor i^l. The function $\mathcal{R}(\rho)$ in Eq.(C.13) represents the single-particle radial wave function with ρ being the single particle radial coordinate. In the present application it was normalized to be positive at infinity. In the case where the shell model wave functions are employed as the nuclear wave functions, the radial coordinate is usually given as that measured from the center of the potential well, i.e. the wave functions do not have their center of mass motion removed, while the transition density is to be calculated using the radial coordinate ρ measured from the center of mass of the nucleus. In order to correct for the center of mass motion the factor $G_{\mathrm{cm}}(q)$ is introduced in Eq.(C.13). For a harmonic oscillator well this is given by [117]

$$G_{\mathrm{cm}}(q) = \exp(q^2 b^2/4A), \tag{C.15}$$

where A is the mass number, and $b(=\sqrt{\hbar/M_p\omega})$ the oscillator length parameter where M_p denotes the proton mass and $\hbar\omega$ the energy quantum of the harmonic oscillator.

Using the plane wave expansion

$$\exp(-i\vec{q}\cdot\vec{r}_{aA}) = 4\pi \sum_{L_{tr}M_{tr}} (-i)^{L_{tr}} j_{L_{tr}}(qr_{aA}) Y^*_{L_{tr}M_{tr}}(\hat{q}) Y_{L_{tr}M_{tr}}(\hat{r}_{aA}), \tag{C.16}$$

and inserting Eqs.(C.4), (C.6), (C.7) and (C.11) into Eq.(C.1), angular integrations on $\vec{r}_{aA}$ and $\vec{q}$ are carried out to yield the deuteron-nucleus T-matrix:

$$\begin{aligned}
T_{M_B m_b M_A m_a} &= 4\pi\mathcal{K} \sum_{j_a L_a} \sum_{j_b L_b} \sum_{\substack{l'm' \\ j_c m_c}} \sum_{L_{tr} M_{L_{tr}}} \sum_{j_{tr}} \sum_{\substack{\lambda\lambda' \\ \nu\nu'}} \delta_{l',L_{tr}} \delta_{m',-M_{L_{tr}}} \\
&\times \langle J_A M_A j_c m_c | J_B M_B \rangle \delta_{T_A T_B} \delta_{M_{T_A} M_{T_B}} i^{L_a - L_b - L_{tr}} \\
&\times \langle L_a 0 S_d m_a | j_a m_{j_a} \rangle \langle L_b M_{L_b} S_d m_b | j_b m_{j_b} \rangle Y_{L_b}^{M_{L_b}}(\hat{k}_b) \\
&\times \hat{L}_{tr} \hat{L}_b \hat{j}_a \hat{L}_a \hat{S}_d \hat{j}^2_{tr} \langle L_b 0 L_{tr} 0 | L_a 0 \rangle \\
&\times \begin{Bmatrix} L_a & L_{tr} & L_b \\ S_d & \lambda & S_d \\ j_a & j_{tr} & j_b \end{Bmatrix} \langle L_{tr} M_{L_{tr}} j_{tr} m_{j_{tr}} | \lambda\nu \rangle \\
&\times \langle j_a m_{j_a} j_{tr} m_{j_{tr}} | j_b m_{j_b} \rangle \\
&\times (-1)^{L_{tr} + j_{tr} - \lambda} \langle l'm'\lambda'\nu' | j_c m_c \rangle \\
&\times \frac{(4\pi)^2}{k_a k_b} \int \mathrm{d}r_{aA} \chi_{j_b L_b S_d}(k_b, r_{aA}) \chi_{j_a L_a S_d}(k_a, r_{aA}) \\
&\times \int q^2 j_{L_{tr}}(qr_{aA}) e^{\lambda\lambda'}_{\nu\nu'}(q) \mathcal{J}_{l'\lambda' j_c}(q) \mathrm{d}q.
\end{aligned} \tag{C.17}$$

By choosing $\vec{k}_a \times \vec{k}_b$ as y-axis (z-axis is along $\vec{k}_a$ as noted above), we have

$$Y_{L_b}^{M_{L_b}}(\hat{k}_b) = \frac{\hat{L}_b}{4\pi} \sqrt{\frac{(L_b - |M_{L_b}|)!}{(L_b + |M_{L_b}|)!}} P_{L_b}^{|M_{L_b}|}(\cos\Theta) \times \begin{cases} (-1)^{M_{L_b}} & M_{L_b} \geq 0 \\ 1 & M_{L_b} < 0, \end{cases} \tag{C.18}$$

where Θ is the center of mass scattering angle.

Starting from the 0^+ target the residual nucleus necessarily has $J_B = j_c$. In this case the natural parity transition ($\Delta\pi = (-1)^{j_c}$) is mediated with an angular momentum transfer value of $l' = j_c$ while two spin transfers to the target of $\lambda' = 0$ and 1 are allowed, except for the $0^+ \rightarrow 0^+$ transition for which no spin transfer is allowed. On the other hand the unnatural parity transition ($\Delta\pi = (-1)^{j_c+1}$) necessarily involves spin transfer of $\lambda' = 1$ with two possible l' values, $l' = j_c - 1$ and $l' = j_c + 1$, except for the $0^+ \rightarrow 0^-$ transition for which only $l' = j_c + 1$ is allowed.

C.2 The dN t-matrix Interactions

C.2.1 Folding dN t-matrix

In the folding model the dN t-matrix is given by

$$\begin{aligned} t^{\text{folding}}_{dN\ \mu_b m_b \mu_a m_a} &= \mathcal{N}_{NN}\mathcal{K}_{NN}\langle \Phi_d \chi_N | f^{\text{IS}} e^{i\frac{1}{2}\vec{q}\cdot\vec{r}} | \Phi_d \chi_N \rangle, \\ &= \mathcal{N}_{NN}\mathcal{K}_{NN} \int d^3r d\xi_d d\xi_N \Phi^{m_b *}_{S_d}(\vec{r}, \xi_d) \chi^{\mu_b}_N(\xi_N) \\ &\times\ f^{\text{IS}} e^{i\frac{1}{2}\vec{q}\cdot\vec{r}} \Phi^{m_a}_{S_d}(\vec{r}, \xi_d) \chi^{\mu_a}_N(\xi_N), \end{aligned} \tag{C.19}$$

with $\mathcal{N}_{NN} = -2(\hbar c)^2/(2\pi)^2 E_c$ where E_c is the total energy of the nucleon in the NN center of mass system, χ_N the nucleon spinor and $\vec{q} = \vec{k}_{\text{in}} - \vec{k}_{\text{out}}$ the momentum transfer, where $\vec{k}_{\text{in}}$ and $\vec{k}_{\text{out}}$ are the incident and outgoing momenta of the deuteron in the dN center of mass system. $f^{\text{IS}} = 3/4 f_1 + 1/4 f_0$ is the isoscalar nucleon-nucleon (NN) scattering amplitude, where f_1 and f_0 represent isospin triplet and singlet NN scattering amplitudes, respectively. The deuteron wave function Φ_d is written by

$$\Phi^m_{S_d}(\vec{r}, \xi_d) = \sum_{L=0,2} i^L U_L(r) \left[Y_L(\hat{r}) \otimes \mathcal{X}_1(\xi_d) \right]^m_{S_d} \mathcal{X}^0_0(\xi_d), \tag{C.20}$$

where $\mathcal{X}_1$ and $\mathcal{X}_0$ refer to the spin and isospin spinors, respectively. The radial wave function $U_L(r)$ consists of S-state ($L = 0$) and D-state ($L = 2$) components, which can be expresses using the U and W radial wave functions [106] by

$$U_0(r) = U(r)/r, \qquad U_2(r) = -W(r)/r. \tag{C.21}$$

The factor $\mathcal{K}_{NN}$ accounts for the mass-number-dependent kinematic effect [92, 112]. It is given by

$$\mathcal{K}_{NN} = \frac{(M_d^2 + M_N^2 + 2E_d M_N)(2M_N + T_N)}{(M_N + E_d)(M_d^2 + E_d M_N)}. \tag{C.22}$$

where E_d refers to the laboratory deuteron total energy, M_d and M_N the deuteron and nucleon masses and T_N the nucleon laboratory kinetic energy for the NN scattering. The dN t-matrix in Eq.(C.19) can be expanded as follows

$$\begin{aligned} t^{\text{folding}}_{dN\ \mu_b m_b \mu_a m_a} &= \mathcal{K}_{NN} \sum_{\substack{\lambda\lambda' \\ \nu\nu'}} \sum_{lm} \sum_{j_p m_p} 4\sqrt{\pi}(-1)^{\lambda + j_p} \hat{j}_p \hat{l} \hat{S}_d \hat{\lambda} \hat{\lambda}' S'(\lambda S_d; 00) \\ &\times\ \langle S_d m_a j_p m_{jp} | S_d m_b \rangle \langle l m \lambda \nu | j_p m_{jp} \rangle \langle \frac{1}{2}\mu_a \lambda' \nu' | \frac{1}{2}\mu_b \rangle \\ &\times\ \sum_{LL'} i^{L-L'-l} \hat{L} \langle L0l0 | L'0 \rangle \begin{Bmatrix} L' & l & L \\ 1 & \lambda & 1 \\ S_d & j_p & S_d \end{Bmatrix} \\ &\times\ d^{\lambda\lambda'}_{\nu\nu'}(q) Y^{m*}_l(\hat{q}) \int U_{L'}(r) U_L(r) j_l(\frac{1}{2}qr) r^2 dr, \end{aligned} \tag{C.23}$$

where $l\lambda j_p$ refer to the orbital, spin and total angular momenta transferred to the deuteron, λ' the transferred spin to the target nucleon. $d^{\lambda\lambda'}_{\nu\nu'}(q)$ refer to the spherical components of the NN t-matrix. [1] Using the reduced matrix element in the convention of Edmonds [115], the projectile spectroscopic amplitude $S'(ss_a;tt_a)$ [118] is defined by

$$S'(ss_a;tt_a) \quad = \quad \hat{s}^{-1}\hat{t}^{-1}\langle \mathcal{X}_{s_a}\mathcal{X}_{t_a}||| \left[a^{\frac{1}{2}\frac{1}{2}\dagger} \otimes \tilde{a}^{\frac{1}{2}\frac{1}{2}}\right]^{st} |||\mathcal{X}_{s_a}\mathcal{X}_{t_a}\rangle, \tag{C.24}$$

where st refer to the transferred spin and isospin to the projectile and $s_a t_a$ the projectile spin and isospin, respectively. For the assumption of S-wave deuteron, we have

$$S'(\lambda S_d;00) \quad = \quad \begin{cases} \sqrt{3} & \text{for} \quad \lambda=0 \\ \sqrt{2} & \text{for} \quad \lambda=1. \end{cases} \tag{C.25}$$

By choosing $\vec{k}_{\text{in}}$ as z-axis, and $\vec{k}_{\text{in}} \times \vec{k}_{\text{out}}$ as y-axis, we have

$$Y_l^{m*}(\hat{q}) = \frac{\hat{l}}{4\pi}\sqrt{\frac{(l-|m|)!}{(l+|m|)!}}P_l^{|m|}(\cos\chi) \times \begin{cases} (-1)^m & m \geq 0 \\ 1 & m < 0, \end{cases} \tag{C.26}$$

where $\chi = \frac{\theta}{2} - \frac{\pi}{2}$ with θ being the center of mass scattering angle. The CD-Bonn potential [80] was used to calculate f^{IS} at half the incident deuteron energy and the deuteron wave function Φ_d.

C.2.2 Three-body dN t-matrix

The three-body dN t-matrix was obtained by solving the three-nucleon ($3N$) Faddeev equation as given in Ref. [31] at E_d=270 MeV. [2] The multiple scattering series for three nucleons interacting through pairwise forces and propagating freely in between is summed up into the Faddeev equation for a T operator given by

$$T = tP + tPG_0T. \tag{C.27}$$

Equation (C.27) is solved numerically for any given NN force which generates the two-nucleon off-shell t-matrix, t. G_0 is the $3N$ free propagator. The identity of the nucleons is accounted for by the permutation operator P whose two parts, a cyclic and an anti-cyclic permutation, are responsible for the respective exchanges of the nucleons. The matrix elements of $(1+P)T$ between the incoming and outgoing states $|\phi\rangle$, which is composed of the deuteron wave function and the momentum eigenstate of the free nucleon-deuteron motion, give the three-body dN t-matrix, t^{Faddeev}_{dN}. The total angular momenta of the two nucleon system up to j=5 were taken into account. The CD-Bonn potential [80] was used for the NN interaction.

[1] The coefficients $d^{\lambda\lambda'}_{\nu\nu'}(q)$ in Eq.(C.23) are $\mathcal{N}_{NN}$ times those in Ref. [29]

[2] The three-body dN amplitudes are provided by Dr. Kamada.

C.2.3 Comparison with Experiment

Given the dN t-matrix, t_{dN}, the cross section and analyzing powers were calculated using the formulae,

$$\frac{d\sigma}{d\Omega} = \frac{1}{6}\frac{(2\pi)^4}{(\hbar c)^4}(\frac{E_d^c E_N^c}{E_d^c + E_N^c})^2 \mathrm{Tr}\{t_{dN}t_{dN}^\dagger\}, \quad (C.28)$$

$$T_{kq} = \mathrm{Tr}\{t_{dN}\Omega_{kq}t_{dN}^\dagger\}/\mathrm{Tr}\{t_{dN}t_{dN}^\dagger\}, \quad (C.29)$$

where Ω_{kq} are the deuteron spin operators (see Appendix C), E_d^c and E_N^c refer to the total energies of the deuteron and the nucleon in their center of mass system.

Figure 1.1 presents the $\vec{d}+p$ elastic scattering data at E_d=270 MeV on $\frac{d\sigma}{d\Omega}$, A_y, A_{yy}, A_{xx} and A_{xz} [32, 33] as a function of the scattering angle $\Theta_{\text{c.m.}}$ (shown by open circles). The solid lines represent the theoretical curves base on t_{dN} derived from the Faddeev calculations. Good agreement is found between the data and the calculations for all observables almost on the entire angular range. The dashed lines represent the results of the folding model calculations. In this model the calculations could be performed up to $\Theta_{\text{c.m.}}$=95° (q_{max}=2.52 fm^{-1}), where the on-shell NN amplitudes f^{IS} are known. One can see that the folding model prediction overestimates the experimental cross section. For instance, the calculated value is about 1.5 times larger than the experimental one at $\Theta_{\text{c.m.}}$=50°. This cross section overestimation with the folding dN interaction confirms the finding reported in Ref. [18]. Below $\Theta_{\text{c.m.}}$=50° calculated analyzing powers using the folding model agree well with the Faddeev calculations, whereas a serious discrepancy is observed beyond this angle. Such a deviation as well as the cross section overestimation with the folding model may be related to various processes, such as the multiple scattering, rearrangement and deuteron break-up, neglected in the folding model. The three-body dN t-matrix, which includes these $3N$ correlations, removes reaction mechanism ambiguities as far as the "elementary" $d+N$ scattering is concerned. Thus it should provides a more realistic projectile-nucleon effective interaction in the DWIA description of the deuteron-nucleus (dA) scattering processes.

It would be instructive to examine individual contributions of the dN t-matrix components to the cross section separately. These are illustrated as a function of the momentum transfer q in Figs. C.2 and C.3 respectively for the folding and three-body dN t-matrices, separately for the $\lambda' = 0$ and $\lambda' = 1$ channels (λ' is the transferred spin to the target nucleon). Also shown in these figures are the d+p cross section data at E_d=270 MeV [32, 33]. In the $\lambda' = 0$ channel one notable feature is the strong dominance of the α term at low q. Contribution from this term decreases rapidly with q producing a minimum near $q = 1.9$ fm^{-1}, which is more prominently seen in Fig. C.3. The minimum may be related to the onset of the short-range repulsion in the NN interaction[30]. At this minimum and beyond relative importance of the other terms increases in Fig. C.3. In the $\lambda' = 1$ channel the γ term has the strongest contribution at $q \sim 0.8$ fm^{-1}, although contributions from the δ, ϵ and ζ terms can also be important. Comparison of Figs. C.2 and C.3 shows that these terms are influenced differently by the $3N$ correlation. For instance, the forward values of the α, β, γ and ζ terms are damped by the correlation, while the δ and ϵ terms are enhanced. The second order terms in the deuteron spin operators (double spin-flip terms) are totally enhanced in both spin channels.

C.2.4 The dN t-matrix in the Madison Convention

The spherical representation of the dN t-matrix in the deuteron-nucleus (dA) center of mass system, needed in the DWIA framework given in Appendix C, is presented below. The rotation of spinor due to the boost of reference frame is ignored. Following the Madison conventions [119] the z-axis is taken to be parallel to $\vec{k}_{\rm in}$, the y-axis parallel to $\vec{k}_{\rm in} \times \vec{k}_{\rm out}$ and the x-axis to form a right-handed coordinate system, where vectors $\vec{k}_{\rm in}$ and $\vec{k}_{\rm out}$ refer to incident and outgoing beam momenta in the dA center of mass system. The dN t-matrix referring to the dA center of mass system can be written as

$$\begin{aligned}
t_{dN}(q) &= \alpha + \beta S_y + \gamma\sigma_y + \delta S_y\sigma_y \\
&+ \epsilon[-\cos\frac{\theta}{2}S_x + \sin\frac{\theta}{2}S_z][-\cos\frac{\theta}{2}\sigma_x + \sin\frac{\theta}{2}\sigma_z] \\
&+ \zeta[\sin\frac{\theta}{2}S_x + \cos\frac{\theta}{2}S_z][\sin\frac{\theta}{2}\sigma_x + \cos\frac{\theta}{2}\sigma_z] \\
&+ \eta[\cos^2\frac{\theta}{2}Q_{xx} - 2\sin\frac{\theta}{2}\cos\frac{\theta}{2}Q_{xz} + \sin^2\frac{\theta}{2}Q_{zz}] \\
&+ \xi[\sin^2\frac{\theta}{2}Q_{xx} + 2\sin\frac{\theta}{2}\cos\frac{\theta}{2}Q_{xz} + \cos^2\frac{\theta}{2}Q_{zz}] \\
&+ \kappa[\cos^2\frac{\theta}{2}Q_{xx} - 2\sin\frac{\theta}{2}\cos\frac{\theta}{2}Q_{xz} + \sin^2\frac{\theta}{2}Q_{zz}]\sigma_y \\
&+ \lambda[\sin^2\frac{\theta}{2}Q_{xx} + 2\sin\frac{\theta}{2}\cos\frac{\theta}{2}Q_{xz} + \cos^2\frac{\theta}{2}Q_{zz}]\sigma_y \\
&+ \mu[-\cos\frac{\theta}{2}Q_{yx} + \sin\frac{\theta}{2}Q_{yz}][-\cos\frac{\theta}{2}\sigma_x + \sin\frac{\theta}{2}\sigma_z] \\
&+ \nu[\sin\frac{\theta}{2}Q_{xy} + \cos\frac{\theta}{2}Q_{zy}][\sin\frac{\theta}{2}\sigma_x + \cos\frac{\theta}{2}\sigma_z],
\end{aligned} \tag{C.30}$$

where σ is the usual Pauli spin operator, S the Cartesian spin operator of rank 1 for the spin-1 particle [119] and Q the Cartesian spin operator of rank 2 given by [79]

$$Q_{ij} = \frac{1}{3}\mathcal{P}_{ij} \equiv \frac{1}{2}\{S_i, S_j\} - \frac{2}{3}\delta_{ij}\cdot I \qquad (i,j = x,y,z), \tag{C.31}$$

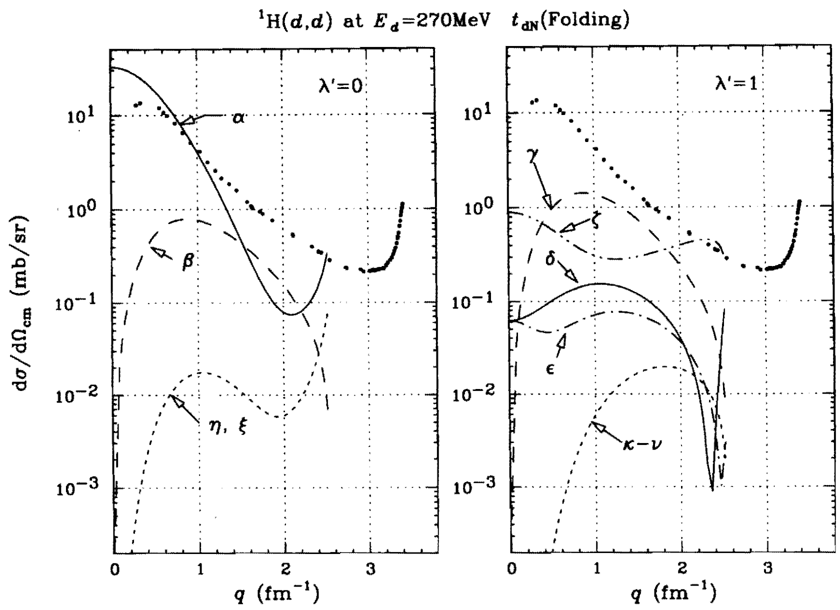

Figure C.2: The individual contributions of components of the dN t-matrix in Eq.(6.3) based on the folding model to the cross section are shown separately for the transferred spin to the target nucleon $\lambda' = 0$ and $\lambda' = 1$. Also shown are the $d + p$ elastic scattering data at E_d=270 MeV[32, 33].

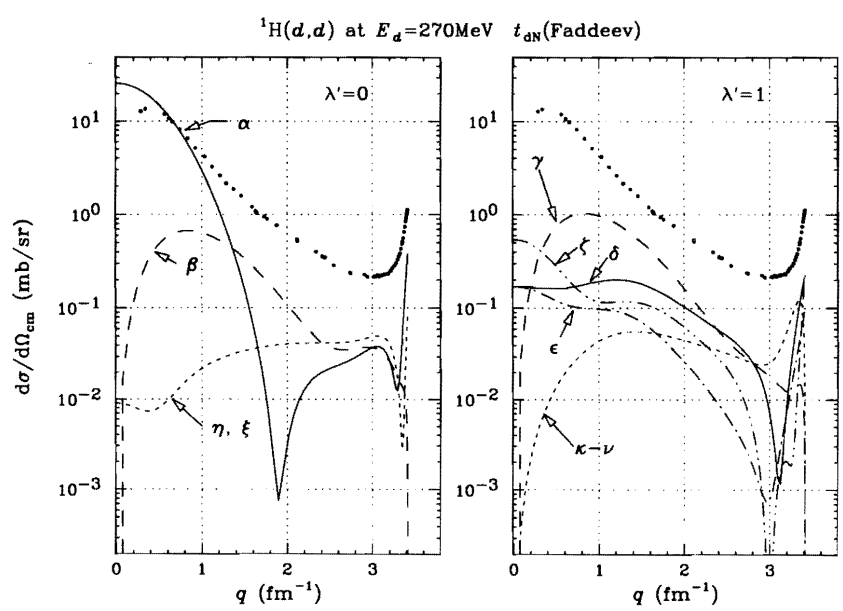

Figure C.3: The same as Fig.C.2 but for the dN t-matrix based on the Faddeev calculations.

where I denotes $3\times$ 3 unit matrix. The angle θ is the scattering angle in the dA center of mass system given by

$$\theta = 2\arcsin\left(\frac{q}{2k_{\text{in}}}\right), \tag{C.32}$$

where q is the momentum transfer. Defining new coefficients A through P by

$$\begin{aligned}
A &= \alpha, \quad B=\beta, \quad C=\gamma, \quad D=\delta, \\
E &= \epsilon\cos^2\frac{\theta}{2}+\zeta\sin^2\frac{\theta}{2}, \\
F &= (\zeta-\epsilon)\cos\frac{\theta}{2}\sin\frac{\theta}{2}, \\
G &= \epsilon\sin^2\frac{\theta}{2}+\zeta\cos^2\frac{\theta}{2}, \\
H &= \eta\cos^2\frac{\theta}{2}+\xi\sin^2\frac{\theta}{2}, \\
I &= 2(\xi-\eta)\cos\frac{\theta}{2}\sin\frac{\theta}{2}, \\
J &= \eta\sin^2\frac{\theta}{2}+\xi\cos^2\frac{\theta}{2}, \\
K &= \kappa\cos^2\frac{\theta}{2}+\lambda\sin^2\frac{\theta}{2}, \\
L &= 2(\lambda-\kappa)\cos\frac{\theta}{2}\sin\frac{\theta}{2}, \\
M &= \kappa\sin^2\frac{\theta}{2}+\lambda\cos^2\frac{\theta}{2}, \\
N &= \mu\cos^2\frac{\theta}{2}+\nu\sin^2\frac{\theta}{2}, \\
O &= (\nu-\mu)\cos\frac{\theta}{2}\sin\frac{\theta}{2}, \\
P &= \mu\sin^2\frac{\theta}{2}+\nu\cos^2\frac{\theta}{2},
\end{aligned} \tag{C.33}$$

the dN t-matrix in Eq.(C.30) can be written as

$$\begin{aligned}
t_{dN}(q) &= A + BS_y + C\sigma_y + DS_y\sigma_y + ES_x\sigma_x + F(S_x\sigma_z + S_z\sigma_x) + GS_z\sigma_z \\
&+ HQ_{xx} + IQ_{xz} + JQ_{zz} + KQ_{xx}\sigma_y + LQ_{xz}\sigma_y + MQ_{zz}\sigma_y \\
&+ NQ_{yx}\sigma_x + O(Q_{xy}\sigma_z + Q_{zy}\sigma_x) + PQ_{yz}\sigma_z.
\end{aligned} \tag{C.34}$$

By using the relation between the Cartesian and spherical representations of spin operators, the coefficients $e^{\lambda\lambda'}_{\nu\nu'}$ can be expressed in terms of coefficients A through P as summarized in Table C.1.

The set of Cartesian operators for spin-1 deuteron is given by

$$I = \begin{pmatrix} 1 & 0 & 0 \\ 0 & 1 & 0 \\ 0 & 0 & 1 \end{pmatrix},$$

$$
\begin{aligned}
S_x &= \frac{1}{\sqrt{2}}\begin{pmatrix} 0 & 1 & 0 \\ 1 & 0 & 1 \\ 0 & 1 & 0 \end{pmatrix}, \\
S_y &= \frac{i}{\sqrt{2}}\begin{pmatrix} 0 & -1 & 0 \\ 1 & 0 & -1 \\ 0 & 1 & 0 \end{pmatrix}, \\
S_z &= \begin{pmatrix} 1 & 0 & 0 \\ 0 & 0 & 0 \\ 0 & 0 & -1 \end{pmatrix}, \\
\mathcal{P}_{xy} &= \frac{3i}{2}\begin{pmatrix} 0 & 0 & -1 \\ 0 & 0 & 0 \\ 1 & 0 & 0 \end{pmatrix}, \\
\mathcal{P}_{xz} &= \frac{3}{2\sqrt{2}}\begin{pmatrix} 0 & 1 & 0 \\ 1 & 0 & -1 \\ 0 & -1 & 0 \end{pmatrix}, \\
\mathcal{P}_{yz} &= \frac{3i}{2\sqrt{2}}\begin{pmatrix} 0 & -1 & 0 \\ 1 & 0 & 1 \\ 0 & -1 & 0 \end{pmatrix}, \\
\mathcal{P}_{xx} &= \frac{1}{2}\begin{pmatrix} -1 & 0 & 3 \\ 0 & 2 & 0 \\ 3 & 0 & -1 \end{pmatrix}, \\
\mathcal{P}_{yy} &= \frac{1}{2}\begin{pmatrix} -1 & 0 & -3 \\ 0 & 2 & 0 \\ -3 & 0 & -1 \end{pmatrix}, \\
\mathcal{P}_{zz} &= \begin{pmatrix} 1 & 0 & 0 \\ 0 & -2 & 0 \\ 0 & 0 & 1 \end{pmatrix}.
\end{aligned}
\tag{C.35}
$$

The set of spherical operators for spin-1 deuteron is given by

$$
\begin{aligned}
\Omega_{00} &= I, \\
\Omega_{11} &= -\frac{\sqrt{3}}{2}(S_x + iS_y) = -\sqrt{\frac{3}{2}}\begin{pmatrix} 0 & 1 & 0 \\ 0 & 0 & 1 \\ 0 & 0 & 0 \end{pmatrix}, \\
\Omega_{10} &= \sqrt{\frac{3}{2}}S_z = \sqrt{\frac{3}{2}}\begin{pmatrix} 1 & 0 & 0 \\ 0 & 0 & 0 \\ 0 & 0 & -1 \end{pmatrix}, \\
\Omega_{1-1} &= \frac{\sqrt{3}}{2}(S_x - iS_y) = \sqrt{\frac{3}{2}}\begin{pmatrix} 0 & 0 & 0 \\ 1 & 0 & 0 \\ 0 & 1 & 0 \end{pmatrix},
\end{aligned}
$$

$$\begin{aligned}
\Omega_{22} &= \frac{1}{2\sqrt{3}}(\mathcal{P}_{xx} - \mathcal{P}_{yy} + 2i\mathcal{P}_{xy}) = \sqrt{3}\begin{pmatrix} 0 & 0 & 1 \\ 0 & 0 & 0 \\ 0 & 0 & 0 \end{pmatrix}, \\
\Omega_{21} &= -\frac{1}{\sqrt{3}}(\mathcal{P}_{xz} + i\mathcal{P}_{yz}) = -\sqrt{\frac{3}{2}}\begin{pmatrix} 0 & 1 & 0 \\ 0 & 0 & -1 \\ 0 & 0 & 0 \end{pmatrix}, \\
\Omega_{20} &= \frac{1}{\sqrt{2}}(\mathcal{P}_{zz}) = \frac{1}{\sqrt{2}}\begin{pmatrix} 1 & 0 & 0 \\ 0 & -2 & 0 \\ 0 & 0 & 1 \end{pmatrix}, \\
\Omega_{2-1} &= \frac{1}{\sqrt{3}}(\mathcal{P}_{xz} - i\mathcal{P}_{yz}) = \sqrt{\frac{3}{2}}\begin{pmatrix} 0 & 0 & 0 \\ 1 & 0 & 0 \\ 0 & -1 & 0 \end{pmatrix}, \\
\Omega_{2-2} &= \frac{1}{2\sqrt{3}}(\mathcal{P}_{xx} - \mathcal{P}_{yy} - 2i\mathcal{P}_{xy}) = \sqrt{3}\begin{pmatrix} 0 & 0 & 0 \\ 0 & 0 & 0 \\ 1 & 0 & 0 \end{pmatrix}.
\end{aligned} \tag{C.36}$$

The Cartesian operators are expressed in terms of the spherical operators as follows:

$$\begin{aligned}
S_x &= \frac{-1}{\sqrt{3}}(\Omega_{11} - \Omega_{1-1}), \\
S_y &= \frac{i}{\sqrt{3}}(\Omega_{11} + \Omega_{1-1}), \\
S_z &= \sqrt{\frac{2}{3}}\Omega_{10}, \\
\mathcal{P}_{xy} &= \frac{-i\sqrt{3}}{2}(\Omega_{22} - \Omega_{2-2}), \\
\mathcal{P}_{xz} &= \frac{-\sqrt{3}}{2}(\Omega_{21} - \Omega_{2-1}), \\
\mathcal{P}_{yz} &= \frac{i\sqrt{3}}{2}(\Omega_{21} + \Omega_{2-1}), \\
\mathcal{P}_{xx} &= \frac{\sqrt{3}}{2}(\Omega_{22} + \Omega_{2-2}) - \frac{1}{\sqrt{2}}\Omega_{20}, \\
\mathcal{P}_{yy} &= -\frac{\sqrt{3}}{2}(\Omega_{22} + \Omega_{2-2}) - \frac{1}{\sqrt{2}}\Omega_{20}, \\
\mathcal{P}_{zz} &= \sqrt{2}\Omega_{20}.
\end{aligned} \tag{C.37}$$

Table C.1: Relation between coefficients $e^{\lambda\lambda'}_{\nu\nu'}$ in Eq.(C.4) and coefficients A through P in Eq.(C.34).

λ	ν	λ'	ν'	$e^{\lambda\lambda'}_{\nu\nu'}$	
0	0	0	0	A	$(\lambda+\lambda'=0)$
1	1	0	0	$\frac{i}{\sqrt{3}}B$	
1	0	0	0	0	
1	-1	0	0	$\frac{i}{\sqrt{3}}B$	
0	0	1	1	$\frac{i}{\sqrt{2}}C$	$(\lambda+\lambda'=1)$
0	0	1	0	0	
0	0	1	-1	$\frac{i}{\sqrt{2}}C$	
1	1	1	1	$\frac{1}{\sqrt{6}}(-D+E)$	
1	0	1	1	$-\frac{1}{\sqrt{3}}F$	
1	-1	1	1	$\frac{1}{\sqrt{6}}(-D-E)$	
1	1	1	0	$-\frac{1}{\sqrt{3}}F$	
1	0	1	0	$\sqrt{\frac{2}{3}}G$	
1	-1	1	0	$\frac{1}{\sqrt{3}}F$	
1	1	1	-1	$\frac{1}{\sqrt{6}}(-D-E)$	
1	0	1	-1	$\frac{1}{\sqrt{3}}F$	$(\lambda+\lambda'=2)$
1	-1	1	-1	$\frac{1}{\sqrt{6}}(-D+E)$	
2	2	0	0	$\frac{1}{2\sqrt{3}}H$	
2	1	0	0	$-\frac{1}{2\sqrt{3}}I$	
2	0	0	0	$-\frac{1}{3\sqrt{2}}H+\frac{\sqrt{2}}{3}J$	
2	-1	0	0	$\frac{1}{2\sqrt{3}}I$	
2	-2	0	0	$\frac{1}{2\sqrt{3}}H$	
2	2	1	1	$\frac{i}{2\sqrt{6}}(K+N)$	
2	1	1	1	$\frac{i}{2\sqrt{6}}(-L-O)$	
2	0	1	1	$-\frac{i}{6}K+\frac{i}{3}M$	
2	-1	1	1	$\frac{i}{2\sqrt{6}}(L-O)$	
2	-2	1	1	$\frac{i}{2\sqrt{6}}(K-N)$	
2	2	1	0	$-\frac{i}{2\sqrt{3}}O$	
2	1	1	0	$\frac{i}{2\sqrt{3}}P$	$(\lambda+\lambda'=3)$
2	0	1	0	0	
2	-1	1	0	$\frac{i}{2\sqrt{3}}P$	
2	-2	1	0	$\frac{i}{2\sqrt{3}}O$	
2	2	1	-1	$\frac{i}{2\sqrt{6}}(K-N)$	
2	1	1	-1	$\frac{i}{2\sqrt{6}}(-L+O)$	
2	0	1	-1	$-\frac{i}{6}K+\frac{i}{3}M$	
2	-1	1	-1	$\frac{i}{2\sqrt{6}}(L+O)$	
2	-2	1	-1	$\frac{i}{2\sqrt{6}}(K+N)$	

C.3 The Deuteron Spin-Flip (Transfer) Probability

Here we consider the expression of the deuteron spin-flip (transfer) probability in terms of the polarization observables. Let $P_{Sm'}$ the projection operator on the spin state $|Sm'\rangle$ of the beam particle:

$$P_{Sm'}|Sm\rangle = \begin{cases} \delta_{mm'}|Sm'\rangle & \text{if } m \leq S, \\ 0 & \text{otherwise.} \end{cases} \tag{C.38}$$

By using $P_{Sm'}$ the cross section associated with the reaction in which the projectile is in the state $|S_a m_a\rangle$ and the ejectile in the state $|S_b m_b\rangle$ $\frac{d\sigma}{d\Omega}(S_a m_a \to S_b m_b)$ is written by

$$\frac{d\sigma}{d\Omega}(S_a m_a \to S_b m_b) = \mathrm{Tr}(T P_{S_a m_a} T^\dagger P_{S_b m_b}). \tag{C.39}$$

The spin transfer probability of $|\lambda|$ units along a projection axis is then given by

$$S_{|\lambda|} = \frac{\Sigma_{m_a m_b} \mathrm{Tr}(T P_{S_a m_a} T^\dagger P_{S_b m_b}) \delta_{m_b m_a \pm |\lambda|}}{\Sigma_{m_a m_b} \mathrm{Tr}(T P_{S_a m_a} T^\dagger P_{S_b m_b})}. \tag{C.40}$$

In the case of the deuteron scattering, the projection operators on the z-axis are related to the Cartesian spin operators:

$$P_0 = \frac{1}{3}(1 - S_{zz}), \tag{C.41}$$

$$P_{\pm 1} = \frac{1}{3} \pm \frac{1}{2} S_z + \frac{1}{6} S_{zz}. \tag{C.42}$$

The projection operators on the y-axis are expressed in terms of S_y and S_{yy} by similar relations as above in which z is replaced by y. The spin transfer probability in Eq.(C.40) can then be written using the Cartesian polarization observables as

$$S_0 = \frac{1}{6}(2 + 3K_y^{y'} + K_{yy}^{y'y'}), \tag{C.43}$$

$$S_1 = \frac{1}{9}(4 - P^{y'y'} - A_{yy} - 2K_{yy}^{y'y'}), \tag{C.44}$$

$$S_2 = \frac{1}{18}(4 + 2P^{y'y'} + 2A_{yy} - 9K_y^{y'} + K_{yy}^{y'y'}), \tag{C.45}$$

(C.46)

where the definition of the polarization observables is given in Table 6.9.

Appendix D

Macroscopic Model Analysis

Collective macroscopic model DWBA calculations were performed for low-lying natural parity states in ^{28}Si. Comparisons of experimental data with macroscopic model calculations are expected to provide important clues for a more microscopic description of the interaction and nuclear wave functions. Another motivation was to establish a way to evaluate the cross section for the 2_6^+ state at 9.48 MeV, which is almost degenerate with the 1_2^+ state at 9.50 MeV. This may be possible by using the proportionality relation, expected to hold among low-lying 2^+ states, between transition rates from the (d, d') reaction and those from other measurements.

D.1 The macroscopic DWBA model

In the macroscopic collective model, the optical potential is assumed to follow the shape of the nucleus and becomes non-spherical. To lowest order in the deformation the non-spherical parts induces excitations. The central part of the inelastic transition potential is given for L $\geq$ 2 by

$$F_L(r) = (2L+1)^{-\frac{1}{2}} \left[\beta_L^R R_R V \frac{\partial f}{\partial r} + \beta_L^I R_I W \frac{\partial g}{\partial r} \right], \tag{D.1}$$

where the β_L is the 2^L pole deformation parameter. The Coulomb part has the form

$$F_L^C(r) = \begin{cases} (3ZZ'e^2\beta_L)/(2L+1)(r^L)/(R_C^{L+1}) & r < R_C \\ (3ZZ'e^2\beta_L)/(2L+1)(R_C^L)/(r^{L+1}) & r \geq R_C. \end{cases} \tag{D.2}$$

In addition, a deformed spin-orbit potential of the full Thomas form [120] was incorporated in the present analysis. The radial shape of the transition potential is just the radial derivative of the optical potential, and the inelastic angular distribution is independent of β_L. The magnitude of the cross section is proportional to the square of the deformation parameter, β_L^2, which was obtained by using the relationship

$$[\beta_L]^2 = [d\sigma/d\Omega]_{\text{exp}} \,/\, [d\sigma/d\Omega]_{\text{calc}}\,. \tag{D.3}$$

In the present analysis, the deformation length ($\beta_i R_i$) was kept constant throughout all terms of the optical potential according to Ref. [121].

Following Bernstein [122] the deformation length can be converted to the isoscalar transition rate according to

$$B(IS, 0 \to L) = (3Z/4\pi)^2 (\beta_L R)^2 R_u^{2L-2} C, \tag{D.4}$$

where $R_u = 1.2A^{1/3}$ fm is the equivalent radius for a uniform mass distribution, and the quantity C is a correction factor for a more realistic Fermi-mass distribution, which has been tabulated in Ref. [122]. Expressed in single-particle units the transition rate becomes

$$G(IS, 0 \to L) = \frac{B(IS, 0 \to L)}{B_{s.p.}(0 \to L)}, \tag{D.5}$$

with

$$B_{s.p.}(0 \to L) = (2L+1)/4\pi \, [3/(3+L)]^2 \, R_u^{2L}. \tag{D.6}$$

The calculations were performed with the ECIS [78] code in a one phonon vibrational model framework.

D.2 Comparison with Experiment

The angular distributions of the differential cross section for states in the excitation energy range below 10.9 MeV and for those between 10.9 and 19 MeV are shown in Figs. D.1 and D.2, respectively. The error bars shown are statistical ones. Solid lines represent theoretical predictions of the collective model. The angular distributions are well described by the calculations, especially near the cross section maxima for the lowest-lying 2_1^+(1.78 MeV), 3_1^-(6.88 MeV), 4_1^+(4.62 MeV) and 5_1^-(5.70 MeV) states.

The extracted deformation lengths (βR) and isoscalar transition rates (G(IS)$_{(d,d')}$) are summarized in Tables D.1 and D.2, where the G(IS)$_{(d,d')}$ values are compared with G(IS)$_{(\alpha,\alpha')}$ values obtained from an (α, α') experiment at 120 MeV [123], and with G(EM) values from the compilation of Endt [88]. It can be seen that the present G(IS)$_{(d,d')}$ values are 30 – 70% smaller than the G(EM) values. The similar reduced values for the isoscalar transition rate have been obtained in proton inelastic scattering for ^{208}Pb at $E_p = 200$ MeV [124, 125]. This, however, disagrees with the conclusions in Ref. [126]. The G(IS)$_{(d,d')}$ also has values smaller than G(IS)$_{(\alpha,\alpha')}$. Despite the disagreement in absolute values among the transition rates, we can see good proportionality relations, for several of low-lying 2^+ states, between G(IS)$_{(d,d')}$ and G(IS)$_{(\alpha,\alpha')}$ (see Fig. D.3 (a)), and between G(IS)$_{(d,d')}$ and G(EM) (see Fig. D.3 (b)). Using the relations the G(IS)$_{(d,d')}$ value for the

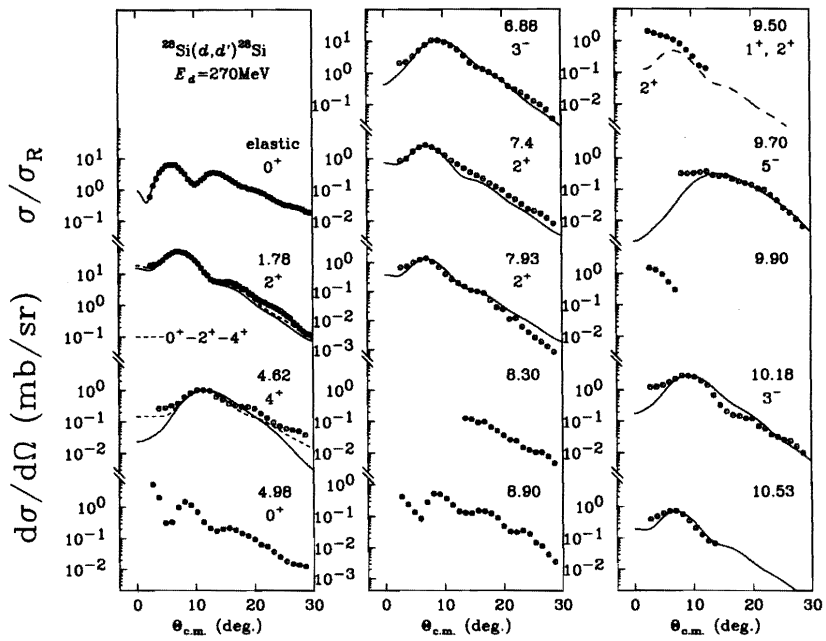

Figure D.1: The differential cross sections for states in ^{28}Si in the excitation energy range below 10.9 MeV excited via the (d, d') reaction at E_d=270 MeV.

2_6^+ (9.48 MeV) state could be estimated to be 0.073 $\pm$ 0.004. The cross section of the 2_6^+ state calculated using the deduced $\mathrm{G(IS)}_{(d,d')}$ value within the collective model is shown as a dashed line in Fig. D.1.

The angular distributions of the analyzing powers, A_y and A_{yy}, for states below 10.9 MeV are shown in Figs. D.4 and D.5, respectively. Solid curves are results of the macroscopic DWBA calculations. The one-step collective model calculations reproduce the oscillation patterns generally well, the agreement is especially quite good for the 2_1^+ and 3_2^- states. It is found that a better description can be obtained for the 4_1^+ angular distributions, if the channel coupling between the 0_1^+, 2_1^+ and 4_1^+ states is taken into account. The results of the coupled-channel (CC) calculations in a 0^+-2^+-4^+ coupling scheme within a rotational model for A_y and A_{yy} are shown as dashed lines in Figs. D.4 and D.5, respectively. The calculation assumes quadrupole and hexadecapole deformations of $\beta_2 R = -1.07$ fm and $\beta_4 R = 0.20$ fm, respectively. It can be seen that the oscillation patterns are correctly predicted for angles larger than 20°, if the effect of channel coupling is taken into account. Such an effect of channel coupling on the analyzing power angular distribution has been reported in the (p, p') reaction on ^{18}O at E_p = 800 MeV [127]. By taking account of the channel coupling effect a slight improvement in the description of the cross section data is also obtained for the 4_1^+ state as shown in Fig. D.1.

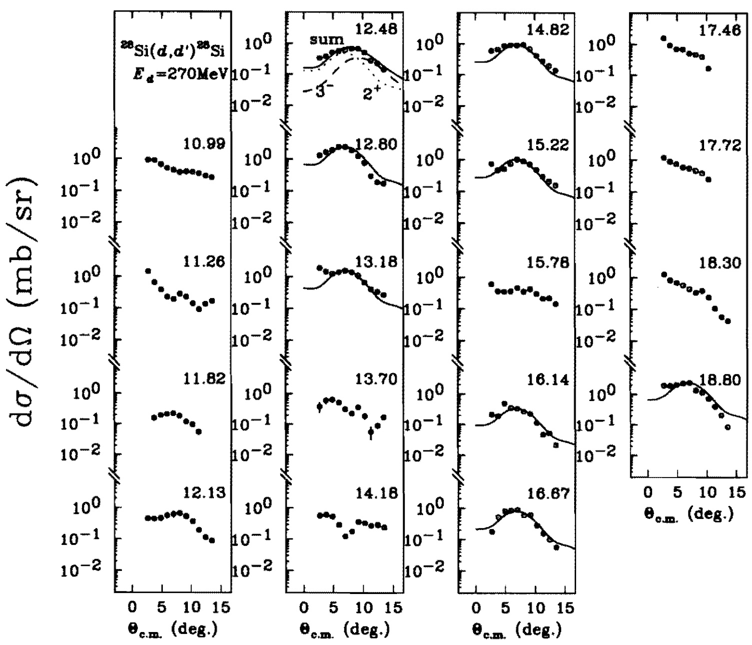

Figure D.2: The same as Fig. D.1 but for states between 10.9 to 19 MeV.

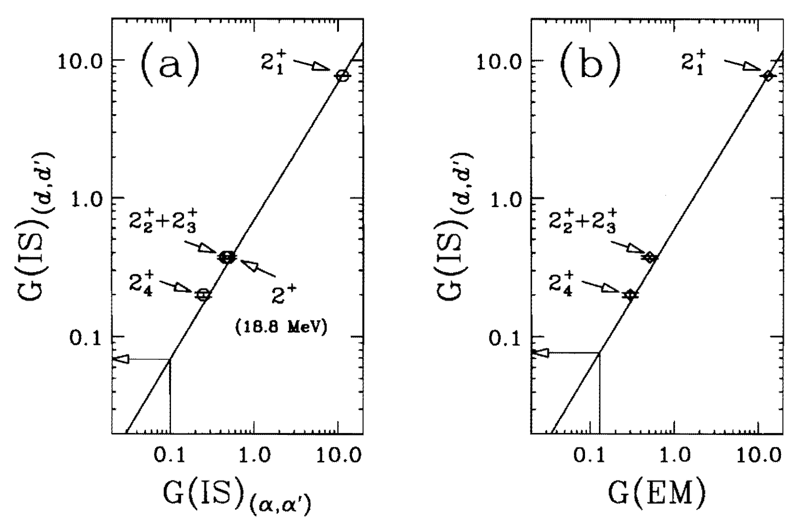

Figure D.3: Proportionality relations among low-lying 2^+ states between (a) $\mathrm{G(IS)}_{(d,d')}$ and $\mathrm{G(IS)}_{(\alpha,\alpha')}$ and (b) $\mathrm{G(IS)}_{(d,d')}$ and G(EM).

Table D.1: Deformation parameters and isoscalar transition rates obtained from the ^{28}Si(d, d') reaction at E_d=270 MeV below E_x=10.9 MeV.

E_x (MeV)	E_x [a] (MeV)	J^π	J^π [a]	βR (fm)	G(IS)$_{(d,d')}$ (W.u.)	G(IS)$_{(\alpha,\alpha')}$ [b] (W.u.)	G(EM) [a] (W.u.)
1.78	1.799	2^+	2^+	1.03	7.69	11.35	13.22
4.62	4.617	4^+	4^+	0.24	0.32	0.53	
4.98	4.979	0^+	0^+				
6.88	6.879	3^-	3^-	0.62	4.04	5.39	13.69
	6.889		4^+				
7.41	7.381	2^+	2^+	0.23	0.37	0.46	0.33
	7.416	2^+	2^+				0.18
	7.799		3^+				
7.93	7.933	2^+	2^+	0.17	0.20	0.25	0.30
8.30	8.259		2^+				0.02
	8.323		1^+				
	8.413		4^-				
8.90	8.904		1^-				
	8.945		5^+				
9.50	9.479	2^+	2^+			0.10	0.13
	9.496	1^+	1^+				
9.70	9.702	5^-	5^-	0.16	0.92		
	9.764		3^-				
	9.796		2^+			0.05	
9.90	9.929		1^-				
10.18	10.182	3^-	3^-	0.32	1.06	1.89	
10.53	10.514	2^+	2^+	0.12	0.11	0.11	
	10.596		1^+				
	10.725		1^+				

[a]) Ref. [88].

[b]) From the α-scattering experiment. Ref. [123].

Table D.2: Deformation parameters and isoscalar transition rates obtained from the ^{28}Si(d, d') reaction at E_d=270 MeV for $E_x > 10.9$ MeV.

E_x (MeV)	E_x [a] (MeV)	J^π	J^π [a]	βR (fm)	G(IS)$_{(d,d')}$ (W.u.)	G(IS)$_{(\alpha,\alpha')}$ [b] (W.u.)
10.99	10.994					
	11.00 [b]		(4^+) [b]			0.40
11.26	11.295		1^-			
	11.388					
	11.670		1^-			
11.82	11.799		$(2,3)^-$			
12.13	12.072		2^-			
	12.181		1^-			
	12.31 [b]		(2^+) [b]			0.05
12.49	12.440	2^+	2^+	0.10	0.07	
	12.488	3^-	3^-	0.11	0.13	
	12.56 [b]		3^- [b]			0.39
12.80	12.802		3^-			
	12.804	(2^+)	$(1^-, 2^+)$	0.23	0.37	
	12.814		1^-			
13.18	13.189		1^+			
	13.19 [b]	2^+	(2^+)	0.18	0.24	0.16
13.70	13.733		1^-			
	13.75 [b]		(2^+)			0.16
14.18	14.17 [b]		(3^-) [b]			0.24
14.82	14.74 [b]	2^+	2^+ [b]	0.14	0.14	0.21
	14.90 [b]		3^- [b]			0.11
15.22	15.28 [b]	2^+	2^+ [b]	0.15	0.15	0.06
15.78						
16.14	16.10 [b]	2^+	(2^+) [b]	0.09	0.05	0.14
16.67	16.54 [b]	2^+	2^+ [b]	0.13	0.12	0.14
17.46						
17.74						
18.30						
18.8	18.67 [b]	2^+	2^+ [b]	0.23	0.37	0.50

[a]) Ref. [88].

[b]) From the α-scattering experiment. Ref. [123].

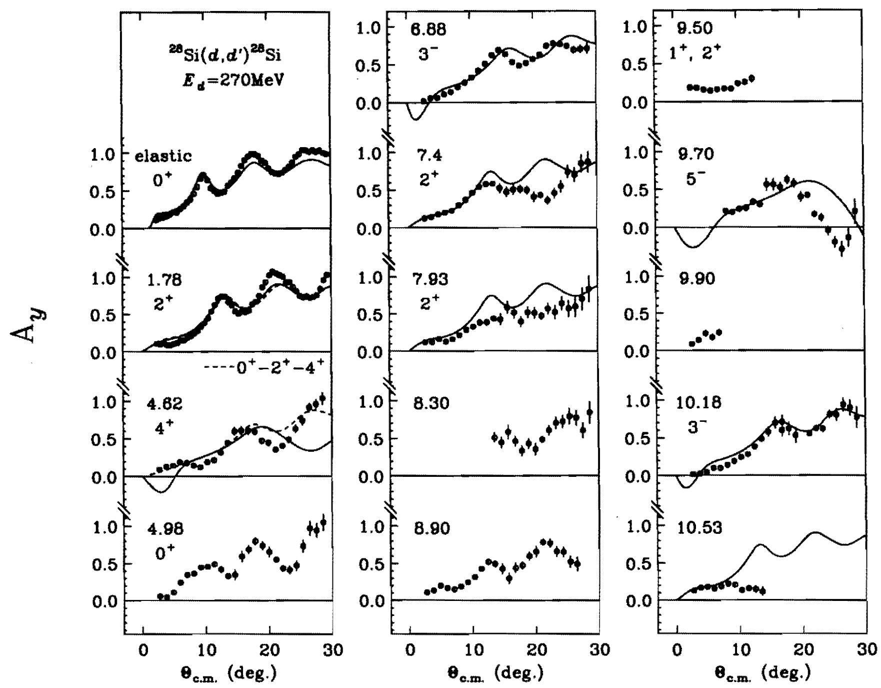

Figure D.4: The vector analyzing power A_y for states in ^{28}Si in the excitation energy range below 10.9 MeV excited via the (d,d') reaction at E_d=270 MeV.

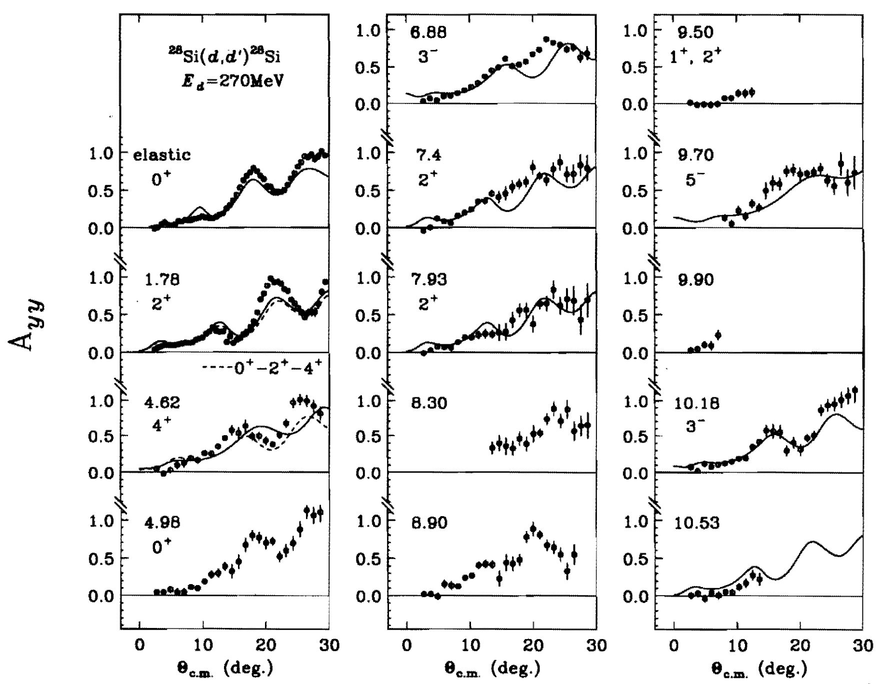

Figure D.5: The same as Fig. D.4 but for tensor analyzing power A_{yy}.

Bibliography

[1] D. E. Bainum, J. Rapaport, C. D. Goodman, D. J. Horen, C. C. Foster, M. B. Greenfield and C. A. Goulding, Phys. Rev. Lett. 44 (1980) 1751.

[2] B. D. Anderson, J. N. Knudson, P. C. Tandy, J. W. Watson, R. Madey and C. C. Foster, Phys. Rev. Lett. 45 (1980) 699.

[3] C. Gaarde, J. Rapaport, T. N. Taddeucci, C. D. Goodman, C. C. Foster, D. E. Bainum, C. A. Goulding, M. B. Greenfield, D. J. Horen and E. Sugarbaker, Nucl. Phys. A 369 (1981) 258.

[4] N. Anantaraman, G. M. Crawley, A. Galonsky, C. Djalali, N. Marty, M. Morlet, A. Willis and J.-C. Jourdain, Phys. Rev. Lett. 46 (1981) 1318.

[5] F. E. Bertrand, E. E. Gross, D. J. Horen, J. R. Wu, J. Tinsley, D. K. McDaniels, L. W. Swenson and R. Liljestrand, Phys. Lett. 103 B (1981) 326.

[6] C. Djalali, N. Marty, M. Morlet, A. Willis, J.-C. Jourdain, N. Anantaraman, G. M. Crawley, A. Galonsky and P. Kitching, Nucl. Phys. A 388 (1982) 1.

[7] G. M. Crawley, N. Anantaraman, A. Galonsky, C. Djalali, N. Marty, M. Morlet, A. Willis, J.-C. Jourdain and P. Kitching, Phys. Rev. C 26 (1982) 87.

[8] S. J. Seestrom-Morris, J. M. Moss, J. B. McClelland, W. D. Cornelius, T. A. Carey, N. M. Hintz, M. Gazzaly, M. A. Franey, S. Nanda and B. Aas, Phys. Rev. C 26 (1982) 2131.

[9] K. W. Jones, C. Glashausser, S. Nanda, R. de Swiniarski, T. A. Carey, W. Cornelius, J. M. Moss, J. B. McClelland, S. J. Seestrom-Morris, J. R. Comfort, J.-L. Escudié, M. Gazzaly, N. Hintz, G. Igo, M. Haji-Saeid and C. A. Whitten, Phys. Lett. 128 B (1983) 281.

[10] S. K. Nanda, C. Glashausser, K. W. Jones, J. A. McGill, T. A. Carey, J. B. McClelland, J. M. Moss, S. J. Seestrom-Morris, H. Ohnuma, M. Franey, M. Gazzaly and N. Hintz, Phys. Rev. Lett. 51 (1983) 1526.

[11] F. T. Baker, L. Bimbot, R. W. Fergerson, C. Glashausser, K. Jones, A. Green, K. Nakayama and S. Nanda, Phys. Rev. C 37 (1988) 1350.

[12] F. T. Baker, L. Bimbot, R. W. Fergerson, C. Glashausser, A. Green, K. Jones, W. G. Love and S. Nanda, Phys. Rev. C 40 (1989) 1877.

[13] F. T. Baker, L. Bimbot, R. W. Fergerson, C. Glashausser, A. Green, O. Häusser, K. Hicks, K. Jones, C. A. Miller, M. Vetterli, R. Abegg, D. Beatty, B. Bonin, B. Castel, X. Y. Chen, V. Cupps, C. Djalali, R. Henderson, K. P. Jackson, R. Jeppesen, K. Nakayama, S. K. Nanda, R. Sawafta and S. Yen, Phys. Rev. C 44 (1991) 93.

[14] C. Glashausser, K. Jones, F. T. Baker, L. Bimbot, H. Esbensen, R. W. Fergerson, A. Green, S. Nanda and R. D. Smith, Phys. Rev. Lett. 58 (1987) 2404.

[15] F. T. Baker, L. Bimbot, B. Castel, R. W. Fergerson, C. Glashausser, A. Green, O. Hausser, K. Hicks, K. Jones, C. A. Miller, S. K. Nanda, R. D. Smith, M. Vetterli, J. Wambach, R. Abegg, D. Beatty, V. Cupps, C. Djalali, R. Henderson, K. P. Jackson, R. Jeppeson, J. Lisantti, M. Morlet, R. Sawafta, W. Unkelbach, A. Willis and S. Yen, Phys. Lett. B 237 (1990) 337.

[16] O. Häusser, M. C. Vetterli, R. W. Fergerson, C. Glashausser, R. G. Jeppesen, R. D. Smith, R. Abegg, F. T. Baker, A. Celler, R. L. Helmer, R. Henderson, K. Hicks, M. J. Iqbal, K. P. Jackson, K. W. Jones, J. Lisantti, J. Mildenberger, C. A. Miller, R. S. Sawafta and S. Yen, Phys. Rev. C 43 (1991) 230.

[17] F. T. Baker, D. Beatty, L. Binbot, V. Cupps, C. Djalali, R. W. Fergerson, C. Glashausser, G. Graw, A. Green, K. Jones, M. Morlet, S. K. Nanda, A. Sethi, B. H. Strom, W. Unkelbach and A. Willis, Phys. Rev. C 48 (1993) 1106.

[18] F. T. Baker, L. Bimbot, C. Djalali, C. Glashausser, H. Lenske, W. G. Love, M. Morlet, E. Tomasi-Gustafsson, J. Van de Wiele, J. Wanbach and A. Willis, Phys. Rep. 289 (1997) 235.

[19] S. Mordechai, N. Auerbach, M. Burlein, H. T. Fortune, S. J. Greene, C. Fred Moore, C. L. Morris, J. M. O'Donnell, M. W. Rawool, J. D. Silk, D. L. Watson, S. H. Yoo and J. D. Zumbro, Phys. Rev. Lett. 61 (1988) 531.

[20] J. Ritman, F.-D. Berg, W. Kühn, V. Metag, R. Novotny, M. Notheisen, P. Paul, M. Pfeiffer, O. Schwalb, H. Löhner, L. Venema, A. Gobbi, N. Herrmann, K. D. Hildenbrand, J. Mösner, R. S. Simon, K. Teh, J. P. Wessels and T. Wienold, Phys. Rev. Lett. 70 (1993) 533.

[21] R. Schmidt, Th. Blaich, Th. W. Elze, H. Emling, H. Freiesleben, K. Grimm, W. Henning, R. Holzmann, J. G. Keller, H. Klingler, R. Kulessa, J. V. Kratz, D. Lambrecht, J. S. Lange, Y. Leifels, E. Lubkiewicz, E. F. Moore, E. Wajda, W. Prokopowicz, Ch. Schütter, H. Spies, K. Stelzer, J. Stroth, W. Walus, H. J. Wollersheim, M. Zinser and E. Zude, Phys. Rev. Lett. 70 (1993) 1767.

[22] J. A. Scarpaci, Y. Blumenfeld, Ph. Chomaz, N. Frascaria, J. P. Garron, M. Lamehi-Rachti, I. Lhenry, J. C. Roynette, T. Suomijärvi, D. Beaumel, P. Massolo, N. Alamanos, A. Gillibert and A. Van der Woude, Phys. Rev. Lett. 71 (1993) 3766.

[23] Ph. Chomaz and N. Frascaria, Phys. Rep. 252 (1995) 275.

[24] P. Vogel, M. Ericson, and J. D. Vergados, Phys. Lett. B 212 (1988) 259.

[25] N. Auerbach, L. Zamick and D. C. Zheng, Ann. Phys. 192 (1989) 77.

[26] J. Blomgren, K. Lindh, N. Anantaraman, S. M. Austin, G. P. A. Berg, B. A. Brown, J.-M. Casandjian, M. Chartier, M. D. Cortina-Gil, S. Fortier, M. Hellström, J. R. Jongman, J. H. Kelley, A. Lepine-Szily, I. Lhenry, M. Mac. Cormick, W. Mittig, J. Nilsson, N. Olsson, N. A. Orr, E. Ramakrishnan, P. Roussel-Chomaz, B. M. Sherrill, P.-E. Tegnér, J. S. Winfield and J. A. Winger, Phys. Lett. B 362 (1995) 34.

[27] G. R. Ohlsen, Rep. Prog. Phys. 35 (1972) 717.

[28] T. Suzuki, Prog. Theor. Phys. 86 (1991) 1129.

[29] J. Van de Wiele, A. Willis and M. Morlet, Nucl. Phys. A 588 (1995) 829.

[30] G. R. Satchler, *Direct Nuclear Reactions*, Clarendon Press, Oxford, 1983.

[31] W. Glöckle, H. Witala, D. Hüber, H. Kamada and J. Golak, Phys. Rep. 274 (1996) 107.

[32] N. Sakamoto, H. Okamura, T. Uesaka, S. Ishida, H. Otsu, T. Wakasa, Y. Satou, T. Niizeki, K. Katoh, T. Yamashita, K. Hatanaka, Y. Koike and H. Sakai, Phys. Lett. B 367 (1996) 60.

[33] H. Sakai, K. Sekiguchi, H. Witala, W. Glöckle, M. Hatano, H. Kamada, H. Kato, Y. Maeda, A. Nogga, T. Ohnishi, H. Okamura, N. Sakamoto, S. Sakoda, Y. Satou, K. Suda, A. Tamii, T. Uesaka, T. Wakasa and K. Yako, Phys. Rev. Lett. 84 (2000) 5288.

[34] H. Kamada, T. Uesaka, W. Glöckle, H. Sakai, S. Gojuki, K. Itoh, T. Ohnishi, H. Okamura, N. Sakamoto, S. Sakoda, Y. Satou, K. Sekiguchi, K. Suda, A. Tamii, T. Wakasa, H. Witala and K. Yako, Prog. Theor. Phys. 104 (2000) 703.

[35] T. Uesaka, H. Sakai, H. Okamura, A. Tamii, Y. Satou, T. Ohnishi, K. Sekiguchi, K. Yako, S. Sakoda, N. Sakamoto, T. Wakasa, K. Itoh and K. Suda, RIKEN Accel. Prog. Rep. 33 (2000) 55.

[36] S. Ishida, H. Sakai, H. Okamura, H. Otsu, N. Sakamoto, K. Hatanaka and A. Okihana, Phys. Lett. B 314 (1993) 279.

[37] S. Kox, C. Furget, J. S. Réal, L. Bimbot, J. P. Bocquet, M. Garçon, C. Djalali, G. W. R. Edwards, C. Glashausser, B. N. R. Johnson, M. Morlet, C. Perrin, D. Rebreyend, L. Rosier, E. Tomasi-Gustafsson, E. Voutier and A. Willis, Nucl. Instr. and Meth. A 346 (1994) 527.

[38] C. Furget, C. Glashausser, S. Kox, J. S. Réal, E. Tomasi-Gustafsson, L. Bimbot, C. Djalali, G. W. R. Edwards, B. N. R. Johnson, M. Morlet, L. Rosier, J. Van de Wiele, E. Voutier and A. Willis, Phys. Rev. C 51 (1995) 1562.

[39] B. Bonin, A. Boudard, H. Fanet, R. W. Fergerson, M. Garçon, C. Giorgetti, J. Habault, J. Le Meur, R. M. Lombard, J. C. Lugol, B. Mayer, J. P. Mouly, E. Tomasi-Gustafsson, J. C. Duchazeaubeneix, J. Yonnet, M. Morlet, J. Van De Wiele, A. Willis, G. Greeniaus, G. Gaillard, P. Markowitz, C. F. Perdrisat, R. Abegg and D. A. Hutcheon, Nucl. Instr. and Meth. A 288 (1990) 389.

[40] M. Morlet, A. Willis, J. Van de Wiele, N. Marty, J. Guillot, H. Langevin-Joliot, L. Bimbot, E. Tomasi-Gustafsson, G. W. R. Edwards, R. W. Fergerson, C. Glashausser, D. Beatty, A. Green, C. Djalali, F. T. Baker and J. C. Duchazeaubeneix, Phys. Lett. B 247 (1990) 228.

[41] M. Morlet, E. Tomasi-Gustafsson, A. Willis, J. Van de Wiele, N. Marty, C. Glashausser, B. N. Johnson, F. T. Baker, D. Beatty, L. Bimbot, C. Djalali, G. W. R. Edwards, A. Green, J. Guillot, F. Jourdan, H. Langevin-Joliot, L. Rosier and M. Y. Youn, Phys. Rev. C 46 (1992) 1008.

[42] B. N. Johnson, M. Morlet, C. Djalali, F. T. Baker, L. Bimbot, C. Glashausser, J. Guillot, H. Langevin-Joliot, N. Marty, L. Rosier, E. Tomasi-Gustafsson, J. Van de Wiele and A. Willis, Phys. Rev. C 51 (1995) 1726.

[43] C. Djalali, M. Morlet, N. Marty, J. Van de Wiele, A. Willis, F. T. Baker, L. Bimbot, C. Glashausser, J. Guillot, H. Langevin-Joliot, L. Rosier and E. Tomasi-Gustafsson, Phys. Rev. C 59 (1999) 118.

[44] C. Wilkin, In *The 20 Years of the Syncrotron SATURNE-2* (A. Boudard and P.-A. Chamouard, eds.), World Scientific, Singapore, 1998.

[45] S. Ishida, Ph.D. Thesis, Department of Physics, Univ. of Tokyo, unpublished, (1997).

[46] Y. Satou, S. Ishida, H. Sakai, H. Okamura, H. Otsu, N. Sakamoto, T. Uesaka, T. Wakasa, T. Ohnishi, T. Nonaka, G. Yokoyama, T. Ichihara, T. Niizeki and N. Nishimori, Nucl. Phys. A 649 (1999) 275c.

[47] N. Anantaraman, B. A. Brown, G. M. Crawley, A. Galonsky, C. Djalali, N. Marty, M. Morlet, A. Willis, J.-C. Jourdain and B. H. Wildenthal, Phys. Rev. Lett. 52 (1984) 1409.

[48] G. M. Crawley, C. Djalali, N. Marty, M. Morlet, A. Willis, N. Anantaraman, B. A. Brown and A. Galonsky, Phys. Rev. C 39 (1989) 311.

[49] Y. Fujita, H. Akimune, I. Daito, M. Fujiwara, M. N. Harakeh, T. Inomata, J. Jänecke, K. Katori, C. Lüttge, S. Nakayama, P. von Neumann-Cosel, A. Richter, A. Tamii, M. Tanaka, H. Toyokawa, H. Ueno and M. Yosoi, Phys. Rev. C 55 (1997) 1137.

[50] F. Osterfeld, Rev. Mod. Phys. 64 (1992) 491.

[51] B. H. Wildenthal, In *Progress in Particle and Nuclear Physics* (D. H. Wilkinson, eds.), Vol. 11, Pergamon, Oxford, 1984, p. 5.

[52] B. A. Brown, W. A. Richter, R. E. Julies and B. H. Wildenthal, Ann. of Phys. 182 (1988) 191.

[53] D. V. Bugg and C. Wilkin, Phys. Lett. B 152 (1985) 37.

[54] D. V. Bugg and C. Wilkin, Nucl. Phys. A 467 (1987) 575.

[55] T. Motobayashi, C. Perrin, J. Carbonell, C. Wilkin, S. Kox, F. Merchez, Nguyen Van Sen, D. Rebreyend, G. Guillaume, J. Arvieux, J. Yonnet, B. Bonin, A. Boudard, M. Garcon, J. Guillot and G. Gaillard, Phys. Lett. B 233 (1989) 69.

[56] S. Kox, C. Perrin, J. Arvieux, J. P. Bocquet, A. Boudard, J. Carbonell, G. Gaillard, M. Garçon, L. Ghedira, G. Guillaume, F. Merchez, T. Motobayashi, D. Rebreyend, C. Wilkin and J. Yonnet, Phys. Lett. B 266 (1991) 264.

[57] S. Kox, J. Carbonell, C. Furget, T. Motobayashi, C. Perrin, C. Wilkin, J. Arvieux, J. P. Bocquet, A. Boudard, G. Gaillard, M. Garçon, L. Ghedira, G. Guillaume, F. Merchez, D. Rebreyend and J. Yonnet, Nucl. Phys. A 556 (1993) 621.

[58] J. Carbonell, M. B. Barbaro and C. Wilkin, Nucl. Phys. A 529 (1991) 653.

[59] H. Okamura, H. Sakai, N. Sakamoto, T. Uesaka, S. Ishida, H. Otsu, T. Wakasa, K. Hatanaka, T. Kubo, N. Inabe, K. Ikegami, J. Fujita, M. Kase, A. Goto and Y. Yano, AIP Conf. Proc. 293 (1994) 84.

[60] K. L. Brown, D. C. Carey, Ch. Iselin and F. Rothacker, CERN/80-04 (1980).

[61] N. Sakamoto, Ph.D. Thesis, Department of Physics, Univ. of Tokyo, unpublished, (1996).

[62] T. Ichihara, T. Niizeki, H. Okamura, H. Ohnume, H. Sakai, Y. Fuchi, K. Hatanaka, M. Hosaka, S. Ishida, K. Kato, S. Kato, H. Kawashima, S. Kubono, S. Miyamoto, H. Orihara, N. Sakamoto, S. Takaku, Y. Tajima, M. H. Tanaka, H. Toyokawa, T. Uesaka, T. Yamamoto, T. Yamashita, M. Yosoi and M. Ishihara, Nucl. Phys. A 569 (1994) 287c.

[63] S. Kato, Nucl. Instr. and Meth. A 254 (1987) 487.

[64] S. Morinobu, OPTRACE, unpublished.

[65] F. Sauli, CERN Report (1977) 77.

[66] T. Ichihara, T. Inamura, T. Wada and M. Ishihara, IEEE Trans. on Nucl. Sci. 36 (1989) 1628.

[67] W. Haeberli, In *Nuclear Spectroscopy and Reactions* (J. Cerny, eds.), Academic Press, New York, 1974.

[68] R. Hagedorn, *Relativistic Kinematics*, Benjamin Inc., New York, 1963.

[69] D. M. Brink and G. R. Satchler, *Angular Momentum*, Clarendon Press, Oxford, 1962

[70] P. M. Endt and C. van der Leun, Nucl. Phys. A 310 (1978) 1.

[71] G. G. Ohlsen, J. L. Gammel and P. W. Keaton, Jr., Phys. Rev. C 5 (1972) 1205.

[72] S. Yen, R. J. Sobie, T. E. Drake, H. Zarek, C. F. Williamson, S. Kowalski and C. P. Sargent, Phys. Rev. C 27 (1983) 1939.

[73] H. P. Blok, J. C. De Lange and J. W. Schotman, Nucl. Instr. and Meth. 128 (1975) 545.

[74] M. Kawai, T. Terasawa and K. Izumo, Prog. Theor. Phys. 27 (1962) 404.

[75] M. Kawai, T. Terasawa and K. Izumo, Nucl. Phys. 59 (1964) 289.

[76] R. M. Haybron and H. McManus, Phys. Rev. 136 (1964) 1730.

[77] R. M. Haybron, Phys. Rev. 160 (1967) 756.

[78] J. Raynal, Computer code ECIS, International Atomic Energy Agency Report IAEA-SMR-8/8, (1972) 75.

[79] T. Suzuki, Nucl. Phys. A 577 (1994) 167c.

[80] R. Machleidt, F. Sammarruca and Y. Song, Phys. Rev. C 53 (1996) 1483.

[81] S. Cohen and D. Kurath, Nucl. Phys. 73 (1965) 1.

[82] D. J. Millener and D. Kurath, Nucl. Phys. A 255 (1975) 315.

[83] B. A. Brown, A. Etchegoyen and W. D. M. Rae, OXBASH, The Oxford, Buenos-Aires, Michigan State, Shell Model Program, MSU, Cyclotron Laboratory Report number, 524 (1988).

[84] K. W. Jones, C. Glashausser, R. de Swiniarski, F. T. Baker, T. A. Carey, J. R. Comfort, W. Cornelius, J. L. Escudié, M. Gazzaly, A. Green, M. Haji-Saeid, N. Hintz, G. Igo, J. B. McClelland, J. M. Moss, S. Nanda and C. A. Whitten, Phys. Rev. C 50 (1994) 1982.

[85] D. J. Rowe and S. S. M. Wong, Nucl. Phys. A153 (1970) 561.

[86] P. D. Kunz and E. Rost, Computer code DWUCK4, In *Computational Nuclear Physics 2* (K. Langanke, J. A. Maruhn and S. E. Koonin, eds.), Springer-Verlag, New York, 1992.

[87] F. Ajzenberg-Selove and C. L. Busch, Nucl. Phys. A 336 (1980) 1.

[88] P. M. Endt, Nucl. Phys. A 521 (1990) 1.

[89] B. A. Brown, R. Radhi and B. H. Wildenthal, Phys. Rep. 101 (1983) 313.

[90] J. R. Comfort, G. L. Moake, C. C. Foster, P. Schwandt, C. D. Goodman, J. Rapaport and W. G. Love, Phys. Rev. C 24 (1981) 1834.

[91] J. R. Comfort, G. L. Moake, C. C. Foster, P. Schwandt and W. G. Love, Phys. Rev. C 26 (1982) 1800.

[92] W. G. Love and M. A. Franey, Phys. Rev. C 24 (1981) 1073.

[93] J. Kelly, W. Bertozzi, T. N. Buti, F. W. Hersman, C. Hyde, M. V. Hynes, B. Norum, F. N. Rad, A. D. Bacher, G. T. Emery, C. C. Foster, W. P. Jones, D. W. Miller, B. L. Berman, W. G. Love and F. Petrovich, Phys. Rev. Lett. 45 (1980) 2012.

[94] W. Bertozzi, T. N. Buti, J. M. Finn, F. W. Hersman, C. Hyde-Wright, M. V. Hynes, M. A. Kovash, B. Murdok, B. E. Norum, B. Pugh, F. N. Rad, A. D. Bacher, G. T. Emery, C. C. Foster, W. P. Jones, D. W. Miller, B. L. Berman, W. G. Love, J. A. Carr and F. Petrovich, Phys. Rev. C 39 (1989) 1222.

[95] M. Hugi, W. Bauhoff and H. O. Meyer, Phys. Rev. C 28 (1983) 1.

[96] L. Rikus, K. Nakano and H. V. von Geramb, Nucl. Phys. A 414 (1984) 413.

[97] F. E. Cecil, L. W. Fagg, W. L. Bendel and E. C. Jones, Jr. Phys. Rev. C 9 (1974) 798.

[98] J. B. Flanz, R. S. Hicks, R. A. Lindgren, G. A. Peterson, J. Dubach and W. C. Haxton, Phys. Rev. Lett. 43 (1979) 1922.

[99] A. Willis, M. Morlet, N. Marty, C. Djalali, J. Guillot, H. Langevin-Joliot, J. Vand de Wiele, A. Mack, B. Bonin, R. Fergerson, E. Tomasi-Gustafsson, J. C. Lugol, J. C. Duchazeaubeneix and H. Sakaguchi, Phys. Rev. C 43 (1991) 2177.

[100] H. Okamura, S. Fujita, Y. Hara, K. Hatanaka, T. Ichihara, S. Ishida, K. Katoh, T. Niizeki, H. Ohnuma, H. Otsu, H. Sakai, N. Sakamoto, Y. Satou, T. Uesaka, T. Wakasa and T. Yamashita, Phys. Lett. B 345 (1995) 1.

[101] G. W. Hoffmann, L. Ray, M. L. Barlett, R. Fergerson, J. McGill, E. C. Milner, Kamal K. Seth, D. Barlow, M. Bosko, S. Iverson, M. Kaletka, A. Saha and D. Smith, Phys. Lev. Lett. 47 (1981) 1436.

[102] M. S. Fayache, P. von Neumann-Cosel, A. Richter, Y. Y. Sharon and L. Zamick, Nucl. Phys. A 627 (1997) 14.

[103] S. Kato, N. Matsuoka, T. Noro, T. Saito, H. Sakai, M. Nakamura, M. Yosoi, T. Ichihara, K. Hatanaka and H. Ogawa, Nucl. Instr. and Meth. 238 (1985) 453.

[104] C. Furget, J. Goy, S. Kox, J. S. Réal, J. Arvieux, E. J. Beise, L. Bimbot, E. Brash, H. Breuer, G. Collins, F. Duncan, J. E. Ducret, M. Garçon, R. Gilman, C. Glashausser, V. P. Ladygine, M. Morlet, F. Merchez, J. Niskanen, P. Rutt, E. Tomasi-Gustafsson and E. Voutier, Nucl. Phys. A655 (1999) 495.

[105] R. V. Reid, Ann. of Phys. 50 411 (1968).

[106] M. Lacombe, B. Loiseau, R. Vinh Mau, J. Côté, P. Pirés and R. de Tourreil, Phys. Lett. B 101 (1981) 139.

[107] J. A. McNeil, L. Ray and S. J. Wallace, Phys. Rev. C 27 (1983) 2123.

[108] X. Q. Zhu, N. Mobed and S. S. Wong, Nucl. Phys. A 466 (1987) 623.

[109] R. A. Arndt, C. H. Oh, I. I. Strakovsky and R. L. Workman, Phys. Rev. C 56 (1997) 3005.

[110] The SAID data base can be viewed through telnet access to said.phys.vt.edu with username said. It can also be seen at the WWW site http://gwdac.phys.gwu.edu/.

[111] S. S. M. Wong, *Computational Methodes in Physics and Engineering*, Prentice Hall, Englewood Cliffs, New Jersey, 1992.

[112] A. K. Kerman, H. McManus and R. M. Thaler, Annals of Phys. 8 (1959) 551.

[113] G. R. Satchler, Nucl. Phys. 55 (1964) 1.

[114] C. J. Joachain, *Quantum Collision Theory*, North-Holland Publish Company, Amsterdam, 1975.

[115] A. R. Edomonds, *Angular Momentum in Quantum Mechanics*, Princeton University Press, Princeton New Jersey, 1957.

[116] P. J. Brussaard and P. W. M. Glaudemans, *Shell-Model Applications in Nuclear Spectroscopy*, North-Holland Publishing Company, Amsterdam, 1977.

[117] L. J. Tassie and F. C. Barker, Phys. Rev. 111 (1958) 940.

[118] V. A. Madsen, Nucl. Phys. 80 (1966) 177.

[119] Proc. 3rd Int. Symp. on Polarization phenomena in nuclear reactions (Univ. of Wisconsin Press, Madison, 1971).

[120] H. Sherif and J. S. Blair, Phys. Lett. 26 B (1968) 489.

[121] A. Ingemarsson, E. Hagberg and H. Sherif, Nucl. Phys. A 216 (1973) 271.

[122] A. M. Bernstein, In *Advances in nuclear physics* (M. Baranger and E. Vogt, eds.), Vol. 3, Plenum Press, New York, 1969, p. 325.

[123] K. Van der Borg, M. N. Harakeh and A. Van der Woude, Nucl. Phys. A 365 (1981) 243.

[124] F. Osterfeld, J. Wambach, H. Lenske and J. Speth, Nucl. Phys. A 318 (1979) 45.

[125] C. Djalali, N. Marty, M. Morlet and A. Willis, Nucl. Phys. A 380 (1982) 42.

[126] D. K. McDaniels, J. R. Tinsley, J. Lisantti, D. M. Drake, I. Bergqvist, L. W. Swenson, F. E. Bertrand, E. E. Gross, D. J. Horen, T. P. Sjoreen, R. Liljestrand and H. Wilson, Phys. Rev. C 33 (1986) 1943.

[127] C. Glashausser, R. De Swiniarski, K. Jones, S. Nanda, F. T. Baker, M. Grimm, V. Penumetcha, A. Scott, G. Adams, G. Igo, G. W. Hoffmann, J. Moss, W. Swenson and B. E. Wood, Phys. Lett. 116 B (1982) 215.